Imperial College London
Department of Aeronautics

Simulation of high-cycle fatigue-driven delamination in composites using a cohesive zone model

Konstanze Kiefer

September 2014

Submitted in part fulfilment of the requirements for the degree of Doctor of Philosophy of Imperial College London and the Diploma of Imperial College London

The research leading to these results has received funding from the European Community's Seventh Framework Programme FP7/2007-2013 under grant agreement n°213371 (www.maaximus.eu).

The copyright of this thesis rests with the author and is made available under a Creative Commons Attribution Non-Commercial No Derivatives licence. Researchers are free to copy, distribute or transmit the thesis on the condition that they attribute it, that they do not use it for commercial purposes and that they do not alter, transform or build upon it. For any reuse or redistribution, researchers must make clear to others the licence terms of this work.

Wissenschaft: Es ist nicht ihr Ziel, der unendlichen Weisheit eine Tür zu öffnen, sondern eine Grenze zu setzen dem unendlichen Irrtum.

Bertolt Brecht (1898-1956), dt. Dramatiker u. Dichter

Declaration

I confirm that the following work is my own. I have referenced all work that is not my own to my best knowledge.

Acknowledgements

A long journey has come to an end with the completion of the thesis. Foremost I would like to thank Dr. Paul Robinson for the many meetings and the support I have been given throughout my PhD. I would also like to thank Dr. Silvestre Pinho for his assistance.

This research was part of the research project Maaximus and I am grateful for the financial support I received.

I want to thank my parents for their confidence in me. In addition, I would like to thank Chris, Fran, and Larry for giving me a home this last year- it was greatly appreciated. Last but not least thanks to Jack. I love you and I could not have done this without you.

Abstract

In this PhD thesis several published strategies for the simulation of high-cycle fatigue-driven delamination using cohesive elements are investigated in mode I using an efficient analytical model which eliminates the numerical errors involved in a finite element simulation. A detailed sensitivity study of all the models is performed with respect to the element size and the cycle-jump. The models are then compared and their advantages and disadvantages highlighted. For two of the models improvements are proposed and investigated using the analytical model.
Necessary conditions for a successful fatigue model are then highlighted and a new model is proposed. A sensitivity study demonstrates a very good performance of this model. The new fatigue degradation strategy is implemented into a user defined element (UEL) within the commercial finite element software ABAQUS. Two simulations are then performed for pure mode I and mode II fatigue-driven delamination. The new strategy is shown to achieve good agreement with the input Paris law and is also shown to perform well in comparison with FE implementations of some of the published cohesive element strategies for fatigue-driven growth of delamination.

Contents

List of Figures **11**

List of Tables **20**

1. Introduction **24**

1.1. Composites 24

1.2. Delamination in composites 26

1.3. Fatigue and fatigue modelling 27

1.4. Aircraft Industry Standards and Design of Structures 30

1.5. Objectives and outline of the thesis 32

2. Fatigue of composites, cohesive zone models, and modelling of fatigue delamination **34**

2.1. Fatigue of composites 34

2.1.1. Environmental factors in the fatigue of composites 36

2.1.2. Fracture characterisation 38

2.1.3. Fatigue loading 38

2.2. Fatigue delamination- modelling and testing 39

2.2.1. Fatigue delamination modelling 39

2.2.2. Fatigue delamination testing 43

2.3. The cohesive zone model 51

2.4. Delamination modelling with cohesive elements 57

2.4.1. Static delamination modelling with cohesive elements 57

2.4.2. Fatigue delamination modelling with cohesive elements . . . 62

2.5. Cylinder model 72

2.5.1. Description of the cylinder model 72
2.5.2. Displacement-controlled analysis 76
2.5.3. Moment-controlled analysis 78
2.5.4. Comparison of static constitutive laws with the cylinder model 79
2.5.5. Summary 88

3. Investigation of existing fatigue degradation strategies 89
3.1. Introduction 89
3.2. Overview of the investigation methodology 90
3.3. Peerlings' degradation model 93
3.3.1. Description of the Peerlings' model 93
3.3.2. Results for the Peerlings's model 97
3.3.3. Discussion of the Peerlings' model 107
3.4. Turon fatigue strategy 108
3.4.1. Description of the Turon model 108
3.4.2. Results for the Turon model 112
3.4.3. Discussion of the Turon model 122
3.5. Harper model 124
3.5.1. Description of the Harper model 124
3.5.2. Results for the Harper model 128
3.5.3. Discussion of the Harper model 137
3.6. Kawashita-Hallett model 139
3.6.1. Description of the Kawashita-Hallett model 139
3.6.2. Results for the Kawashita-Hallett model 141
3.6.3. Summary and Discussion for the Kawashita-Hallett model . . 150
3.7. Comparison of the investigated degradation strategies and Conclusion150

4. Improvements to existing fatigue strategies and a new model 155
4.1. Improving existing strategies 156
4.1.1. Two faster alternatives to the Peerlings' model 156
4.1.2. Improved Paris law for the Turon model 164
4.2. Development and evaluation of a new strategy for fatigue-driven delamination growth 167

4.2.1. Unsuccessful modelling attempts . . . 167
4.2.2. Input data from the Paris law . . . 168
4.2.3. The constitutive response of the cohesive zone in fatigue . . . 169
4.2.4. The link between cycles to fail an element and the delamination growth rate . . . 169
4.2.5. Description of proposed model . . . 170
4.2.6. Results from the cylinder model for the new fatigue degradation strategy . . . 173
4.2.7. Discussion of the new model . . . 181
4.3. Conclusions for the improvements and the new model . . . 182

5. Finite element implementation of the improved fatigue model 184
5.1. Implementation of the interface element . . . 185
5.1.1. Equilibrium for the cohesive crack . . . 185
5.1.2. Discretization of the cohesive zone . . . 186
5.1.3. Implementation into the finite element solver . . . 191
5.2. Investigation of the finite element implementation . . . 196
5.2.1. Features common to both test cases . . . 196
5.2.2. Fatigue simulation of the Double Cantilever Beam . . . 196
5.2.3. Fatigue simulation of the End-loaded split specimen . . . 204
5.3. Conclusion . . . 211

6. Conclusions and Future Work 213
6.1. Conclusions . . . 213
6.1.1. Comparison of existing fatigue models . . . 213
6.1.2. Improvement to existing fatigue models . . . 214
6.1.3. Development of an improved fatigue model . . . 215
6.1.4. Finite element implementation of the new fatigue model . . . 216
6.2. Suggestions for future work . . . 218
6.2.1. Further improvements of the new fatigue degradation strategy 218
6.2.2. Reliance on experimental data and data acquisition . . . 220
6.2.3. Alternative numerical techniques . . . 220

A. User-defined element (UEL) for modelling mode I fatigue delamination in ABAQUS **221**

B. Input file for fatigue delamination simulation of the DCB **239**

Bibliography **245**

List of Figures

1.1. Use of composites in airbus aircraft [DC03] 25
1.2. Classifications of composites 26
1.3. Typical locations of delaminations from [O'B09] 27
1.4. Exemplary S-N curve for steels 28
1.5. Fatigue testing of a Boeing 787 31
1.6. Building blocks approach 31

2.1. Damage development during the fatigue life of a laminated composite [Har03] 35
2.2. Damage accumulation during the fatigue life of a laminated composite [Har03] 36
2.3. Fatigue life for unidirectional composites under on-axis loading [Tal08] 37
2.4. Modes of fracture 38
2.5. Sinusoidal loading 39
2.6. Fatigue crack propagation 41
2.7. Comparison of mode I and mode II delamination growth onset at R=0.1 [MM90] 44
2.8. Crack propagation rate vs. maximum energy release rate [O'B81] . . 45
2.9. Relation between crack propagation and energy release rate for T300/914C [HTGH87] 46

2.10. Delamination growth rate versus strain energy release rate range [KB97] 47
2.11. Modified Paris plot showing the strain energy release rate for each mode normalised by the corresponding fracture toughness [ASG01],[Bla04] 48
2.12. Double cantilever beam specimen and loading [Bla04] 49
2.13. End loaded split specimen and loading [Bla04] 49
2.14. End notched flexure specimen and loading [Bla04] 50
2.15. Mixed mode bending specimen and loading [Bla04] 50
2.16. (a) Barenblatt cohesive zone model and (b) Cohesive zone model by Dugdale 52
2.17. Assumed variation of stress σ with crack width δ, cohesive zone . . . 52
2.18. Concrete beam in tension, FE model 53
2.19. Static cohesive zone laws mode I 54
2.20. Static cohesive zone laws mode II 54
2.21. Interface element 56
2.22. (a) Cohesive element taken from [OP99]. The surfaces S^+ and S^- originally coincide (b) Assembly of a 12-node triangular cohesive element and two 10-node tetrahedral elements 56
2.23. Bilinear law with stiffness based damage degradation 57
2.24. Mixed-mode response bilinear law [PIR06] 59
2.25. Predicted fatigue crack growth and constitutive response for (a) step-wise change in maximum load and (b) step-wise change in R from [Sie04] 63
2.26. Numerically computed load 63
2.27. Numerically computed displacement 64
2.28. Fatigue damage D_f and cohesive law damage D_s [KCKA10] 68
2.29. Constitutive response with fatigue damage D_s and D_f [LL12] 70
2.30. Cohesive zone in DCB under opening displacement [LL12] 70
2.31. Cylinder model 73
2.32. Projection of cylinder model 73
2.33. Cohesive zone and critical spring angle ϕ_c 74
2.34. Cylinder with first spring at maximum extension δ_c at angle α 75
2.35. Angle α vs. Radius R for various δ_c 76

2.36. Detailed view of cohesive zone 77
2.37. Constitutive laws 80
2.38. Bilinear law 82
2.39. Polynomial law 83
2.40. Exponential law 84
2.41. Maximum relative error e_{max} in the calculation of M_T against the number of elements in the cohesive zone for three different constitutive laws for $M_{th} = 0.05M_c$ 85
2.42. Interface traction distribution of the bilinear law in the CZ 86
2.43. Interface traction distribution of the polynomial law in the CZ 86
2.44. Interface traction distribution of the exponential law in the CZ 87

3.1. Experimental data for for HTA/6376C from [ASG01], Paris law and error lines 91
3.2. Bilinear law with stiffness based damage degradation 94
3.3. Experimental data, paris law, and Peerlings' model crack growth rates for different element sizes and cycle jumps. Δl in [mm], ΔN in [cycles] 98
3.4. Relative error in % of crack growth rate $\frac{da}{dN}$ for different element sizes and cycle jumps. Δl in [mm], ΔN in [cycles] 98
3.5. Traction-separation curves for different percentages of G_c. (a) $\Delta l = 0.005$ mm, $\Delta N = 100$ cycles, (b) $\Delta l = 0.005$ mm $\Delta N = 2500$ cycles, (c) $\Delta l = 0.25$ mm, $\Delta N = 100$ cycles, (d)$\Delta l = 0.25$ mm, $\Delta N = 2500$ cycles 100
3.6. Relative error in % of $\frac{da}{dN}$ in Peerling model with respect to element size Δl and cycle jump ΔN for $G_a = 0.25G_c$ 101
3.7. Projection of figure 3.6 102
3.8. Relative error in % of $\frac{da}{dN}$ in Peerling model with respect to the number of elements in the cohesive zone and the number of cycle jumps to fail one element for $G_a = 0.25G_c$ 102
3.9. Relative error in % of $\frac{da}{dN}$ in Peerling model with respect to element size Δl and cycle jump ΔN for $G_a = 0.35G_c$ 103

3.10. Relative error in % of $\frac{da}{dN}$ in Peerling model with respect to the number of elements in the cohesive zone and the number of cycle jumps to fail one element for $G_a = 0.35G_c$ 104
3.11. Relative error in % of $\frac{da}{dN}$ in Peerling model with respect to element size Δl and cycle jump ΔN for $G_a = 0.45G_c$ 104
3.12. Relative error in % of $\frac{da}{dN}$ in Peerling model with respect to the number of elements in the cohesive zone and the number of cycle jumps to fail one element for $G_a = 0.45G_c$ 105
3.13. Relative error in % of $\frac{da}{dN}$ in Peerling model with respect to element size Δl and cycle jump ΔN for $G_a = 0.55G_c$ 105
3.14. Relative error in % of $\frac{da}{dN}$ in Peerling model with respect to the number of elements in the cohesive zone and the number of cycle jumps to fail one element for $G_a = 0.55G_c$ 106
3.15. Consumed energy ξ in bilinear law 109
3.16. Schematic drawing of crack growth during fatigue algorithm 110
3.17. Calculation of energy release rate range ΔG_a 111
3.18. Experimental data, Paris law, and Turon model crack growth rates for different element sizes and damage increments. Δl in [mm] 113
3.19. Relative error in % in crack growth rate $\frac{da}{dN}$ for different element sizes and damage increments. Δl in [mm] 113
3.20. Numerical and input Paris law or different static cohesive zone lengths L_{cz}, $\Delta l = 0.005$ mm, $\Delta D = 0.00005$ 114
3.21. Traction-separation curves for different applied energy release rates G_a as percentages of G_c. (a) $\Delta l = 0.005$ mm, $\Delta D = 0.00005$, (b) $\Delta l = 0.005$ mm $\Delta D = 0.005$, (c) $\Delta l = 0.25$ mm, $\Delta D = 0.00005$, (d)$\Delta l = 0.25$ mm, $\Delta D = 0.005$ 115
3.22. Relative error in % of $\frac{da}{dN}$ in Turon model with respect to element size Δl and damage increment ΔD for $G_a = 0.25G_c$ 116
3.23. Relative error in % of $\frac{da}{dN}$ in Turon model as a function of the number of elements in the cohesive zone n_{cz} and the number of cycle jumps to fail one element n_f for $G_a = 0.25G_c$ 117

3.24. Relative error in % of $\frac{da}{dN}$ in Turon model with respect to element size Δl and damage increment ΔD for $G_a = 0.35G_c$ 118
3.25. Relative error in % of $\frac{da}{dN}$ in Turon model as a function of the number of elements in the cohesive zone n_{cz} and the number of cycle jumps to fail one element n_f for $G_a = 0.35G_c$ 119
3.26. Relative error in % of $\frac{da}{dN}$ in Turon model with respect to element size Δl and damage increment ΔD for $G_a = 0.45G_c$ 119
3.27. Relative error in % of $\frac{da}{dN}$ in Turon model as a function of the number of elements in the cohesive zone n_{cz} and the number of cycle jumps to fail one element n_f for $G_a = 0.45G_c$ 120
3.28. Relative error in % of $\frac{da}{dN}$ in Turon model with respect to element size Δl and damage increment ΔD for $G_a = 0.55G_c$ 121
3.29. Relative error in % of $\frac{da}{dN}$ in Turon model as a function of the number of elements in the cohesive zone n_{cz} and the number of cycle jumps to fail one element n_f for $G_a = 0.55G_c$ 121
3.30. Static damage 125
3.31. Cohesive zone 126
3.32. Accumulation of $D_{f,u}$ 127
3.33. Static and fatigue damage 128
3.34. Experimental data, paris law, and Harper model crack growth rates for different element sizes and cycle-jumps. Δl in mm, ΔN in cycles . 129
3.35. Relative error in % in crack growth rate $\frac{da}{dN}$ for different element sizes and and cycle-jumps. Δl in mm, ΔN in cycles 130
3.36. Traction-separation curves for different percentages of G_c. (a) $\Delta l = 0.005$ mm, $\Delta N = 100$ cycles, (b) $\Delta l = 0.005$ mm $\Delta N = 2500$ cycles, (c) $\Delta l = 0.25$ mm, $\Delta N = 100$ cycles, (d)$\Delta l = 0.25$ mm, $\Delta N = 2500$ cycles 130
3.37. Relative error in % of $\frac{da}{dN}$ in Harper model with respect to element size Δl and cycle jump ΔN for $G_a = 0.25G_c$ 131
3.38. Relative error in % of $\frac{da}{dN}$ in Harper model with respect to the number of elements in the cohesive zone and the number of cycle jumps to fail one element for $G_a = 0.25G_c$ 132

3.39. Relative error in % of $\frac{da}{dN}$ in Harper model with respect to element size Δl and cycle jump ΔN for $G_a = 0.35G_c$ 132
3.40. Relative error in % of $\frac{da}{dN}$ in Harper model with respect to the number of elements in the cohesive zone and the number of cycle jumps to fail one element for $G_a = 0.35G_c$ 133
3.41. Relative error in % of $\frac{da}{dN}$ in Harper model with respect to element size Δl and cycle jump ΔN for $G_a = 0.45G_c$ 134
3.42. Relative error in % of $\frac{da}{dN}$ in Harper model with respect to the number of elements in the cohesive zone and the number of cycle jumps to fail one element for $G_a = 0.45G_c$ 134
3.43. Relative error in % of $\frac{da}{dN}$ in Harper model with respect to element size Δl and cycle jump ΔN for $G_a = 0.55G_c$ 135
3.44. Relative error in % of $\frac{da}{dN}$ in Harper model with respect to the number of elements in the cohesive zone and the number of cycle jumps to fail one element for $G_a = 0.55G_c$ 136
3.45. (a) Cohesive zone shape, (b) corresponding fatigue cohesive laws . . 137
3.46. (a) Assumed cohesive zone law, (b) Static cohesive zone shape 138
3.47. Cohesive zone with crack tip tracing 140
3.48. Experimental data, paris law, and crack tip tracing model crack growth rates for different element sizes and cycle-jumps. Δl in mm, ΔN in cycles 141
3.49. Relative error in % in crack growth rate $\frac{da}{dN}$ for different element sizes and and cycle-jumps. Δl in mm, ΔN in cycles 142
3.50. Traction-separation curves for different percentages of G_c. (a) $\Delta l = 0.005$ mm, $\Delta N = 100$ cycles, (b) $\Delta l = 0.005$ mm $\Delta N = 2500$ cycles, (c) $\Delta l = 0.25$ mm, $\Delta N = 100$ cycles, (d) $\Delta l = 0.25$ mm, $\Delta N = 2500$ cycles 143
3.51. Relative error in % of $\frac{da}{dN}$ in crack tip tracing model with respect to element size Δl and cycle jump ΔN for $G_a = 0.25G_c$ 144
3.52. Projection of figure 3.51 onto Δl-ΔN plane 145

3.53. Relative error in % of $\frac{da}{dN}$ in crack tip tracing model with respect to the number of elements in the cohesive zone and the number of cycle jumps to fail one element for $G_a = 0.25G_c$ 145
3.54. Relative error in % of $\frac{da}{dN}$ in crack tip tracing model with respect to element size Δl and cycle jump ΔN for $G_a = 0.35G_c$ 146
3.55. Relative error in % of $\frac{da}{dN}$ in crack tip tracing model with respect to the number of elements in the cohesive zone and the number of cycle jumps to fail one element for $G_a = 0.35G_c$ 147
3.56. Relative error in % of $\frac{da}{dN}$ in crack tip tracing model with respect to element size Δl and cycle jump ΔN for $G_a = 0.45G_c$ 147
3.57. Relative error in % of $\frac{da}{dN}$ in crack tip tracing model with respect to the number of elements in the cohesive zone and the number of cycle jumps to fail one element for $G_a = 0.45G_c$ 148
3.58. Relative error in % of $\frac{da}{dN}$ in crack tip tracing model with respect to element size Δl and cycle jump ΔN for $G_a = 0.55G_c$ 149
3.59. of $\frac{da}{dN}$ in crack tip tracing model with respect to the number of elements in the cohesive zone and the number of cycle jumps to fail one element for $G_a = 0.55G_c$ 149
3.60. Paris laws for $\Delta l = 0.005mm$ and $\Delta N = 100cycles/\Delta D = 0.00005$ . . 151
3.61. Relative error vs. G_a for $\Delta l = 0.005$ mm and $\Delta N = 100$ cycles$/\Delta D = 0.00005$ 152

4.1. Numerical paris law showing the influence of μ_1 for $\mu_2 = 0.7$ 157
4.2. Numerical paris law showing the influence of μ_2 for $\mu_1 = 0.7$ 157
4.3. Static damage vs displacement 158
4.4. Difference in relative error between explicit and implicit damage for $G_a = 0.25G_c$ 159
4.5. Speed in s to simulate 2,000,000 cycles, implicit damage for $G_a = 0.25G_c$ 159
4.6. Speed in s to simulate 2,000,000 cycles, explicit damage for $G_a = 0.25G_c$ 160
4.7. Experimental data, paris law, and fast Peerlings' model crack growth rates for different element sizes and cycle jumps. Δl in mm, ΔN in cycles 161

4.8. Relative error in % in crack growth rate $\frac{da}{dN}$ for different mesh sizes and cycle-jumps. Δl in mm, ΔN in cycles 162
4.9. Relative error in % of $\frac{da}{dN}$ in with respect to the number of elements in the cohesive zone and the number of cycle jumps to fail one element for $G_a = 0.25G_c$ 162
4.10. Relative error in % of $\frac{da}{dN}$ with respect to the number of elements in the cohesive zone and the number of cycle jumps to fail one element for $G_a = 0.55G_c$ 163
4.11. Calculation of G_a for equation (3.44) 164
4.12. Experimental Paris law and numerical Paris law from Turon model . 165
4.13. Relative error in % of $\frac{da}{dN}$ with respect to input Paris law in Turon model 165
4.14. Traction-separation response with equal area absorption 168
4.15. Fatigue constitutive law 171
4.16. Cohesive zone 172
4.17. Comparison $\frac{da}{dN}$ vs. G_a of experimental data, Paris law and numerical model 173
4.18. Relative error in % in crack growth rate $\frac{da}{dN}$ for different mesh sizes and cycle-jumps. Δl in mm, ΔN in cycles 174
4.19. Cycles vs. contact point at $G_a = 0.45G_c$, Δl=0.1 mm, ΔN = 500 cycles 175
4.20. Traction-separation response for fractions of G_c. (a) $\Delta l = 0.005$ mm, $\Delta N = 100$ cycles, (b) $\Delta l = 0.005$ mm, $\Delta N = 2500$ cycles, (c) $\Delta l = 0.25$ mm, $\Delta N = 100$ cycles, (d) $\Delta l = 0.25$ mm, $\Delta N = 2500$ cycles 175
4.21. Relative error in % of $\frac{da}{dN}$with respect to Paris law for $G_a = 0.25G_c$ vs. element size and cycle jump 176
4.22. Relative error in % of $\frac{da}{dN}$ with respect to the number of elements in the cohesive zone and the number of cycle jumps it takes to fail one element at $G_a = 0.25G_c$ 177
4.23. Relative error in % of $\frac{da}{dN}$ with respect to Paris law for $G_a = 0.35G_c$ vs. element size and cycle jump 177
4.24. Relative error in % of $\frac{da}{dN}$ with respect to the number of elements in the cohesive zone and the number of cycle jumps it takes to fail one element at $G_a = 0.35G_c$ 178

4.25. Relative error in % of $\frac{da}{dN}$ with respect to Paris law for $G_a = 0.45G_c$ vs. element size and cycle jump 178
4.26. Relative error in % of $\frac{da}{dN}$ with respect to the number of elements in the cohesive zone and the number of cycle jumps it takes to fail one element at $G_a = 0.45G_c$ 179
4.27. Relative error in % of $\frac{da}{dN}$ with respect to Paris law for $G_a = 0.55G_c$ vs. element size and cycle jump 180
4.28. Relative error in % of $\frac{da}{dN}$ with respect to the number of elements in the cohesive zone and the number of cycle jumps it takes to fail one element at $G_a = 0.55G_c$ 180

5.1. Body with cohesive crack 185
5.2. Cohesive element 187
5.3. Global and local coordinate system 189
5.4. Reversed loading in mode II 193
5.5. Information exchange of subroutines and solver 195
5.6. DCB specimen, L = 50 mm, h = 1 mm, a_0 = 20 mm, W= 1 mm 197
5.7. Loading of DCB FE model 198
5.8. Paris law,experimental data and numerical results 198
5.9. Relative error in Paris law 199
5.10. Fatigue constitutive behaviour in mode I for a range of G_a as a percentage of G_c, $\Delta l = 0.05$ mm, $n_f = 50$ 200
5.11. Cycles vs. Crack growth for different mesh sizes 201
5.12. Analysis increments vs. applied energy release rate G_a 201
5.13. Cohesive zone profile of traction and displacement for coarse and fine mesh at $G_a = 0.25G_c$, $N = 1,000,000$ cycles 202
5.14. Relative error in Paris law compared to previous models 203
5.15. ELSspecimen, $a_0 = 60$ mm, $L = 90$ mm, $W = 1$ mm, $h = 1$ mm 204
5.16. Loading of ELS FE model 205
5.17. Paris law, experimental data, and numerical results 205
5.18. Relative error in Paris law 206

5.19. Fatigue constitutive response in mode II for a range of G_a as a percentage of G_c, $\Delta l = 0.1$ mm, $n_f = 50$ 207
5.20. Crack growth vs. Cycles, (a) $G_a = 0.15G_c$, (b) $G_a = 0.25G_c$ 208
5.21. Analysis increments vs. applied energy release rate G_a for $\Delta l = 0.1$ mm, $n_f = 150$(obtained from crack tip) 209
5.22. Cohesive zone profile of traction and displacement for coarse and fine mesh at $G_a = 0.15G_c$, $N = 1,000,000$ cycles 210
5.23. Relative error in Paris law compared to previous models 211

List of Tables

2.1. Constitutive law parameters 81
2.2. Cylinder parameters 81
2.3. Minimum number of elements n_{cz} required in cohesive zone, so that the relative error is below the specified one . Bilin=Bilinear law, Poly=Polynomial law, Exp=Exponential law 85

3.1. Paris law parameters for HTA/6376C based on the experimental data from [ASG01] 90
3.2. Peerlings' law parameters 97
3.3. Crack growth parameters for Peerlings' law. Δl in [mm], ΔN in [cycles] 99
3.4. Minimum values for $n_f(\Delta N)$ and $n_{cz}(\Delta l)$ with respect to the relative errors in $\frac{da}{dN}$. Δl in [mm], ΔN in cycles 107
3.5. Input parameters Turon model 112
3.6. Crack growth for Turon model, Δl_{005} = 0.005 mm, Δl_{25} = 0.25 mm . . 114

3.7. Minimum values for $n_f(\Delta D)$ and $n_{cz}(\Delta l)$ with respect to the relative errors in $\frac{da}{dN}$. Δl in [mm] 122
3.8. Model input 128
3.9. Crack growth parameters for Harper model 131
3.10. Minimum values for $n_f(\Delta N)$ and $n_{cz}(\Delta l)$ with respect to the relative errors in $\frac{da}{dN}$. Δl in [mm], ΔN in cycles 136
3.11. Crack growth parameters for crack tip tracing strategy 142
3.12. Minimum values for $n_f(\Delta N)$ and $n_{cz}(\Delta l)$ with respect to the relative errors in $\frac{da}{dN}$. Δl in [mm], ΔN in cycles 150
3.13. Comparison of strategies I: input parameters and point-localness . . 151
3.14. Comparison of strategies II: advantages and disadvantages 154

4.1. Input parameters 161
4.2. Minimum values for $n_f(\Delta l)$ and $n_{cz}(\Delta l)$ with respect to the relative errors in $\frac{da}{dN}$. Δl in [mm], ΔN in cycles 181

5.1. Material properties of HTA/6376C from [ASG01] 196
5.2. Mode I interface properties 197
5.3. Cohesive zone length, and cycle-jump in mode I 199
5.4. Comparison of material and interface properties between different studies 203
5.5. Mode II interface properties 204
5.6. Cohesive zone length, and cycle-jump in mode II 206
5.7. Comparison of material and interface properties between different studies, mode II 210

Nomenclature

M	-	Moment [Nmm]
L_{cz}	-	Static cohesive zone length [mm]
l_{cz}	-	Cohesive zone length in fatigue [mm]
a	-	Crack length [mm]
N	-	Cycles
ΔN	-	Cycle jump
N_f	-	Numer of cycles to fail one element
n_f	-	Number of cycle-jumps to fail one element
t	-	Time [s]
L,l	-	Length [mm]
P	-	Load [N]
D	-	Damage
d	-	distance [mm]
Δl	-	Element size [mm]
$\frac{da}{dN}$	-	Crack growth rate [$\frac{mm}{cycle}$]
G	-	Energy release rate [$\frac{N}{mm}$]
C, m	-	Paris law parameters
W	-	Width [mm]
R	-	Radius [mm]
$\boldsymbol{\theta}$	-	Cylinder rotation angle
$\boldsymbol{\phi}$	-	Spring rotation angle
R	-	Radius [mm]
δ	-	relative displacement [mm]
σ	-	cohesie traction [$\frac{N}{mm^2}$]
n_{cz}	-	Number of elements in cohesive zone
F	-	Force [N]
e	-	Error
α,β,γ	-	Peerlings' law parameters
K	-	Elastic stiffness [$\frac{N}{mm^3}$]
$\mathbf{n}$	-	Surface normal

$\mathbf{u}$ - Displacement

$\boldsymbol{\epsilon}$ - Strain

$\boldsymbol{\sigma}$ - Stress

$\mathbf{C}$ - Constitutive tensor

Γ - boundary

Ω - Domain

v - Test function

$\mathbf{D}$ - Cohesive constitutive tensor

$\mathbf{K}$ - Stiffness matrix

$\mathbf{f}$ - Residual forces

$\mathbf{J}$ - Jacobian

E_{ii} - Young's moduli [GPa]

G_{ij} - Shear moduli [GPa]

ν_{ij} - Poisson ratios

I - Moment of area

Frequent subscripts

a - applied

th - threshold

c - critical

I - mode I

II - mode II

fat,f - fatigue

s - static

cz - cohesive zone

d - damage

e - element

T - total

0 - constitutive law parameters

N - nodal

1. Introduction

1.1. Composites

A composite material is a natural or engineered combination of two or more materials with physical properties differing significantly from those of the constituents. The combination takes place on a macroscopic level so that the components remain distinct. The advantage of composites is that they can be tailored to exhibit the best qualities of their constituents and often some qualities that neither constituent possesses. Some properties that may be improved by forming a composite material are strength, stiffness, weight, temperature-dependent behaviour,thermal insulation, corrosion resistance, and fatigue life. It is therefore no surprise that composites are gaining increasing popularity in modern high-performance products although they are not a recent invention. Straw-reinforced bricks even get a biblical mention in the old testament (Exodus 6:5)

> Ye shall no more give the people straw to make brick, as heretofore: let them go and gather straw for themselves.

These days, making a composite is often a complex process and sending the people to gather their own carbon fibres is out of the question. A major field of application for highly engineered composites is the aerospace industry. The first aeroplane embarked on its virgin flight not much more than a century ago and for more than half that time composite materials have been used to build structural components. The first usage of man-made composites dates back to 1940 when a main spar on a Blenheim aircraft was built from flax thread skin which was infused with phenolic resin followed by the first fibrous composite in 1947 [DC03]. Ever since, the use of composites in aviation has been almost steadily increasing as shown in figure

1.1. But composites have not only been increasingly used in fixed-wing aircraft,

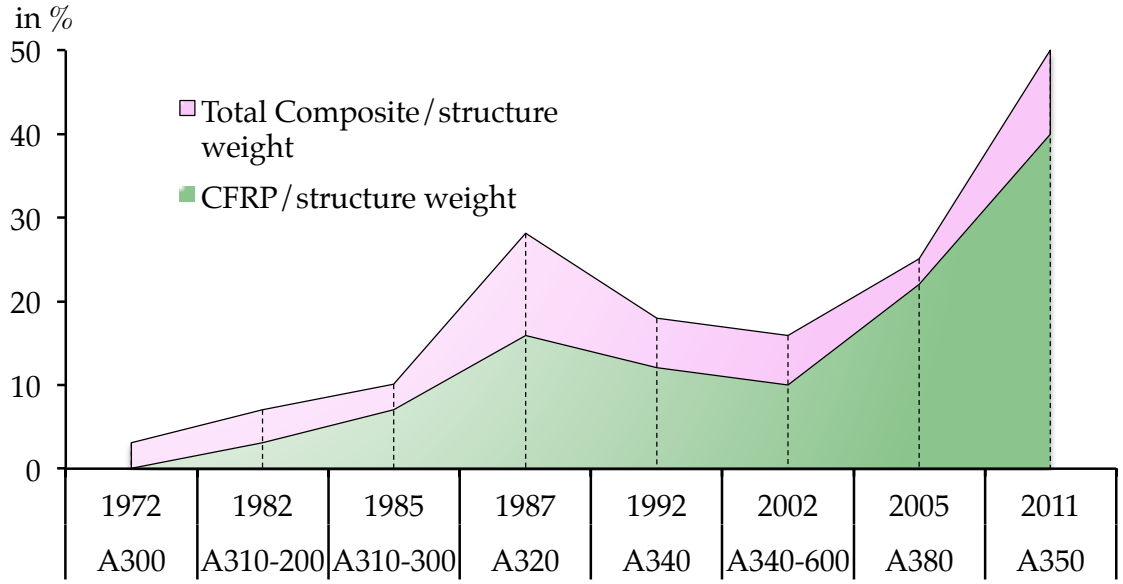


Figure 1.1.: Use of composites in airbus aircraft [DC03]

they also play a very important role in the rotary-wing industry. In the 1960s most rotor blades were still metallic while today most of them are made from composites. Metallic rotor blades used to last for about 1000 hours of use while composite blades last at least 20 000 hours due to their much better fatigue performance.

Composites can be classified in many ways. According to Barbero [Bar10] the main factors are reinforcement and laminate configuration. Figure 1.2 shows the classification according to these two paramaters. The composites of interest in this thesis are laminates made of carbon fibre-reinforced plastics (CFRP), which consist of layers of unidirectional laminae. By changing the fibre-orientation of the the individual laminae, the laminate can be designed to exhibit specific material properties. Laminates are usually made from sheets of pre-impregnated fibres, so called prepregs which are fibres embedded in a partially cured thermoset matrix material. The laminae are then stacked and bonded together through a final curing step.

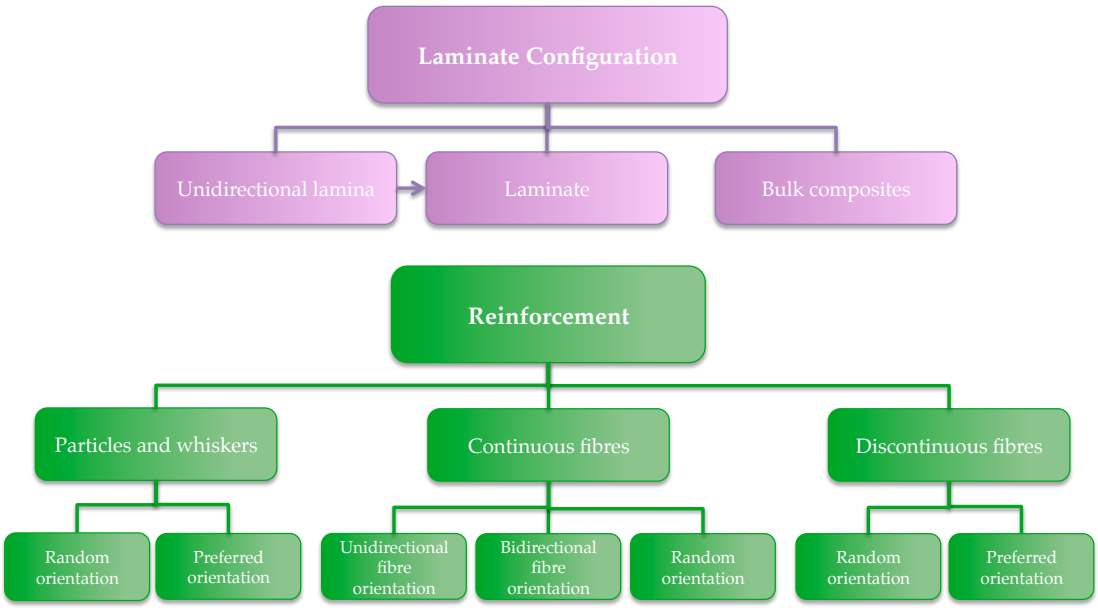


Figure 1.2.: Classifications of composites

1.2. Delamination in composites

Due to its complexity a carbon fibre reinforced composite may fail in a variety of ways which can interact with each other including the breaking of the fibres, micro-cracking of the matrix, debonding of the fibres from the matrix, and delamination which is the separation of the layers in the laminate. Delamination is a critical type of damage for several reasons. It is quite common in laminated composites due to relatively low interlaminar strength. Within a structure, delaminations usually form at points of through-thickness stress concentration such as free edges, ply-drops, curved segments and bonded joints. Some of these locations are shown in Fig.1.3. Once initiated, delaminations can propagate due to static and cyclic loads and lead to a significant reduction in the strength and buckling performance of the composite. Their formation is not limited to a specific stage in the life cycle of a structure. For example, delaminations can be introduced during the manufacturing process due to matrix shrinking or around drilled holes. They can also be caused by impact damage, which can occur during the assembly of the structure for example due to a dropped tool, and in service. An additional characteristic of considerable concern is, that delaminations can develop inside the material with-

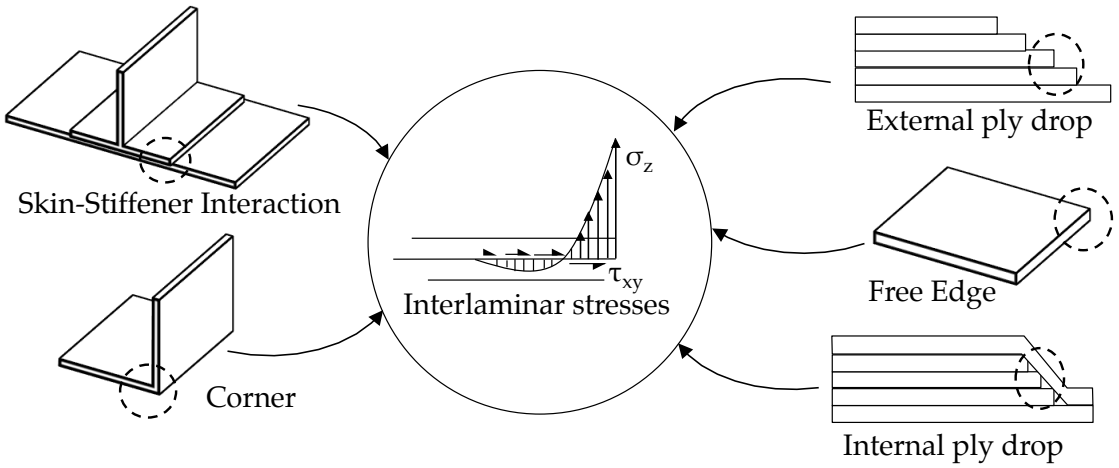


Figure 1.3.: Typical locations of delaminations from [O'B09]

out being visible on the surface and can therefore usually only be detected with the use of a nondestructive testing (NDT) method, for example ultrasonic inspection (UT). It is therefore very important to understand where and when delaminations are likely to occur and what influence propagation has on the integrity of the part when designing structures made from laminated composites.

1.3. Fatigue and fatigue modelling

Even providing a definition of fatigue is challenging. According to the Merriam Webster dictionary, it is "the tendency of a material to break under repeated stress" [Mer03]. Another much quoted definition by Boyer [Boy85] is this: "Fatigue is the progressive, localised permanent structural change that occurs in materials subjected to fluctuating stresses and strains that may result in cracks or fracture after a sufficient number of fluctuations." These two definitions- one stating fatigue as a tendency, the other as a change in a material which may or may not lead to fracture already give a hint about the difficulties involved when studying the subject. Just like delamination, fatigue can be quite invisible for a long time as it is a very gradual process but can lead to catastrophic failure of a structure. One famous example from the history of aeronautics are the crashes of the Comet aeroplanes in the 1950s where it was eventually discovered that stress concentrations in the corners

of the square windows led to fatigue crack growth which resulted in the rupture of the hull in midair [Evi13]. Dramatic fatigue failures like this highlight the need for being able to predict the influence of fatigue on a material and much research has been conducted on the fatigue of metals in particular. One early but still standard way of including fatigue considerations into the design of a structure are S-N diagrams shown in figure 1.4 also called Wöhler diagrams because of Albert Wöhler, who conducted the first fatigue tests with specific stress amplitudes and published his findings in 1870 [Bha10]. In the S-N diagram, S_f is the stress amplitude and N_f

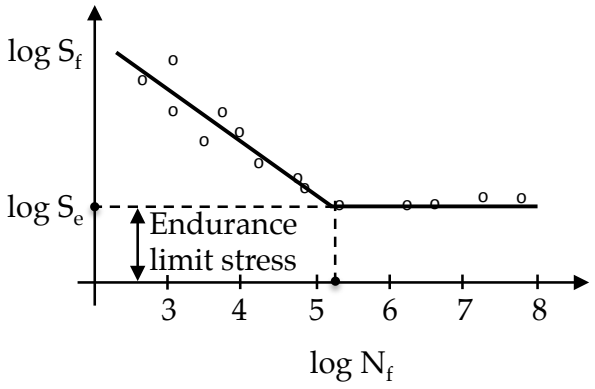


Figure 1.4.: Exemplary S-N curve for steels

the number of cycles plotted on a base 10 log-log graph. Each point corresponds to the fatigue failure of a specimen. For steels there is a stress S_e, the endurance limit stress, below which no fatigue is observable however many cycles are applied, but this is not the case for other materials and the endurance limit is not a material property but depends on the geometry and environmental conditions. In figure 1.4 the number of cycles N_f starts at about 1,000. This is because a distinction is made between high-cycle fatigue, where the stress amplitudes are relatively low and low-cycle-fatigue, where the stress amplitudes are higher, which leads to plastic strains. According to Chung [Chu10] low-cycle fatigue involves a life of 1,000 cycles or less but no clear distinction is drawn in the literature. According to Lemaitre [LSD99] for example, low-cycle fatigue involves a fatigue-life of up to 10,000 cycles and a ratio of the plastic strain to the elastic strain amplitude between 1 and 10. In this thesis the focus is placed solely on high-cycle fatigue. S-N diagrams have been generated for many materials but due to the anisotropic nature of composites additional fail-

ure criteria have to be specified for the fatigue-life prediction of composites. One of the earliest fatigue-life models for fibrous composites was proposed by Hashin and Rotem [HR73], which distinguishes fibre-failure and matrix failure in the following way:

$$\sigma_{11} = S_1^f \tag{1.1}$$

$$(\frac{\sigma_{22}}{S_{12}^f})^2 + (\frac{\tau_{12}}{S_2^f})^2 = 1. \tag{1.2}$$

σ_{11} and σ_{22} are the in-plane stresses along and transverse to the fibres respectively, τ_{12} is the in-plane shear stress. S_1^f S_2^f, and S_{12}^f are the ultimate tensile, transverse and shear stress respectively. Three S-N curves are necessary to apply the criterion, which is only valid for laminates with unidirectional plies, where it is possible to differentiate between fibre and matrix failure. Reviews on fatigue models in composites have been published by Talreja [Tal87], Andersons [And94], and Degrieck [DP01] who all presented their own classifications. More recently Pascoe et.al [PAR13] published a more specialised review for modelling fatigue delamination growth in composites and adhesive bonds. Perhaps the simplest among these all the classes are fatigue-life models like the one just discussed. This is a relatively straightforward way for considering fatigue, but it has a severe drawback: no information about fatigue damage initiation and propagation is taken into account. However, as mentioned earlier, localised damage in the form of, for example, delamination starts very early if not at the beginning of the lifetime of a composite part leading to a gradual deterioration, which is not necessarily catastrophic. Incorporating fatigue only in terms of the total life leads to very conservative designs and makes the scheduling of maintenance or replacement of parts before catastrophic failure occurs more difficult or impossible. In order for a composite structure to be reliable during its service life there needs to to be an accurate prediction of the accumulation of fatigue damage. A detailed review of models for the prediction of delamination propagation, which is the key focus of this thesis, is given in the next chapter.

1.4. Aircraft Industry Standards and Design of Structures

Due to the lack of reliable tools for the prediction of fatigue damage in aircraft composite structures, a widely applied standard in aircraft design today is still the no-growth approach. This means that the loads which are applied to a structure are low enough for no fatigue damage to grow during several lifetimes of the airplane. In the guideline Accepted Means of Compliance (AMC 25-603), the European Aviation safety Agency (EASA) writes

> "§ 6.2.1 Structural details, elements, and subcomponents of critical structural areas should be tested under repeated loads to define the sensitivity of the structure to damage growth. This testing can form the basis for validating a no-growth approach to the damage tolerance requirements.[...]
> § 6.2.3 ...The evaluation should demonstrate that the residual strength of the structure is equal to or greater than the strength required for the specified design loads... For the no-growth concept, residual strength testing should be performed after repeated load cycling."

These paragraphs have been mentioned by Chantal Fualdes, the Head of Composite stress analysis at Airbus in 2006 [Fua06], as forming the guideline for the treatment of fatigue at Airbus.
The no-growth philosophy is also reflected in a newspaper article of "The Times" from December 2009[1] concerning the launch of Boeing's 787 Dreamliner, a boeing statesman was quoted "...Additionally, composite materials do not suffer from fatigue and therefore require fewer maintenance checks..."
Despite this statement to the press, from 2010 to 2013 one Dreamliner airplane has undergone extensive fatigue-testing in a three-year procedure that simulated 100,000 flights to make sure that the aircraft withstands the loads applied during its service life without a catastrophic failure (see figure 1.5[2]).

[1] http://business.timesonline.co.uk/tol/business/industry_sectors/transport/article6958064.ece
[2] http://www.boeing.com



Figure 1.5.: Fatigue testing of a Boeing 787

The fact that composite laminates can be tailored to very specific engineering needs implies complex material behaviour and developing any structure made from composites involves a large number of experimental tests. The design of a complex structure is based on a pyramid of physical tests shown in figure 1.6 for the development of an aircraft. Further up the pyramid tests become more and more expensive

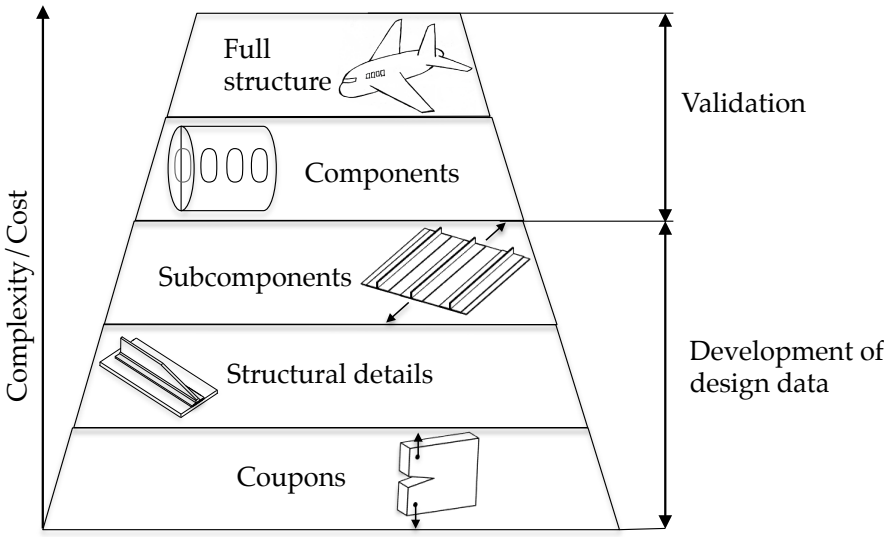


Figure 1.6.: Building blocks approach

and fewer tests are carried out at higher levels. The total number of tests conducted for the certification of an aeroplane is around 10,000 [SGL08]. The design parameters of the higher levels are determined by the results from lower levels. This robust and effective 'building blocks' approach has been applied to all aeroplane develop-

ments in recent decades. The testing is, however very expensive both in time and cost. For the Airbus 380 physical testing took 7 years with a budget of several hundred million Euros [maa08]. In the long term it is desirable to reduce the number of experimental tests by adopting a simulation-based design approach also called Virtual Mechanical Testing. Computer modelling is used to make decisions at each level of the pyramid speeding up the design process and reducing the cost. Ideally, experimental testing would only be required at coupon level to measure basic material properties, and for the validation of the choices made through the computer simulations at the top two levels of the pyramid. In order for this change of design practice accurate modelling methodologies have to be developed.

1.5. Objectives and outline of the thesis

This PhD is part of the MAAXIMUS ("More affordable aircraft structure through extended, integrated and mature numerical sizing") project which is funded by the European Union and Airbus. Its focus is on improving the composition and design of fuselages, to cut assembly time in half and reduce structural weight by 10%.
The objective of this research project was to develop a modelling methodology for the accurate prediction of delamination growth in carbon fibre reinforced composites under high-cycle fatigue. This objective was divided into several steps.

1. A detailed investigation and comparison of existing models for high-cycle fatigue-driven delamination.

2. Improvement of existing fatigue degradation strategies based on the findings of the investigation.

3. Development of a new fatigue degradation strategy based on the findings of the investigation.

4. Implementation of the chosen improved fatigue degradation strategy into a commercial finite element package (ABAQUS).

5. Numerical validation of the fatigue degradation strategy through appropriate simulations and comparison with experimental data.

The thesis is structured as follows:
Chapter 2 gives an overview of fracture mechanics. The virtual crack closure technique is presented and a review of models for fatigue-driven delamination is presented. An overview of the procedures for the acquisition of experimental data is provided. The chapter concludes with an introduction to cohesive zone models, and an overview of modelling high-cycle fatigue-driven delamination using cohesive elements.

In chapter 3 the cylinder model is explained, which is a non-finite-element model allowing a rapid analysis and comparison of fatigue-degradation strategies for cohesive zone modelling of delamination growth in mode I.

Chapter 4 contains an overview of the investigation methodology and a detailed investigation and comparison of four existing high-cycle fatigue degradation strategies.

Chapter 5 deals with improvements of two of the fatigue-degradation strategies examined in Chapter 4. It also contains the development of a new model which is able to predict fatigue delamination growth very accurately. The performance of this model is investigated using the cylinder model.

In chapter 6 the implementation of the new fatigue degradation strategy into the finite element software ABAQUS is described. This is accomplished in the form of a user-defined interface element (UEL). This element is first tested quasi-statically and then two simulations in mode I and mode II are performed to show that the fatigue model is able to accurately predict the delamination propagation under high-cycle fatigue.

Chapter 7 contains a summary of the findings as well as overall conclusions and insights gained from the research. Also, suggestions for future research are made.

2. Fatigue of composites, cohesive zone models, and modelling of fatigue delamination

2.1. Fatigue of composites

As mentioned in the introduction, a material fails in fatigue due to a cyclic loading that causes stresses within the material which are lower than the static strength of the material whereby the gradually accumulating material changes are irreversible. With the increasing use of composite materials and replacement of metals in engineered structures, the investigation of the fatigue properties of composites becomes more and more important. Fatigue in metals is comparatively simple because metals are homogeneous and isotropic materials which display only one mode of failure [Sal72]. On the other hand, the damage process in composites is very complex due to their anisotropic and heterogeneous nature. Figure 2.1 shows the various stages of damage development of a unidirectional laminated composite during its fatigue life under a tensile loading [Har03]. The damage mechanisms involved during fatigue loading are: matrix cracking, crack coupling, debonding of the fibre/-matrix interface, delamination, and fibre breaking resulting eventually in fracture. Figure 2.2 shows the damage accumulation during the fatigue life of the laminated composite in figure 2.2. The fatigue process starts with micro-cracks in the matrix in the layers whose fibres are non-parallel to the loading direction. As the loading progresses cracks appear in other layers as well and the crack density increases, so that cracks can join. This can also lead to fibre-breaking and the debonding of

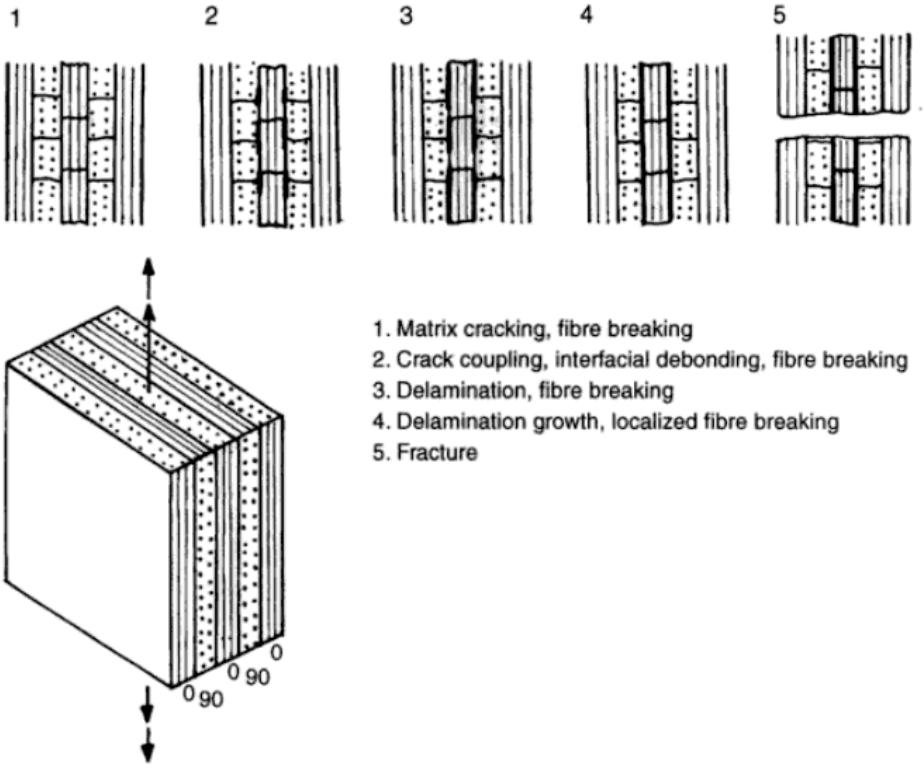


Figure 2.1.: Damage development during the fatigue life of a laminated composite [Har03]

the fibre/matrix interface. Eventually, the cracking reaches an equilibrium state with no new cracks forming. The state of damage reached at this point depends on the type of laminate not on the loading history and is called the characteristic damage state (CDS) [Rei91]. The next damage mechanism is delamination initiation and propagation. Delaminations can spread from free edges but can also develop inside the laminate because of high inter laminar stresses caused by the previous damage processes. While all damage processes occur almost simultaneously the dominant mechanisms in the early stage is matrix-cracking followed by delamination in the intermediate stage. At the last stage the accumulation of damage ultimately leads to fracture. The damage mechanisms in unidirectional composites and their fatigue life have also been treated extensively by Talreja [R.T81] who did a review on fatigue-life diagrams for on-axis fatigue loading shown schematically in figure 2.3 but also for off-axis loading resulting in mixed-mode crack growth. The review covers single plies as well as angle-plied and cross-plied laminates. Talreja draws

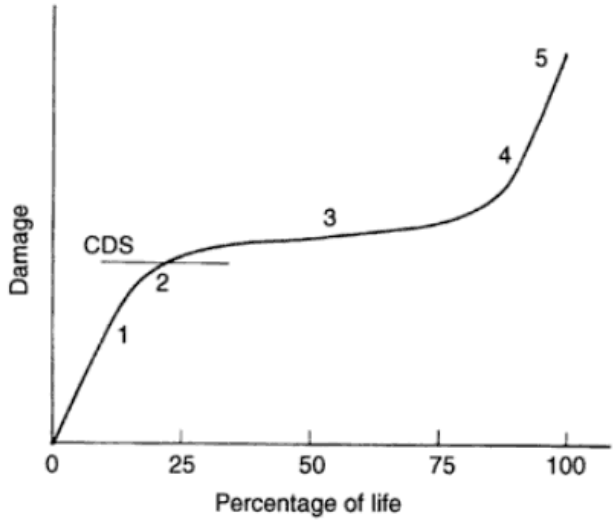


Figure 2.2.: Damage accumulation during the fatigue life of a laminated composite [Har03]

the conclusion that the fatigue performance of a composite is mainly determined by the matrix properties and that in order to improve the fatigue performance of the composite, the fatigue performance of the matrix has to be improved. In reality, a composite will generally not experience fatigue-loading in only one direction. A recent analysis of the fatigue behaviour of composites under multiaxial loading has been carried out by Quaresimin et al. [ST09] who compared experimental data from the literature and examined multi axial fatigue criteria.

2.1.1. Environmental factors in the fatigue of composites

There are several environmental factors which can influence the fatigue life and fatigue performance of a composite. Among these are:

Temperature Temperature has an important effect on the fatigue life of FRP composites. This effect has been investigated by Mivehchi et al. who developed pier-law stress-life relation which takes into account the effect of temperature and the fatigue strength of the composite. In this review five different composites where examined. The study showed that the fatigue strength of the laminated AS-4/PEEK composite examined decreases with increasing temperature for a temperature range of 298 K<T<423 K.

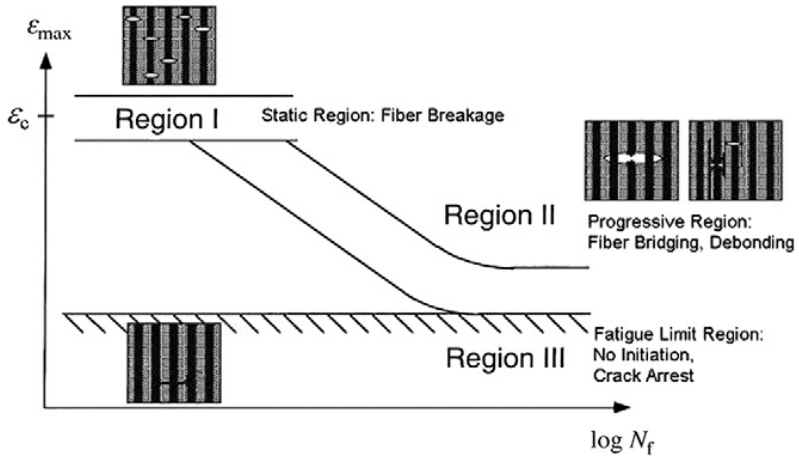


Figure 2.3.: Fatigue life for unidirectional composites under on-axis loading [Tal08]

Mositure Moisture can affect the resin properties in a negative way where thermoset resins are more sensitive than thermoplastic ones [Pro12]. Miyano et. al [miy04] found a reduction in fatigue strengths of unidirectional epoxy composites with increasing water absorption.

Radiation Kumar et al. [BST02] have conducted a study on a IM7/997 carbon fibre reinforced epoxy exposed to both UV radiation and water condensation and found a significant reduction of 29% in the transverse tensile strength after 1000 hours of cyclic exposure of the material. They concluded that catastrophic structural failure could occur from matrix erosion due to repeated exposure to sunlight and rain.

Corrosion While one of the advantages of resinous fibre-reinforced composites is that they do not react with oxygen from the air the resin can react with acidic encironments which cause deterioration of the material. A study on the exact nature of corrosion in composites has been conducted by Hojo et. al [HTO91] who applied the concept of corrosion rates to polymeric materials and found that these rates were dependent on the chemical structure of the resin, its reactivity and the ability of the surrounding environment to penetrate into the material.

2.1.2. Fracture characterisation

Fractures in composites are very often characterised by three different fracture modes according to the direction of the relative displacement of the crack-surfaces at the crack front as shown in figure 2.4.

1. Mode I (opening mode) - corresponds to a normal separation due to tensile stress
2. Mode II (sliding mode) - corresponds to shearing normal to the crack front
3. Mode III (scissoring mode) - corresponds to shearing parallel to the crack front

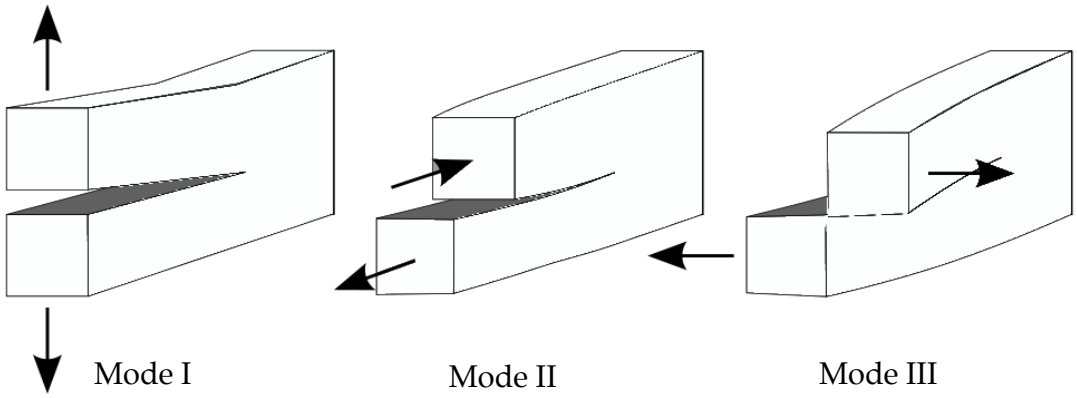


Figure 2.4.: Modes of fracture

A crack can grow in pure modes but generally a crack will be a combination of fracture modes which is then referred to as mixed-mode.

2.1.3. Fatigue loading

A typical sinusoidal fatigue loading curve of stress σ vs. time t taken from [RA02] is shown in figure 2.5. In this figure, σ_{max} and σ_{min} are the maximum and minimum stress and T is the period, where $T := \frac{1}{\omega}$ and ω is the frequency. From these values the three most relevant parameters for the characterisation of the loading can be calculated. These are the average stress σ_m and the stress amplitude σ_a and the

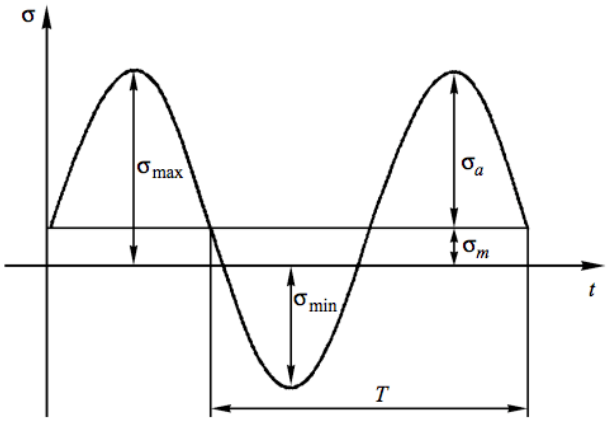


Figure 2.5.: Sinusoidal loading

R-ratio.

$$\sigma_m = \frac{\sigma_{max} + \sigma_{min}}{2} \tag{2.1}$$

$$\sigma_a = \frac{\sigma_{max} - \sigma_{min}}{2} \tag{2.2}$$

$$R = \frac{|\sigma_{min}|}{|\sigma_{max}|} \tag{2.3}$$

2.2. Fatigue delamination- modelling and testing

2.2.1. Fatigue delamination modelling

As mentioned in the previous chapter there are various reviews on modelling fatigue of composites. Due to the complexity and the number of different approaches to fatigue modelling there is no generally agreed classification. Degrieck et al. [DP01] have categorised fatigue models into three different classes: fatigue-life models, phenomenological models, and progressive damage models. Fatigue-life models use S-N curves to predict fatigue life without consideration of crack initiation and propagation. Phenomenological models describe the degradation of macroscopically observable material properties due to fatigue loading and progressive damage models take into account the actual underlying damage mechanisms to predict fatigue degradation of the composite. A similar classification has been presented by Turon [Tur06] who differentiates between fatigue-life models, fracture

mechanics models relating the stress-intensity factor or the energy release rate to the crack growth, and damage mechanics models. The fact that the model developed by Turon uses both fracture mechanics and damage mechanics and is therefore a hybrid of two classes highlights the difficulty of classification. The most recent review of methods for the prediction of fatigue delamination growth in composites and adhesive bonds by Pascoe [PAR13] splits models into four categories: stress/strain based methods, which relate delamination growth to the stress or strain within the material, fracture mechanics based models, cohesive zone models, and extended finite element method based models. The latter two are numerical methods based on the finite element method and most of the models implemented into the two methods rely on fracture mechanics. The cohesive zone model (CZM) will be described in more detail below as it is the method chosen in this PhD. The extended finite element method (XFEM) allows cracks to grow within the elements through the use of enrichment functions. It has been developed by Belytchko et al. [BB99]. Moes and Belytchko have included a traction-separation law to model cohesive cracking [MB02]. XFEM has mainly been used to model static crack-propagation but as mentioned earlier Bacarreza et al. [BA11] have developed a model for fatigue delamination using VCCT to find the energy release rate and XFEM to update the geometry.

Fracture mechanics models rely on the concepts of stress intensity factor or the energy release rate which are equivalent. All fracture mechanics models are based on the so-called Paris law relating the stress intensity factor/energy release rate to the crack growth rate $\frac{da}{dN}$. In its general form the Paris law is

$$\frac{da}{dN} = Cf(G)^m, G_l \leq G \leq G_u. \tag{2.4}$$

Here f is a function of G, which is the energy release rate, C and m are fitting parameters which have to be determined experimentally. G_l and G_u are lower and upper limits where the Paris law is valid. The relationship between the normalised energy release rate $f(G) := \left(\frac{G_a}{G_c}\right)$ and the crack growth rate is shown in figure 2.6 on a log-log plot. G_a is the maximum energy release rate during the loading cycle, mostly referred to as G_{max} in the literature and G_c is the fracture toughness. The plot is divided into three regions: Region I, where the applied energy release rate

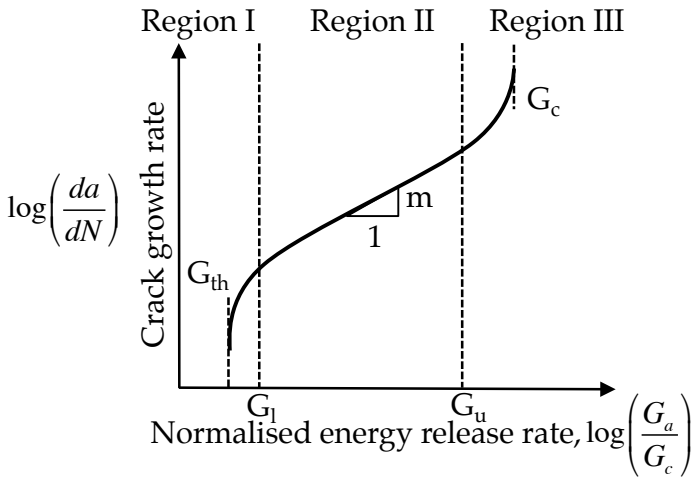


Figure 2.6.: Fatigue crack propagation

is below or near the threshold value G_{th} below which no measurable fatigue crack growth occurs. Region II forms the log-linear part of the curve which is described by the Paris law (2.4). In the nonlinear Region III, the applied energy release rate is close to the static fracture toughness G_c. The use of the Paris law for modelling delamination in composites stems from the fact that it has been used successfully to model the fatigue crack propagation in metals [PGA61] but the exponent m is about an oder of magnitude higher for composites [Mar03], so the crack growth rate is very sensitive to errors in the energy release rate. O'Brien [O'B81] presented the first adaptation of the Paris law in terms of the energy release rate for the delamination of fibre-reinforced composites using $f(G) = G_a$. The energy release rate range $\Delta G := G_{max} - G_{min}$ has been first used by Mohlin et al. [MALA85] to simulate delamination in a CFRP laminate in compression loading. Hosoi et al. [HAKK07] have also used a Paris law with $f(G) = \Delta G$ to model delamination growth for fatigue in excess of 10^8 cycles.

Fatigue loading can be of constant or variable amplitude. Variable amplitude loading has not been studied very extensively due to the modelling complications involved. It is suggested in the Composite Materials Handbook [CMH12] that load history effects are small but that further work needs to be carried out for different materials and lay-ups.

Constant amplitude loading can be completely defined in terms of two parameters: the energy release rate range $\Delta G = G_{max} - G_{min}$ and the R-ratio which is defined as

$$R^2 = \frac{G_{min}}{G_{max}}. \tag{2.5}$$

The observation that the crack propagation rate depends on the R-ratio is called the R-ratio effect. This R-effect has been included into a modified Paris law by Allegri et al. [AJMH11] for mode II:

$$\frac{da}{dN} = C \left(\frac{G_{IIa}}{G_{IIc}} \right)^{\frac{m}{(1-R)^2}} \tag{2.6}$$

Efforts have also been made to extend the validity of the Paris law to all three regions in figure 2.6 for example by Martin et al. [MM90] who proposed the following modified Paris law relationship:

$$\frac{da}{dN} = C \left(G_a \right)^m \frac{1 - \left(\frac{G_{th}}{G_a} \right)^{m_1}}{1 - \left(\frac{G_a}{G_c} \right)^{m_2}}. \tag{2.7}$$

The crack propagation rate depends heavily on the mix of fracture modes (see figure 2.4). Not much research has been done on mode III so when referring to research on fatigue-driven mixed-mode delamination growth this normally means a mixture of mode I and mode II. A detailed review of various models to include mixed-mode based on experimental data for the pure modes has been conducted by Blanco [Bla04]. Based on a model by Kenane and Benzeggagh [KB97], Blanco [BGAC04] developed the following mixed-mode model:

$$\frac{da}{dN} = C \left(\frac{\Delta G}{G_c} \right)^m \tag{2.8}$$

$$\log C = \log C_I + \log C_m \left(\frac{G_{II}}{G_T} \right) + \log \frac{C_{II}}{C_I C_m} \left(\frac{G_{II}}{G_T} \right)^2 \tag{2.9}$$

$$m = m_I + m_m \left(\frac{G_{II}}{G_T} \right) + (m_{II} - m_I - m_m) \left(\frac{G_{II}}{G_T} \right)^2 \tag{2.10}$$

In this model C_I, m_I, C_{II}, and m_{II} are the pure mode Paris law parameters. $G_I I$ and G_T are the mode II and total energy release rates respectively. G_c, C_m ,and m_m are additional mixed-mode parameters which have to be determined through curve fitting of experimental results. As opposed to the Kenane et al. model this model includes an additional quadratic term. This extra term was added because Blanco

noted form previous experimental results Asp et al. [ASG01] that the Paris law parameters for mixed-mode delamination are not in between the parameters for mode I and mode II. Instead the constant C was below that for mode I and mode II and the mixed-mode exponent m was higher than in mode I and mode II. A comparison of the various mixed-mode models with two different sets of experimental results by Asp et al. [ASG01] and Tanaka et al.[TT95] showed a significant improvement in predicting the mixed-mode Paris law coefficients over the previous models. The reason for this is that it allows for a non-monotonic variation of the coefficients with varying mode ratio. The Blanco model has also been used by Harper for simulating the delamination of bonded joints [Har08].

2.2.2. Fatigue delamination testing

Reviews on the characterisation of fatigue delamination have been published Tay [Tay03]. A more recent review on delamination resistance testing of polymer-matrix testing for static and fatigue delamination has been conducted by by Brunner et al. [BBD08]. Fatigue delamination testing is generally split into fracture modes with a focus on mode I, mode II and mixed-mode delamination, where mixed-mode delamination usually refers to a mix between mode I and mode II. The process of delamination is often split into three stages as shown in figure 2.6. The first stage is a period of very slow or no measurable crack growth near the threshold value G_{th}. This is followed by a region of stable crack propagation which finally leads to the last stage where abrupt failure within a single cycle occurs. The second stage is very often numerically quantified in terms of a power law. The Paris law was originally developed for metals but is now used for composites as well. A large difference between composites and metals however is that the exponents are much higher and therefore a small fluctuation in the energy release rate has a great effect on the delamination propagation rate [Har03].

Fatigue delamination threshold

The sensitivity of the crack growth rate to fluctuations of the energy release rate has led to some studies measuring the delamination threshold G_{th} since this value can

be used for a no-growth design. One of these studies has been carried out by Martin et al. [MM90] to measure the delamination threshold and crack propagation in mode I and mode II in AS4/PEEK composites. The delamination threshold G_{th} was defined to be the strain energy release rate at which no delamination occurred until at least 10^6 cycles. The delamination growth onset was measured at two different R-ratios of 0.1 and 0.5. An initial delamination was introduced in two ways: once with an aluminium insert and once with a shear precrack introduced by a static load. Figure 2.7 shows a typical G vs. N curve for delamination growth onset for the pre-cracked specimens in mode I and II at R=0.1. Martin et. al then go on

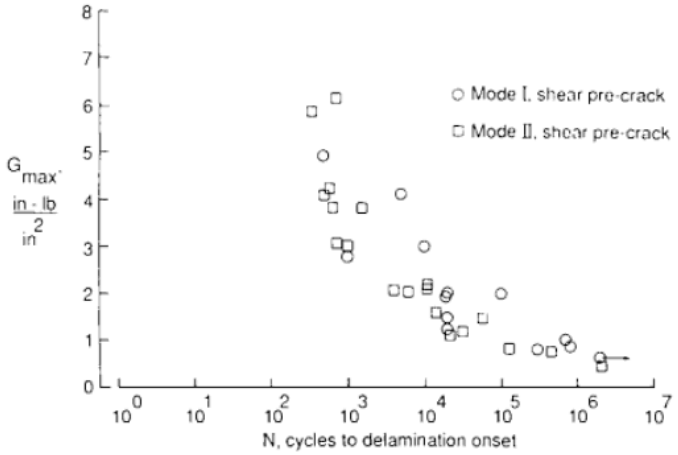


Figure 2.7.: Comparison of mode I and mode II delamination growth onset at R=0.1 [MM90]

to develop an empirical model that captures the whole delamination process (see equation (2.7). Efforts are still being made fairly recently to determine the fatigue threshold for example by Kenane et. al [KZSB11] who developed a semi-empririal model for the mixed-mode case for unidirectional glass/epoxy composites based on the total and pure mode energy release rates using the Benzeggagh and Kenane criterion to predict the mixed-mode fracture toughness.

Fatigue delamination propagation

An early study on measuring delamination propagation in fibre-reinforced composites has been carried out by O'Brien [O'B81] who tested the onset and growth

of free edge mixed-mode delamination in a graphite-epoxy composite and related the crack-growth rate and the maximum strain energy release rate through the delamination size and the stiffness loss of the laminate (see figure 2.8). This study

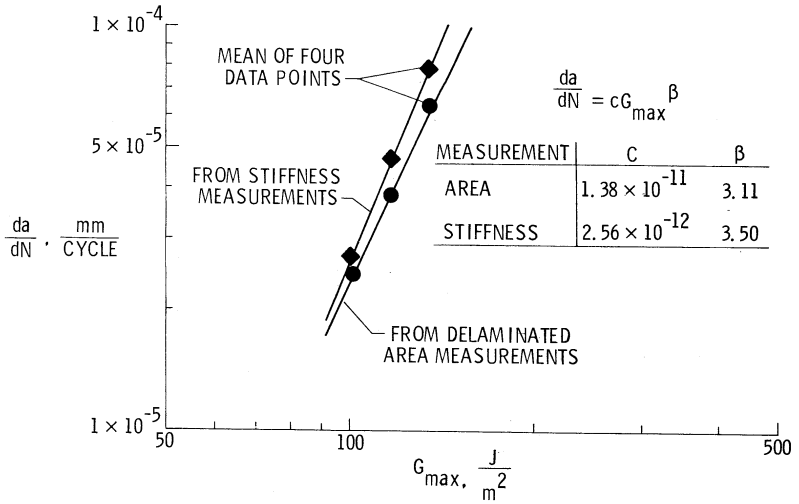


Figure 2.8.: Crack propagation rate vs. maximum energy release rate [O'B81]

has been followed by many other which usually focus on certain aspects of fatigue delamination. Hojo et al. [HTGH87] examined the effect of the stress ratio on delamination propagation in unidirectional laminates made from T300/914C and T300/#2500 laminates. The study was conducted for mode I for R ratios between 0.1 and 0.7. Figure 2.9 (a) shows the crack growth rate with respect to the maximum energy release rate for four different R-ratios while 2.9 (b) shows the same data plotted against the energy release rate range ΔG. This figure demonstrates that the scatter due to the R ratio is reduced when the growth rate was plotted against the energy release rate range rather than the maximum value. Hojo et. al then go on to use an equivalent stress intensity factor K_{eq} as a product of maximum stress intensity factor and stress intensity factor range raised to the power of γ and $1-\gamma$ respectively where $0 < \gamma < 1$ thus taking the influence of the R-ratio into account. A further study on T300/914C composite laminates was carried out by Gustafson et al. [GH87] for three different stress ratios for mode I and mixed-mode fatigue delamination. Hojo et al.[HOGT94] also carried out mode I fatigue delamination tests to examine the effect of the matrix resin under different R-ratios and found that for epoxy laminates the R-effect almost disappears when plotting the growth

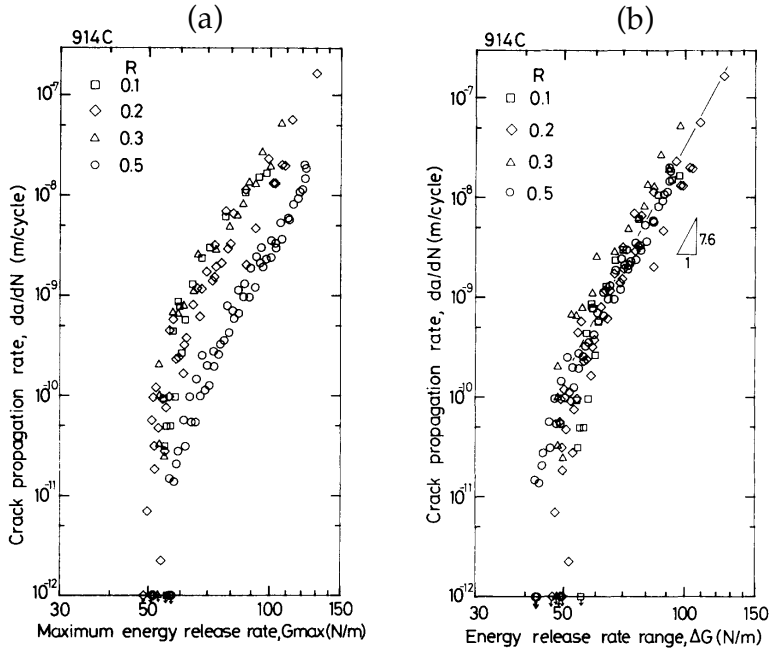


Figure 2.9.: Relation between crack propagation and energy release rate for T300/914C [HTGH87]

rate vs. the energy release rate range while for PEEK composites it does not. They then use the model from [HTGH87] to model the Paris law for the different matrix materials taking into account the R-ratio. They concluded that for the tested epoxy laminates with a brittle matrix the maximum load is the dominating factor for the crack growth rate while for laminates with toughened matrix the cyclic load range is more important. While the PEEK composites have a higher growth threshold and a lower growth rate, the ratio of the fatigue threshold to the static fracture toughness is much lower so toughening of the matrix does not lead to an improvement into fatigue delamination resistance. Kenane and Benzeggagh [KB97] did an extensive study on mixed-mode fatigue delamination of Glass/epoxy laminates using the mixed-mode bending test at tan R-ratio of 0.1. They measured crack growth rates vs. the strain energy release rate range for six different mode-mixtures and from this developed a mixed-mode Paris law based on the mode I and mode II parameters. This Paris law is shown in figure 2.10 for a mode mix of 28% mode II and 53% mode II. Asp et. al [ASG01] have studied the delamination initiation and growth in mode I,mode II and mixed-mode of HTA/6376C with an R-ratio of

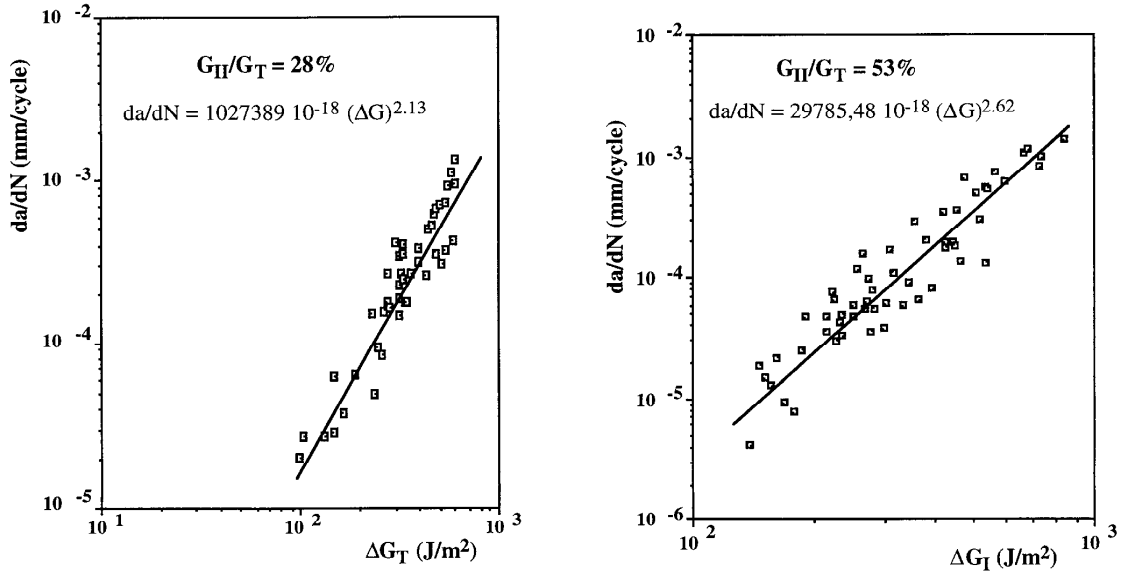


Figure 2.10.: Delamination growth rate versus strain energy release rate range [KB97]

$R = 0.1$. The crack propagation vs. normalised maximum energy release rate for all three modes is shown in figure 2.11. Fractographic images showed that the initial delamination mechanisms under static and cycle loading were the same. The delamination threshold for mode II was the lowest and only 10% of the fracture toughness but this was attributed due to a high strain energy release rate at the specimen edges. The authors concluded that the end-notched flexure (ENF) test used was not appropriate to determine the fatigue delamination threshold. epoxy composite under mode-I fatigue loading

Fatigue delamination testing methods

In order to gather the experimental fatigue data necessary for the development of any empirical Paris law model and in turn to develop delamination models based on the Paris law, it is necessary to devise a testing method to do so. There are different types of specimens and loading conditions commonly used for each mode which are briefly summarised in the following paragraphs.

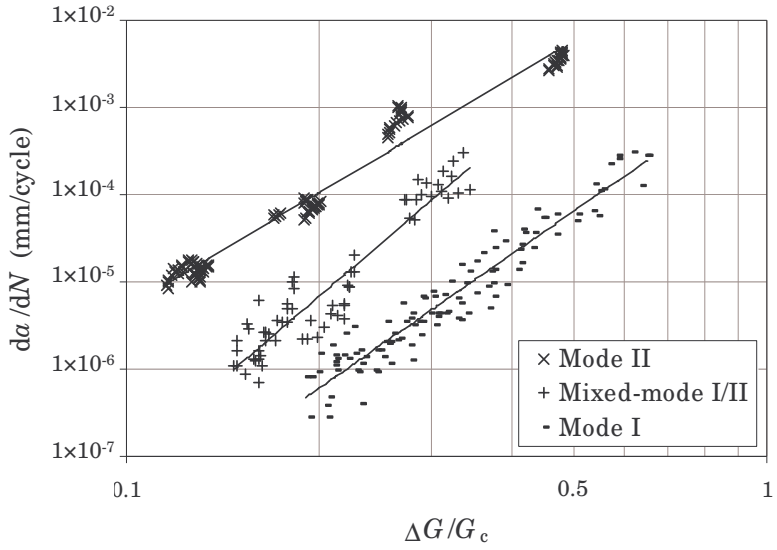


Figure 2.11.: Modified Paris plot showing the strain energy release rate for each mode normalised by the corresponding fracture toughness [ASG01],[Bla04]

Mode I

For measuring the static mode I interlaminar fracture toughness and fatigue delamination growth onset, testing standards exist from ASTM International [13a], [9711]. Both of these use a double cantilever beam (DCB) specimen. The double cantilever beam specimen consists of a laminated beam which is separated into two beams by an initial delamination which is created by inserting a thin non-stick film during manufacture of the composite laminate (see figure 2.12). The beam is constrained at one end and at the other end opposing opening loads are applied to the delaminated part of the specimen, so that the delamination is forced to grow as shown in figure 2.12. There is no testing standard for measuring the crack propagation and therefore the Paris law but the principles of the testing standard for growth onset are often used [ASG01], [GHMJ08]. Efforts have been made to develop a testing standard for measuring mode I fatigue delamination propagation. A review and evaluation of several parameters which include among others the loading frequency, the initial delamination length, the test control (load or displacement), and the test duration has been conducted by Brunner et al. [BMP09]. The DCB tests

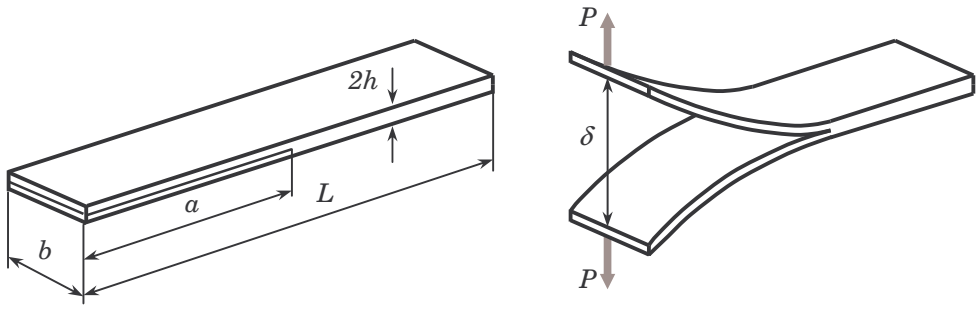


Figure 2.12.: Double cantilever beam specimen and loading [Bla04]

were carried out with IM7/977-2 carbon-epoxy with a fixed R-ratio of $R = 0.1$. A more recent study has been conducted by Murri [Mur12] who tested IM7/8552 composite laminate DCB specimens from two different sources to evaluate a proposed ASTM standard for determining the Paris law in mode I.

Mode II

For mode II there is no specified testing standard for static or fatigue delamination. The three common types of tests are the end loaded split (ELS) test [Dav96], end-notched flexure (ENF) test [Rus82], and the four-point end-notched flexure (4ENF) test [MD99]. The ELS and ENF tests are shown in figure 2.13 and 2.14.

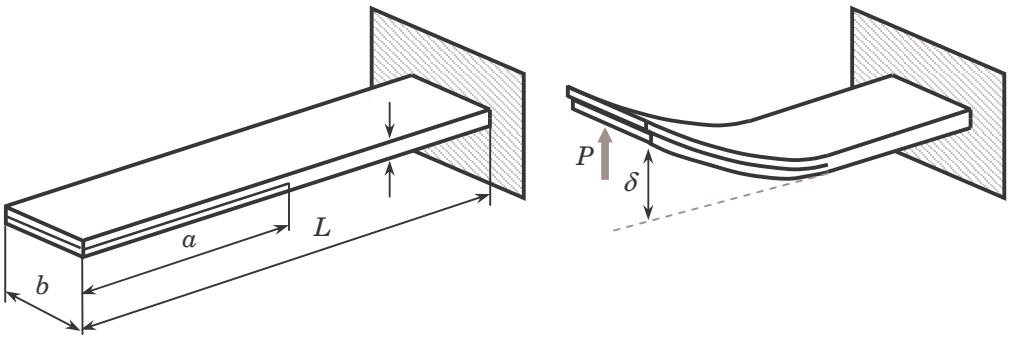


Figure 2.13.: End loaded split specimen and loading [Bla04]

Asp et al. [ASG01] used the ENF test to measure mode II delamination growth in HTA/6376C. The ELS has been used by Gilchrist et al. [GS95] to examine the fractographic features associated with delamination in multidirectional laminates of T300/914. A recent study by Brunner et al. [BSPT13] showed that the ENF and

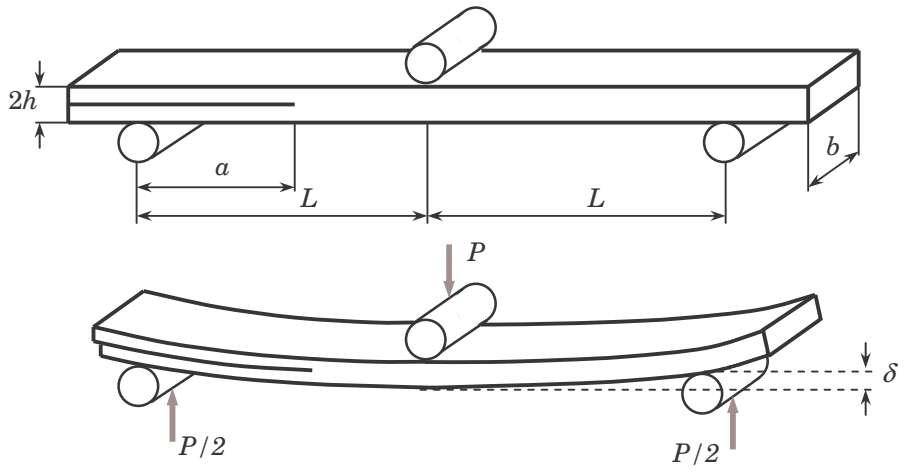


Figure 2.14.: End notched flexure specimen and loading [Bla04]

ELS do not yield the same Paris plots for identical laminates. The reason for this is not clear but Brunner speculates that it may be due to the ELS test rig and the variation in the clamping of the ELS, the different types of data analysis or the different test parameters.

Mixed-mode

For mixed mode the testing standard is the Mixed Mode Bending (MMB) test [13b] originally proposed by Reeder and Crews [RC90] using a specimen which is very similar to the DCB specimens. The MMB test is shown in figure 2.15 The MMB was

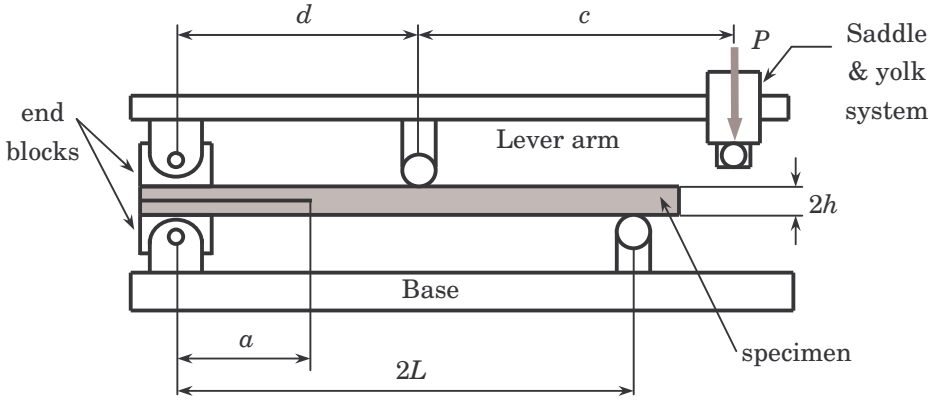


Figure 2.15.: Mixed mode bending specimen and loading [Bla04]

used by Asp et al [ASG01] to measure mixed-mode fatigue delamination propa-

gation of HTA/6367c laminates at a mode-mixety of $\frac{G_{II}}{G} = 0.5$. Kenane and Benzeggagh [KB97] used the MMB to measure fatigue delamination propagation in unidirectional laminates of E-glass fibre with M10 epoxy resin at six different mode ratios.

In order to calculate the energy release rate and thus determine the Paris law form the experimentally measured load/displacement crack length data, the following equation is used [RDW04]

$$G_a = \frac{P^2}{2b}\frac{dC}{da}, \tag{2.11}$$

where P is the applied load, b the specimen width, δ the displacement, a the crack length and C the compliance, which has to be measured directly or is calculated using beam theory.

2.3. The cohesive zone model

Based on the insight of the inelastic behaviour of most materials at the crack tip Dugdale [Dug60] and Barenblatt [PBRdB62] layed the foundations of the cohesive zone model (CZM). Their models assumed that there exists a plastic zone near the crack tip where stresses act across the crack. This cohesive zone removes the problem of an infinite stress concentration at a localised crack tip by spreading out the area where mechanical energy is transformed to surface energy. Figure 2.16 shows the mode I cohesive zones according to Barenblatt and Dugdale respectively. The Dugdale model is more macroscopic in nature with yielding of the material being identified as the physical cause for separation and the stress along the cohesive zone is constant.

In Barenblatt's model the stresses represent the molecular cohesive forces. Barenblatt made two assumptions about the cohesive zone:

1. The length of the cohesive zone l_{cz} is constant for a given material and small compared to other dimensions

2. The stresses in the cohesive zone are distributed according to the function $\sigma(x)$ where x is the distance from the crack tip, and this distribution is material specific and independent of the global loading conditions.

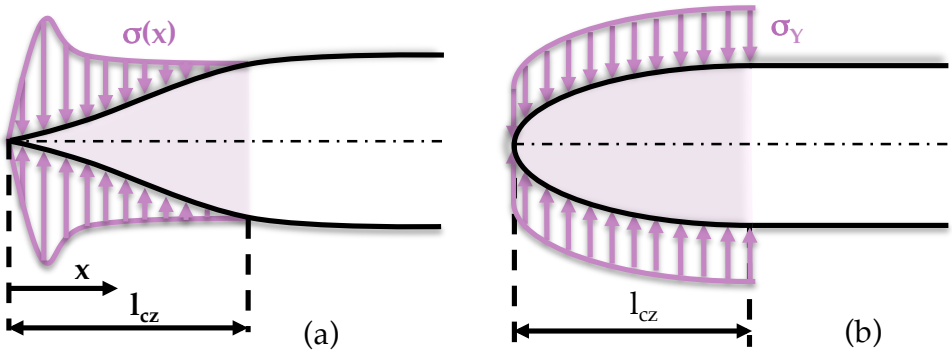


Figure 2.16.: (a) Barenblatt cohesive zone model and (b) Cohesive zone model by Dugdale

The first application of the cohesive zone model within the Finite Element Method was proposed by Hillerborg for mode I in 1976 [HMP76] whose model follows Barenblatt's approach and is similar to current cohesive zone models. A main difference to Barenblatt's model is that the cohesive stress is not a function of the distance from the crack tip x, but of the crack width δ. In it the crack is assumed to propagate when the stress at the crack tip reaches the tensile limit σ_0. When the crack opens the stress does not fall to 0 at once but decreases with increasing crack opening δ. At a critical crack opening of δ_c, the stress has decreased to 0. Figure 2.17 shows a schematic drawing of the cohesive zone and a possible stress-displacement curve $\sigma(\delta)$. The zone of the crack where $\delta < \delta_c$ is described by Hillerborg as a "microc-

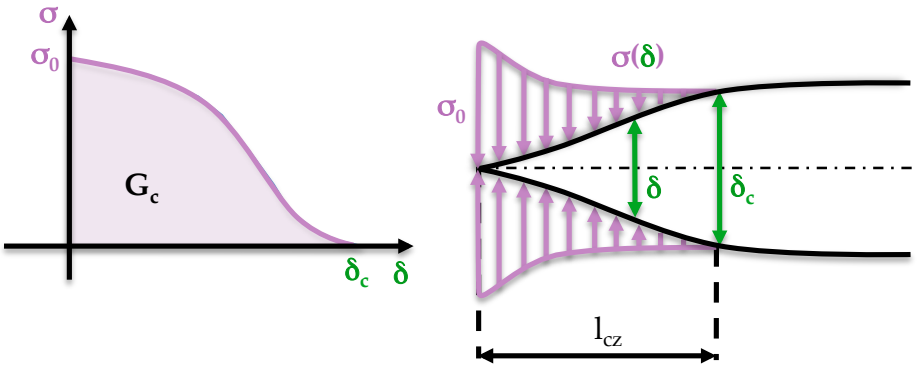


Figure 2.17.: Assumed variation of stress σ with crack width δ, cohesive zone

racked zone with some remaining ligaments for stress transfer." During the opening of the crack, energy is absorbed in the formation of new crack surfaces. The stress-displacement curve may have different shapes and is chosen, so that the amount of energy absorbed per unit crack area in the opening of the crack from 0 to δ_c is equal to the critical energy release rate G_c, so

$$\int_0^{\delta_c} \sigma(\delta) d\delta = G_c. \tag{2.12}$$

The model was used to model an unreinforced concrete beam in bending which is shown in Figure 2.18. This beam is loaded with a bending moment M, so that the

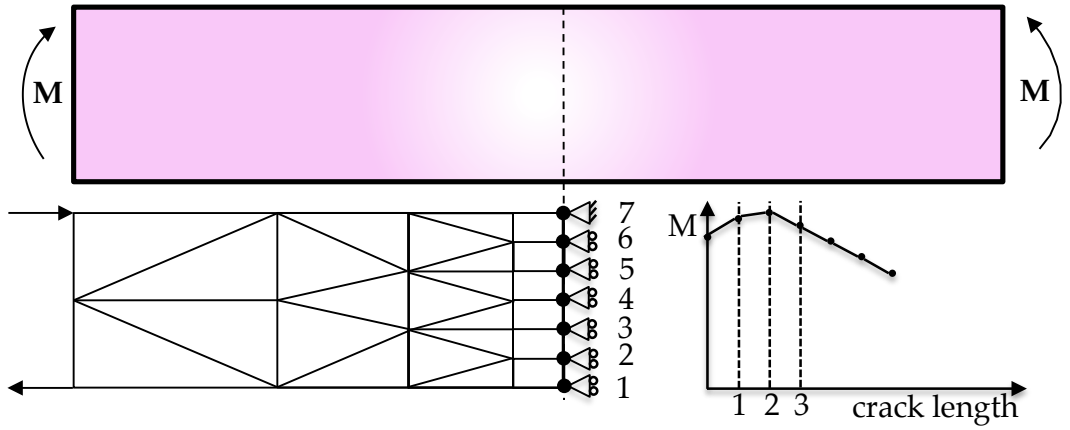


Figure 2.18.: Concrete beam in tension, FE model

tensile stress at point 1 reaches σ_0 and the crack begins to open. A force is then introduced at the corner according to the relationship $\sigma(\delta)$ defined previously. The moment is then calculated, so that σ_0 is reached at point 2. Another force is then introduced there according to $\sigma(\delta)$ and a new moment is computed. In this way the crack propagates through the material.

The variation of the cohesive stress σ with the displacement δ has been the subject of much discussion and various shapes of this constitutive law have been proposed in the literature. Three of them are shown in figure 2.19 and 2.20 for mode I and mode II respectively. These are the third-order polynomial law, the exponential law and the bilinear law. (Their analytical expressions are given in the next chapter.) As opposed to the Hillerborg model, the interfacial stress increases up to a maxi-

mum value and is then reduced until it reaches 0 in the polynomial case, when the interface is completely degraded. The polynomial and the exponential law were

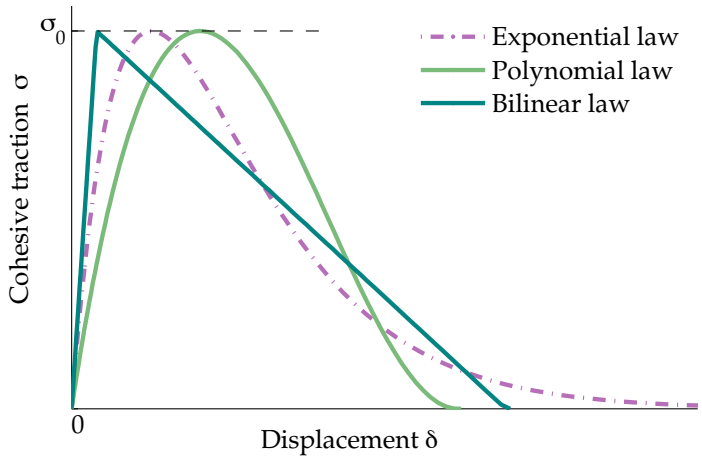


Figure 2.19.: Static cohesive zone laws mode I

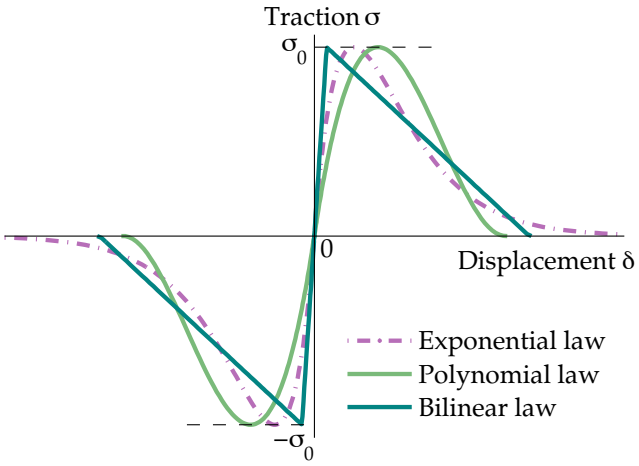


Figure 2.20.: Static cohesive zone laws mode II

proposed by Needleman[Nee90]. As opposed to most other constitutive laws, the exponential law does not reach 0 for some fixed δ_c, but approaches 0 as $\delta \to \infty$. The bilinear law was introduced by Geubelle and Baylor [GB98] to simulate delamination in a composite plate under low velocity impact and is generally used to simulate quasi-brittle fracture. While Tveergard and Hutchinson [TH92] argued that the exact shape of the constitutive law is not very important, Chandra et. al

[CLSG02] compared two different laws, the bilinear and the exponential one to simulate the debonding of silicon carbide reinforced titanium matrix composites and found that while the bilinear CZM reproduced the mechanical behaviour exhibited in experiments, the exponential did not because of the relatively large displacement necessary in the exponential law until debonding takes place. Chandra et al. also present an overview of various cohesive zone models and their modelling application. It is generally assumed that the exact mathematical shape is less important than the exact representation of interfacial strength σ_0 and critical fracture energy G_c.

Cohesive zone models can be implemented into finite elements in two ways. One approach is to implement the cohesive law as a mixed boundary condition, relating the tractions to displacements at boundaries or interfaces. The modelling of the concrete beam in bending by Hillerborg described above is an example of this method.

Another method which is widely used for modelling delamination is to directly embed the cohesive law into a finite element. These elements have a spatial dimension which is one less than that of the continuum elements in the model and are called interface or cohesive elements in the literature. These are most commonly zero-thickness elements which are placed between continuum elements where delamination is thought to occur. Initially the top and bottom nodes coincide. As the crack grows, the cohesive tractions are determined through the cohesive law and the displacement difference between the upper and the lower surface. As opposed to VCCT the crack can propagate to wherever there are interface elements between elements and crack initiation can also be modelled. Figure 2.21 shows a 4-noded one-dimensional cohesive element in its initial zero-thickness configuration between two continuum elements and in the deformed state. There are many formulations for cohesive elements. Following the ideas of Xu and Needleman [XN94] to model a cohesive surface between finite elements, Ortiz and Pandolfi [OP99] developed a surface element to be placed between tetrahedral solid elements as shown in Figure 2.22. They also implemented an irreversible cohesive law which linearly unloads and reloads. One way to introduce this irreversibility is within the framework of damage mechanics. In this theory one or several damage variables D are

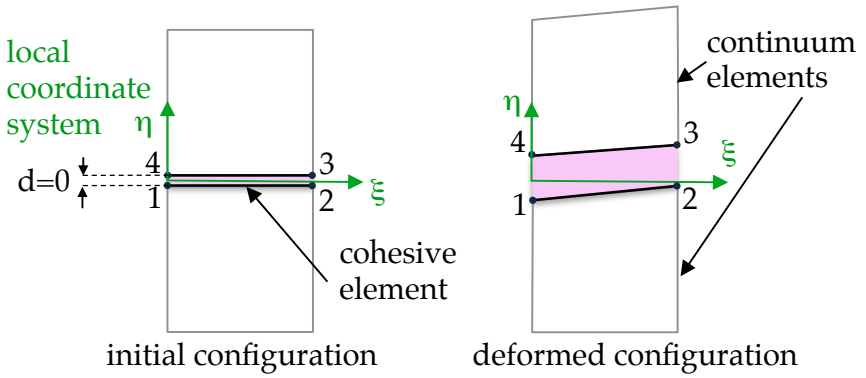


Figure 2.21.: Interface element

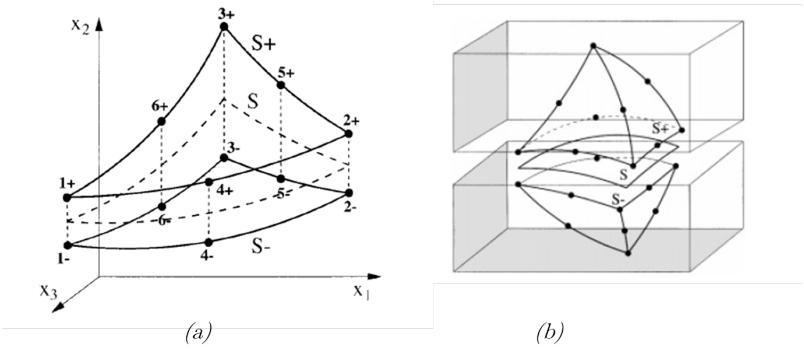


Figure 2.22.: (a) Cohesive element taken from [OP99]. The surfaces S^+ and S^- originally coincide (b) Assembly of a 12-node triangular cohesive element and two 10-node tetrahedral elements

introduced to simulate the degradation of the interface. The research of Allix et al. [ALC95] represents an early example of modelling delamination with interface damage modelling based on the strain energy of the interface in the three different fracture modes.

An undamaged element corresponds to $D = 0$ whereas for a fully degraded element $D = 1$. Different damage variables can be assigned to the different fracture modes. Two of the fatigue degradation strategies examined in the following chapters use a static damage formulation based on the residual stiffness as shown in figure 2.23, where K is the initial elastic constant $K = \frac{\sigma_0}{\delta_0}$. This means that an interface element accumulates damage once the traction passes the peak value σ_0 and is completely degraded when the traction reaches 0. A more detailed derivation

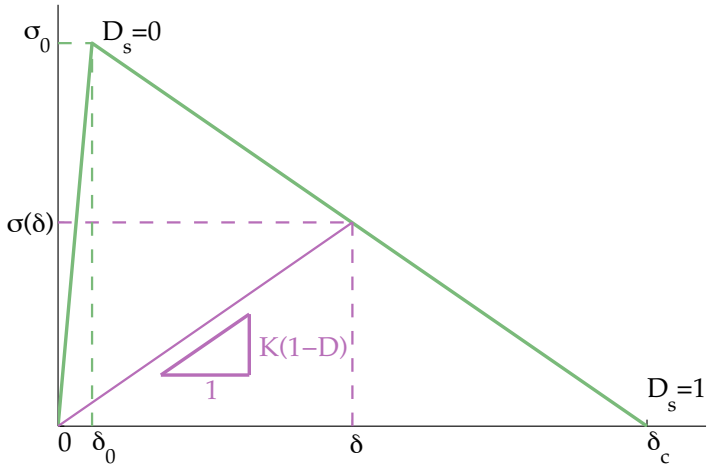


Figure 2.23.: Bilinear law with stiffness based damage degradation

of the cohesive element formulation adopted in the research for this thesis can be found in chapter 6.

2.4. Delamination modelling with cohesive elements

2.4.1. Static delamination modelling with cohesive elements

In recent years cohesive elements are increasingly used for the simulation of static delamination. Chen et. al [CCK+99] simulated the static 2D delamination of a DCB, ENF and FRMM (fixed rate mixed-mode) specimens using a bilinear and a cubic polynomial cohesive law in plane-strain conditions with linear and quadratic interface elements using the material model and the mixed-mode criterion described by Mi et al. [MCHD98]. The model also included linear unloading and a stiffness-based damage formulation. They compared their numerical results to analytical solutions and for the ELS and FRMM also to experimental results and found good agreement. However, for the ELS and FRMM the stiffness E_{11} had to be lowered and in order to achieve convergence the peak stiffness of the cohesive zone law σ_0 had to be dropped significantly. They also found a better convergence for the linear element when keeping the number of nodes in the model constant.
The model by Mi et al. [MCHD98] has been extended by Qiu et al. [QCA01] with

a formulation where the rotation of the interface element is considered to allow the simulation of delamination with large deformation. The interface elements where then used to simulate delamination due to buckling. The authors found that a relatively fine mesh was required with 15 integration points in the cohesive zone to obtain a smooth solution.

Alfano et al. [AC01] went on to improve the 2D formulation with a mixed-mode formulation that does not require an initial simulation to determine the mode-ratio in order to calculate the mixed-mode energy release rate G_c. They modified the formulation, so that debonding in mode I and mode II occur at the same time which was not the case before. This is the case when $\frac{\delta_{0I}}{\delta_{cI}} = \frac{\delta_{0II}}{\delta_{cII}}$. They also found that increasing the number of integration points in an element can reduce the robustness of the algorithm and lead to an increase of required increments. Decreasing the value of the peak stiffness σ_0 allowed for a coarser mesh and an increased increment size. Alfano et al. used the tangent stiffness matrix instead of the secant matrix which led to an improved rate of convergence and enhanced numerical stability.

Camanho et al. [CD02] developed a 3D mixed-mode cohesive element using the bilinear law with stiffness-based damage and linear unloading. The mixed-mode criterion is from Benzeggagh and Kenane [BK96] incorporating all three modes. First, a mode mix parameter β is calculated from the ratio of shear displacement to opening displacement where the shear displacement is defined as $\delta_s = \sqrt{\delta_{II}^2 + \delta_{III}^2}$. Together with the mixed-mode criterion this allows for a mixed-mode critical displacement δ_m to be calculated which defines the mixed-mode constitutive law. This mixed-mode law is shown in figure 2.24. Camanho et al. also use a Newton-Raphson algorithm to solve the non-linear equations for the displacement and thus require the tangent stiffness matrix. They simulated DCB, ENF and MMB specimens achieving good agreement with experimental results apart from the cases where the B-K criterion predicts different fracture toughness values from the ones experimentally measured.

Goyal et al. implemented a 3D linear interface element using the exponential cohesive zone law and en empirical mixed-mode damage criterion for the simulation of DCB, ELS, FRMM, and MMB specimens with known mixed-mode ratio.

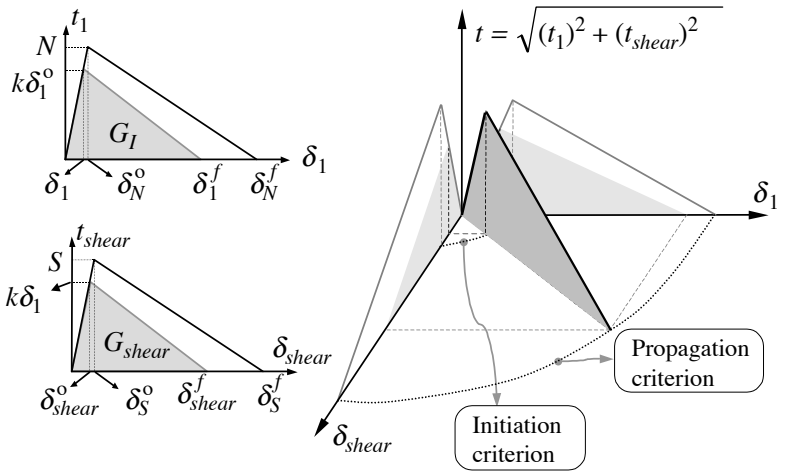


Figure 2.24.: Mixed-mode response bilinear law [PIR06]

Alfano [Alf06] did a study on the influence of the cohesive zone law on the application of cohesive-zone model. He compared the bilinear, linear-parabolic, exponential and trapezoidal cohesive laws and used them to simulate the delamination of a DCB specimen. He found that the trapezoidal law requires the finest mesh size but that there is otherwise no difference as long as the mesh is fine enough.

Pinho [PIR06] also implemented three different cohesive laws and simulated the 3D delamination of DCB, 4ENF, and MMB specimens in an explicit code. The mixed-mode initiation and propagation is based on the element developed by Camanho et al. [CD02]. The cohesive laws chosen were the bilinear law, a linear-quadratic law and the third-order polynomial. All three cohesive laws produced good agreement of experimental and numerical results. Under unfavourable conditions using the bilinear law resulted in numerical instabilities.

Balzani and Wagner [BW08] compared the model by Camanho [CD02] with an exponential model inspired by de-Andres [dAPO99]. They simulated mode I and mixed-mode delamination. While both models achieved good agreement with experimental results the exponential model showed better convergence behaviour.

Jiang et al. [JSGW07] developed an interface constitutive law which is implemented in a spring interface element for analysing the delamination in scaled notched tensile specimens. The cohesive law used is the bilinear law with a mixed-mode cohesive law as defined by Camanho and Davila. Delamination onset is based on a

quadratic damage initiation criterion by Brewer and Lagace [BL88] and the propagation is governed by a mixed-mode power law. The damage is defined according to the loss of stiffness. The cohesive element is implemented in an explicit code and used to simulate open hole tensile tests. It can capture the progressive delamination and splitting process and shows good agreement for the stress prediction.

Benzerga et al. [BHSL08] have also used spring elements to simulate mode I, mode II and mixed-mode delamination of a woven laminated composite. They use a quadratic failure criterion for mixed-mode delamination onset and the power law for propagation. The element used is a 1D spring element so for each pair of nodes on the top and bottom surface of the interface three of these spring elements are associated with each of the fracture modes. They use these spring elements to simulate delamination of a DCB, 3ENF, and an MMB specimen achieving good agreement with experimental data.

Harper and Hallett [HH08] conducted a study on the cohesive zone length in simulations of composite delamination. The cohesive zone length is an important factor as it determines how many elements there are in the process zone for a given mesh size. They studied the cohesive zone length with respect to the material properties involved to determine a minimum number of elements in the cohesive zone and to test analytical formulas to calculate the cohesive zone length developed by other authors in mode I, mode II, and mixed-mode. The cohesive element is implemented in an explicit finite element code. They conclude that at least two to three elements should be present in the cohesive zone for an accurate load-displacement curve. The study suggests that the peak stiffness σ_0 can be reduced in order to make the cohesive zone longer, so that the mesh size can be increased. However, caution has to be taken in mode II where the cohesive zone is often very long. when compared to the numerical values it was found that the analytical formulae often over-predict the cohesive zone length.

One attempt to deal with the oscillations that occur in bilinear cohesive elements when the mesh size is too large has been made by Elmarakbi et al. [EHF09]. In this study the authors develop an adaptive cohesive zone model where the cohesive zone is divided into two parts with different cohesive law. In the pre-softening part of the cohesive zone, the initial stiffness K is set to a high value and is then

gradually reduced until an element enters the softening part where K reaches a final value almost equal to a minimum defined ahead of the simulation. The fracture toughness is constant throughout the process. The cohesive element was implemented in LS-Dyna and used to simulate mode I delamination of a DCB specimen. The simulations show that the adaptive model produces smooth crack propsgation compared to the normal bilinear law especially when the mesh size and the peak stresses are high.

Another possibility for the simulation of delamination with coarser mesh sizes has been presented by Guiamatsia et al. [GADI09]. In this approach the cohesive element is enriched with an enrichment function that mimics the high gradients of the stress field ahead of the crack tip. The cohesive element used was a quadratic 2D line element implemented as a UEL into ABAQUS. The simulation of the mode I delamination of a DCB shows that the element can cope with mesh sizes up to 5 mm. Another type of enrichment has recently been proposed by Samimi et al. [SvDG11]. Here the enrichment of the linear 2D element is a linear function. In this formulation the continuum elements and the cohesive elements are enriched. The authors simulate a peel-off test resulting in mixed-mode delamination which shows that the enriched formulation results in a smoothened load-displacement curve.

A recent study of the mesh-size requirement in the static mode I simulation of delamination with cohesive elements by Alvarez et al. [ÁBGK14] showed that for fine meshes with three to five elements in the cohesive zone the numerical load-displacement curves where in very good agreement with experimental data for linear cohesive elements. However, for coarser meshes the linear elements could not reproduce the load-displacement curves while this was possible when using quadratic elements. The authors note that this is particularly true for thin substrates due to the higher curvature. They also found that while the linear models ran faster at the same mesh size, they were able to coarsen the mesh using quadratic elements to reduce the overall computational time.

2.4.2. Fatigue delamination modelling with cohesive elements

With the increasing use of cohesive elements for the modelling of static delamination efforts have also been undertaken to use cohesive zone models for the modelling of fatigue delamination. One of the earlier studies has been conducted by Roe and Sigmund [RS03]. They proposed a loading-unloading damage model where each cycle is modelled individually based on the exponential cohesive law. The unloading path follows the current stiffness $K = \frac{\sigma_{max}}{\delta_0}$ where σ_{max} is calculated according to the current damage as $\sigma_{max} = (1 - D)\sigma_0$. The damage accumulation is separated into damage rate due to monotonic loading and due to cycle loading. The actual damage after each increment is then calculated as the maximum of the two damage rates integrated over the time increment. The model was implemented in 2D linear cohesive elements and used to simulate the delamination of a DCB, ELS and MMB specimen. However, the numerical results were no compared with experimental data. The damage rate is defined in terms of a resultant traction σ_m and separation δ_m which are calculated from the mode I and mode II contributions as $\sigma_m = \sqrt{\sigma_I^2 + \frac{\sigma_{II}^2}{2eq^2}}$ and $\delta_m = \sqrt{\delta_I^2 + \delta_{II}^2}$, where $2eq^2$ is a factor providing equal weight to the traction components. With this model it is quite straightforward to simulate variable amplitude loading. An example of this is shown in figure 2.25 from [Sie04] which demonstrates the effects of two different type of loadings. The model has no automatic adaptation to the effects of the mode-mix for a given material and the damage rate requires the fitting of two additional parameters.

Other models that are based on a loading unloading hysteresis have been developed by Nguyen et al. [NROR01] Yang et al. [YMRC01], and Maiti and Geubelle [MG05].

All of the more recent models for fatigue delamination with cohesive elements are envelope load damage models. In this type of model only the maximum load of a cycle is modelled as shown in figure 2.26. Therefore, the relative displacement is also not cyclic as shown in figure 2.27. If $\tilde{\delta}(t)$ is the actual cyclic displacement, the numerically applied displacement $\delta(t)$ is

$$\delta(t) = \max_{0 \leq \tau \leq t} \tilde{\delta}(\tau). \tag{2.13}$$

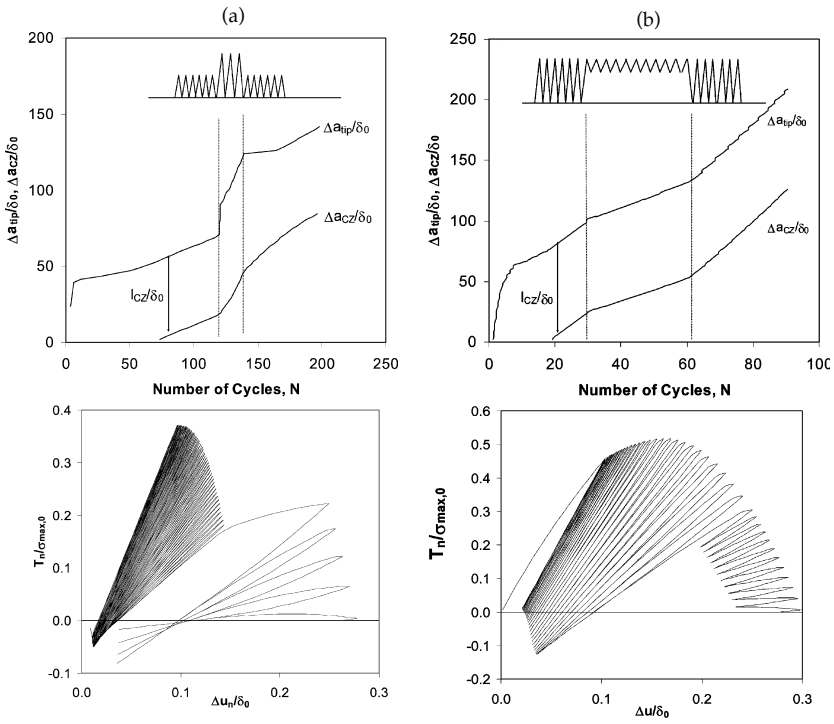


Figure 2.25.: Predicted fatigue crack growth and constitutive response for (a) step-wise change in maximum load and (b) step-wise change in R from [Sie04]

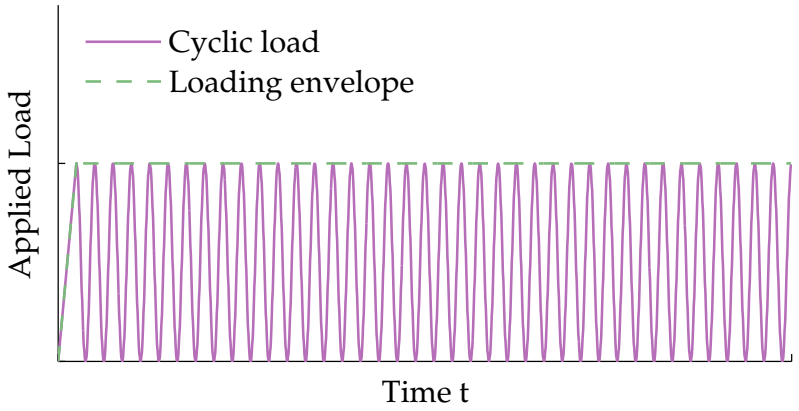


Figure 2.26.: Numerically computed load

The fatigue damage rate is often expressed in terms of cycles N, where N is treated as a continuous variable and the damage accumulation is smeared across the whole

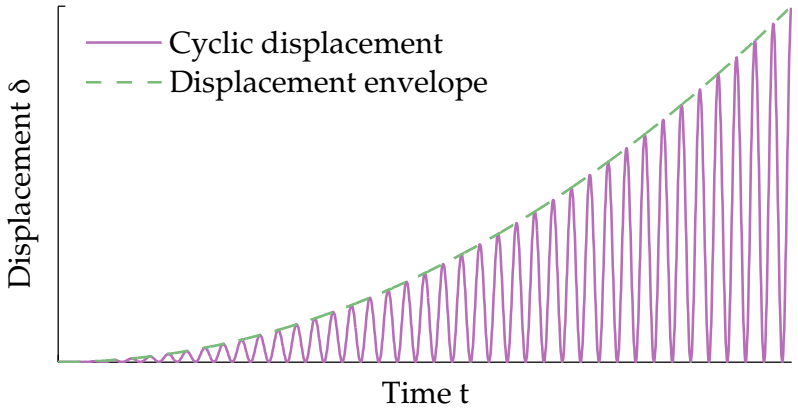


Figure 2.27.: Numerically computed displacement

cycle The time t and cycles N are related through the cyclic frequency ω,

$$N = \omega t. \tag{2.14}$$

The second common feature of these models is that they are all based on damage mechanics and therefore use a damage variable D, which is a combination of static damage due to separation of the interface ahead of the crack tip and fatigue damage accumulated due to cyclic loading. The damage evolution is a sum of static damage and fatigue damage, so

$$\frac{dD}{dN} = \dot{D}_{static} + \dot{D}_{cyclic}. \tag{2.15}$$

Robinson et al. [RGT+05] used the following exponential function containing three fitting parameters, α, β, and λ to describe the damage evolution for a specific fracture mode

$$\frac{dD_f}{dN} = \frac{\alpha}{1+\beta} e^{\lambda D} \left(\frac{\delta}{\delta_c}\right)^{\beta} \tag{2.16}$$

The damage accumulation is calculated by integrating the damage rate from one increment at N cycles to the next increment at $N + \Delta N$. The model was implemented in a 2D cohesive element and used to simulate a DCB, ENF, and MMB specimen. The numerical results were then compared to experimental data by Asp et al. [ASG01]. Additional parameter studies had to be performed to determine the constants for the fatigue damage rate for each fracture mode.

This model was further developed by Tumino and Capello [TC07] who eliminated the parameter λ from the fatigue damage rate. They incorporated a variable mixed-

mode adaptation which interpolates the two fitting parameters α and β for the damage evolution from the parameters for mode I, mode II and one fixed mixed-mode case which have to be determined a priori.

Albert Turon [TCCD07] developed a model linking fracture mechanics and damage mechanics. In this model the damage rate

$$\frac{\partial D_f}{\partial N} = \frac{1}{l_{cz}} \frac{(\delta_c(1-D) + D\delta_0)^2}{\delta_c \delta_0} \frac{\partial a}{\partial N}. \tag{2.17}$$

is directly related to the Paris law $\frac{da}{dN}$ and thus does not require parameter studies. However it needs as input the cohesive zone length l_{cz} which Turon derives from an analytical expression. The model is capable of capturing the delamination onset and also allows for a varying R-ratio. Turon uses the model developed by Blanco [BGAC04] for the calculation of the mixed-mode Paris law parameters. The mixed-mode delamination threshold value G_{th} is determined using an expression from Benzeggagh and Kenane [BK96]. Instead of processing a fixed-cycle jump ΔN in each increment, Turon defines a maximum damage increment ΔD_{max} that is then used to define ΔN. This ensures that the maximum damage increase per increment never exceeds ΔD_{max}. A comparison of a Paris law curve fit to the numerical results shows reasonable agreement for mode I. For mode II and mixed-mode the agreement is not very good which Turon attributes to friction effects that are not considered and not using the same equation to calculate the cohesive zone length as for mode I.

The Turon fatigue degradation strategy has been used by Naghipour et al. [NBV22] to simulate mixed-mode fatigue delamination in CF/PEEK laminates. However, Naghipour et al. chose to use a different equation for the calculation of the cohesive zone length based on a parameter study by Harper and Hallett [HH08] with an adjusted mixed-mode scaling factor. They use the model to simulate an MMB test and find better agreement with the curve-fitted Paris law as in the original implementation by Turon.

The principle of the Turon fatigue degradation strategy has also been used by Pirondi and Moroni [PM10] to predict 2D fatigue crack growth in bonded joints for mode I and mode II. Pirondi et al. do not consider the static damage in the fatigue damage

rate and therefore arrive at a simplified version compared to Turon.

$$\frac{\partial D_f}{\partial N} = \frac{1}{l_{cz}} \frac{\partial a}{\partial N}. \tag{2.18}$$

The cohesive zone length is calculated in the same manner before. While Turon calculates the strain energy release rate from the constitutive response of the cohesive element, Pirondi et al. use a J-Integral to do this. They also apply the ΔD_{max} strategy to adjust the cycle jump. They perform a simulation of the DCB, ENF and ELS test. For mode I the Paris law exponent is too low while for the mode II simulations there is good agreement with the Paris law. A parameter study demonstrates that there should be at least four to five elements in the cohesive zone.
The model was later extended to mixed-mode [MP12] using a mixed-mode bilinear cohesive law with a quadratic stress criterion for delamination onset and a model by Kenane and Benzeggagh [BK96] to determine the mixed-mode fracture toughness. For the mixed-mode Paris law which is required as an input for the fatigue damage calculation Moroni and Pirondi use three different models by Kenane and Benzeggagh [BK96] , Quaresimin [QR06], and a simplified version from Abdel Wahab [WACS02]. They simulated an MMELS specimen with a mixed-mode ratio of 0.41. All three models show good agreement with the predicted Paris law but show an under prediction of the crack length. Moroni et al. explain this with the different step size used for the number of cycles integration compared to the analytical solution.

The fatigue degradation strategy by Harper and Hallett [HH10] uses a different static damage formulation the the Robinson and Turon strategies. While the former use the static damage to degrade the initial stiffness K, this model uses a stress-based damage. As with the Turon model the damage evolution in this model also relates the Paris law to the fatigue damage rate

$$\frac{\partial D_f}{\partial N} = \frac{1 - D_s - D_{f,u}}{l_{fat}} \frac{\partial a}{\partial N} \tag{2.19}$$

and requires the cohesive zone length as input. The cohesive zone length is estimated from the quasi-static value $l_{cz,s}$ which has to be determined a priori as the ratio of the strain energy release rate and the fracture toughness, so the cohesive

zone length in fatigue is $l_{fat} = \frac{G_t}{G_c} l_{cz,s}$. The cohesive zone is then split into a static and a fatigue part where the elements undergo only static or fatigue failure respectively. $D_{f,u}$ is unwanted static damage that accumulates in the fatigue part of the cohesive zone. The mixed-mode parameters for delamination onset are calculated according to a criterion by Brewer [BL88] while the mixed-mode fracture toughness is determined using a power law failure criterion. The mixed-mode Paris law is determined using the model by Blanco [BGAC04]. The model is then compared to mode I, mode II and mixed-mode experimental data from Asp et al. [ASG01]. The mode I agreement is quite good while for mode II the Paris law is under predicted. Harper attributes this to an over prediction of the fatigue part of the cohesive zone. The model by Harper et al. has been further extended by May et al. [MH11] to be able to capture delamination initiation based on S-N curves. A failure index is defined as the ratio of the current mixed-mode energy release rate and the mixed-mode fracture toughness. In a zone within a predefined radius of the element with the highest failure index a delamination initiation criterion is applied to all elements on the linear-elastic part of the bilinear constitutive law. The elements are implemented in an explicit code and the fatigue damage initiation rate is defined with respect to time as

$$\frac{\partial D_{fi}}{\partial t} = \frac{\partial N}{\partial t} \cdot 10^{-\frac{1-sev_{zone}}{s_{zone}}} \tag{2.20}$$

Here, $\frac{\partial N}{\partial t}$ is the cycle frequency, sev_{zone} the average severity in the initiation zone and s_{zone} the mean parameter describing the S-N curve. The S-N curve is defined as $sev = 1 - s \cdot \log N$, where $sev := \frac{\sigma}{\sigma_{stat}}$ is the severity. The model was used to simulate a double notched shear test and a short beam short test and compared with experimental results showing reasonable agreement. Both damage initiation and final failure are under predicted which is attributed to inaccuracies in the extraction of the severity from the interface elements and the simplified linear S-N curve used.

Khoramishad et al. [KCKA10] developed a model for predicting fatigue damage in bonded joints. In this model the damage evolution is related to the principal strain

$$\frac{\partial D_f}{\partial N} = \begin{cases} \alpha(\epsilon_{max} - \epsilon_{th})^{\beta} & , \epsilon_{max} > \epsilon_{th} \\ 0 & , \epsilon_{max} \leq \epsilon_{th} \end{cases} . \tag{2.21}$$

The maximum strain ϵ_{max} is calculated from the normal and the shear strain, where $\epsilon_{max} = \frac{1}{2}(\epsilon_n + \sqrt{\epsilon_n^2 + \epsilon_s^2})$. The parameters α, β, and ϵ_{th} need to be calibrated with experimental tests. This is the only model where the interface is not zero-thickness and the strain is calculated from the displacement as $\epsilon = \frac{\delta}{t}$ where t is the tickles of the adhesive bond. The model has been implemented into ABAQUS and each integration point is assigned two damage variables D_s and D_f for static and fatigue damage respectively. The value of the fatigue damage is used to degrade the constitutive law, while the static damage is then defines the remaining traction on this constitutive law as shown in figure 2.28. Mixed-mode was incorporated into the

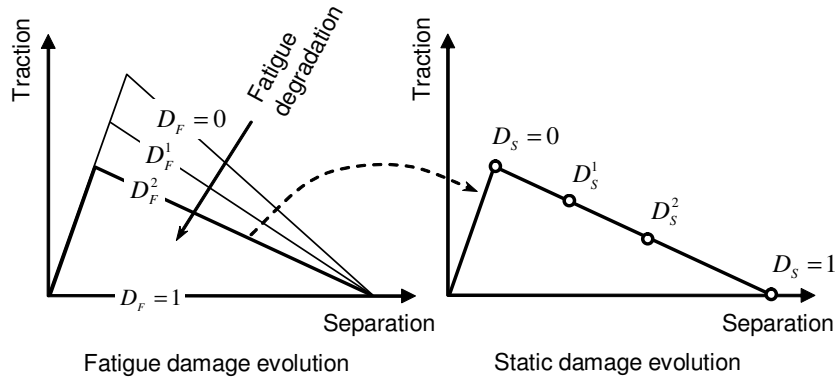


Figure 2.28.: Fatigue damage D_f and cohesive law damage D_s [KCKA10]

model using a maximum nominal stress criterion for the initiation where damage is assumed to initiate when either the mode I or mode II tractions exceed the critical value. Propagation was modelled using the BK-criterion [KB97]. The strategy was used to simulate the delamination of a single lap joint and laminated doubler in bending. A comparison of numerical data with experimental load-life data shows good agreement.

Kawashita and Hallett [KH12] developed another model for fatigue delamination using a crack-tip tracing algorithm. This model was also implemented in an explicit FE-code. The damage rate is defined as follows

$$\frac{dD_f}{dN} = \frac{1 - D_s}{l_e}\frac{da}{dN}, \tag{2.22}$$

where l_e is the element length which depends on the direction of delamination propagation, $\frac{da}{dN}$ the Paris law and D_s the static damage. While in the cohesive zone all elements experience fail statically according to a bilinear constitutive law, fatigue damage is only applied to the crack-tip elements so an algorithm is employed that identifies these. The energy release rate G^{NL} required for the Paris law is calculated as the maximum value of the energy release rate of the crack-tip element G^{inst} and the energy release rates of the neighbouring elements that have already failed. The crack-tip tracing allows 3D delamination propagation and compared to the previous models by Turon and Harper, no cohesive zone length needs to be calculated. For mixed-mode delamination initiation a quadratic criterion is applied and a linear criterion for failure. The mixed-mode Paris law is calculated based on the model by Blanco [BGAC04]. The fatigue degradation strategy is used to simulate the delamination propagation of a cut-ply specimen and a composite circular plate which is loaded centrally. For the cut-ply specimen the numerically extracted Paris law shows very good agreement with experimental results. Comparison with VCCT analyses of the crack growth rate vs. delamination radius for the circular plate show that especially with the coarse mesh, which has an element size of 1 mm in this case, using G^{NL} provides a much more accurate measure of the strain energy release rate than G_{inst}.

Landry and LaPlante [LL12] modelled delamination growth under varying amplitude fatigue in mode I. The fatigue model formulation is based on those by Turon [TCCD07] and Harper and Hallett [HH10] and the fatigue damage rate is defined as

$$\frac{dD_f}{dN} = \frac{1 - D_s}{L_{eff}} \frac{da}{dN}. \tag{2.23}$$

L_{eff} is the undamaged length of the crack-tip element which is required for the transitions between static and fatigue loading and D_s is the damage parameter related to the stress-based damage. Figure 2.29 shows the fatigue and static damage representation. The cohesive zone is shown in figure 2.30. The strain energy release rate G_{max} required for the Paris law is interpolated from the extracted energy

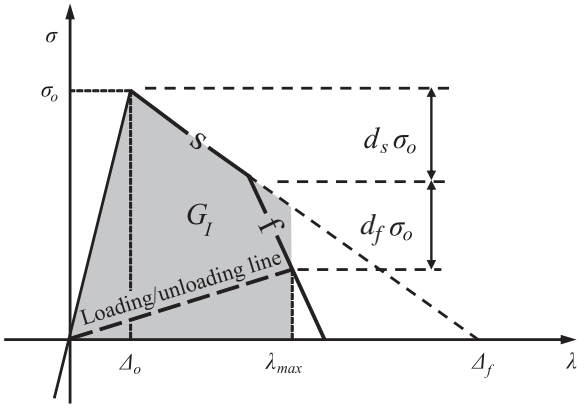


Figure 2.29.: Constitutive response with fatigue damage D_s and D_f [LL12]

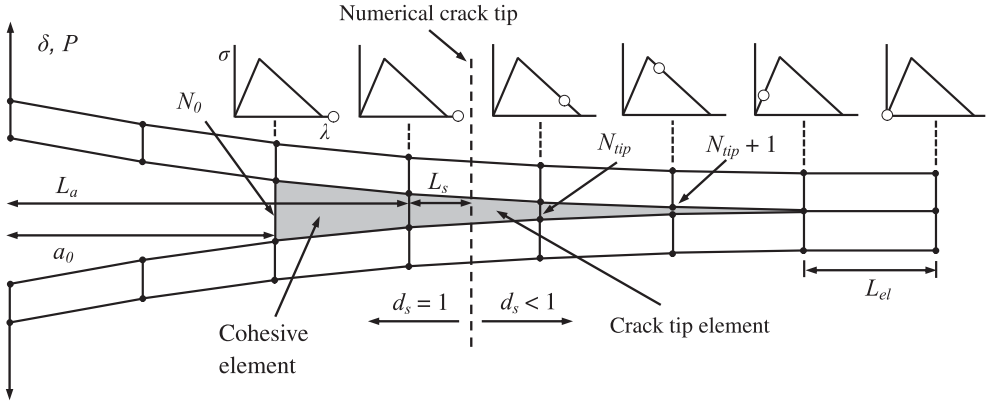


Figure 2.30.: Cohesive zone in DCB under opening displacement [LL12]

release rate values of the two node pairs at the crack tip.

$$G_{max} = \frac{1 - D_{s,N_{tip}} - D_{f,N_{tip}}}{1 - D_{s,N_{tip}}} G_{N_{tip}} + \frac{D_{f,N_{tip}}}{1 - D_{s,N_{tip}}} G_{N_{tip+1}} \tag{2.24}$$

$G_{N_{tip}}$ and $G_{N_{tip+1}}$ are calculated as the area under the static cohesive law (see figure 2.29) The model was used to simulate 12,000 cycles with three fatigue regimes and two quasi-static loadings. The displacement vs. delamination length results show good agreement with experimental data. The value of G_{max} is over predicted during the fatigue loading which may be due to the calculation of the energy release rate from the static curve rather than the fatigue constitutive response. Very recently Moura and Goncalves [dMG14] developed a model for the delamination of bonded joints in mode II. It is based on a bilinear static cohesive law with stiffness-based

damage. The fatigue damage rate in each integration point is

$$\frac{dD_f}{dN} = \frac{\delta_0 \delta_c}{\delta^2 A_{ip}} \frac{dA_p}{dN} \tag{2.25}$$

The input Paris law $\frac{dA_p}{dN}$ for each integration point is a fraction of the global Paris law according to the Newton-Cotes weight of the integration point and the number of integration points in the cohesive zone, and A_p is the area that corresponds to the integration point. The algorithm has been used to simulate 2D ENF tests with up to 12,000 cycles. The model is able to predict the Paris law relatively accurately up to a certain number of cycles where according to the authors spurious behaviour induced by the normal compressive stresses developing near the central loading point occurs. The simulation was conducted with two different mesh sizes with a length of 1.5 mm and 0.375 mm which led to very similar results.

There has been much development over recent years to develop a model for the simulation of delamination due to fatigue but apart from the model by Kawashita and Hallett [KH12] which requires a crack-tip tracing algorithm none of the models suitable for high-cycle fatigue are able to predict the Paris law perfectly. It is therefore still of interest to develop a new model which can accurately and effectively predict the Paris law.

In order to develop a new fatigue degradation strategy, four of the existing models have been chosen to be analysed with the cylinder model which will be discussed in the next section. These are the model by Robinson [RGT+05] as a representative of a model with a fatigue damage degradation that requires material parameters to be calibrated (like the model by Khoramishad [KCKA10]). The Turon model [TCCD07] was chosen, because it was used by a number of authors to perform simulations ([NBV22]) or develop their own model ([PM10], [MP12], [LL12]). The same is true for the Harper model [HH10] which also influenced the development of some other models ([MH11], [LL12]). The Kawashita model [KH12] was examined because it provided the best agreement with the Paris law.

2.5. Cylinder model

This section contains the description of the cylinder model, a computationally inexpensive analytical model which allows rapid assessment, comparison, parameter studies, and sensitivity studies of constitutive laws, damage definitions and fatigue degradation strategies in mode I. The motivation for the analytical model discussed in this chapter lies in the fact that a direct finite element (FE) analysis is relatively slow. Not only does it take a long time to run a single simulation, setting up the model, and post-processing the results is also very time-consuming. Moreover, the complex algorithms necessary to arrive at a converged solution introduce more variables which make it harder to assess the effectiveness of a particular fatigue degradation strategy. The cylinder model, originally developed by Lopez et al. [Arm08] makes it possible to rapidly test and compare different fatigue degradation strategies and, if necessary find parameters and adjust the models accordingly. It is also a feasible way of conducting sensitivity studies to analyse the influence of various parameters, which is otherwise too time-consuming. The outline of the chapter is as follows: first, the cylinder model is described and then three static constitutive laws are examined. The implementation and comparison of fatigue-degradation strategies is discussed in the next chapter.

2.5.1. Description of the cylinder model

The model consists of two zero-thickness layers of width W and unspecified length. The bottom layer is fully attached to the ground and the top layer is attached to a cylinder of radius R as shown in figure 2.31. A moment M_a is applied to the cylinder, which causes it to rotate and the two layers to delaminate. Figure 2.32 depicts a 2D projection of the initial and the rotated state of the cylinder. A horizontal axis is aligned with the direction of delamination propagation and the origin $x = 0$ is the initial point of contact of the cylinder and the top-layer. The point of contact where the cylinder touches the x-axis is referred to as x_a. This point marks the start of the cohesive zone. At the heart of this model lies an energy balance that relates the work done by the externally applied load M_a to the energy, which is consumed in separating the interface. The work done by the moment is the product of the change

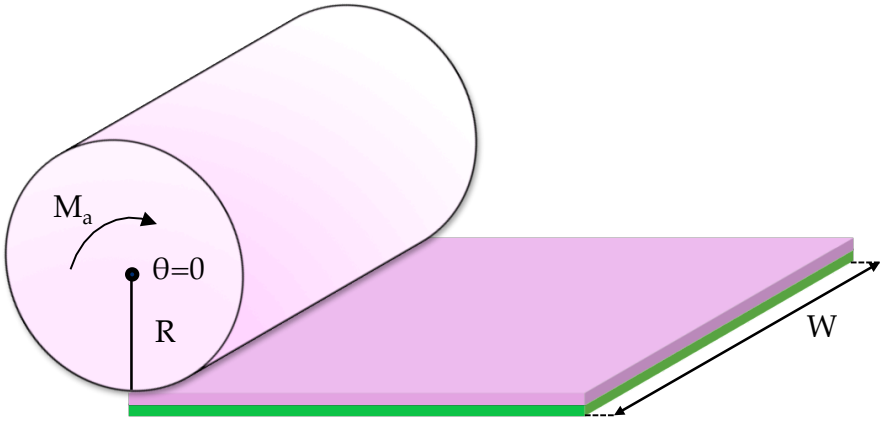


Figure 2.31.: Cylinder model

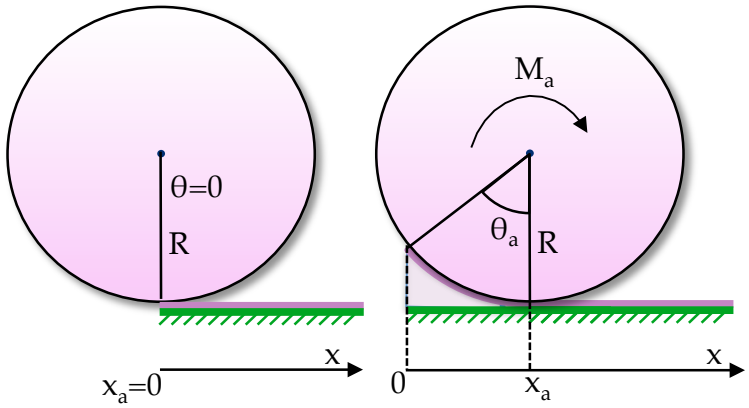


Figure 2.32.: Projection of cylinder model

in angle $\Delta\theta$ and the moment M_a. The internal energy consumed is a product of the applied energy release rate G_a and the crack area created. Therefore,

$$M_a \Delta\theta = \Delta x W G_a. \tag{2.26}$$

The moment at which quasi-static crack propagation occurs is called the critical moment M_c. From the interface toughness G_c, M_c can be computed by first relating the arc-length Δx and the change in rotation $\Delta\theta$

$$\frac{\Delta\theta}{2\pi} = \frac{\Delta x}{2\pi R} \tag{2.27}$$

and then, using equation (2.26)

$$\begin{aligned} & M_c \Delta\theta = \Delta x G_c W \\ \Leftrightarrow \quad & M_c \tfrac{\Delta x}{R} = \Delta x G_c W \\ \Leftrightarrow \quad & M_c = G_c W R. \end{aligned} \tag{2.28}$$

Combining equations (2.26) and (2.27), the applied energy release rate G_a can be expressed as

$$G_a = \frac{M_a}{WR} \tag{2.29}$$

In order to investigate static cohesive zone laws and fatigue degradation strategies for cohesive elements, the cohesive zone is now discretized. The interface response between the two layer is simulated by springs, which take the place of interface elements in a finite element analysis. Δl is the horizontal distance between the individual springs corresponding to the mesh size in a finite element model as shown in figure 2.33. The springs are assigned a traction-separation relationship $\sigma(\delta)$. The

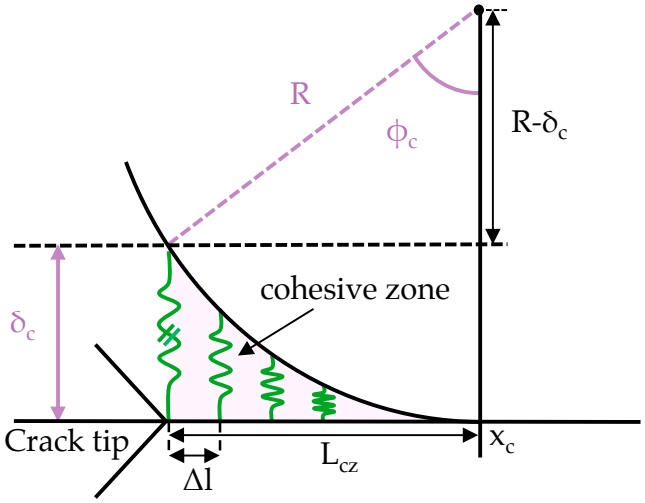


Figure 2.33.: Cohesive zone and critical spring angle ϕ_c

critical displacement at which a spring fails δ_c statically and the corresponding angle ϕ_c are also shown in figure 2.33. From this, the static cohesive zone length L_{cz} can be calculated as follows

$$L_{cz} = \sqrt{R^2 - (R - \delta_c)^2} = \sqrt{2R\delta_c - \delta_c^2}. \tag{2.30}$$

Given a fixed static cohesive law, the radius R of the cylinder determines the cohesive zone length of the model. In order to be able to compare a finite element

analysis with a cylinder model analysis, a quasi-static analysis of the FE-model can be run to determine the static cohesive zone length L_{cz}. This cohesive zone length can then be used to determine the radius of the cylinder R. Alternatively, the cohesive zone length can first be estimated using a predictive formula and then the radius can be adjusted to match the predicted cohesive zone length. These predictive formulae have been studied extensively by Harper and Hallett [HH08] for composite materials.

Equation (2.30) is only valid under the assumption that the springs remain vertical as they reach an extension of δ_c. In a mathematical sense this is not the case if $\delta_c > 0$. The angle α, shown in figure 2.34 is influenced by two parameters, the radius R and the final displacement δ_c. Suppose that the spring has one endpoint O at the origin

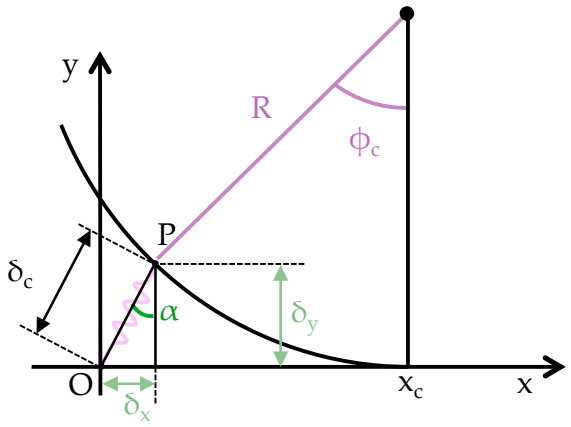


Figure 2.34.: Cylinder with first spring at maximum extension δ_c at angle α

of the coordinate system and the other at P on the circle. O and P originally coincide and as the cylinder moves, P is tracing a cycloid curve. Therefore, the coordinates of P are

$$x = R(\phi_c - \sin\phi_c) \tag{2.31}$$

$$y = R(1 - \cos\phi_c). \tag{2.32}$$

δ_c can then be expressed in terms of R and ϕ_c using the Pythagorean theorem

$$\delta_c^2 = (R(\phi_c - \sin\phi_c))^2 + (R(1 - \cos\phi_c))^2 \tag{2.33}$$

$$= R^2(\phi_c^2 - 2\phi_c \sin\phi_c - 2\cos\phi_c + 2). \tag{2.34}$$

The unknown ϕ_c can be found using an iterative algorithm like the Newton-method and once ϕ_c is known, the angle of inclination α is calculated.

$$\alpha = \sin^{-1} \frac{R(1 - \cos \phi_c)}{\delta_c}. \tag{2.35}$$

The inclination angle α vs. the radius of the cylinder R for a range of critical displacements δ_c is shown in figure 2.35. The experiments conducted with the cylinder

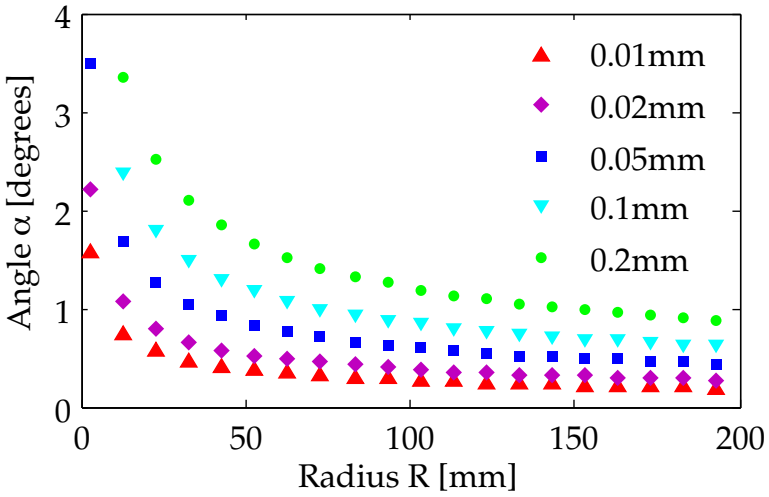


Figure 2.35.: Angle α vs. Radius R for various δ_c

model in this thesis generally have input values of $\delta_c = 0.0173$ mm and $R = 100$ mm resulting in an inclination of the spring at the static breaking point of 0.37°, so the relative error in the angle is only 0.4 %.

2.5.2. Displacement-controlled analysis

In order for the cylinder to be in equilibrium when a moment M_a is applied, a moment M_t which is equal in magnitude and opposite in orientation must be supplied through the resistance of the springs about the contact point x_a. This moment can be calculated by first calculating the spring extensions and from those the spring tractions. From the tractions the spring forces can be calculated and from those forces the moment M_i exerted by each spring. For a known equilibrium angle θ_a, the contact point x_a of the delaminating upper layer and the bottom layer is $R\theta_a$.

The first spring is located at $x = 0.5\Delta l$, so the total number of springs n_{cz} in the cohesive zone is

$$n_{cz} = \left\lfloor \frac{x_a + 0.5\Delta_l}{\Delta_l} \right\rfloor = \left\lfloor \frac{x_a}{\Delta_l} + 0.5 \right\rfloor, \tag{2.36}$$

where $\lfloor x \rfloor$ denotes the greatest integer smaller than x. The x-coordinate of the i th

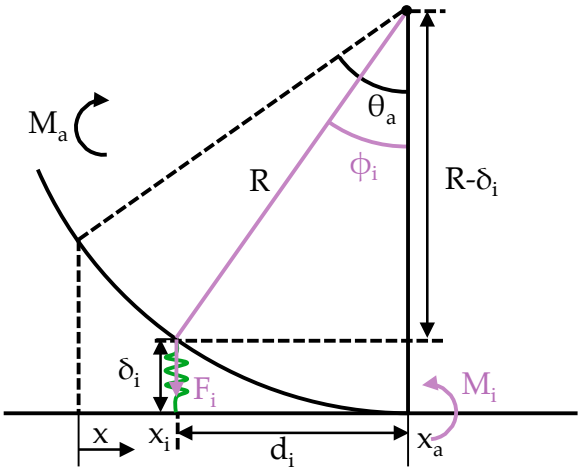


Figure 2.36.: Detailed view of cohesive zone

spring (see figure 2.36) is

$$x_i = (i - 0.5) \cdot \Delta l. \tag{2.37}$$

The horizontal distance d_i between the i th spring and the contact point is

$$d_i = x_a - x_i. \tag{2.38}$$

The angle ϕ_i can be expressed in terms of d_i and R in the following way

$$\phi_i = \sin^{-1} \frac{d_i}{R}, \tag{2.39}$$

and the extension of the spring δ_i is then

$$\delta_i = R - R\cos\phi_i. \tag{2.40}$$

Since the springs act as cohesive elements in this model, the spring stress σ_i is related to the spring extension δ_i through a constitutive law, which could, for example, be a bilinear law, polynomial law or an exponential law.

The spring force F_i is the product of the area represented by the spring and the traction $\sigma_i(\delta_i)$, so

$$F_i = \sigma_i(\delta_i) \cdot W \cdot \Delta l. \tag{2.41}$$

Finally, the moment contribution M_i of the ith spring is

$$M_i = F_i \cdot d_i, \tag{2.42}$$

and the total moment M_T is the sum of the spring moments M_i

$$M_T = \sum_{i=1}^{n_{cz}} M_i. \tag{2.43}$$

2.5.3. Moment-controlled analysis

When an external moment $M_a < M_c$ is applied, the equilibrium position of the cylinder is unknown, so the resulting equilibrium angle θ_a has to be found. This amounts to solving the following equation for θ_a

$$M_a = \sum_{i=1}^{\lfloor \frac{R\theta_a}{\Delta l} + 0.5 \rfloor} \sigma(R - R\cos(\sin^{-1} \frac{R\theta_a - (i - 0.5) \cdot \Delta l}{R}))\Delta l \cdot W. \tag{2.44}$$

This equation is solved by approximating θ_a through an iterative nested intervals process using the following algorithm 1, where the initial search interval is $[\theta_l, \theta_u] = [0, \theta_c]$. θ_u and θ_l denote the current upper and lower limit of the search interval, and θ_a is the current estimate for the applied angle. tol is the tolerance for the relative error in the calculation of M_T.

Data: Tolerance tol, M_a, Constitutive law $\sigma(\delta)$, R

Result: Equilibrium angle θ_a

Initialization: $\theta_a = \frac{M_a}{M_c} \cdot \theta_c$, $\theta_u = \theta_c$, $\theta_l = 0$;

while $\frac{|M_t - M_a|}{M_a} > tol$ **do**

  Find contact point $x_a = R\theta_a$;

  Find $n_{cz} = \left\lfloor \frac{x_a}{\Delta_l} + 0.5 \right\rfloor$;

  for $i = 1, n_{cz}$ **do**

    $\delta_i = R - R\cos(\sin^{-1} \frac{R\theta_a - (i-0.5)\cdot\Delta l}{R})$;

    According to cohesive law find $\sigma_i(\delta_i)$;

    $M_i = \sigma_i(\delta_i) \cdot \Delta l \cdot W$;

  end

  Compute $M_t(\theta_a) = \sum_{i=1}^{n_{cz}} M_i$;

  if $M_t > M_a$ **then**

    $\theta_u = \theta_a$;

  else

    $\theta_l = \theta_a$

  end

  $\theta_a = \frac{\theta_u + \theta_l}{2}$

end

Algorithm 1: Finding the equilibrium angle θ_a

2.5.4. Comparison of static constitutive laws with the cylinder model

A key part of any cohesive zone model is the constitutive law relating displacements and cohesive stresses. Three constitutive laws found in the literature are examined in the following section. These are the bilinear law [HMP76], the polynomial law [Nee87], and the exponential law [XA93]. Figure 2.37 shows a plot of all three. In order to make the constitutive laws more comparable they are all set up with the same fracture toughness G_c, which is the area under the respective graphs, so

$$\int_0^{\delta_c} \sigma(\delta) d\delta = G_c. \tag{2.45}$$

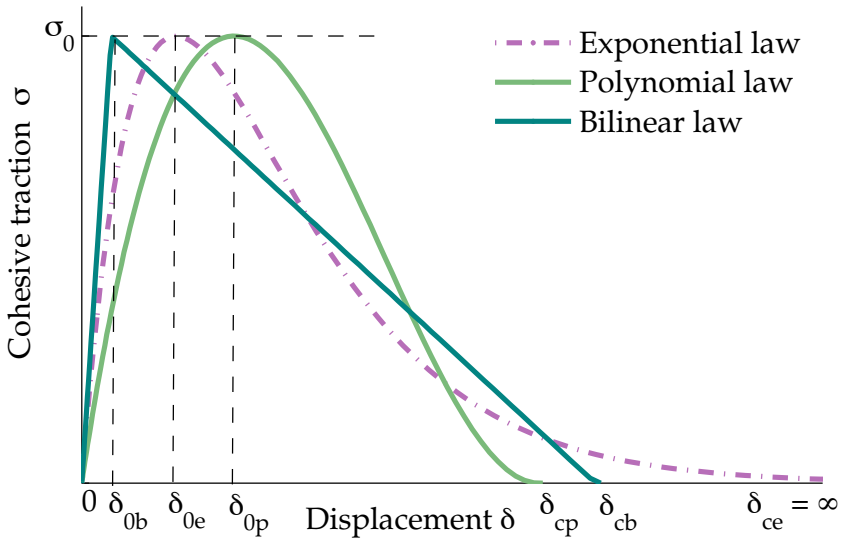


Figure 2.37.: Constitutive laws

The bilinear law is a piecewise function consisting of three linear parts

$$\sigma(\delta) = \begin{cases} \frac{\sigma_0}{\delta_0}\delta & ,0 \leq \delta \leq \delta_0 \\ \sigma_0 \left(\frac{\delta_c - \delta}{\delta_c - \delta_0}\right) & ,\delta_0 < \delta \leq \delta_c, \\ 0 & ,\delta_c < \delta \end{cases} \tag{2.46}$$

which is specified by δ_0 (δ_{ob} in fig. 2.37) and any two of three variables G_c, σ_0, and δ_c. Their relationship is defined by the area of the triangle with vertices $(0,0)$, (δ_0, σ_0), and $(\delta_c, 0)$, so

$$G_c = \frac{1}{2}\sigma_0 \cdot \delta_c. \tag{2.47}$$

The second constitutive law in figure 2.37 is the third-order polynomial law

$$\sigma(\delta) = \begin{cases} \sigma(\delta) = \frac{27}{4}\sigma_0 \cdot (1 - \frac{\delta}{\delta_c})^2 \cdot \frac{\delta}{\delta_c}; & ,0 \leq \delta \leq \delta_c \\ 0 & ,\delta_c < \delta \end{cases} \tag{2.48}$$

where the first part is a cubic polynomial with a maximum at (δ_0, σ_0), so that

$$G_c = \frac{27}{48}\sigma_0 \cdot \delta_c \qquad \text{and} \qquad \delta_0 = \frac{\delta_c}{3}. \tag{2.49}$$

It is specified by any two of the four variables G_c, δ_0 (δ_{op} in fig. 2.37) , δ_c and σ_0.

The exponential law which is the third constitutive law in figure 2.37, has the following analytical expression in mode I

$$\sigma(\delta) = \frac{G_c}{\delta_0^2} \cdot \delta \cdot e^{\frac{-\delta}{\delta_0}}. \tag{2.50}$$

It is specified by any two of the three variables G_c, δ_0 (δ_{oe} in fig. 2.37) , and σ_0. The exponential law has its maximum at δ_0, where the traction is σ_0, so that

$$\sigma_0 = \sigma(\delta_0) = \frac{G_c}{\delta_0 \cdot e}. \tag{2.51}$$

There is no maximum displacement δ_c, where the traction is reduced to 0 as the δ-axis is an asymptote, so in order to specify a cohesive zone length a numerical maximum displacement has to be defined. In the following investigation δ_c for the exponential law is defined, so that $\sigma(\delta_c) = 0.01\sigma_0$.
The numerical values used for this study are shown in Table 2.1. Since all three

	Bilinear	Polynomial	Exponential
G_c $[\frac{N}{mm}]$	0.26	0.26	0.26
σ_0 $[\frac{N}{mm^2}]$	30	30	30
δ_0 $[mm]$	3.e-05	0.0051	0.0032
δ_c $[mm]$	0.0173	0.0154	-

Table 2.1.: Constitutive law parameters

constitutive laws were chosen with the same G_c the critical moment M_c is the same. The critical angles however are different due to the difference in δ_c. The cylinder dimensions used are shown in Table 2.2. Figures 2.38, 2.39, and 2.40 show the total

Radius R	Width W	Critical Moment M_c
100 mm	1 mm	26 Nmm

Table 2.2.: Cylinder parameters

moment M_T exerted by the springs on the contact point x_a versus the rotational angle θ for a varying number of springs n_{cz} in the cohesive zone, where $1 \leq n_{cz} \leq 20$.

The total moment is calculated according to equations 2.37 through 2.43. The plateau in all three figures shows the range of angles where the critical moment M_c has been reached and the cohesive zone is fully developed. The springs then fail statically so M_T does not increase. The maximum angle θ_{max} was chosen to be double that of the critical angle θ_c, so $\theta_{max} = 2 \cdot \theta_c$. Choosing θ_c like this means that the

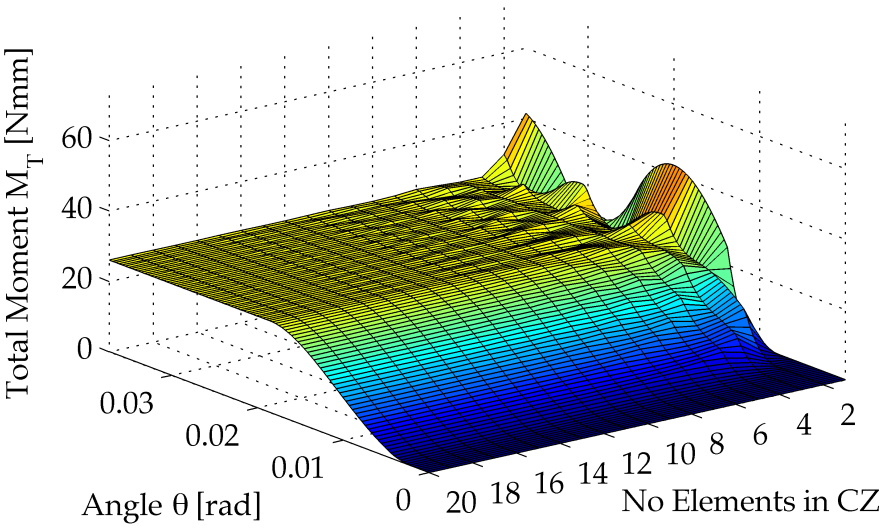


Figure 2.38.: Bilinear law

final crack length is equal to the length of the cohesive zone. All three of the surfaces display oscillations which become very pronounced for a low number of elements in the cohesive zone. The surfaces all reach their extreme values when there is a single spring in the cohesive zone. The maximum points of the oscillations vary depending on the underlying constitutive law. The exponential constitutive law has the greatest maximum value for M_T, which is close to 70 Nmm, followed by the polynomial law with a maximum value of close to 60 Nmm. The constitutive law resulting in the lowest maximum value for M_T of slightly over 40 Nmm is the bilinear law. Another feature of all three surfaces are the 'ripples' extending from these maximum values towards the region with more cohesive elements. These ripples have the furthest extension for the bilinear law, where they are still visibly pronounced when there are 12 elements in the cohesive zone. For the polynomial and the exponential constitutive laws they smooth out when there are more than 8 and more than 6 elements in the cohesive zone respectively.

Due to the presence of these oscillations at low element numbers, a sufficient number of elements n_{cz} need to be in the cohesive zone to obtain reliable results for the resisting moment M_T. Therefore, a study of the relative error in M_T with respect to n_{cz} was conducted, taking $M_{T,20}$, which is the moment calculated with 20 elements

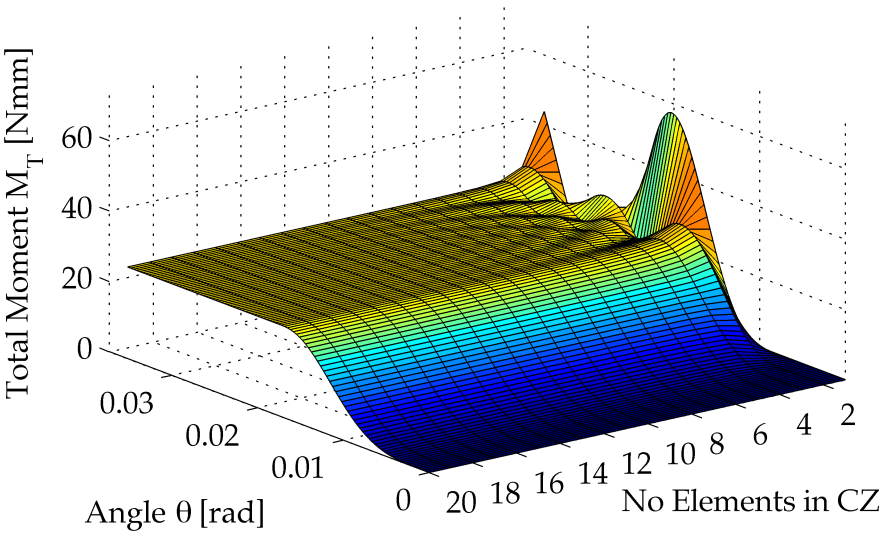


Figure 2.39.: Polynomial law

present in the cohesive zone as the baseline. For a particular rotational angle θ, the relative error $e_i(\theta)$ of $M_{T,i}(\theta)$ is then

$$e_i(\theta) = \frac{|M_{T,20}(\theta) - M_{T,i}(\theta)|}{M_{T,20}(\theta)} \cdot 100, \tag{2.52}$$

where i is the number of elements in the cohesive zone and $1 \leq i \leq 20$. Since the eventual goal is to study high-cycle fatigue-degradation strategies rather than static crack propagation, the range of angles was limited to $0 \leq \theta \leq \theta_c$. As a measure for the number of elements in the cohesive zone necessary, the maximum relative error across all angles $e_{i,max}$ is determined as follows

$$e_{i,max} = \max_{\theta_{th} \leq \theta \leq \theta_c} e_i(\theta), 1 \leq i \leq 20, \tag{2.53}$$

where θ_{th} is a threshold angle. The threshold angle is introduced because for very low total moments, e_i can become very large as the relative difference in the total moment M_T can be large even though the absolute values are small. For the materials studied in this thesis, there is a threshold value M_{th} corresponding to a threshold energy release rate G_{th} below which no fatigue crack growth occurs, so if $M_T < M_{th}$ the corresponding errors are not relevant and are ignored when calculating e_{max}. The angle θ_{th} is defined, so that $M_T(\theta_{th}) = M_{th}$. Such a cutoff point has to be defined for the notion of a minimum number of elements in the cohesive zone

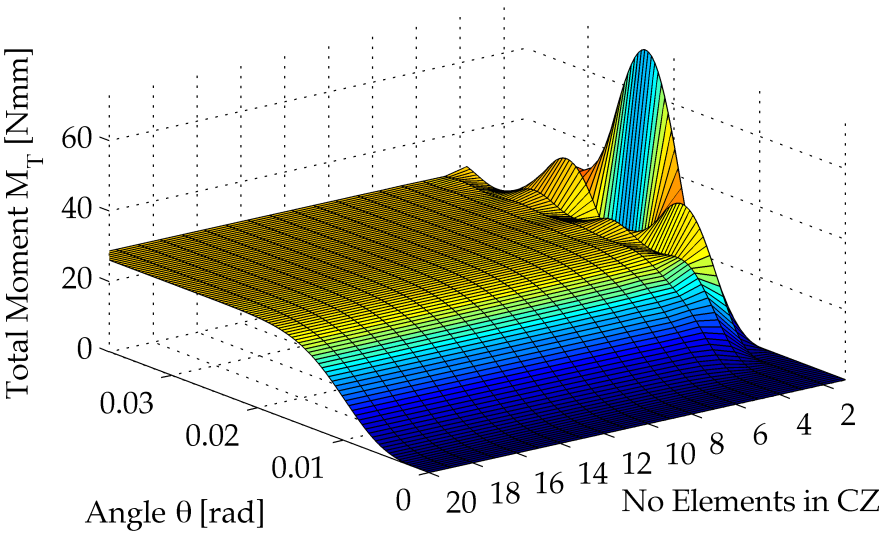


Figure 2.40.: Exponential law

to make practical sense when using the relative error as a measure.

Figure 2.41 shows the relative maximum error e_{max} versus the number of elements in the cohesive zone for all three interface laws. The threshold value M_{th} in this figure is set as $M_{th} = 0.05 \cdot M_c = 1.3$ Nmm. The two parallel dotted lines correspond to a relative error of 10% and 5% which are set as arbitrary error limits to determine the minimum number of elements to be used during an analysis. Since e_{max} exceeds 100 % for all three constitutive laws when $n_{cz} < 3$ there are no points in the plot for this range. The maximum error e_{max} is highest for the exponential law, followed by the polynomial law. The bilinear law has the lowest maximum error but the error is oscillating as n_{cz} changes which is not the case for the other two cohesive laws. These oscillations can be picked out visually in figure 2.38 as well. The other two surfaces in figure 2.39 and figure 2.40 look more smooth, however the error in the calculation of M_T is higher for both of them. From figure 2.41 the minimum number of elements n_{cz} that should be present can be concluded, which is where the data points fall below the dotted lines. For a maximum error below 5% corresponding to the lower line, n_{cz} is therefore 8 elements, 11 elements, and 15 elements for the bilinear, polynomial, and exponential law respectively. Table 2.3 shows n_{cz} for all three interface laws for a range of threshold moments M_{th}. It should be noted that

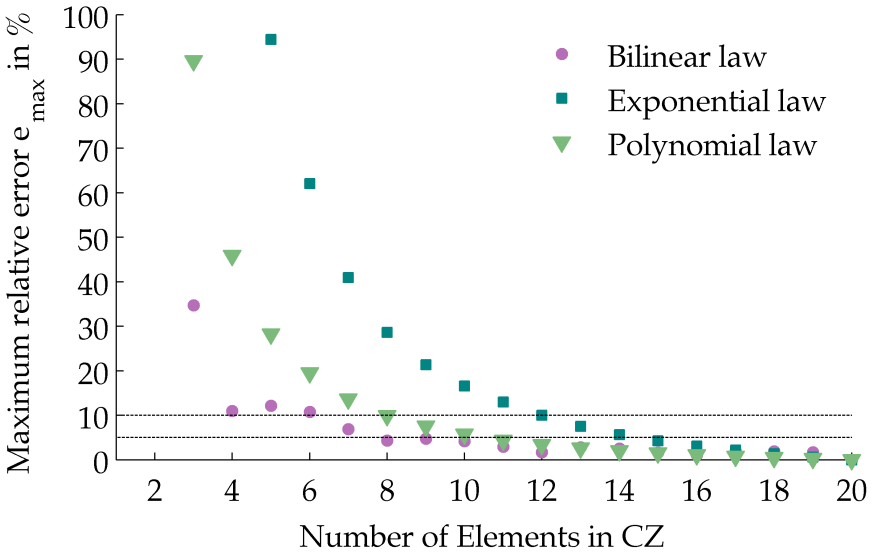


Figure 2.41.: Maximum relative error e_{max} in the calculation of M_T against the number of elements in the cohesive zone for three different constitutive laws for $M_{th} = 0.05M_c$

this is the minimum number of elements needed in the cohesive zone to calculate an accurate total moment M_T. Since the cylinder model elements are represented by single springs, there is only one integration point per element and this is likely the main cause that the number of required elements is higher than in other studies carried out using a finite element analysis. Harper et al. [HH08] have found that for a static DCB the number of elements in the cohesive zone should be at least two, while it should be at least three according to Turon et. al. [TDCC05].

	Relative error in M_T < 5%			Relative error in M_T< 10%		
M_{th}	Bilin	Poly	Exp	Bilin	Poly	Exp
$0.05M_c$	8	11	15	7	8	12
$0.1M_c$	6	9	12	5	7	10
$0.2M_c$	5	7	9	4	5	7

Table 2.3.: Minimum number of elements n_{cz} required in cohesive zone, so that the relative error is below the specified one . Bilin=Bilinear law, Poly=Polynomial law, Exp=Exponential law

In order to find the cause for the difference in e_{max} among the three interface laws, the distribution of the traction in the cohesive zone was examined. Figures 2.42, 2.43, and 2.44 show the cohesive traction and the opening displacement δ in the process zone for the bilinear, polynomial, and exponential interface law respectively.

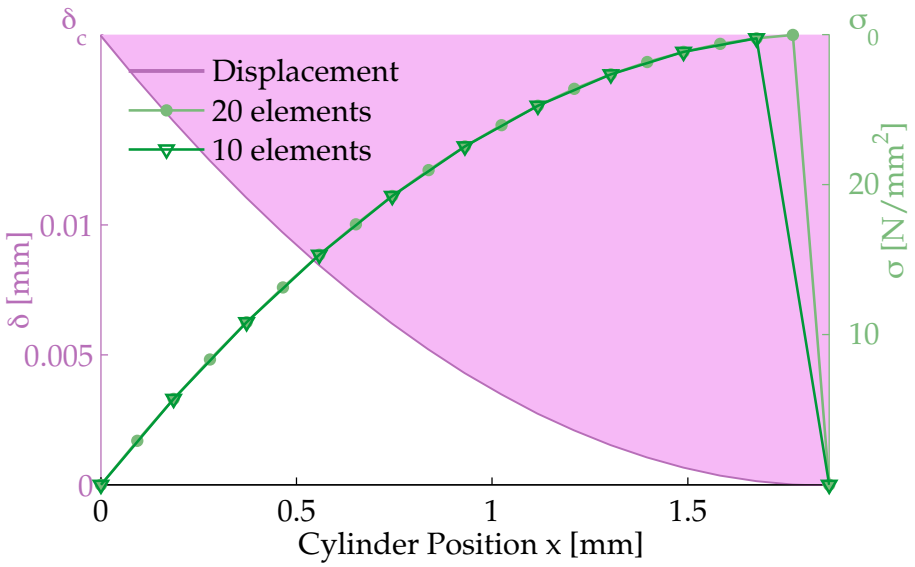


Figure 2.42.: Interface traction distribution of the bilinear law in the CZ

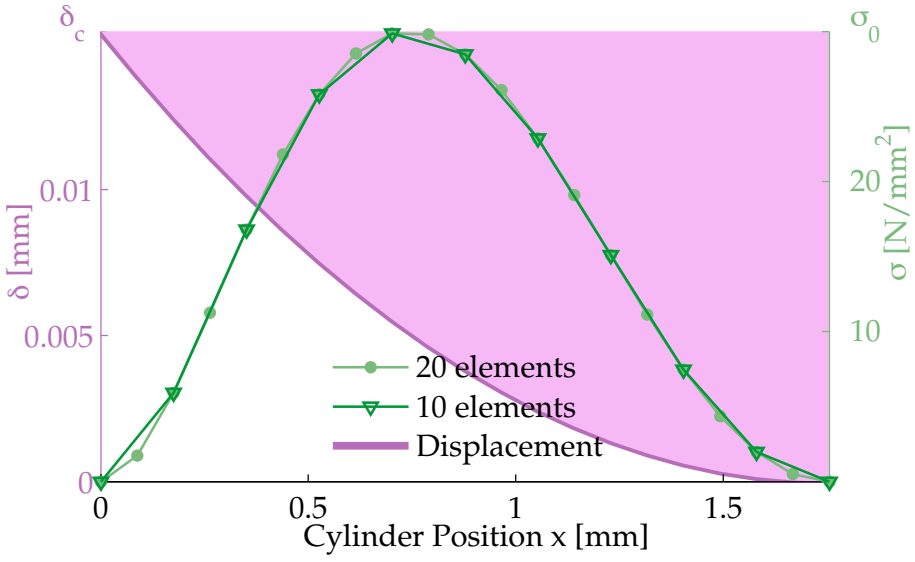


Figure 2.43.: Interface traction distribution of the polynomial law in the CZ

The pink region represents the cylinder. Its boundary marks the opening displace-

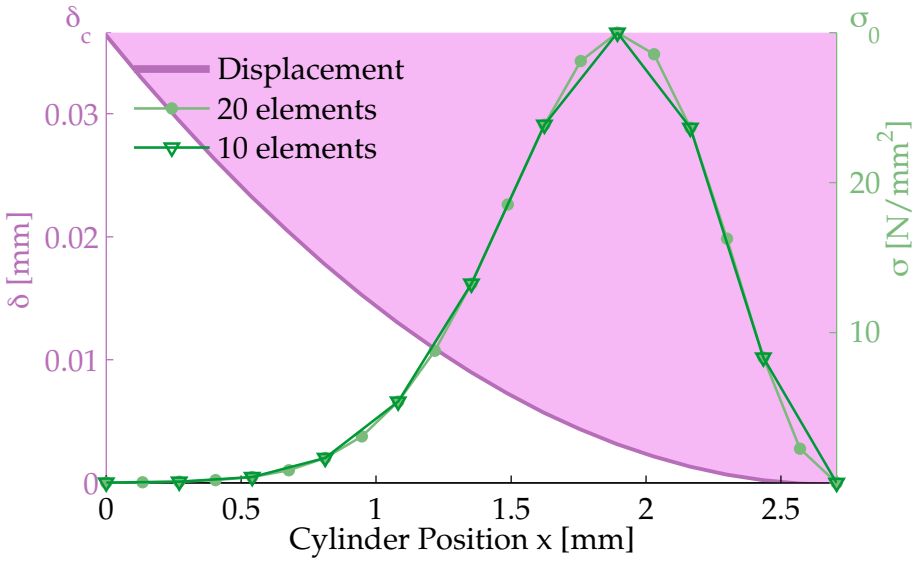


Figure 2.44.: Interface traction distribution of the exponential law in the CZ

ment δ which is measured on the pink vertical axis on the left. The two marked, green lines show the cohesive traction for 20 and 10 elements in the cohesive zone respectively. Traction is measured on the green vertical axis on the right. The range of the horizontal axis is the interval $[0, L_{cz}]$ in all three figures, so the fully developed static cohesive zone is shown.

For the bilinear law the biggest difference between the two traction graphs is at the start of the cohesive zone, where $x = L_{cz}$. Apart from this, the two graphs match quite well. For the polynomial law the greatest differences are at also at the peak, and at the two endpoints. The traction curves for the exponential law also do not match very well at the peak and since the peak is steeper than for the polynomial law, the difference is more pronounced. The elements at the start of the cohesive zone have a smaller influence on the moment M_T because they are closer to the contact point. This explains that the bilinear law has the smallest error e_{max} since the curves match very well for the elements further away from the contact point and the large difference in the traction distribution at the contact point does not cause a big difference in the moment. The exponential law has the longest cohesive zone length. This means that when looking at the same number of elements in the process zone for all three laws, the element size for the exponential law is larger, so

the approximation will not be as accurate.

2.5.5. Summary

In this section the cylinder model was introduced, a non-FE model which allows rapid evaluation of constitutive laws, damage formulations, and fatigue degradation strategies. The model was used to compare the performance of three commonly used static constitutive laws.
All fatigue degradation strategies examined in the next chapter use the bilinear law as a basis, which has the lowest maximum relative error e_{max} due to the maximum traction being reached close to the start of the cohesive zone.

3. Investigation of existing fatigue degradation strategies

3.1. Introduction

In the last chapter, strategies for the fatigue-driven simulation of delamination have been reviewed. In order to develop a possible new fatigue degradation strategy it is advisable to analyse previous approaches to identify the advantages and disadvantages of previous fatigue models which can then help in the construction of a new strategy. Four of the models discussed were chosen to be analysed with the cylinder model, an analytical non-FE model that allows straightforward implementation and fast testing of the strategies, which was also described in the last chapter. The selected fatigue degradation strategies are the Peerlings' model [RGT$^+$05], the Turon model [TCCD07], the Harper model [Har08], and a crack tip tracing model by Kawashita and Hallett [KH12]. The chapter is structured in the following way: it commences with a brief discussion of the investigation methodology and the implementation into the cylinder model. These are followed by a description of the individual strategies. For each of the models sensitivity studies are conducted to determine the mesh sensitivity and the sensitivity to the cycle-jump at four different load levels. This is followed by a discussion of the advantages and the disadvantages of the fatigue algorithms. Each section starts with a table, stating the required input parameters for the fatigue degradation and a comment about the original implementation, as well as whether the model is point-local. A model is point-local if there is no exchange of information between the cohesive elements during the analysis.

3.2. Overview of the investigation methodology

To assess the accuracy of the models with the cylinder model, the fatigue degradation strategies are compared to the same Paris law which is based on experimental mode I interlaminar fatigue data for for HTA/6376C from Asp, Sjoegren and Greenhalgh [ASG01] shown in figure 3.1. The Paris law has the form

$$\frac{da}{dN} = C \cdot (\frac{G_a}{G_c})^m, G_{th} < G_a < G_c. \tag{3.1}$$

and the parameters for the material investigated are shown in table 3.1 Figure 3.1

G_{th}=0.052 N/mm	G_c=0.26 N/mm	C=0.0066	m=5.9

Table 3.1.: Paris law parameters for HTA/6376C based on the experimental data from [ASG01]

also shows some error lines representing errors of +/- 10%, +/- 50% and +/- 90% respectively. The figure shows that an error of 10 % makes the Paris law look still very accurate, and even an error of +/-50% is well within the scatter of the experimental data. The figure also demonstrates that the log-log scale makes negative errors appear larger than positive ones. Caution is therefore warranted when assessing the accuracy of a fatigue degradation strategy by the log-log crack growth graph alone.

In the following sections the relative error compared to the input Paris law will be plotted as well as the crack growth rate vs. $\frac{G_a}{G_c}$ graph. In order to generate one point on the Paris plot, the applied moment M_a corresponding to the applied energy release rate G_a is calculated through

$$M_a = G_a \cdot R. \tag{3.2}$$

Then an equilibrium step is completed using algorithm 1 to find the static equilibrium angle θ_s and contact point $x_s = \theta_s \cdot R$, so that $M_t(\theta_s) = M_a$. Following that, the number of cycles is increased by ΔN, the static and fatigue damage are calculated and a new equilibrium angle θ_1 and contact point $x_1 = \theta_1 \cdot R$ is found. This process is repeated until reaching the total number of cycles to be simulated N_{tot}. The data pairs (x_i, N_i) are linearly interpolated and the slope of this line is the crack growth

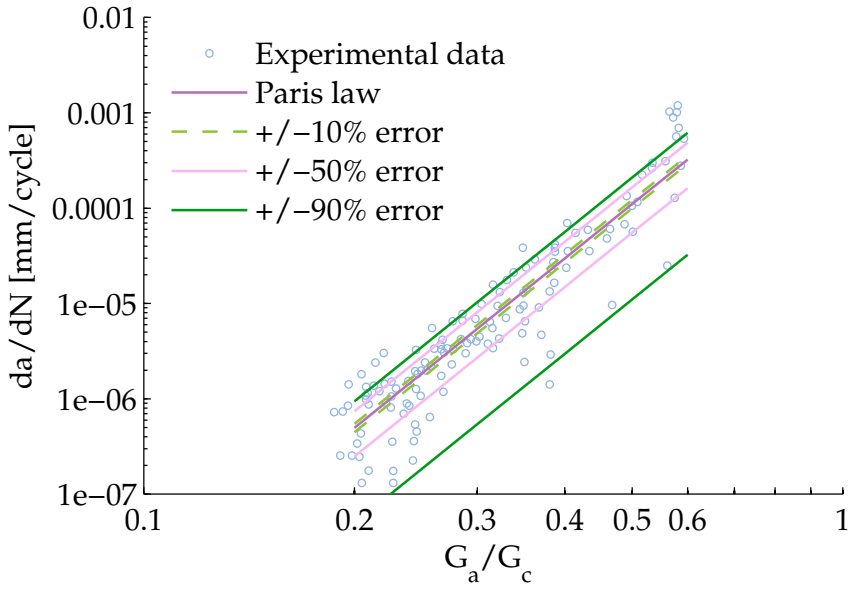


Figure 3.1.: Experimental data for for HTA/6376C from [ASG01], Paris law and error lines

rate $\frac{da}{dN}$ for G_a.

An important aspect of a fatigue degradation strategy is its sensitivity to changes in modelling parameters. In the following sections, the sensitivity of each strategy to changes in element size as well as the cycle-jump ΔN, which is directly related to the time step, is examined.

The fatigue analysis always starts from static equilibrium. This is not only the case in the cylinder model but also in the finite element implementation. When finding the static equilibrium all the elements follow the static cohesive law. After the crack has grown a certain distance due to fatigue a steady state is reached where all the elements follow the same 'fatigue cohesive law'. The area underneath the curve is equal to G_a, so the shape of this traction-separation relationship depends on the applied load G_a but also on the fatigue degradation strategy which will be shown in the following sections. In the cylinder model, the cohesive zone length in fatigue, l_{cz} is measured as the distance between the contact point x_c and the last failed element. When the cohesive zone length is stated in tables, this value is always taken to be the cohesive zone length in the steady state. For the cylinder, the dimensions from table 2.2 have been used. This gives a static cohesive zone length L_{cz} =1.86

mm. A comparison of models for the calculation of cohesive zone lengths has been carried out by Turon [TDCC05]. All these models are of the form

$$L_{cz} = M\frac{EG_c}{\sigma_0^2}, \tag{3.3}$$

where M is a model parameter, G_c the fracture energy rerelease rate, σ_0 the maximum interfacial strength, and E the Young's modulus. For the material HTA/6376C for which the above Paris law has been derived and the constitutive law parameters in table 2.1, equation (3.3) becomes

$$L_{cz} = M\frac{10500\frac{N}{mm^2} \times 0.26\frac{N}{mm}}{(30\frac{N}{mm^2})^2} = M \times 3.033 \ \ mm, \tag{3.4}$$

where $M \in \{0.21, 0.31, 0.4, 0.88, 1\}$, so that 0.64 mm $< L_{cz} <$ 3.033 mm.
For the comparison of the strategies, three variables are introduced. These are N_f, which is the number of cycles it takes for an element to go through the degradation process from entering the cohesive zone to failure, so

$$N_f = \frac{l_{cz}}{\frac{da}{dN}}. \tag{3.5}$$

The number of elements in the cohesive zone is

$$n_{cz} = \frac{l_{cz}}{\Delta l} \ , \tag{3.6}$$

and the number of steps it takes to fail one element from entering the cohesive zone to failure is

$$n_f = \frac{N_f}{\Delta N}. \tag{3.7}$$

The relative error in the surface plots is calculated with respect to the input Paris law for the Turon model, the Harper model, the Kawashita-Hallett model and also the new model in the next chapter. For the fatigue degradation strategy discussed first, the Peerlings' model, there is no input Paris law so the relative error is calculated with respect to the crack growth rate for the smallest element size and cycle-jump.

3.3. Peerlings' degradation model

Input:	Fatigue damage evolution parameters α and λ, β
	Numerical integration parameters μ_1 and μ_2
Point-local:	Yes
FE Implementation:	Implicit

The model discussed in this section has been developed by Robinson et.al [RGT$^+$05]. As mentioned above the damage evolution is calculated as a sum of static and fatigue damage. The fatigue damage rate is based on a continuum damage mechanics formulation, given in terms of equivalent strains. It was introduced by Peerlings' [PBRdB00] with an evolution function slightly different than that from Paas [Paa90]. In the present formulation the equivalent strain is replaced by the normalised displacement $\frac{\delta}{\delta_c}$, where δ_c is the critical displacement.

3.3.1. Description of the Peerlings' model

The cohesive law that forms the basis for the static delamination in this strategy is the bilinear law, which is shown in figure 3.2. An analytical expression has been given in the previous chapter (see equation (2.46)). The static damage is introduced into the cohesive law in the following way

$$\sigma = (1 - D_s)K\delta, \tag{3.8}$$

where K is the initial stiffness,

$$K = \frac{\sigma_0}{\delta_0}. \tag{3.9}$$

This is also called the stiffness-based damage. Introducing it like this, the damage is 0 when the opening displacement is less or equal to δ_0. The damage reaches 1 when the traction is reduced to 0 for displacements greater than δ_c. Combining equation (2.46) and (3.8) leads to an analytical expression for the static damage

$$D_s(\delta) = \begin{cases} 0 & ,0 \leq \delta \leq \delta_0 \\ \frac{\delta_c}{\delta}\frac{\delta-\delta_0}{\delta_c-\delta_0} & ,\delta_0 < \delta \leq \delta_c \\ 1 & ,\delta_c < \delta \end{cases}. \tag{3.10}$$

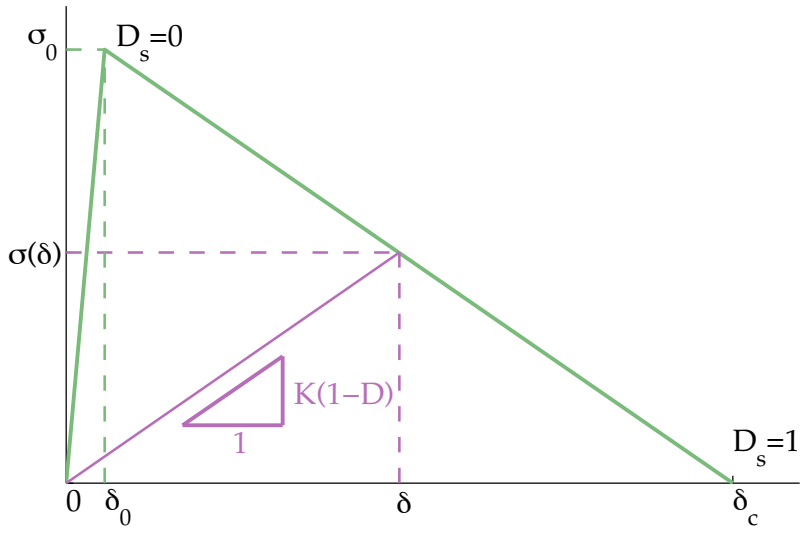


Figure 3.2.: Bilinear law with stiffness based damage degradation

This type of static damage is often called the stiffness-based damage, since for a point $(\delta, \sigma(\delta))$ on the cohesive law, the current stiffness, which is the slope of the straight line that connects this point and the origin is a fraction of the initial stiffness K which is determined by D_s as shown in figure 3.2.

The static damage rate is obtained by differentiating equation (3.10) with respect to cycles N

$$\frac{\partial D_s}{\partial N} = \frac{\delta_c \delta_0}{\delta_c - \delta_0} \frac{\dot{\delta}}{\delta^2} \quad \delta_0 < \delta < \delta_c. \tag{3.11}$$

In order to find the increase in static damage ΔD_s due to a number of fatigue cycles ΔN, equation (3.11) is integrated

$$\Delta D_s = \int_N^{N+\Delta N} \frac{\delta_c \delta_0}{\delta_c - \delta_0} \frac{\dot{\delta}}{\delta^2} dN = \frac{\delta_0 \delta_c}{\delta_c - \delta_0} \left(\frac{1}{\delta(N)} - \frac{1}{\delta(N + \Delta N)} \right). \tag{3.12}$$

$\delta(N)$ and $\delta(N + \Delta N)$ are the maximum displacements (see equation (2.13)) at cycle N and $N + \Delta N$ respectively.

The fatigue damage evolution with respect to time is given by

$$\frac{\partial D_f}{\partial t} = \begin{cases} g(D, \frac{\delta(t)}{\delta_c}) \frac{\dot{\delta}(t)}{\delta_c} & , \dot{\delta} \geq 0 \quad \text{and} \quad f \geq 0 \\ 0 & , \dot{\delta} < 0 \quad \text{or} \quad f < 0 \end{cases}, \tag{3.13}$$

where g is a dimensionless function, and f is a damage loading function, making it possible to define a threshold value for the onset of fatigue damage. If the fatigue

threshold is δ_{th}, then f could be $f := \delta - \delta_{th}$. In the following study $f = 0$. The function g is an adapted form from Peerlings' et al [PBRdB00] and will therefore be called Peerlings' law

$$g(D, \frac{\dot{\delta}(t)}{\delta_c}) = \alpha e^{\lambda D} \left(\frac{\delta}{\delta_a}\right)^{\beta}. \tag{3.14}$$

α, β, and λ are parameters, which have to be determined through a parameter study. The cycle-based damage rate is derived by rearranging equation (3.13), and integrating over one cycle. This leads to the cyclic damage rate

$$\frac{\partial D_f}{\partial N} = \frac{\alpha}{1+\beta} e^{\lambda D} \left(\frac{\delta}{\delta_c}\right)^{1+\beta}. \tag{3.15}$$

A more detailed derivation of this damage rate can be found in [RGT+05]. The change in fatigue damage ΔD_f from a number of cycles N to $N + \Delta N$ can be calculated by integrating (3.15)

$$\Delta D_f = \int_N^{N+\Delta N} \frac{\partial D_f}{\partial N} dN. \tag{3.16}$$

The first mean value theorem for integration states that two constants μ_1 and μ_2 exist with $0 \leq \mu_1, \mu_2 \leq 1$, so that

$$\int_N^{N+\Delta N} \frac{\partial D_f}{\partial N} dN = \Delta N \frac{\partial D_f(D_{\mu_1}, \delta_{\mu_2})}{\partial N}, \tag{3.17}$$

where $D_{\mu_1} \in [D(N), D(N+\Delta N]$ and $\delta_{\mu_2} \in [\delta(N), \delta(N+\Delta N)]$, and

$$\begin{aligned} D_{\mu_1} &= (1-\mu_1) D(N) + \mu_1 D(N+\Delta N) \\ \delta_{\mu_2} &= (1-\mu_2)\delta(N) + \mu_2 \delta(N+\Delta N). \end{aligned} \tag{3.18}$$

μ_1 and μ_2 are therefore integration constants related to the numerical integration of equation (3.16), which also have to be determined by a parameter study. The influence of the values of μ_1 and μ_2 on the fatigue degradation strategy are examined in the next chapter in section 4.1.1.

The increase in fatigue damage ΔD_f due to one cycle-jump ΔN is then

$$\Delta D_f = \Delta N \frac{\alpha}{1+\beta} e^{\lambda D_{\mu_1}} \left(\frac{\delta_{\mu_2}}{\delta_c}\right)^{1+\beta}. \tag{3.19}$$

The constants μ_1 and μ_2 have been determined numerically. A value of $\mu_1 = \mu_2 = 0.7$ yields satisfactory results, but it is not a trivial problem to determine μ_1 and μ_2.

The new damage $D(N + \Delta N)$ after one cycle-jump is obtained by adding the sum of the changes in static and fatigue damage to the damage $D(N)$ at N cycles and therefore

$$D(N + \Delta N) = D(N) + \Delta D_s + \Delta D_f, \tag{3.20}$$

where ΔD_f is calculated according to equation (3.19) and ΔD_s according to equation (3.12). (3.20) is an implicit equation, since both sides contain the new damage $D(N + \Delta N)$, which cannot be solved analytically. A solution is found by using a Newton-Raphson-iteration scheme with a starting value of $D(N)$. The proof of convergence for this problem is given in the following section.
The Newton method for solving $f(x) = 0$ converges when the following three criteria are met:

$$(i)\ \ f'(x) \neq 0, \forall x \in [D(N + \Delta N) - \Delta D, D(N + \Delta N) + \Delta D] =: I \tag{3.21}$$

$$(ii)\ \ f''(x) \text{ finite}, \forall x \in I \tag{3.22}$$

$$(iii)\ \ \sup_{x \in I} \frac{1}{2} \left| \frac{f''(x)}{f'(x)} \right| \cdot |x - D(N)| < 1, \tag{3.23}$$

where (from equation (3.20))

$$f(x) := a + b \cdot e^{cx} - x, \tag{3.24}$$

with the substitutions (see equations (3.12), (3.18), and (3.19))

$$x := D(N + \Delta N) \tag{3.25}$$

$$a := D(N) + \frac{\delta_0 \delta_c}{\delta_c - \delta_0} \left(\frac{1}{\delta(N)} - \frac{1}{\delta(N + \Delta N)} \right) \tag{3.26}$$

$$b := \Delta N \frac{\alpha}{1 + \beta} e^{\lambda(1-\mu_1)D(N)} \left(\frac{\delta_{\mu_2}}{\delta_c} \right)^{1+\beta} \tag{3.27}$$

$$c := \lambda \cdot \mu_1, \tag{3.28}$$

$$\tag{3.29}$$

(i) The first condition is met, since $f'(x) = bce^{cx}$, and $b, c \neq 0$ for $x \in I$.
(ii)The second condition is also met, since $f''(x) = bc^2e^{cx} < \infty$ for $x \in I$.
(iii) The third condition is

$$\sup_{x \in I} \frac{1}{2} \left| \frac{f''(x)}{f'(x)} \right| \cdot |x - D(n)| = \sup_{x \in I} \frac{1}{2} \cdot \lambda \mu_1 |x - D(N)| < 1. \tag{3.30}$$

The maximum of the absolute value of the difference between x and $D(N)$ is reached at the end of the interval I, where $|x - D(N)| = |D(N + \Delta N) + \Delta D - D(N)| = 2 \cdot \Delta D$, and $\Delta D \ll 1$. μ_1 is also smaller than 1. This leaves only λ, which in the parameter study is less than 2, thus fulfilling the third condition as well. When changing the parameter λ care has to be taken to not choose a λ which is too large. If the increase in damage ΔD is small in each step, a greater value for λ can be chosen.

3.3.2. Results for the Peerlings's model

The Peerlings' law has been calibrated previously [Arm08] to match the Paris law given earlier in 3.1 The earlier study concluded that the static cohesive law has a great influence on the Peerlings' law parameters. In this study, a lower initial stiffness K for the static cohesive law was chosen, so δ_0 is different. This means that the Peerlings' law parameters had to be recalibrated. The parameters are stated in Table 3.2. Figure 3.3 shows the comparison of the Peerlings' law fatigue degra-

α=2.2e-04	β=2.5	λ=0.5	μ_1=0.7	μ_2=0.7

Table 3.2.: Peerlings' law parameters

dation strategy to the calibrated Paris law together with the experimental data for two different mesh sizes and cycle jumps. As explained earlier, the log-log scale is deceptive when it comes to interpreting the accuracy of a fatigue degradation strategy. Therefore, the relative error in $\frac{da}{dN}$ has been plotted for the same four sets of element size and cycle jump. These errors are shown for the same range of energy release rates in figure 3.4. The cohesive zone length l_{cz} and the number of cycles to failure N_f are shown in table 3.3 for a range of energy release rates. The table also shows the number of elements in the cohesive zone n_{cz} and the the number of steps to failure n_f for two different element sizes.

For a load level of 60%, i.e. $\frac{G_a}{G_c} = 0.6$, convergence was not achieved when ΔN=2500 cycles, because the number of steps to failure n_f is below 2. It is clear from table 3.3 and figure 3.4 that for larger values of G_a a cycle-jump of 2500 cycles is too large to obtain accurate results, while a cycle-jump of 100 cycles requires many steps at low

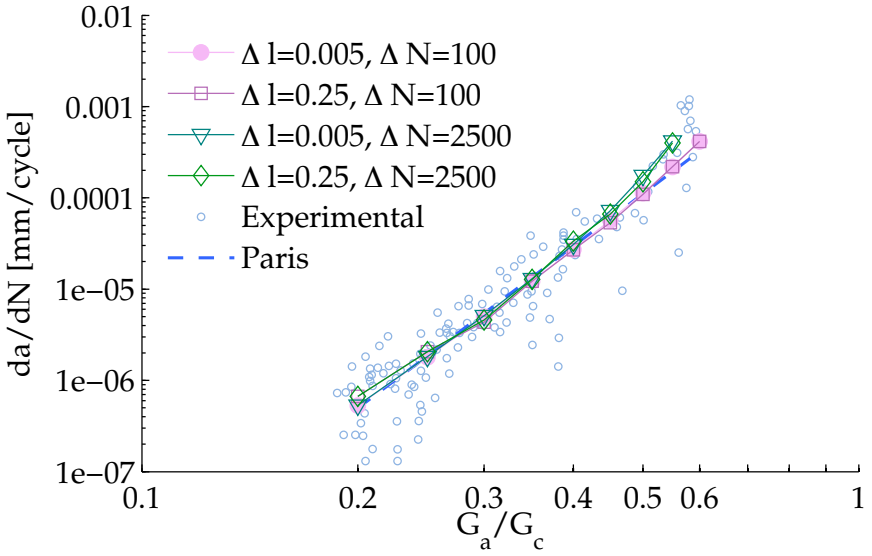


Figure 3.3.: Experimental data, paris law, and Peerlings' model crack growth rates for different element sizes and cycle jumps. Δl in [mm], ΔN in [cycles]

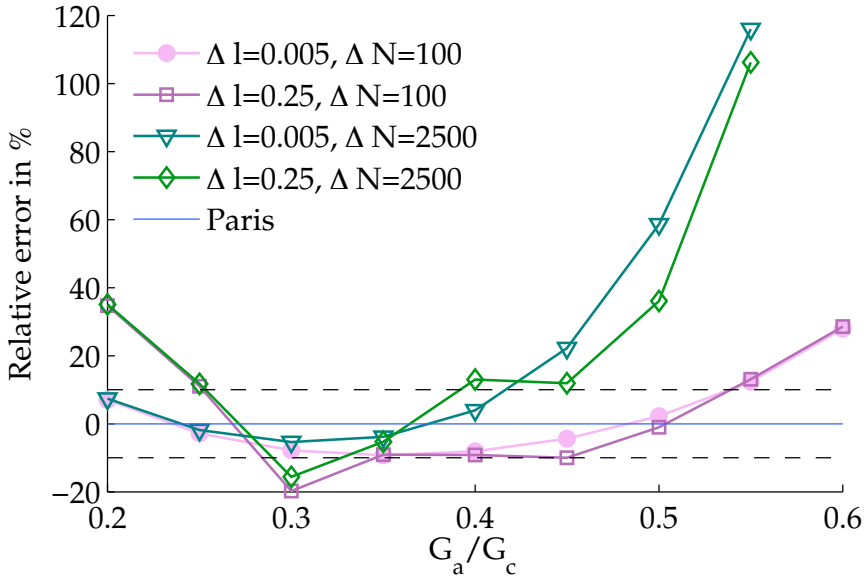


Figure 3.4.: Relative error in % of crack growth rate $\frac{da}{dN}$ for different element sizes and cycle jumps. Δl in [mm], ΔN in [cycles]

energy release rates, making the analysis very slow. For low energy release rates, the element size has a greater influence on the error, since the error curves with equal element size almost coincide for $0.2 < G_a/G_c < 0.3$. In this range, the number of steps to fail one element is large so the algorithm is very accurate in terms

			Elements in CZ n_{cz}		Steps to failure n_f	
Ga/Gc	l_{cz} [mm]	N_f[cycles]	$\Delta l = 0.005$	$\Delta l = 0.25$	$\Delta N = 100$	$\Delta N = 2500$
0.2	0.67	$1.25 \cdot 10^6$	133	2.7	12500	500
0.25	0.75	$4.17 \cdot 10^5$	150	3	4170	167
0.3	0.82	$1.64 \cdot 10^5$	164	3.3	1640	66
0.35	0.9	$7.4 \cdot 10^4$	180	3.6	740	30
0.4	0.97	$3.6 \cdot 10^4$	194	3.9	360	14
0.45	1.03	$1.8 \cdot 10^4$	206	4.1	180	7.2
0.5	1.1	$9.7 \cdot 10^3$	220	4.4	97	3.9
0.55	1.16	$5.3 \cdot 10^3$	232	4.6	53	2.1
0.6	1.23	$3.0 \cdot 10^3$	246	4.9	30	-

Table 3.3.: Crack growth parameters for Peerlings' law. Δl in [mm], ΔN in [cycles]

of the cycle-jump. For larger energy release rates $0.35 < G_a/G_c < 0.6$, the error is dominated by the cycle jump, so the curves of equal cycle-jump are close together. At the same time, larger energy release rates result in longer cohesive zone lengths, so when keeping the element size constant, there are more elements in the cohesive zone, which makes the algorithm more accurate in terms of element size. The fatigue cohesive laws for four different values of G_a and the same combinations of element size and cycle jump as before are shown in figure 3.5. The shape of the fatigue cohesive law changes significantly when the element size is increased and the cohesive zone length is slightly greater for a larger element size, since the final opening displacement is greater. For a higher number of cycles per step, the fatigue cohesive law demonstrates again that when the applied energy release rate is high, caution has to be taken that there are enough steps to fail one element in order to obtain accurate results for the crack growth.

Thesensitivity study focuses on the sensitivity of the algorithm to element size and cycle-jump at different load levels. For each of the four load levels there are two plots, one surface plot showing the relative error of the crack growth rate versus the element size and cycle jump, and one contour plot showing the relative error versus the number of elements in the cohesive zone and the number of steps nec-

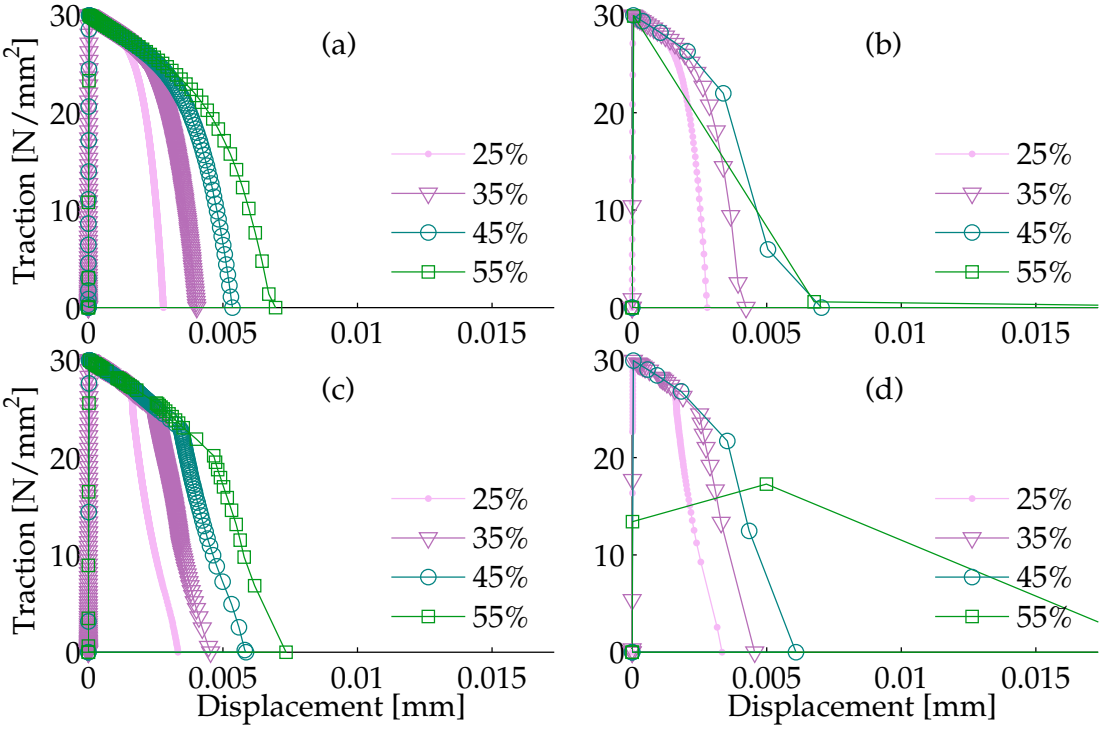


Figure 3.5.: Traction-separation curves for different percentages of G_c. (a) $\Delta l = 0.005$ mm, $\Delta N = 100$ cycles, (b) $\Delta l = 0.005$ mm $\Delta N = 2500$ cycles, (c) $\Delta l = 0.25$ mm, $\Delta N = 100$ cycles, (d)$\Delta l = 0.25$ mm, $\Delta N = 2500$ cycles

essary to fail one element. Figure 3.6 shows the relative error for a load level of $G_a = 0.25G_c$. The maximum cycle jump is 40000 cycles which means that an element fails within about 10 iterations. The maximum element size is 0.25 mm, when there are three elements in the cohesive zone. Within this range the maximum error is around 50%. The figure shows that as the cycle-jump ΔN increases, the error increases linearly. When the element size is increased, the error oscillates. These oscillations are caused by there being a whole number of elements in the cohesive zone and the error is lowest when Δl satisfies the following equation

$$\frac{l_{cz}}{\Delta l} = m, m \in \mathbb{N}. \tag{3.31}$$

The third clearly visible feature are the diagonal peaks running towards the origin. The valleys in between the peaks mark lines of low error where the ratio of element

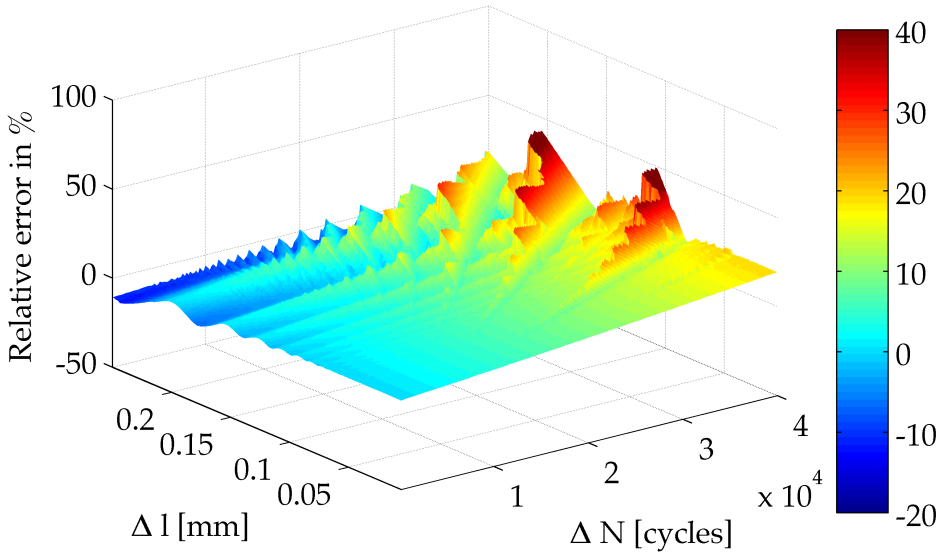


Figure 3.6.: Relative error in % of $\frac{da}{dN}$ in Peerling model with respect to element size Δl and cycle jump ΔN for $G_a = 0.25G_c$

size over cycle-jump and crack growth rate is an integer, so

$$\frac{\frac{\Delta l}{\Delta N}}{\frac{da}{dN}} = m, m \in \mathbb{N}. \tag{3.32}$$

Figure 3.7 shows a projection of figure 3.6 onto the Δl-ΔN plane. The solid white lines are defined by equation (3.32) for $1 \leq m \leq 13$. For the calculation of these lines the original Paris law with $C = 0.0066$ and $m = 5.9$ was used and the lines agree well with the valleys of low error for $m > 4$ and low cycle-jumps ΔN, but do not coincide exactly for $m \leq 4$. The dotted white line which lies on top of the valley of low error where $m = 2$ corresponds to a Paris law with $C = 0.0066$ and $m = 5.86$. The difference in value between these two Paris coincides with the relative error in $\frac{da}{dN}$ thus explaining the shifted location of the white lines.

Figure 3.8 shows a contour plot of the relative error versus the number of elements in the cohesive zone n_{cz}, where $3 < n_{cz} < 25$ and the number of cycle-jumps to fail one element n_f, where $10 < n_f < 100$. This corresponds to 0.036 mm $< \Delta l <$ 0.25 mm and 4000 cycles $< \Delta N <$ 40,0000 cycles. This plot clearly shows the oscillations due to the increase in element size. The relative error is positive as the cycle-jump increases, but is negative for increases in Δl. Figure 3.9 shows the relative error at a load level of $G_a = 0.35G_c$. The maximum cycle jump is 20000 cycles which

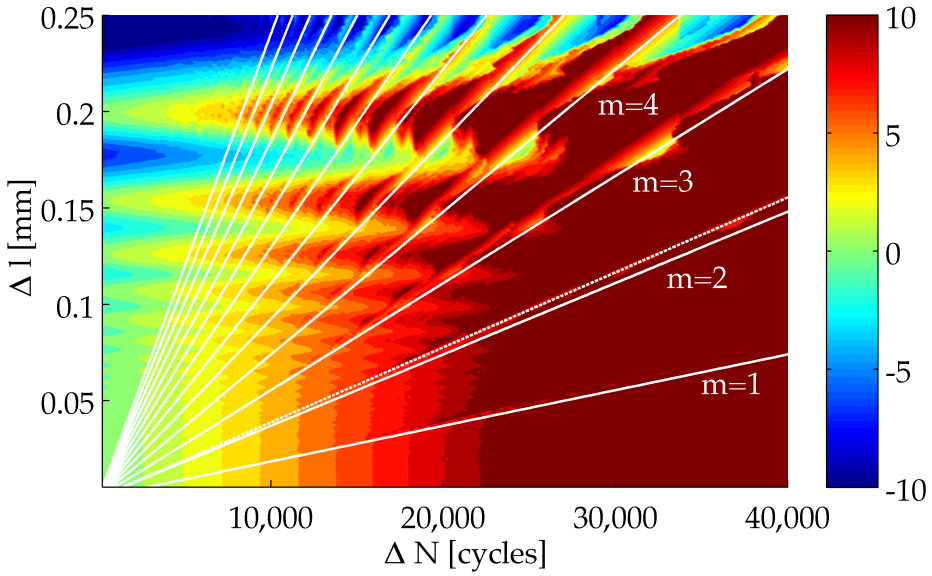


Figure 3.7.: Projection of figure 3.6

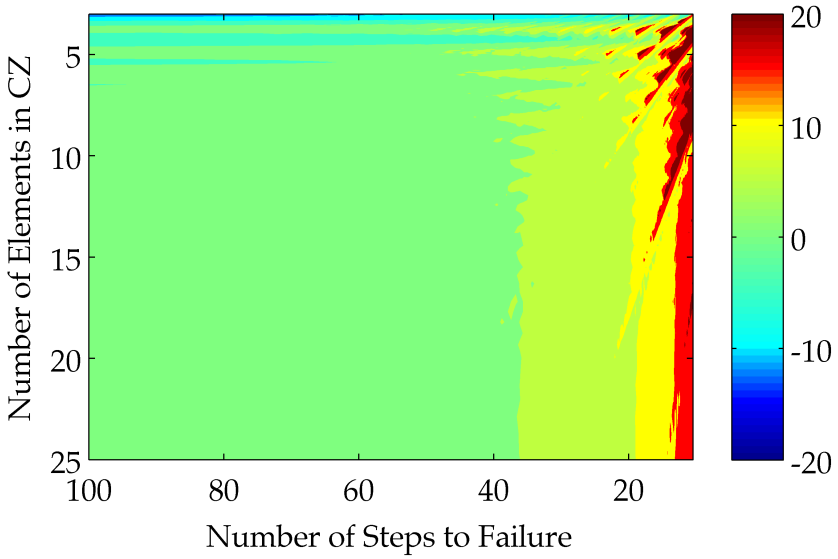


Figure 3.8.: Relative error in % of $\frac{da}{dN}$ in Peerling model with respect to the number of elements in the cohesive zone and the number of cycle jumps to fail one element for $G_a = 0.25G_c$

means that an element fails within about 4 iterations. The maximum element size is 0.3 mm, when there are three elements in the cohesive zone. The error plot show the same features as the previous one, with linearly increasing error for increasing cycle-jump and low Δl, oscillations for higher element sizes and diagonal lines,

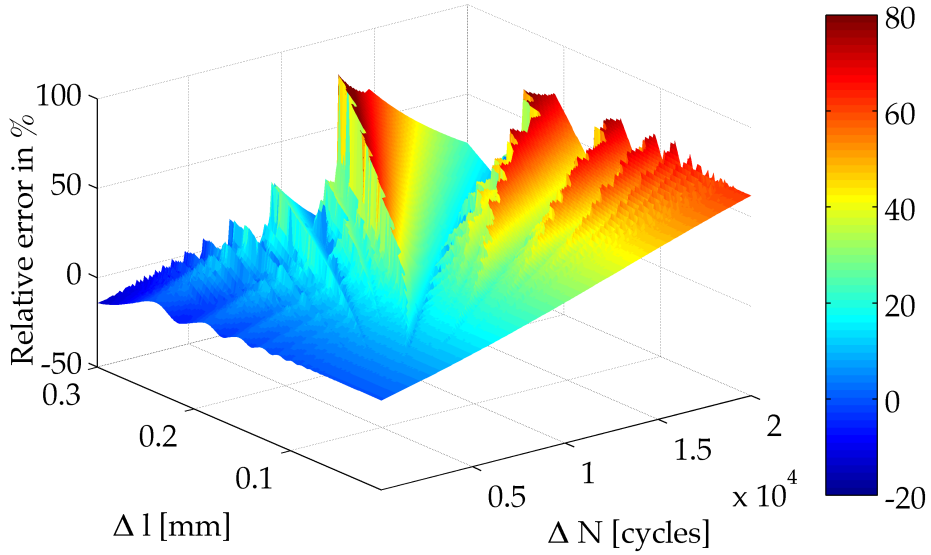


Figure 3.9.: Relative error in % of $\frac{da}{dN}$ in Peerling model with respect to element size Δl and cycle jump ΔN for $G_a = 0.35G_c$

marking large drops in the error. The maximum error is higher than before which is to be expected, since the minimum n_f is lower than before.

Figure 3.10 shows a contour plot of the relative error versus the number of elements in the cohesive zone n_{cz} and the number of steps to failure n_f for the same load level $G_a = 0.35G_c$. The range of n_f and n_{cz} is the same as in figure 3.8. However, due to the increased load level, this now corresponds to 0.03 mm$< \Delta l <$ 0.3 mm and 740 cycles $< \Delta N <$ 7400 cycles. The maximum error is higher than when $G_a = 0.25G_c$ and there are more diagonal lines.

Figure 3.11 shows the relative error at a load level of $G_a = 0.45G_c$. The maximum cycle jump is 7500 cycles which means that an element fails within about 3 iterations. The maximum element size is 0.345 mm, when there are three elements in the cohesive zone. The error plot show the same features as the previous ones, with more diagonal lines due to the increase in crack growth rate. The maximum error is higher than before which is to be expected, since the minimum n_f is lower than previously.

Figure 3.12 shows a contour plot of the relative error versus the number of elements in the cohesive zone n_{cz} and the number of steps to failure n_f for the same load level

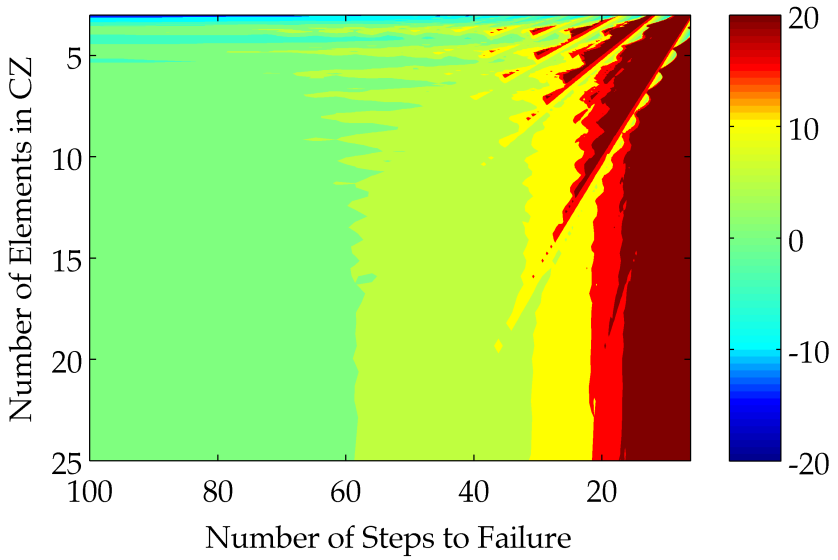


Figure 3.10.: Relative error in % of $\frac{da}{dN}$ in Peerling model with respect to the number of elements in the cohesive zone and the number of cycle jumps to fail one element for $G_a = 0.35G_c$

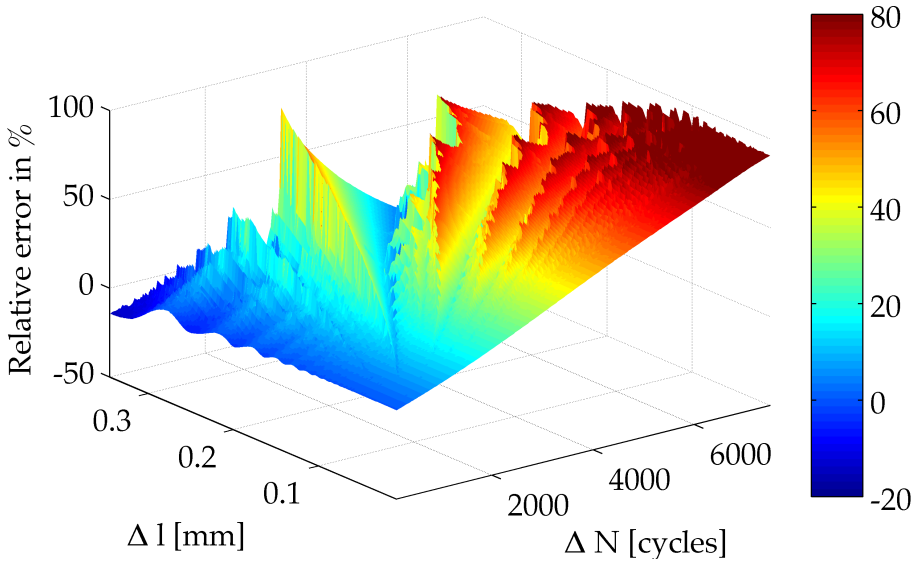


Figure 3.11.: Relative error in % of $\frac{da}{dN}$ in Peerling model with respect to element size Δl and cycle jump ΔN for $G_a = 0.45G_c$

$G_a = 0.45G_c$. The range of n_f and n_{cz} is the same as before. This corresponds to a range of 0.04 mm $< \Delta l <$ 0.345 mm and 180 cycles $< \Delta N <$ 1800 cycles. The maximum error is similar to when $G_a = 0.35G_c$.

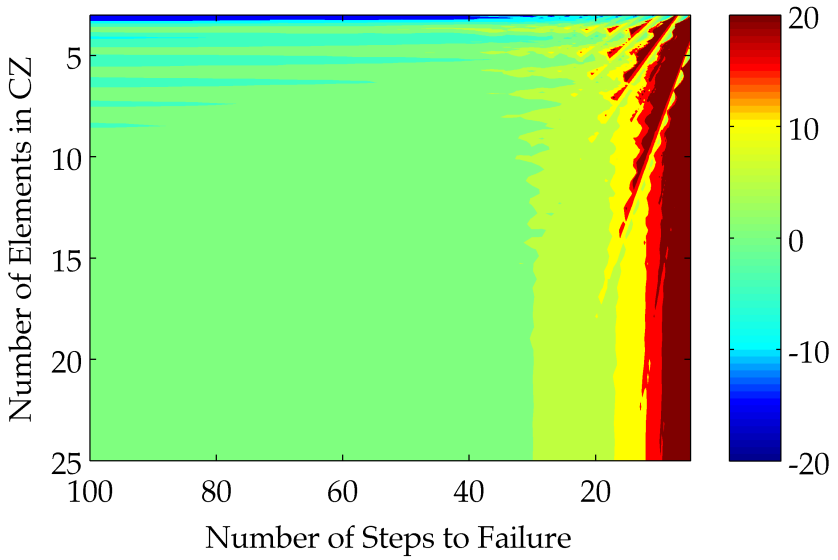


Figure 3.12.: Relative error in % of $\frac{da}{dN}$ in Peerling model with respect to the number of elements in the cohesive zone and the number of cycle jumps to fail one element for $G_a = 0.45G_c$

Figure 3.13 shows the relative error at a load level of $G_a = 0.55G_c$. The maximum

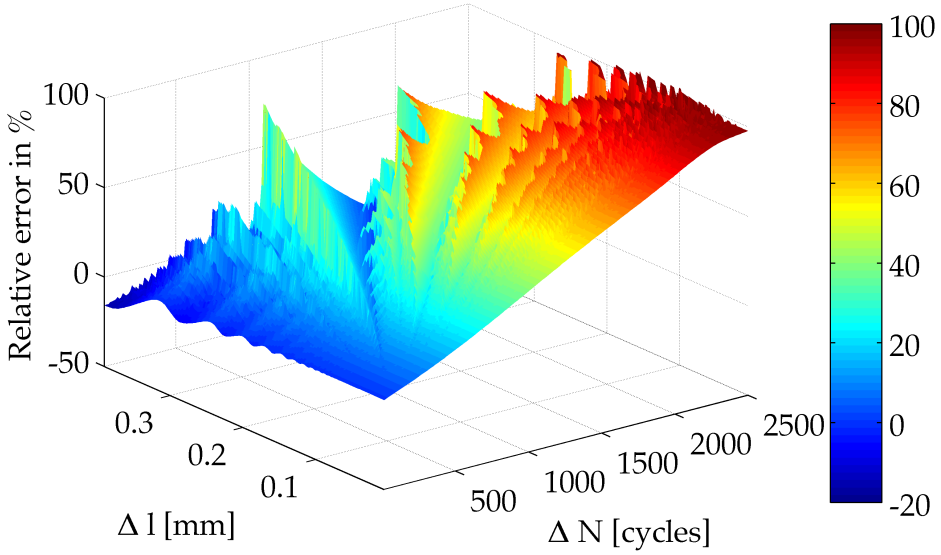


Figure 3.13.: Relative error in % of $\frac{da}{dN}$ in Peerling model with respect to element size Δl and cycle jump ΔN for $G_a = 0.55G_c$

cycle jump is 2500 cycles which means that an element fails within about 2 itera-

tions. The maximum element size is 0.39 mm, when there are three elements in the cohesive zone. The error plot shows the same features as the previous ones, with linearly increasing error for increasing cycle-jump, oscillations for higher element sizes and diagonal lines.

Figure 3.14 shows a contour plot of the relative error versus the number of elements in the cohesive zone n_{cz} and the number of steps to failure n_f for the same load level $G_a = 0.55G_c$. The range of n_f and n_{cz} is the same as before corresponding to 0.046

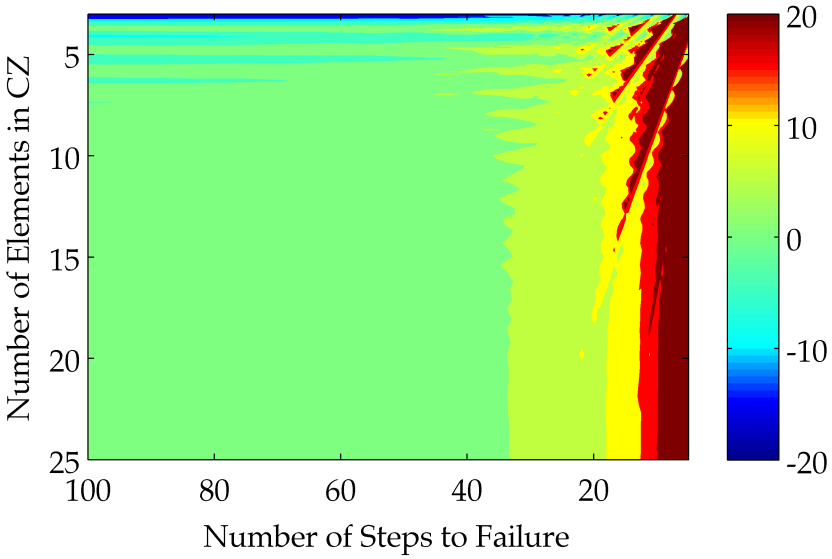


Figure 3.14.: Relative error in % of $\frac{da}{dN}$ in Peerling model with respect to the number of elements in the cohesive zone and the number of cycle jumps to fail one element for $G_a = 0.55G_c$

mm $< \Delta l <$ 0.39 mm and 53 cycles $< \Delta N <$ 530 cycles. The maximum error is similar to when $G_a = 0.45G_c$. Table 3.4 shows the required number of elements in the cohesive zone n_{cz} and the number of steps to failure n_f, so that the relative error in absolute value is below 10% and 20 % respectively. This is the same as the number of elements required in the static cohesive zone for the bilinear law in the cylinder model which is four for $M_{th} > 0.2M_c$, $M_T < 10\%$ (see table 2.3).

	$\|e_r\|$<10%		$\|e_r\|$<20%	
Ga/Gc	$n_{cz}>(\Delta l<)$	$n_f>(\Delta N<)$	$n_{cz}>(\Delta l<)$	$n_f>(\Delta N<)$
0.25	4 (0.23)	30 (14,000)	4 (0.23)	15 (28,000)
0.35	3 (0.3)	40 (1850)	4 (0.3)	30 (2470)
0.45	4 (0.26)	40 (450)	4 (0.26)	30 (600)
0.55	4 (0.29)	40 (133)	4 (0.29)	30 (177)

Table 3.4.: Minimum values for $n_f(\Delta N)$ and $n_{cz}(\Delta l)$ with respect to the relative errors in $\frac{da}{dN}$. Δl in [mm], ΔN in cycles

3.3.3. Discussion of the Peerlings' model

In the previous subsection the Peerlings' model has been analysed with respect to the mesh sensitivity and the cycle-jump. One positive aspect of the Peerlings' model is that despite the oscillations, it is quite insensitive to increases in element size, so the mesh can be relatively coarse ($n_{cz} > 4$) and the model will still be accurate. Also, once the fatigue parameters are adjusted, no information has to be exchanged between the elements, so the model is point-local, which makes it easier to implement in a commercial FE software.

However, when changing any aspect of the static cohesive law, for example the initial opening displacement δ_0, or the Paris law itself, the parameters need to be readjusted. The cylinder model is a relatively quick way of doing this but as there is no direct analytical relationship between the parameters and the Paris law and the static cohesive law, this requires an extensive parameter study to find the optimum combination of the three main parameters α, β, and λ.

The second great drawback of this model is its speed. Of all the models examined in this chapter it is by far the slowest, especially for fine meshes and low cycle-jumps. This is due to the fact, that in order to find the fatigue damage for each element at each step it is necessary to solve an implicit equation, which introduces additional iterations.

3.4. Turon fatigue strategy

Input:	Paris law parameters m and C, (cohesive zone length l_{cz})
Point-local:	No
FE Implementation:	Implicit

The model discussed in this section has been developed by Turon et.al. [TCCD07]. One of the main differences to the previous fatigue degradation strategy is that this model directly uses the two parameters of the Paris law C and m as an input as well as the cohesive zone length l_{cz}. Rather than using the actual cohesive zone length Turon et. al. estimated the cohesive zone length using Rice's [Ric80] closed-form equation

$$l_{cz} = \frac{9\pi}{32}\frac{EG_a}{\sigma_0^2}, \tag{3.33}$$

where G_a is the maximum applied energy release rate during the loading cycle, and E is the Young's modulus of the bulk material in the direction perpendicular to the crack-plane. A more detailed discussion can be found in [TDCC05].
Since the cohesive zone length is readily available in the cylinder model, the actual cohesive zone length is used in the following investigation. As opposed to all other models, the Turon model does not have a fixed cycle-jump ΔN, but uses a damage increment ΔD to adjust the cycle-jump in each iteration.

3.4.1. Description of the Turon model

Like the previous fatigue degradation strategy, the model uses the static bilinear cohesive law with a stiffness-based damage, so the traction $\sigma(\delta)$ is

$$\sigma(\delta) = (1 - D)K\delta, \tag{3.34}$$

and as before for $\delta_0 < \delta < \delta_c$ the static damage is

$$D(\delta) = \frac{\delta_c(\delta - \delta_0)}{\delta(\delta_c - \delta_0)}. \tag{3.35}$$

There is no damage before the initial traction σ_0 is reached, so $D = 0 \Leftrightarrow \delta < \delta_0$ and the damage reaches its maximum of 1 for the critical displacement and above, so

$D = 1 \Leftrightarrow \delta \geq \delta_c$. This damage is then related to the ratio of the damaged length l_d and the element length Δl, which is assumed to be equal to the ratio of the energy dissipated ξ shown in figure 3.15 and the fracture toughness G_c:

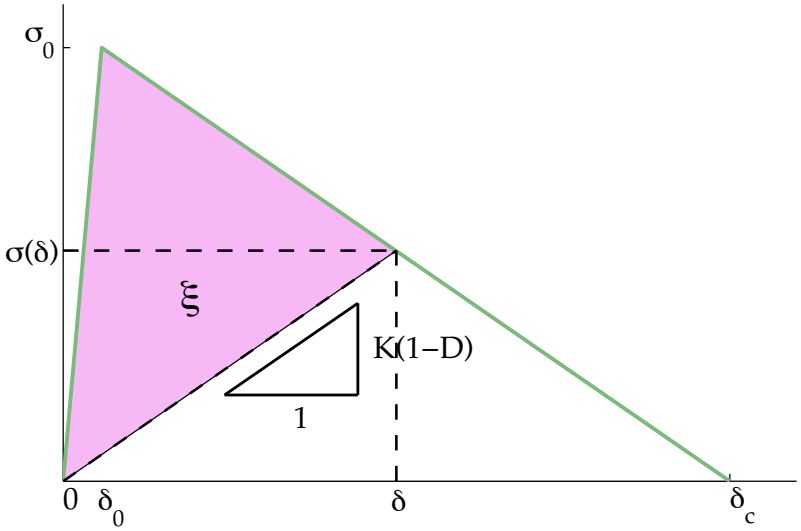


Figure 3.15.: Consumed energy ξ in bilinear law

$$\frac{l_d}{\Delta l} = \frac{\xi}{G_c} = \frac{G_c - \frac{1}{2}\sigma(\delta)\delta_c}{G_c} = 1 - \frac{\frac{1}{2}(1-D)\frac{\sigma_0}{\delta_0}\delta\delta_c}{\frac{1}{2}\sigma_0\delta_c} = 1 - \frac{\delta}{\delta_0}(1-D). \tag{3.36}$$

Combining equations (3.35) and (3.36) and eliminating δ leads to the following expression linking the damaged length ratio of an element to the element damage

$$\frac{l_d}{\Delta l} = \frac{D\delta_0}{\delta_c(1-D) + D\delta_0}. \tag{3.37}$$

As mentioned earlier, the time t is linked to the cycles N through the frequency ω, so $N = \omega t$, and in the following derivation, all rates of change are computed with respect to the number of cycles N. First, the evolution of the damage variable D with respect to the cycles is expressed as a related rate

$$\frac{\partial D}{\partial N} = \frac{\partial D}{\partial l_d} \cdot \frac{\partial l_d}{\partial N}. \tag{3.38}$$

The first term of equation (3.38) is found by differentiating equation (3.37) implicitly with respect to l_d

$$\frac{\partial D}{\partial l_d} = \frac{1}{\Delta l}\frac{(\delta_c(1-D) + D\delta_0)^2}{\delta_c\delta_0}. \tag{3.39}$$

The second term $\frac{\partial l_d}{\partial N}$ is found by relating the increase in damaged area to the crack growth rate according to the Paris law $\frac{da}{dN}$. Figure 3.16 shows the relationship be-

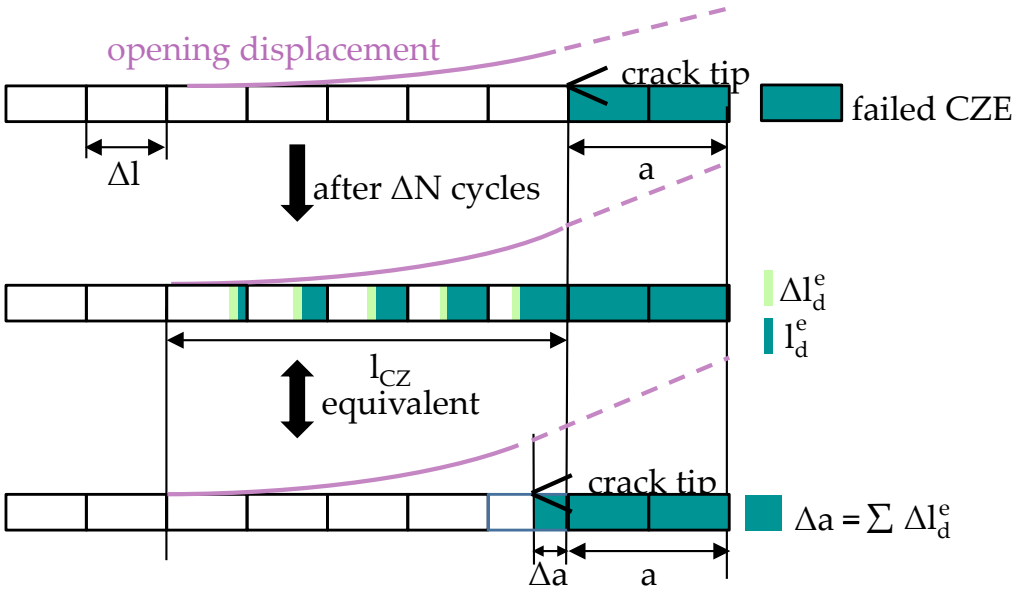


Figure 3.16.: Schematic drawing of crack growth during fatigue algorithm

tween damaged length and the crack length. At the top is the state at the beginning of a step showing the current crack tip, the failed elements, the crack length a and the element size Δl. The fatigue process leads to an accumulation of damaged length Δl_d^e in each element in the cohesive zone. The total rate of change of the damaged length, obtained by summing up all the individual rates in the cohesive zone is assumed to be equal to the global crack growth rate, so

$$\frac{\partial a}{\partial N} \approx \frac{\Delta a}{\Delta N} = \sum_{e \in CZ} \frac{\Delta l_d^e}{\Delta N} \approx \sum_{e \in CZ} \frac{\partial l_d^e}{\partial N}. \tag{3.40}$$

Assuming that the damage change rate $\frac{\partial l_d^e}{\partial N}$ is constant over the cohesive zone and equal to the damaged length rate $\frac{\partial l_d}{\partial N}$, the sum can be replaced by multiplying with the number of elements in the cohesive zone $\frac{l_{cz}}{\Delta l}$

$$\frac{\partial a}{\partial N} = \sum_{e \in CZ} \frac{\partial l_d^e}{\partial N} = \frac{l_{cz}}{\Delta l} \frac{\partial l_d}{\partial N} \tag{3.41}$$

$$\Leftrightarrow \frac{\partial l_d}{\partial N} = \frac{\Delta l}{l_{cz}} \frac{\partial a}{\partial N}. \tag{3.42}$$

Finally, combining equations (3.39) and (3.42) the damage rate is calculated in the following way

$$\frac{\partial D}{\partial N} = \frac{1}{l_{cz}} \frac{(\delta_c(1-D) + D\delta_0)^2}{\delta_c \delta_0} \frac{\partial a}{\partial N}. \tag{3.43}$$

The calculation of this damage rate requires the Paris law

$$\frac{da}{dN} = \begin{cases} C\left(\frac{\Delta G_a}{G_c}\right)^m & G_{th} < \Delta G_a < G_c \\ 0 & \text{, otherwise} \end{cases}. \tag{3.44}$$

C, m, G_{th} and G_c are material constants which have to be specified at the beginning of the fatigue degradation. The energy release rate range ΔG_a is calculated by integrating the static cohesive law as shown in figure 3.17

$$\Delta G_a = \int_{\delta_{min}}^{\delta_{max}} \sigma(\delta) d\delta. \tag{3.45}$$

The increase in damage for the i-th element at the j-th step can then be calculated

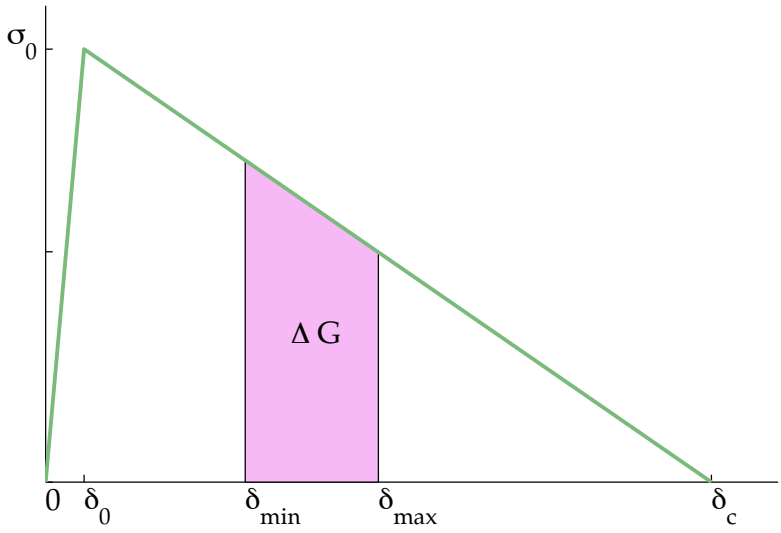


Figure 3.17.: Calculation of energy release rate range ΔG_a

in the following way

$$D_j^i = D_{N+\Delta N_j}^i = D_{j-1}^i + \frac{\partial D_{j-1}^i}{\partial N} \Delta N_j. \tag{3.46}$$

The number of cycles processed in each step is controlled by the input parameter ΔD. The cycle-jumpΔN is calculated as follows

$$\Delta N = \frac{\Delta D}{\max_i \left\{ \frac{\partial D^i}{\partial N} \right\}}. \tag{3.47}$$

This means that the number of cycles in a step is chosen, so that the maximum damage accumulated in one step in any one element due to fatigue is ΔD.

3.4.2. Results for the Turon model

The input parameters used in the Turon model are shown in table 3.5. As stated above, in the original model an analytical equation was used for the cohesive zone length. In this implementation, the actual cohesive zone length was used. However, this resulted in a very large underestimation of the Paris law. Therefore the cohesive zone length had to be adjusted to match the Paris law. It was found that the best match is achieved, when the cohesive zone length in equation (3.43) is 32% of the actual cohesive zone length. Figure 3.18 shows experimental data, the ana-

$C = 0.0066$	$m = 5.9$	$G_{th} = 0.2G_c$

Table 3.5.: Input parameters Turon model

lytical Paris law used as input and the resulting Paris law from the Turon model using the best fit cohesive zone length for four different pairs of maximum damage increment and element size. The figure shows that as G_a approaches G_{th}, the crack growth slows, which is a phenomenon that is also observed experimentally. Figure 3.19 shows the relative error compared to the Paris law. All four error plots show that the error is positive at first and then turns negative. This is because it is not possible to exactly capture the exponent of the Paris law, even when shortening the cohesive zone length, a fact that can also be observed in the original implementation by Albert Turon [TCCD07]. For large element sizes there is no crack growth rate when the applied energy release rate is 25% G_c. This is due to the fact that there is only one integration point per element and the initially calculated $G_a < G_{th}$ for all elements, so the crack growth rate is always 0. All four error curves have similar shapes, apart from the curve with largest element size and damage increment,

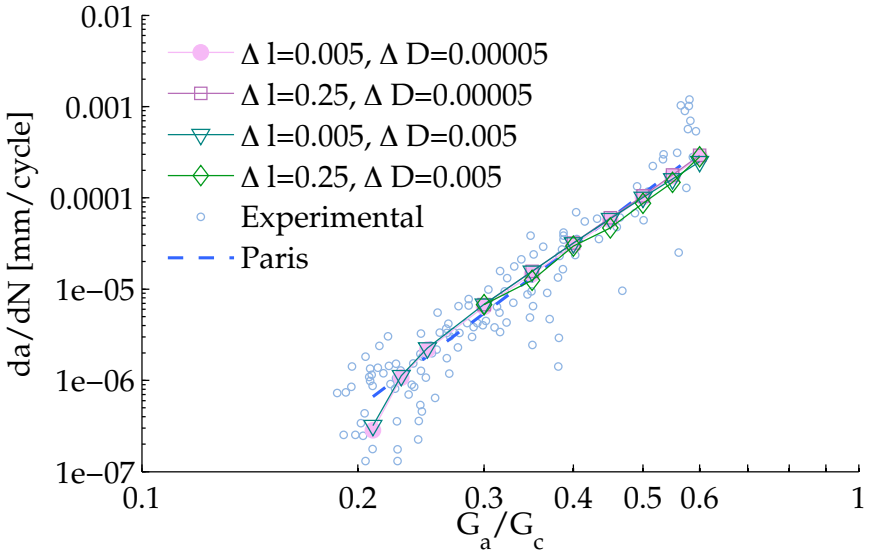


Figure 3.18.: Experimental data, Paris law, and Turon model crack growth rates for different element sizes and damage increments. Δl in [mm]

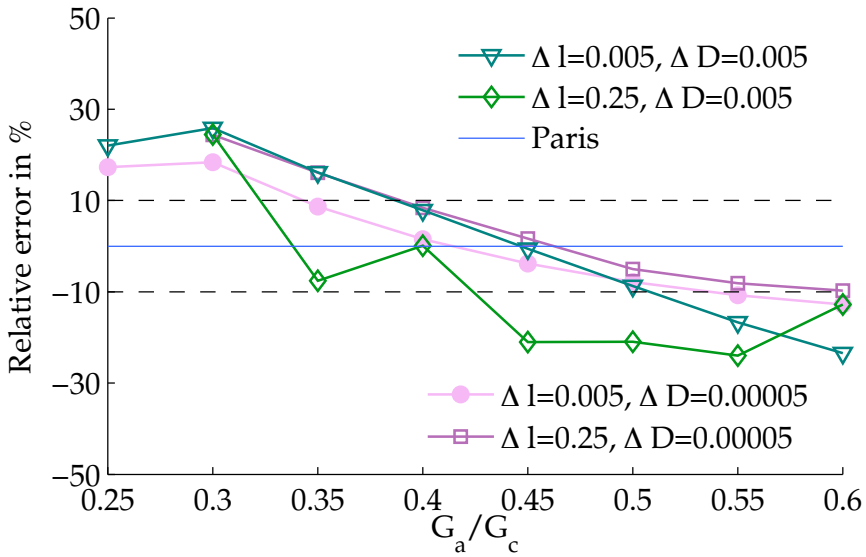


Figure 3.19.: Relative error in % in crack growth rate $\frac{da}{dN}$ for different element sizes and damage increments. Δl in [mm]

which oscillates and produces an error which is significantly larger than the other curves. This suggests that care has to be taken when using both a large element size and large damage increment. The cohesive zone length, number of elements in the cohesive zone, and steps to failure for the four element size/damage increment

pairs are shown in table 3.6. As mentioned earlier, the Turon model does not have

		Elements in CZ n_{cz}		Steps to failure n_f			
				$\Delta D = 5\text{x}10^{-5}$		$\Delta D = 0.005$	
Ga/Gc	l_{cz} [mm]	Δl_{005}	Δl_{25}	Δl_{005}	Δl_{25}	Δl_{005}	Δl_{25}
0.25	0.76	152	3	2190 (160)	-	27 (12150)	-
0.35	0.93	186	3.7	1105 (56)	802 (73)	13 (4490)	9 (8030)
0.45	1.06	212	4.2	770 (24)	600 (29)	10 (1760)	8 (2670)
0.55	1.18	236	4.7	565 (12)	470 (14)	8 (840)	6 (1508)

Table 3.6.: Crack growth for Turon model, Δl_{005} = 0.005 mm, Δl_{25} = 0.25 mm , $(\cdot)$ denotes the average cycle-jump ΔN

a fixed cycle-jump ΔN but uses a maximum damage increment ΔD. This means that the average cycle jump changes drastically across the range of applied energy release rates, so the model adapts to the exponential increase in crack growth rate. The table demonstrates that the cycle-jump depends not only on the damage increment and the applied energy release rate, but also on the element size which makes a significant difference when the damage increment is large. Since the accu-

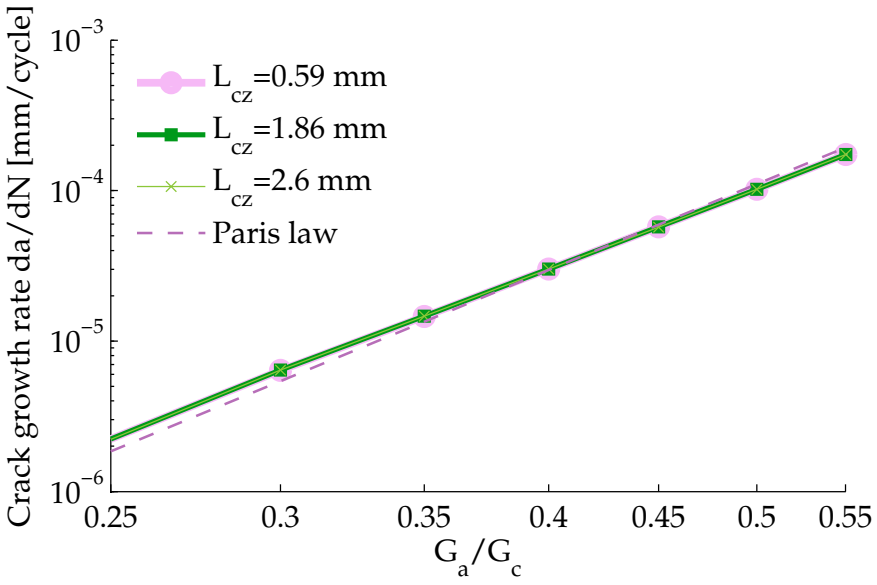


Figure 3.20.: Numerical and input Paris law or different static cohesive zone lengths L_{cz}, $\Delta l = 0.005$ mm, $\Delta D = 0.00005$

racy of the Turon model seems to depend strongly on the cohesive zone length, it was tested with different static cohesive zone lengths by changing the radius R of the cylinder. The results are shown in figure 3.20. The static cohesive zone lengths shown correspond to a radius of $R = 10$ mm, $R = 100$ mm, and $R = 200$ mm respectively. For the three graphs in the figure this corresponds to fatigue cohesive zone lengths of 0.25 mm $< l_{cz} <$ 0.37 mm ($L_{cz} = 0.59$ mm), 0.76 mm $< l_{cz} <$ 1.18 mm ($L_{cz} = 1.86$ mm), and 1.11 mm $< l_{cz} <$ 1.65 mm ($L_{cz} = 2.6$ mm). The static cohesive zone length L_{cz}=2.6 mm corresponds to the value used by Turon originally for HTA/6376C according to equation (3.33). As before, the correction factor of 0.32 was used, showing that at least in the cylinder model, the cohesive zone length does not influence the accuracy of the algorithm. Figure 3.21 shows the cohesive law in fatigue for the above element size/damage increment pairs. Apart from the

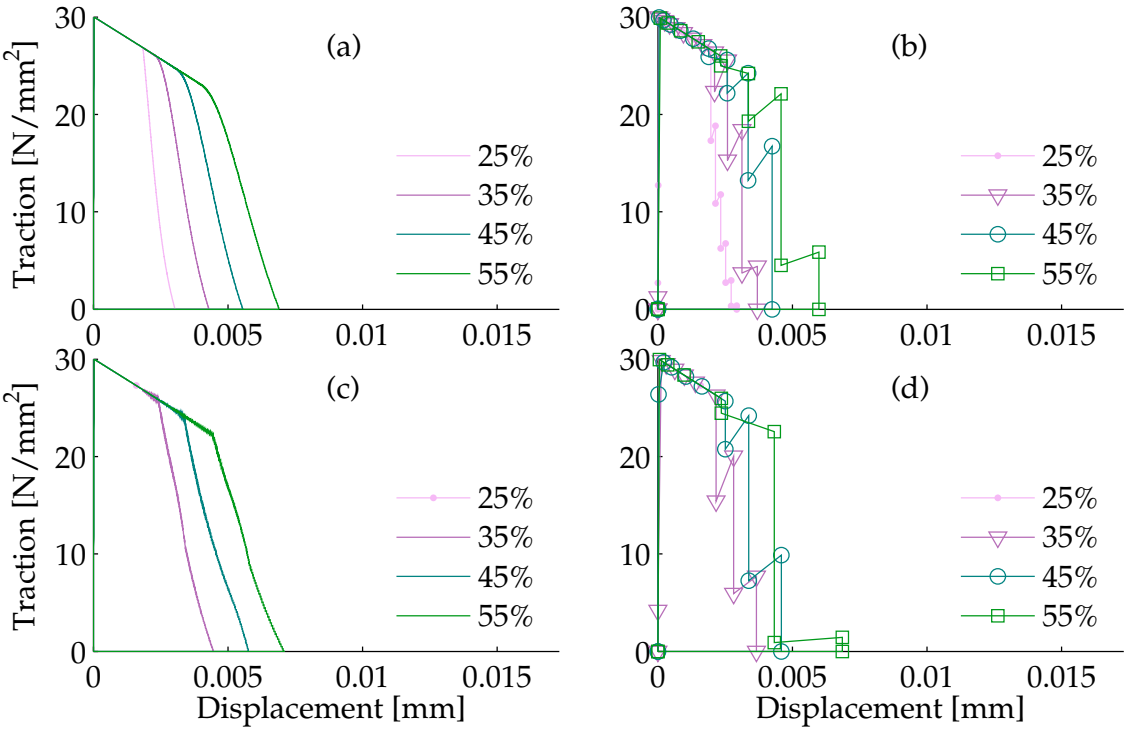


Figure 3.21.: Traction-separation curves for different applied energy release rates G_a as percentages of G_c. (a) $\Delta l = 0.005$ mm, $\Delta D = 0.00005$, (b) $\Delta l = 0.005$ mm $\Delta D = 0.005$, (c) $\Delta l = 0.25$ mm, $\Delta D = 0.00005$, (d)$\Delta l = 0.25$ mm, $\Delta D = 0.005$

$G_a = 0.25 G_c$ graph, which does not show any crack growth for $\Delta l = 0.25$ mm, the

fatigue cohesive laws are almost invariant with respect to the element size. The fatigue cohesive laws for larger damage increments look saw-toothed because for every increment, first the fatigue-damage is calculated leading to an intermediate drop in traction, which is then followed by an equilibrium step where the traction at the end of the increment is found. The drop due to fatigue has been included in the graph to give an idea of the magnitude of fatigue damage.

A sensitivity study has then been carried out to examine the influence of mesh size and damage increment on the crack growth rate $\frac{da}{dN}$ at different applied energy release rates G_a. Figure 3.22 shows a surface plot of the relative error of the crack growth rate $\frac{da}{dN}$ versus the element size and the damage increment at an applied energy release rate $G_a = 0.25G_c$. The maximum damage increment ΔD is 0.12, which

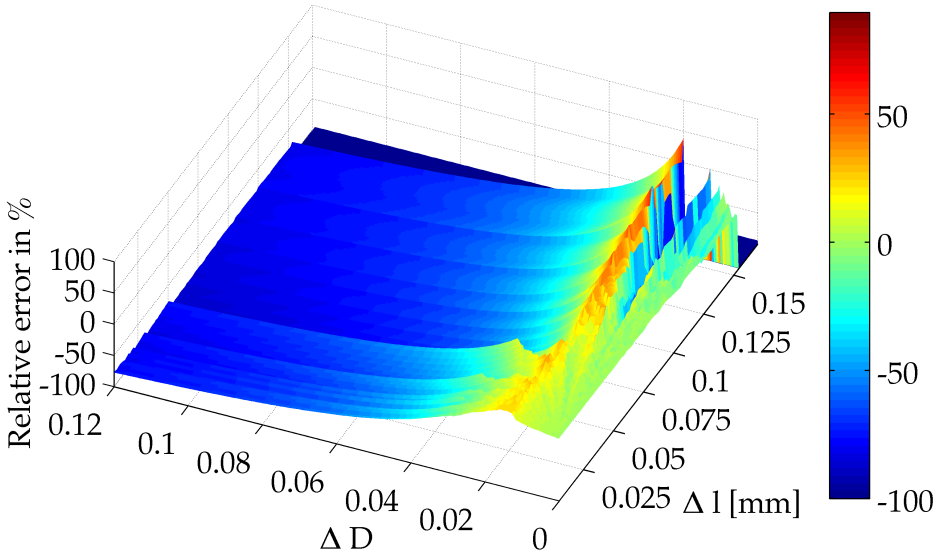


Figure 3.22.: Relative error in % of $\frac{da}{dN}$ in Turon model with respect to element size Δl and damage increment ΔD for $G_a = 0.25G_c$

corresponds to an average cycle-jump of ΔN = 40000 cycles, and the maximum element size is $\Delta l = 0.25$ mm which means that there are 3 elements in the cohesive zone. This is the same range as for the Peerlings' model. Since the applied energy release rate does not exceed G_{th} when the element size is greater than 0.15 mm, the error is -100% for element sizes larger than 0.15 mm. As the damage increment increases, the relative error first increases in the positive direction, but then changes

signs and increases in the negative direction. The maximum relative error is around 85% which is much higher than in the Peerlings' model. There are instabilities for certain values of the damage increment and the element size, resulting in a ridge of high error, when $\Delta D \approx 0.03$ and a kink, when $\Delta l = 0.075$ mm.

Figure 3.23 shows a contour plot of the relative error at the same energy release rate with respect to the number of elements in the cohesive zone and the number of steps to failure at $G_a = 0.25G_c$. The range of the number of cycles to failure is

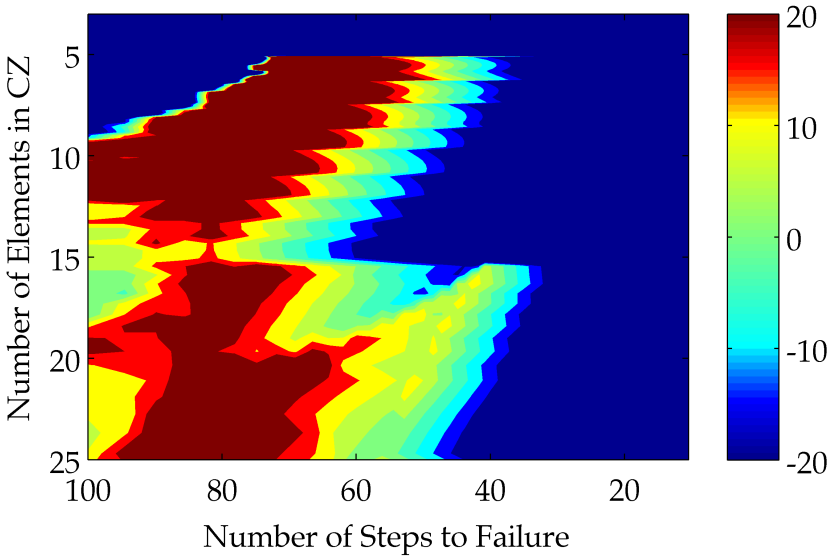


Figure 3.23.: Relative error in % of $\frac{da}{dN}$ in Turon model as a function of the number of elements in the cohesive zone n_{cz} and the number of cycle jumps to fail one element n_f for $G_a = 0.25G_c$

$10 \leq n_f \leq 100$ and the range of the number of elements in the cohesive zone is $3 \leq n_{cz} \leq 25$. This corresponds to 0.03 mm $\leq \Delta l \leq$ 0.25 mm and $0.01 \leq \Delta D \leq 0.11$. This contour plot again shows the two disturbances mentioned previously. It also shows that an integral number of elements in the cohesive zone causes oscillations. The kink in figure 3.22 when $\Delta l = 0.075$ mm is clearly recognisable. There are areas of low error for lower values of n_f because the error changes signs. Figure 3.22 and 3.23 show that at $G_a = 0.25G_c$ which is close to G_{th}, the algorithm is not very accurate unless a very small damage increment is used, so that $n_f > 100$.

Figure 3.24 shows a surface plot of the relative error at a higher energy release rate

$G_a = 0.35G_c$. The maximum damage increment ΔD is 0.05, which corresponds

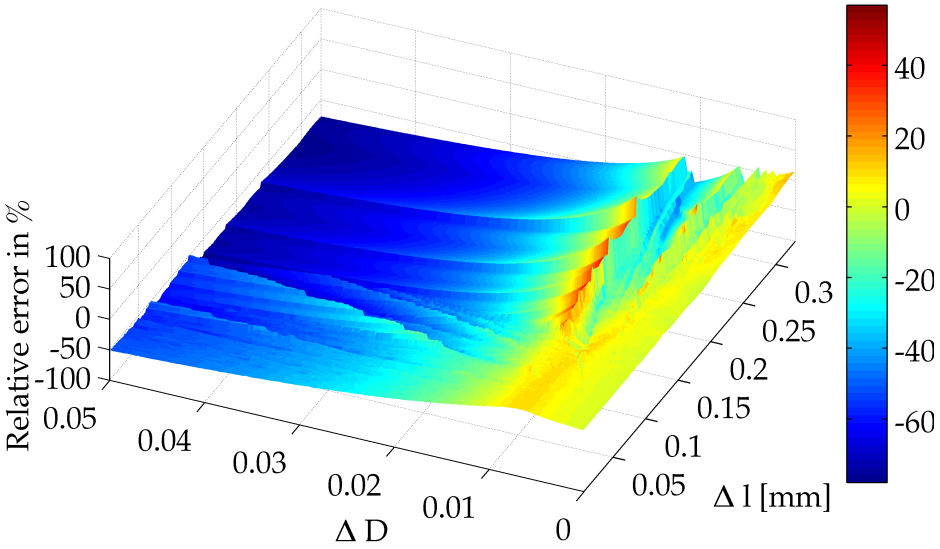


Figure 3.24.: Relative error in % of $\frac{da}{dN}$ in Turon model with respect to element size Δl and damage increment ΔD for $G_a = 0.35G_c$

to an average cycle-jump of ΔN = 20000 cycles, and the maximum element size is $\Delta l = 0.35$ mm which means that there are 3 elements in the cohesive zone. This surface plot displays the same characteristics as the one for lower applied energy release rates. However, the maximum absolute value of the relative error is lower than before at around 75%. Again there is a ridge of high error, but it occurs at a higher element size than before.

Figure 3.25 shows the contour plot of the relative error as a function of n_{cz} and n_f for $G_a = 0.35G_c$. In this contour plot, $5 \leq n_f \leq 100$ and $3 \leq n_{cz} \leq 25$. This corresponds to 0.037 mm $\leq \Delta l \leq$ 0.31 mm and $0.0014 \leq \Delta D \leq 0.026$. This plot looks very different than the previous one in figure 3.23, because the ridge is shifted with respect to the number of elements in the cohesive zone n_{cz} and the number of steps to failure n_f.

Figure 3.26 shows a surface plot of the relative error of the crack growth rate $\frac{da}{dN}$ versus the element size and the damage increment at an applied energy release rate of $G_a = 0.45G_c$. The maximum damage increment ΔD is 0.03, which corresponds to an average cycle-jump of ΔN = 5000 cycles, and the maximum element size is

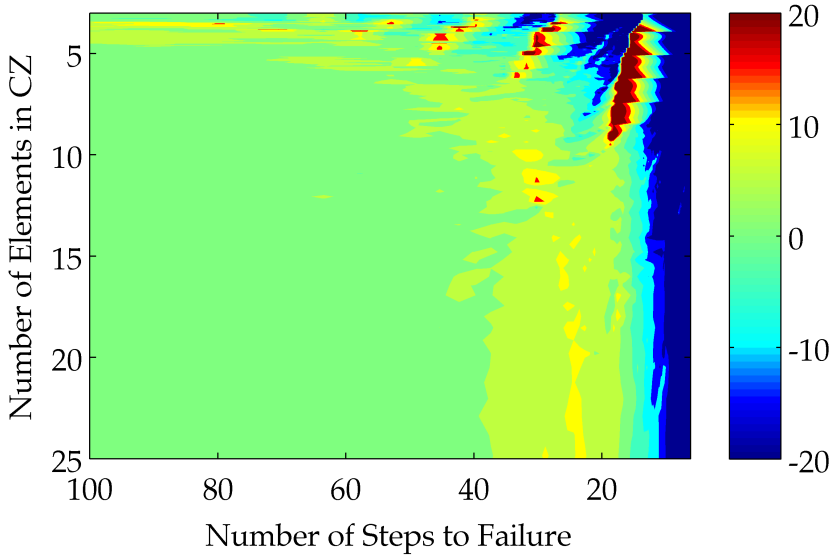


Figure 3.25.: Relative error in % of $\frac{da}{dN}$ in Turon model as a function of the number of elements in the cohesive zone n_{cz} and the number of cycle jumps to fail one element n_f for $G_a = 0.35G_c$

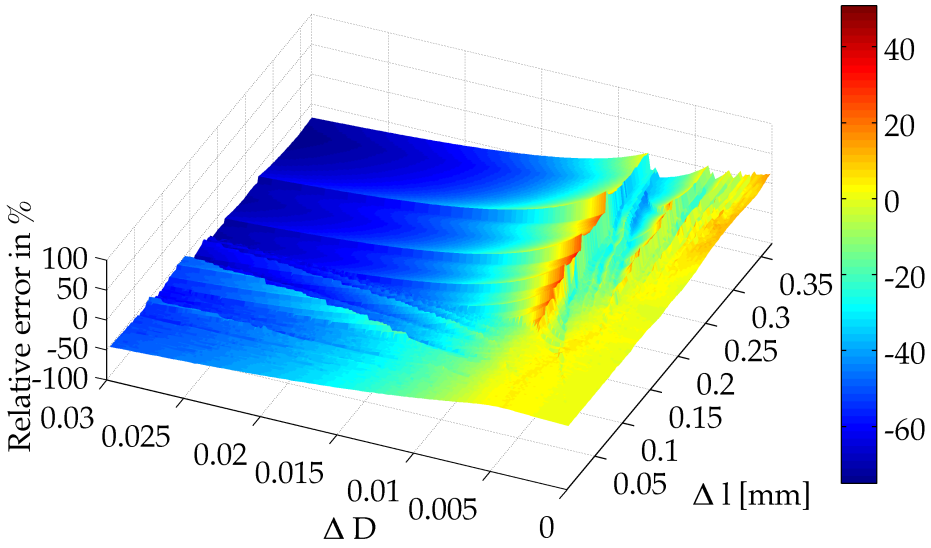


Figure 3.26.: Relative error in % of $\frac{da}{dN}$ in Turon model with respect to element size Δl and damage increment ΔD for $G_a = 0.45G_c$

$\Delta l = 0.37$ mm which means that there are 3 elements in the cohesive zone. This surface plot displays the same characteristics as the one for lower applied energy release rates. Again there is a ridge of high error, which occurs at the same element

size as in figure 3.24.

Figure 3.27 shows the contour plot of the relative error in $\frac{da}{dN}$ at $G_a = 0.45G_c$ as a function of n_{cz} and n_f. The range of n_f and n_{cz} is the same as before. This corre-

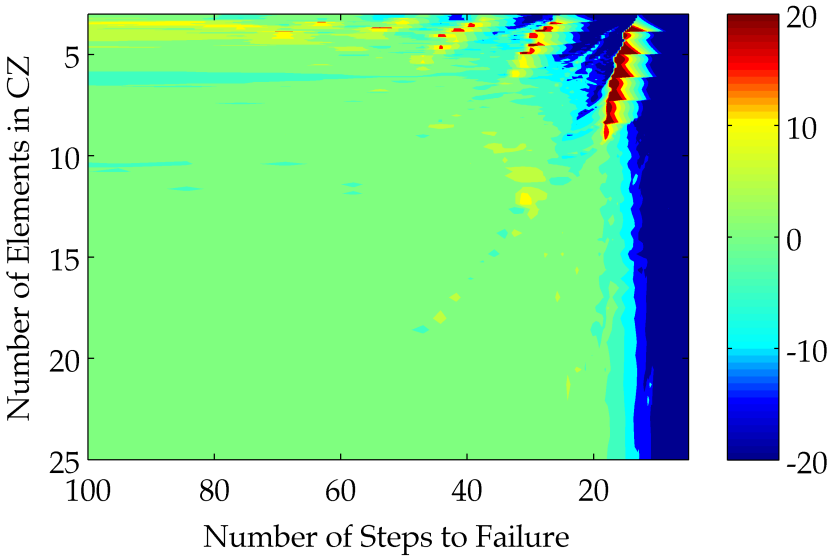


Figure 3.27.: Relative error in % of $\frac{da}{dN}$ in Turon model as a function of the number of elements in the cohesive zone n_{cz} and the number of cycle jumps to fail one element n_f for $G_a = 0.45G_c$

sponds to 0.04 mm $\leq \Delta l \leq$ 0.35 mm and $8.3 \cdot 10^{-4} \leq \Delta D \leq 0.02$. This plot displays the same characteristics as the contour plot at $G_a = 0.35G_c$. However, there are some oscillations of higher error when the number of elements in the cohesive zone is below 10.

Figure 3.28 shows the surface plot of the relative error of the crack growth rate $\frac{da}{dN}$ versus the element size and the damage increment at an applied energy release rate of $G_a = 0.55G_c$. The maximum damage increment ΔD is 0.025, which corresponds to an average cycle-jump of ΔN = 2500 cycles, and the maximum element size is $\Delta l = 0.4$ mm which means that there are 3 elements in the cohesive zone. This surface plot displays the same characteristics as the one for lower applied energy release rates, with the ridge of high error occuring at an element size of $\Delta l = 0.17$ mm.

Figure 3.29 shows the contour plot of the relative error at $G_a = 0.55G_c$. This plot

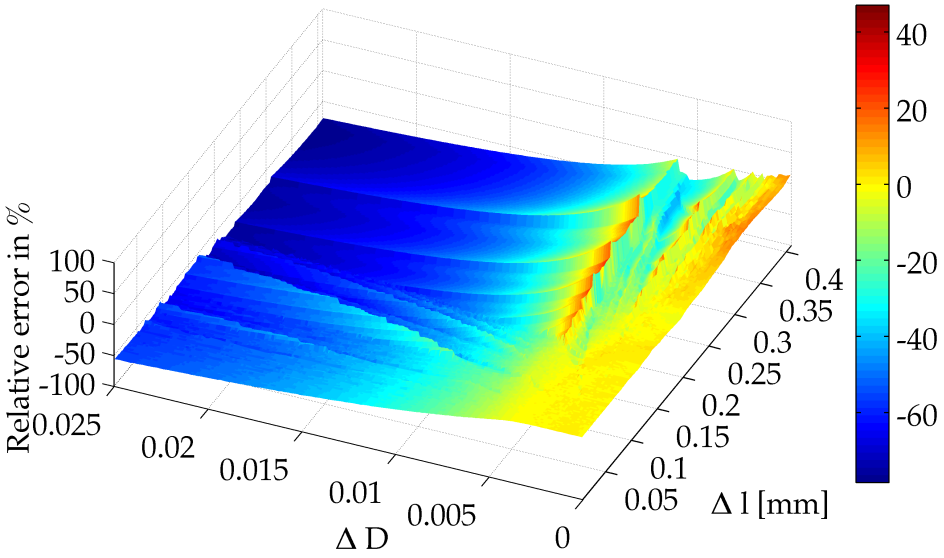


Figure 3.28.: Relative error in % of $\frac{da}{dN}$ in Turon model with respect to element size Δl and damage increment ΔD for $G_a = 0.55G_c$

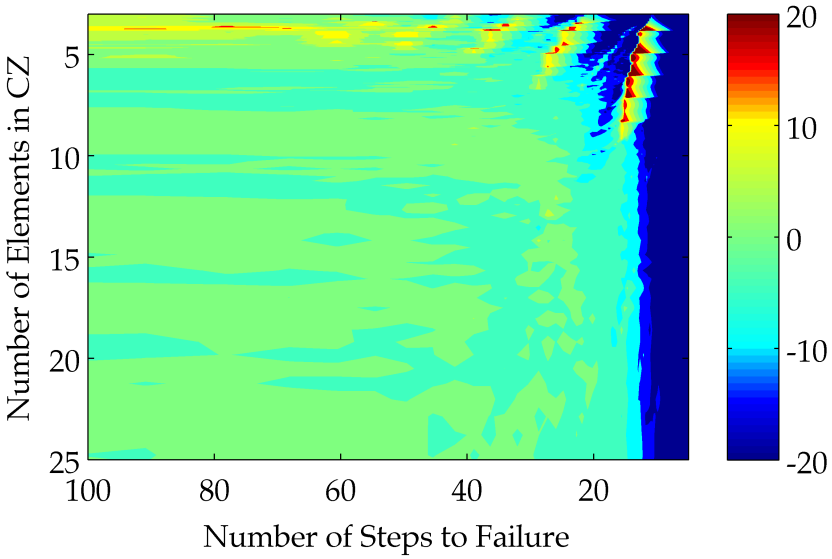


Figure 3.29.: Relative error in % of $\frac{da}{dN}$ in Turon model as a function of the number of elements in the cohesive zone n_{cz} and the number of cycle jumps to fail one element n_f for $G_a = 0.55G_c$

is similar to the contour plots at $G_a = 0.35G_c$ and $G_a = 0.45G_c$. The range of n_f and n_{cz} is the same as before. This corresponds to 0.047 mm $\leq \Delta l \leq$ 0.39 mm and $5.6 \cdot 10^{-4} \leq \Delta D \leq 0.014$. Table 3.7 shows the required number of elements in the

cohesive zone n_{cz} and the number of steps to failure n_f, so that the relative error in absolute value is below 10% and 20 % respectively.

	$\|e_r\|$<10%		$\|e_r\|$<20%	
Ga/Gc	$n_{cz} > (\Delta l <)$	$n_f >(\Delta D <)$	$n_{cz} > (\Delta l <)$	$n_f >(\Delta D <)$
0.25	-	-	-	-
0.35	8 (0.11)	35 (0.0046)	8 (0.11)	20 (0.0079)
0.45	10 (0.1)	50 (0.0021)	7 (0.15)	20 (0.0055)
0.55	7 (0.15)	20 (0.0033)	5 (0.17)	20 (0.0033)

Table 3.7.: Minimum values for $n_f(\Delta D)$ and $n_{cz}(\Delta l)$ with respect to the relative errors in $\frac{da}{dN}$. Δl in [mm]

3.4.3. Discussion of the Turon model

One advantage of the Turon model over the Peerlings' model is that there is no need to calibrate fatigue parameters using the Paris law, because the Paris law serves as a direct input. However, at least for the cylinder model, it is necessary to adjust the cohesive zone length l_{cz}, so that the Paris law is predicted well, and this calibration does not result in an excellent prediction, as the exponent in the numerically predicted Paris law is too low even for very small element sizes and damage increments. This is also the case in the original publication [TCCD07].

Another advantage of the model is its use of a damage increment ΔD rather than a fixed cycle-jump ΔN. This means that when keeping ΔD constant as in the case during a fatigue simulation, the cycle-jump will adjust to the load level, which is a useful feature considering the exponential growth of the Paris law. While Turon is the only one to have used this adaptation, it could be implemented into other fatigue degradation strategies as well. On the other hand, the Turon model could be made point-local by using a fixed time step ΔN.

A key step in the derivation of the fatigue damage rate is the related rate equation (3.38). The first term $\frac{dD}{dl_d}$ is derived by differentiating equation (3.37). However, equation (3.37) is only valid for the static damage and the static cohesive law. Another problem is the calculation of the applied energy release rate as the area under

the static cohesive law (see figure 3.17). Since the traction-separation curve changes with the addition of fatigue, this energy release rate is inaccurate. The sensitivity study showed that when the applied energy release rate is close to the threshold value G_{th} a very small damage increment ΔD has to be used in order to get an accurate prediction of the Paris law.

3.5. Harper model

Input:	Paris law parameters m and C
	quasi-static cohesive zone length L_{cz}
Point-local:	Yes
FE Implementation:	Explicit

This is a brief description of the fatigue-degradation model as it appeared in the PhD by Paul Harper [Har08]. The model requires the Paris law parameters C and m and the static cohesive zone length L_{cz}. The fatigue cohesive zone length l_{cz} is calculated from the static cohesive length L_{cz} using the integrated applied energy release rate from each element

$$l_{cz} = \frac{G_a}{G_c} \cdot L_{cz}. \tag{3.48}$$

The static cohesive zone length is obtained by carrying out a static analysis of the finite element model first. In the cylinder model the fatigue cohesive zone length is easily determined, so this value has been used instead.

3.5.1. Description of the Harper model

The fatigue-degradation strategy starts out with a different static damage formulation than the previous two models. Rather than defining static damage in terms of a loss of stiffness, this formulation defines damage in terms of the loss of traction as shown in figure 3.30. The static damage can then be expressed in terms of the displacement δ as

$$D_s = \frac{\delta - \delta_0}{\delta_c - \delta_0}, \tag{3.49}$$

and the traction in terms of damage and displacement is

$$\sigma = (1 - D_s)\sigma_0. \tag{3.50}$$

As before total damage is a sum of static and fatigue damage and an element is failed when the total damage reaches 1

$$D_{tot} = D_s + D_f. \tag{3.51}$$

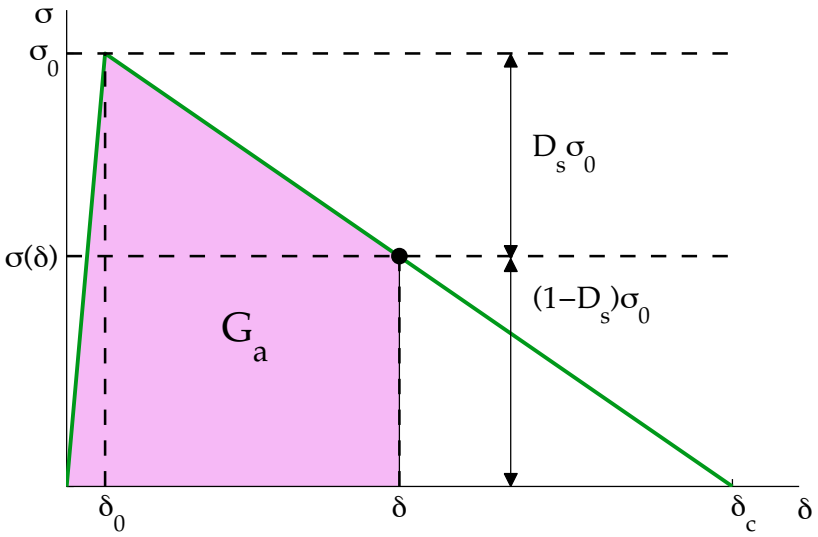


Figure 3.30.: Static damage

The cohesive zone is thought to be divided into two parts. One fatigue part of length l_{fat} where the elements acquire predominantly fatigue damage, which is close to the crack tip and one quasi-static part of length l_{qs} where the elements acquire predominantly static damage which is further away from the crack tip. It is assumed that l_{fat} is equal to half the length of the cohesive zone l_{cz}, so

$$l_{fat} = \frac{1}{2} \cdot l_{cz} \,. \tag{3.52}$$

An important assumption for this model is the separation of static and fatigue parts of the cohesive zone. In the quasi-static part an element should only acquire static damage and once an element enters the fatigue part of the cohesive zone, it does not accumulate any additional significant amount of static damage, but fails in fatigue only. A damaged element length l_D is defined for this fatigue part. The element enters the fatigue part of the cohesive zone with a damage length of 0. The damaged length then increases to 1 during the fatigue degradation. The damage length ratio is defined as follows

$$\frac{l_D}{\Delta l} = \frac{D_f}{1 - D_s}, \tag{3.53}$$

Figure 3.31 shows the quasi-static and fatigue parts of the cohesive zone and the damaged length l_D. Equation (3.53) implies a specific shape for the fatigue cohesive law, where the elements follow the static cohesive law until they enter the

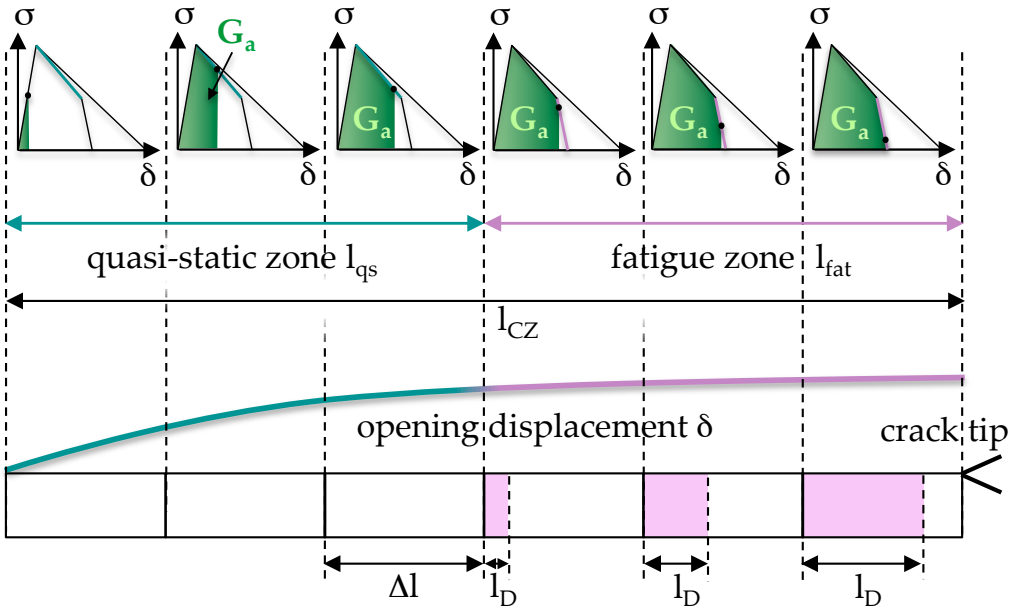


Figure 3.31.: Cohesive zone

fatigue zone and then drop down vertically. However, all elements in the cohesive zone undergo the same algorithm and since the model is point-local, they have no knowledge of their position in the cohesive zone. This means that the elements in the quasi-static zone will accumulate some unwanted fatigue damage and the elements in the fatigue zone will accumulate some additional static damage. This is why the original damaged length ratio has to be adjusted to account for the unwanted fatigue damage accumulation, so equation (3.53) is modified to

$$\frac{l_D}{\Delta l} = \frac{D_f - D_{f,u}}{1 - D_s - D_{f,u}}, \tag{3.54}$$

where $D_{f,u}$ is the unwanted fatigue damage accumulated in the quasi-static part of the cohesive zone. Introducing $D_{f,u}$ insures that every element enters the fatigue part of the cohesive zone with a damaged length $l_D = 0$ as shown in figure 3.31 .$D_{f,u}$ is shown in figure 3.32 and is calculated as

$$D_{f,u} = \frac{\text{Area ABC}}{0.5(\delta - \delta_0) \cdot \sigma_0}. \tag{3.55}$$

Figure 3.33 shows the fatigue damage D_f, static damage D_s and unwanted fatigue damage $D_{f,u}$, and the integrated applied energy release rate G_a. G_a is used to find

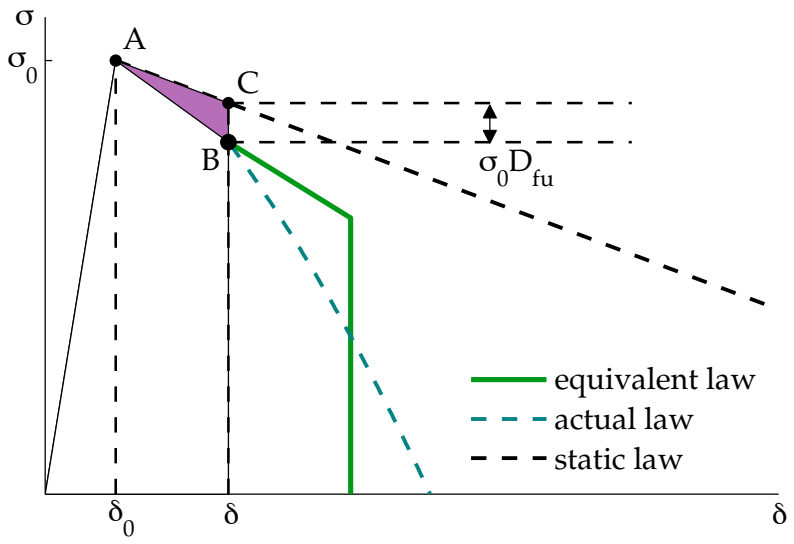


Figure 3.32.: Accumulation of $D_{f,u}$

the crack growth rate from the input Paris law

$$\frac{\partial a}{\partial N} = C\left(\frac{G_a}{G_c}\right)^m. \tag{3.56}$$

This crack growth rate is related to the fatigue damage to find the fatigue damage rate $\frac{\partial D_f}{\partial N}$. The increase in crack length a is assumed to be equal to the sum of the damaged lengths l_D of the elements in the fatigue part of the cohesive zone, so

$$a = \sum_{e \in l_{fat}} l_D \tag{3.57}$$

Differentiating equation (3.57) with respect to cycles gives

$$\frac{\partial a}{\partial N} = \sum_{e \in l_{fat}} \frac{\partial l_D}{\partial N} \tag{3.58}$$

Similarly to the Turon model it is assumed that the damaged length derivative is constant across the fatigue cohesive zone, so

$$\sum_{e \in l_{fat}} \frac{\partial l_D}{\partial N} = \frac{l_{fat}}{\Delta l}\frac{\partial l_D}{\partial N} \tag{3.59}$$

Combining and rearranging equations (3.58) and (3.59) leads to

$$\frac{\partial l_D}{\partial N} = \frac{\Delta l}{l_{fat}}\frac{\partial a}{\partial N}. \tag{3.60}$$

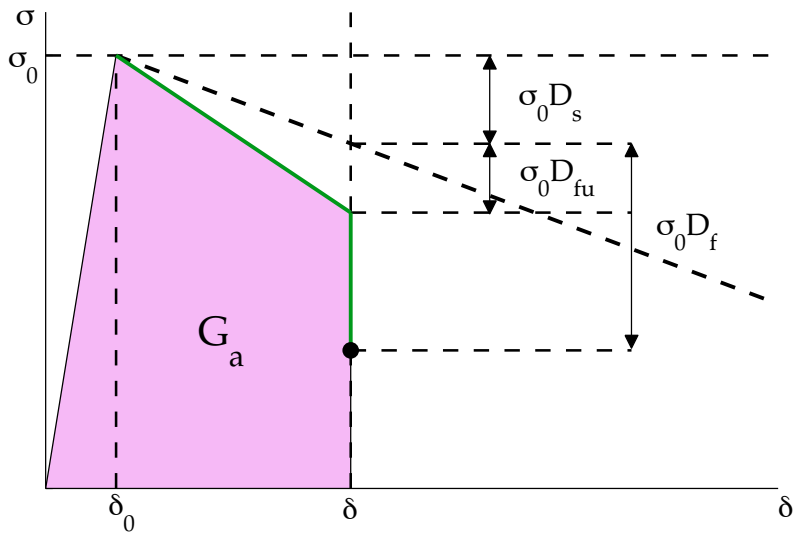


Figure 3.33.: Static and fatigue damage

Differentiating equation (3.54) with respect to the damage length l_D gives

$$\frac{\partial D_f}{\partial l_D} = \frac{1 - D_s - D_{f,u}}{\Delta l} \tag{3.61}$$

Multiplying equations (3.60) and (3.61) gives the following related rate, which then leads to an equation for the fatigue damage rate with respect to cycles

$$\frac{\partial D_f}{\partial l_D} \cdot \frac{\partial l_D}{\partial N} = \frac{1 - D_s - D_{f,u}}{\Delta l} \cdot \frac{\Delta l}{l_{fat}} \frac{\partial a}{\partial N} \tag{3.62}$$

$$\iff \frac{\partial D_f}{\partial N} = \frac{1 - D_s - D_{f,u}}{l_{fat}} \frac{\partial a}{\partial N} \tag{3.63}$$

3.5.2. Results for the Harper model

The input parameters used in the Harper model are shown in table 3.8. The original

$C = 0.0066$	$m = 5.9$	$L_{cz} = 1.8$ mm

Table 3.8.: Model input

model used a fatigue length ratio $\frac{l_{fat}}{l_{cz}}$ of 0.5 (see equation 3.52). In order to get an accurate prediction of the cohesive zone length with the cylinder model this ratio had to be adjusted to 0.23. Figure 3.34 shows experimental data, the analytical Paris

law used as input and the resulting Paris law from the model for four different pairs of cycle-jump and element size. The Paris law cannot be reproduced for high cycle-

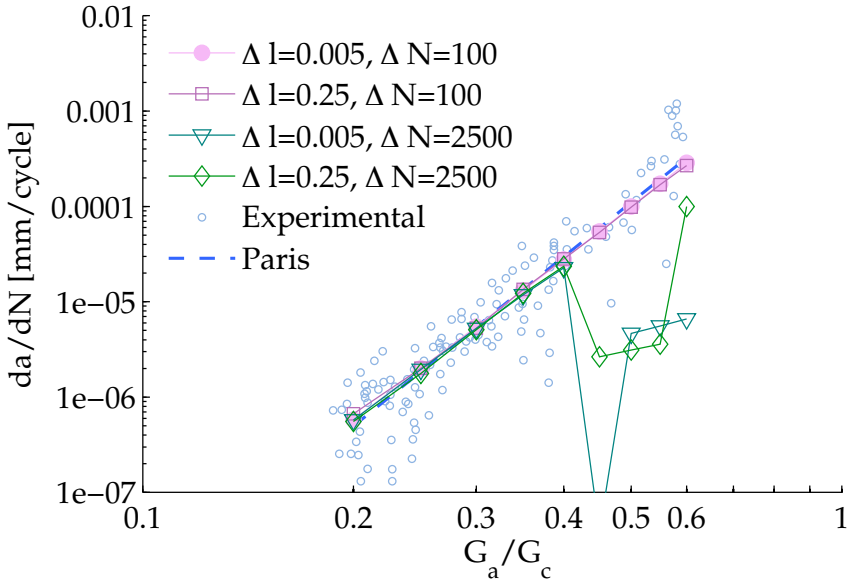


Figure 3.34.: Experimental data, paris law, and Harper model crack growth rates for different element sizes and cycle-jumps. Δl in mm, ΔN in cycles

jumps, when the energy release rate is high ($G_a > 0.4G_c$). This is due to the cohesive elements not tracing the elastic part of the cohesive law, where $\delta < \delta_0$. This leads to a wrong calculation of the fatigue damage rate which stops the analysis from converging. Figure 3.35 shows the relative error for these four numerical Paris laws with respect to the input parameters. The figure shows that the error curves are similar for equal element sizes, apart from the curves with the larger mesh size at high energy release rates, where no convergence is reached, making the Paris law erratic. Similarly to the Turon model, the adjustment of the fatigue length does not lead to the accurate exponent m for the Paris law, making the error positive for low energy release rates and negative for larger energy release rates. The cohesive zone length, number of cycles to failure and number of elements in the cohesive zone are shown in table 3.9. Figure 3.36 shows the interface law for the above parameter pairs. Since the model does not converge for $\Delta N = 2500$ cycles and $G_a > 0.4G_c$, fig. 3.36 (b) and (d) only show two fatigue cohesive laws. The shape of the fatigue cohesive laws is very similar for equal element sizes. While the interface law is convex

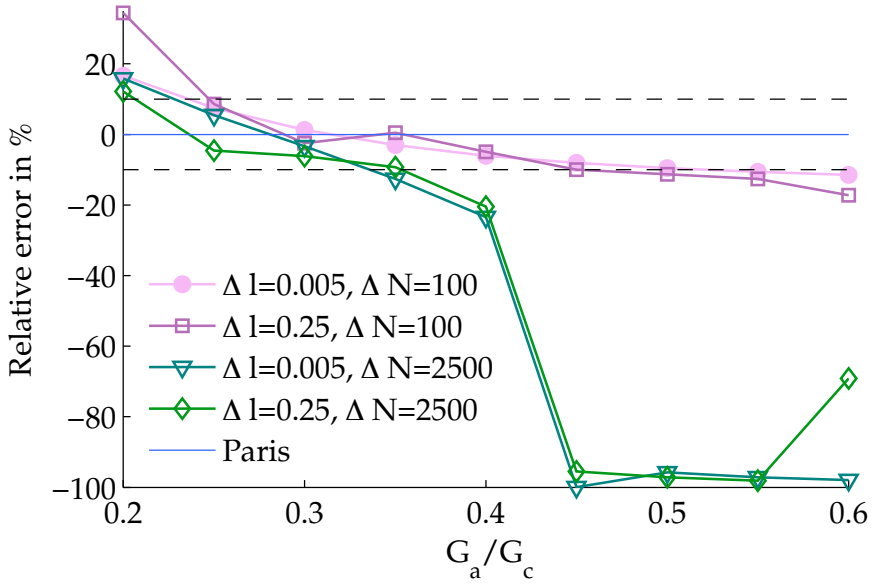


Figure 3.35.: Relative error in % in crack growth rate $\frac{da}{dN}$ for different element sizes and and cycle-jumps. Δl in mm, ΔN in cycles

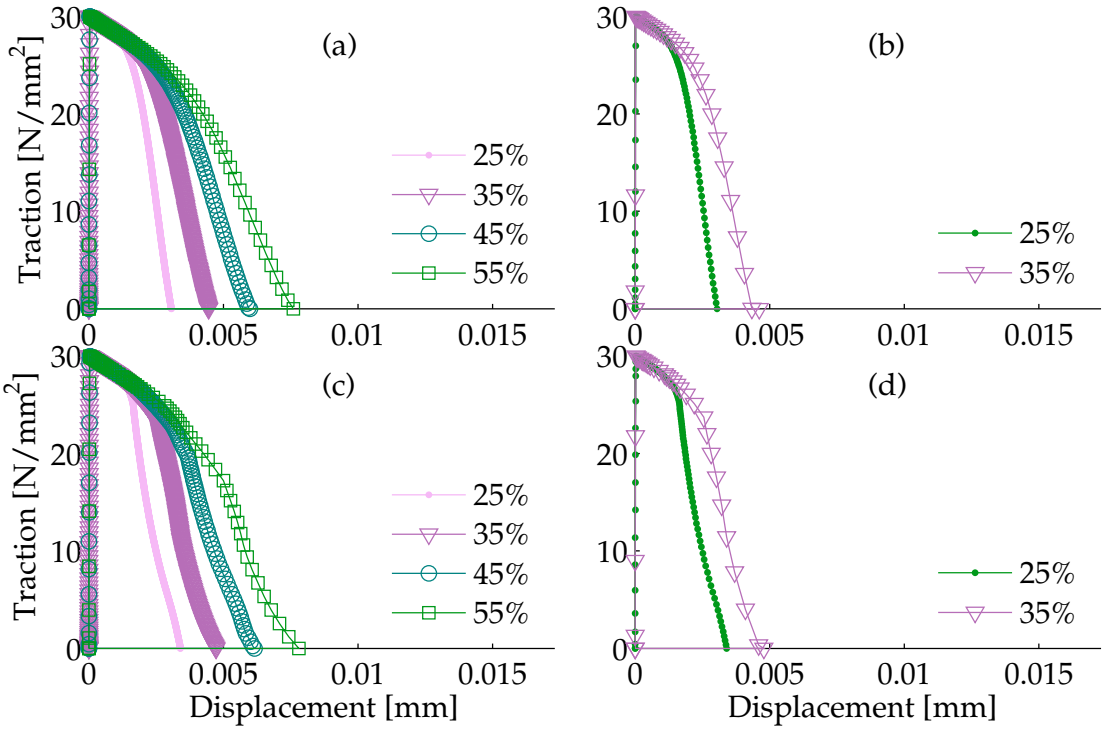


Figure 3.36.: Traction-separation curves for different percentages of G_c. (a) $\Delta l = 0.005$ mm, $\Delta N = 100$ cycles, (b) $\Delta l = 0.005$ mm $\Delta N = 2500$ cycles, (c) $\Delta l = 0.25$ mm, $\Delta N = 100$ cycles, (d)$\Delta l = 0.25$ mm, $\Delta N = 2500$ cycles

			Elements in CZ n_{cz}		Steps to failure n_f	
Ga/Gc	l_{cz} [mm]	N_f[cycles]	$\Delta l = 0.005$	$\Delta l = 0.25$	$\Delta N = 100$	$\Delta N = 2500$
0.25	0.79	$4.26 \cdot 10^5$	158	3.2	4260	170
0.35	0.95	$7.05 \cdot 10^4$	190	3.8	705	28
0.45	1.09	$1.83 \cdot 10^4$	218	4.4	183	-
0.55	1.23	$6.3 \cdot 10^3$	246	4.9	63	-

Table 3.9.: Crack growth parameters for Harper model

for the lower element size, it has a point of inflection for the higher element-size. For higher applied energy release rates the fatigue cohesive laws do not follow the static curve very well, therefor accumulating significant unwanted fatigue damage $D_{f,u}$. Figure 3.37 shows the relative error at a load level of $G_a = 0.25G_c$. The maxi-

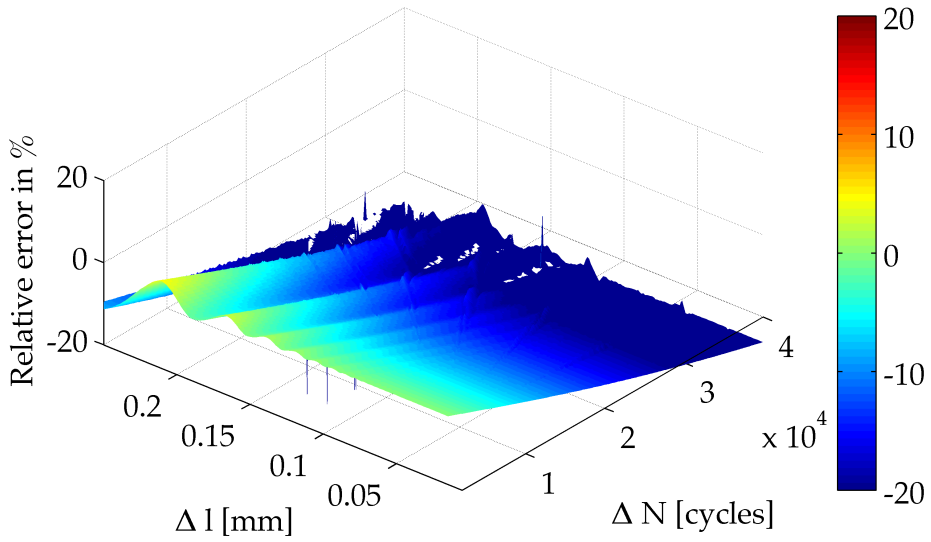


Figure 3.37.: Relative error in % of $\frac{da}{dN}$ in Harper model with respect to element size Δl and cycle jump ΔN for $G_a = 0.25G_c$

mum cycle jump is 40,000 cycles which means that an element fails within about 11 iterations. The maximum element size is 0.25 mm, when there are three elements in the cohesive zone. Figure 3.38 shows a contour plot of the relative error versus the number of elements in the cohesive zone n_{cz} and the number of steps to failure n_f for the same load level $G_a = 0.25G_c$, where $10.6 < n_f < 100$ and $3.2 < n_{cz} < 25$.

This corresponds to 0.03 mm$< \Delta l <$ 0.25 mm and 4,260 cycles $< \Delta N <$ 40,000

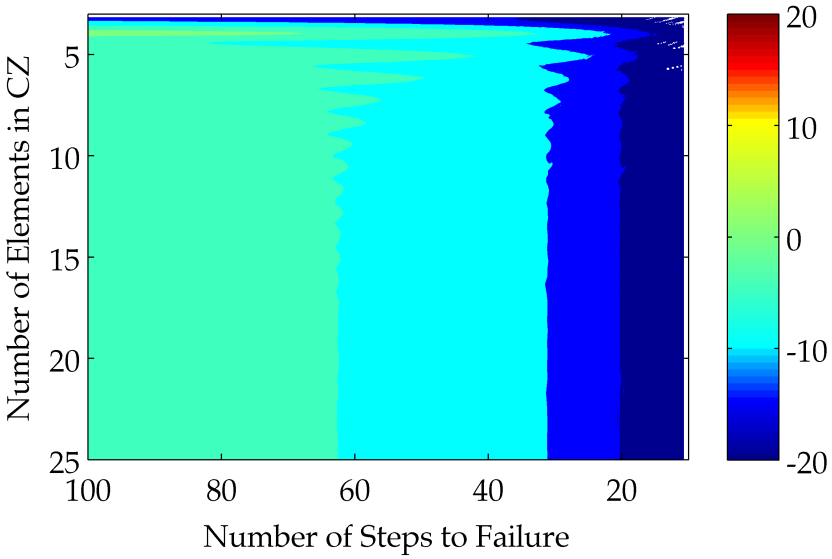


Figure 3.38.: Relative error in % of $\frac{da}{dN}$ in Harper model with respect to the number of elements in the cohesive zone and the number of cycle jumps to fail one element for $G_a = 0.25G_c$

cycles. Figure 3.39 shows the relative error at a load level of $G_a = 0.35G_c$. The max-

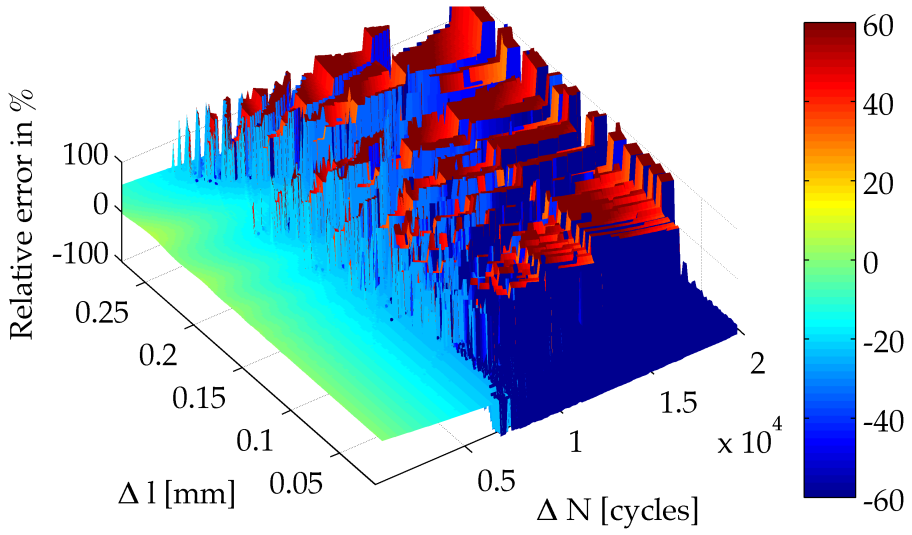


Figure 3.39.: Relative error in % of $\frac{da}{dN}$ in Harper model with respect to element size Δl and cycle jump ΔN for $G_a = 0.35G_c$

imum cycle jump is 20,000 cycles which means that an element fails within about 3.5 iterations. The maximum element size is 0.3 mm, when there are three elements in the cohesive zone. This figure shows two distinct parts. When the cycle-jump is below about 7500 cycles, the error grows linearly, but for any cycle-jump above 7500 the error becomes very erratic. This was already indicated in figure 3.34, where the Paris law is erratic when the cycle-jump is too large. Figure 3.40 shows a contour plot of the relative error versus the number of elements in the cohesive zone n_{cz} and the number of steps to failure n_f for the same load level $G_a = 0.25G_c$, where $10 < n_f < 100$ and $3 < n_{cz} < 25$. This corresponds to 0.038 mm$< \Delta l <$ 0.3 mm

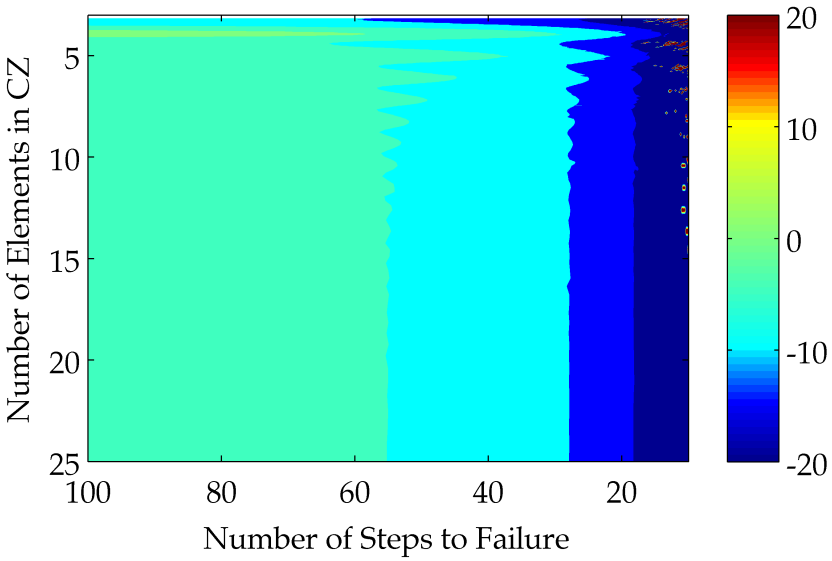


Figure 3.40.: Relative error in % of $\frac{da}{dN}$ in Harper model with respect to the number of elements in the cohesive zone and the number of cycle jumps to fail one element for $G_a = 0.35G_c$

and 705 cycles $< \Delta N <$ 7050 cycles. Figure 3.41 shows the relative error at a load level of $G_a = 0.45G_c$. The maximum cycle jump is 7500 cycles which means that an element fails within about 2.4 iterations. The maximum element size is 0.35 mm, when there are three elements in the cohesive zone. The figure exhibits the same features as figure 3.39 with an erratic error when the cycle jump is larger than about 1700 cycles.

Figure 3.42 shows a contour plot of the relative error versus the number of ele-

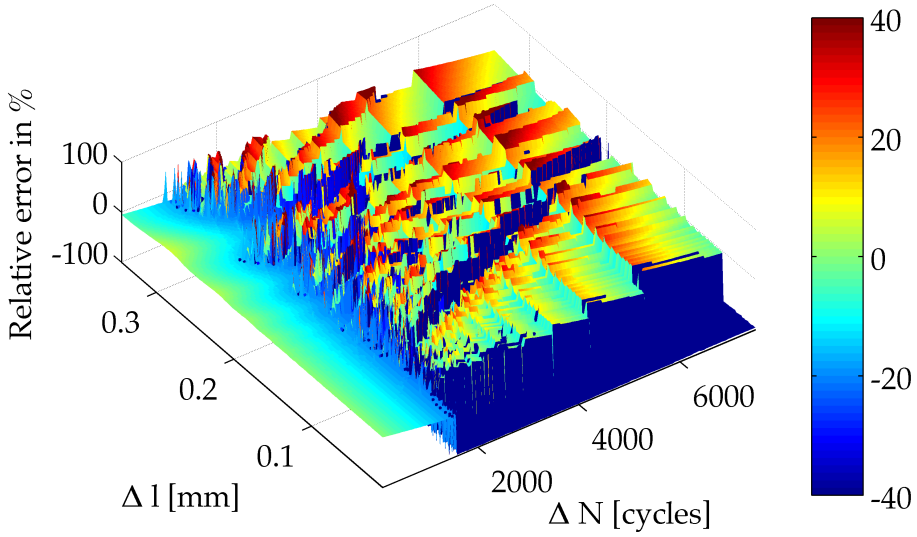


Figure 3.41.: Relative error in % of $\frac{da}{dN}$ in Harper model with respect to element size Δl and cycle jump ΔN for $G_a = 0.45G_c$

ments in the cohesive zone n_{cz} and the number of steps to failure n_f for the same load level $G_a = 0.45G_c$, where $10 < n_f < 100$ and $3 < n_{cz} < 25$. This corresponds

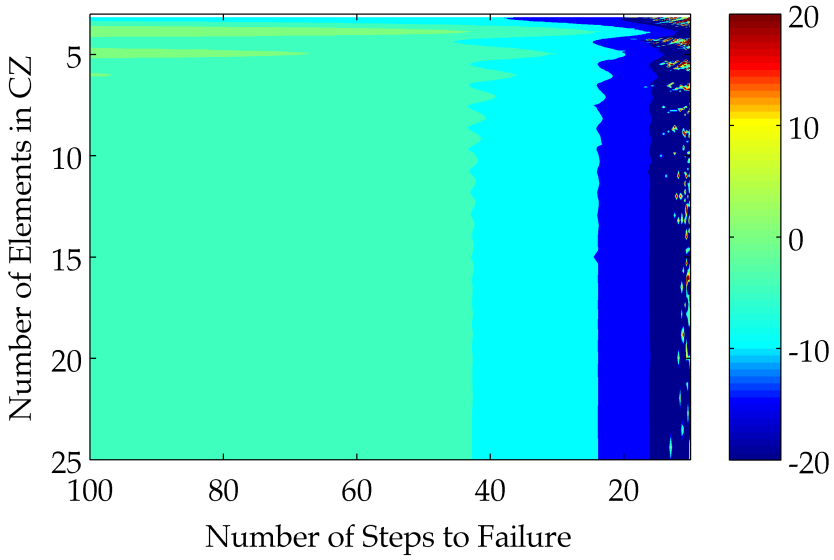


Figure 3.42.: Relative error in % of $\frac{da}{dN}$ in Harper model with respect to the number of elements in the cohesive zone and the number of cycle jumps to fail one element for $G_a = 0.45G_c$

to 0.04 mm$< \Delta l <$ 0.35 mm and 183 cycles $< \Delta N <$ 1830 cycles. Figure 3.43 shows the relative error at a load level of $G_a = 0.55G_c$. The maximum cycle jump is 2500

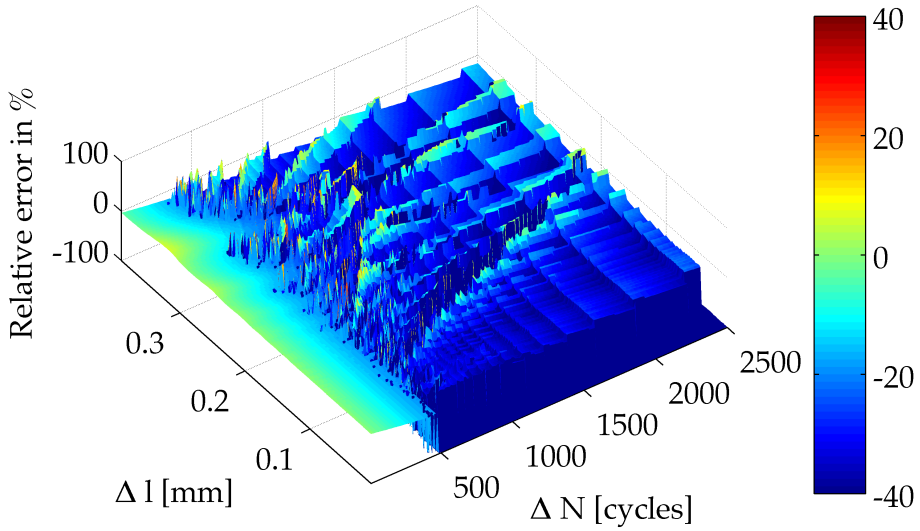


Figure 3.43.: Relative error in % of $\frac{da}{dN}$ in Harper model with respect to element size Δl and cycle jump ΔN for $G_a = 0.55G_c$

cycles which means that an element fails within about 2.5 iterations. The maximum element size is 0.39 mm, when there are three elements in the cohesive zone. The figure exhibits the same features as the previous two surface plots with an erratic error when the cycle jump is larger than about 500 cycles.

Figure 3.44 shows a contour plot of the relative error versus the number of elements in the cohesive zone n_{cz} and the number of steps to failure n_f for the same load level $G_a = 0.55G_c$, where $10 < n_f < 100$ and $3 < n_{cz} < 25$. This corresponds to 0.05 mm$< \Delta l <$ 0.39 mm and 63 cycles $< \Delta N <$ 630 cycles. Table 3.10 shows the required number of elements in the cohesive zone n_{cz} and the number of steps to failure n_f, so that the relative error in absolute value is below 10% and 20 % respectively.

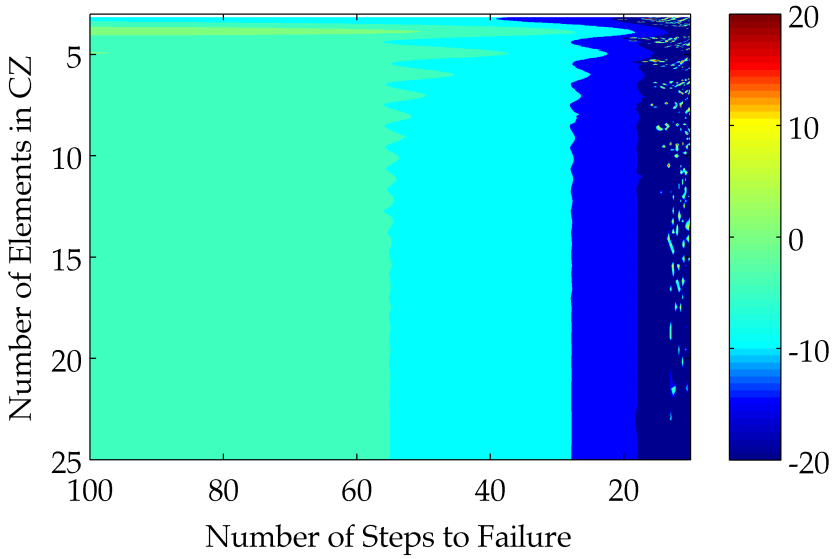


Figure 3.44.: Relative error in % of $\frac{da}{dN}$ in Harper model with respect to the number of elements in the cohesive zone and the number of cycle jumps to fail one element for $G_a = 0.55G_c$

	$\|e_r\|$<10%		$\|e_r\|$<20%	
Ga/Gc	$n_{cz}>(\Delta l<)$	$n_f>(\Delta N<)$	$n_{cz}>(\Delta l<)$	$n_f>(\Delta N<)$
0.25	4 (0.2)	30 (14,200)	4 (0.2)	15 (28,400)
0.35	4 (0.24)	30 (2350)	4 (0.24)	20 (3525)
0.45	4 (0.27)	30 (610)	4 (0.27)	20 (915)
0.55	4 (0.3)	30 (210)	4 (0.3)	20 (315)

Table 3.10.: Minimum values for $n_f(\Delta N)$ and $n_{cz}(\Delta l)$ with respect to the relative errors in $\frac{da}{dN}$. Δl in [mm], ΔN in cycles

3.5.3. Discussion of the Harper model

The model by Harper is able to predict the Paris law when the fatigue length l_{fat} is accurately determined. The model is also point-local, thus requiring no exchange of information between the elements during a finite element analysis. The input parameters are the Paris law, and the quasi-static cohesive zone length L_{cz}, which has to be determined prior to the fatigue analysis, requiring an additional step. In the cylinder model the shape of the cohesive zone is predetermined as the arc of a circle. This shape does not suit the model well, since it is assumed that in the fatigue zone l_{fat} the opening displacement stays almost constant and therefore once an element reaches this zone, the applied energy release rate is almost equal to the actual crack tip value. In order for this to be a good assumption the shape of the cohesive zone needs to be concave rather than convex (see figure 3.45). In order to

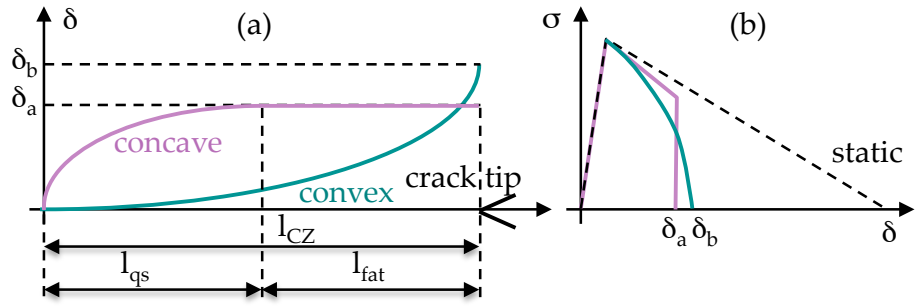


Figure 3.45.: (a) Cohesive zone shape, (b) corresponding fatigue cohesive laws

keep the model point-local, the cohesive zone-length has to be estimated for every element at each time-step. This is accomplished by using the current applied energy release rate and the estimated cohesive zone length in fatigue is

$$l_{cz} = \frac{G_a}{G_c} L_{cz}, \quad 0 < G_a < G_c. \tag{3.64}$$

The ideal shape of the fatigue cohesive law for the degradation strategy is a bilinear function as shown in figure 3.46 (a), where the elements acquire no unwanted fatigue damage while they are in the quasi-static zone, so $D_{f,u} = 0$ and have reached the maximum G_a by the time they enter the fatigue zone. Assuming such an ideal fatigue cohesive law shape and assuming that equation (3.64) is correct at the same time, the shape of the quasi-static cohesive zone is determined.

The applied energy release rate G_a which corresponds to the pink shaded area in 3.46 (a) can then be expressed as

$$G_a = \begin{cases} \frac{\sigma_0}{2\delta_0}\delta_{cf}^2 & ,0 < G_a < \frac{1}{2}\sigma_0\delta_0 \\ G_c - \frac{1}{2}\sigma_{cf}\cdot(\delta_c - \delta_{cf}) & ,\frac{1}{2}\sigma_0\delta_0 \leq G_a \leq G_c \end{cases}, \tag{3.65}$$

where

$$\sigma_{cf} = -\frac{\sigma_0}{\delta_c - \delta_0}(\delta_{cf} - \delta_c), \tag{3.66}$$

where δ_{cf} is the final displacement reached under fatigue. Solving for δ_{cf} gives

$$\delta_{cf}(G_a) = \begin{cases} \sqrt{\frac{2G_a\delta_0}{\sigma_0}} & ,0 < G_a < \frac{1}{2}\sigma_0\delta_0 \\ \delta_c - \sqrt{\frac{2\cdot(\delta_c-\delta_0)}{\sigma_0}\cdot(G_c - G_a)} & ,\frac{1}{2}\sigma_0\delta_0 \leq G_a \leq G_c \end{cases}, \tag{3.67}$$

The profile of the cohesive zone is determined by plotting $l_{cz}(G_a)$ (from equation (3.64)) vs. $\delta_{cf}(G_a)$ (from equation (3.67)). It is plotted in figure 3.46 (b) for different quasi-static cohesive zone lengths. The cohesive zone shapes in figure 3.46 (b) are

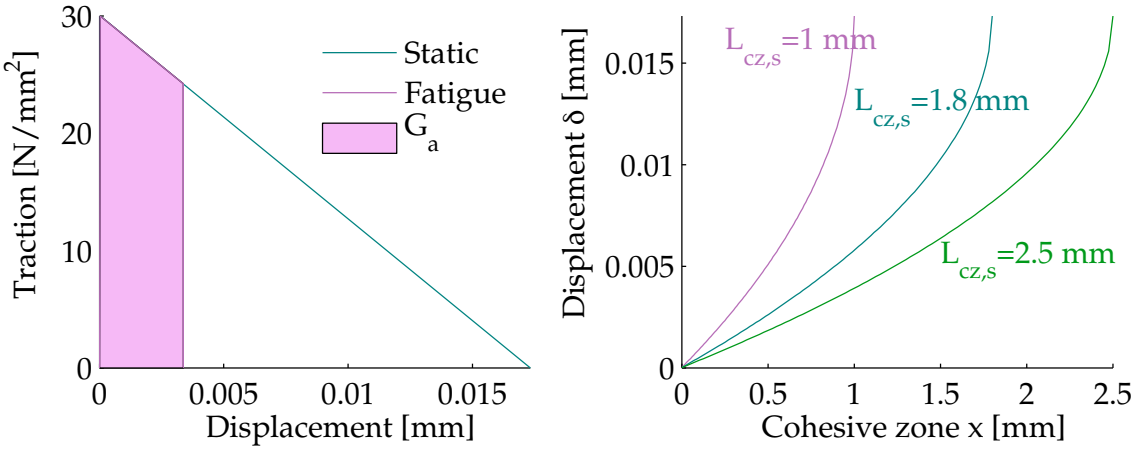


Figure 3.46.: (a) Assumed cohesive zone law, (b) Static cohesive zone shape

convex, contradicting the earlier conclusion that the cohesive zone shape should be concave. Therefore, if the fatigue cohesive law is similar to the one shown in 3.46 (a), then either equation (3.48) is not a good approximation to the actual cohesive zone length, and the actual cohesive zone length should be used or the fatigue length l_{fat} has to be shortened, so that the displacement for the elements in the fatigue part of cohesive zone does not increase significantly.

Since the cylinder model has a convex cohesive zone shape the model is only accurate when the fatigue length l_{fat} is reduced.

3.6. Kawashita-Hallett model

Input:	Paris law parameters m and C
Point-local:	No
FE Implementation:	Explicit

More recently, another model for fatigue delamination was proposed by Kawashita and Hallett [KH12]. In this model, a crack-tip tracing algorithm is used so that fatigue can be applied to only the crack-tip element. This makes it easier to apply the correct fatigue crack growth rate, since the crack growth is not spread over the whole cohesive zone, where it is necessary to distribute the crack growth rate among the elements as happens in the previous two models (see equations (3.43) and (3.63)). Like the previous two models, this model requires the Paris law as an input parameter.

3.6.1. Description of the Kawashita-Hallett model

As in the previous model by Harper, the static damage is defined in terms of a loss of traction (see figure 3.30), so the traction is

$$\sigma(\delta) = (1 - D_s)\sigma_0, \tag{3.68}$$

and the static damage is then expressed as

$$D_s = \frac{\delta - \delta_0}{\delta_c - \delta_0}. \tag{3.69}$$

Again, the total damage D_{tot} is a sum of static and fatigue damage and an element is failed when the total damage reaches 1

$$D_{tot} = D_s + D_f. \tag{3.70}$$

The crack growth in this model is limited to the crack tip element. When an element enters the cohesive zone it accumulates static damage until it becomes the crack tip element, where it accumulates only fatigue damage. The total fatigue damage to be accumulated by this crack-tip element until failure is equal to

$$\Delta D_f = 1 - D_s. \tag{3.71}$$

The number of cycles ΔN_f in which this element should fail is the number of cycles it takes to advance the crack by one element length Δl, so

$$\Delta N_f = \frac{\Delta l}{\frac{da}{dN}}, \tag{3.72}$$

where $\frac{da}{dN}$ is calculated according to the Paris law

$$\frac{da}{dN} = C \left(\frac{G_a}{G_c} \right)^m. \tag{3.73}$$

In order to calculate this crack growth rate, the applied energy release rate G_a has to be known. It is calculated as the maximum of two values: the instantaneous applied energy release rate G_{inst} of the crack tip element, which is the area under the traction-separation response and the failure energy release rate G_f of the neighbouring element that has already failed, so

$$G_a = \max\{G_{inst}, G_f\}. \tag{3.74}$$

Figure 3.47 shows the cohesive zone and the two energy release rates. If there is no

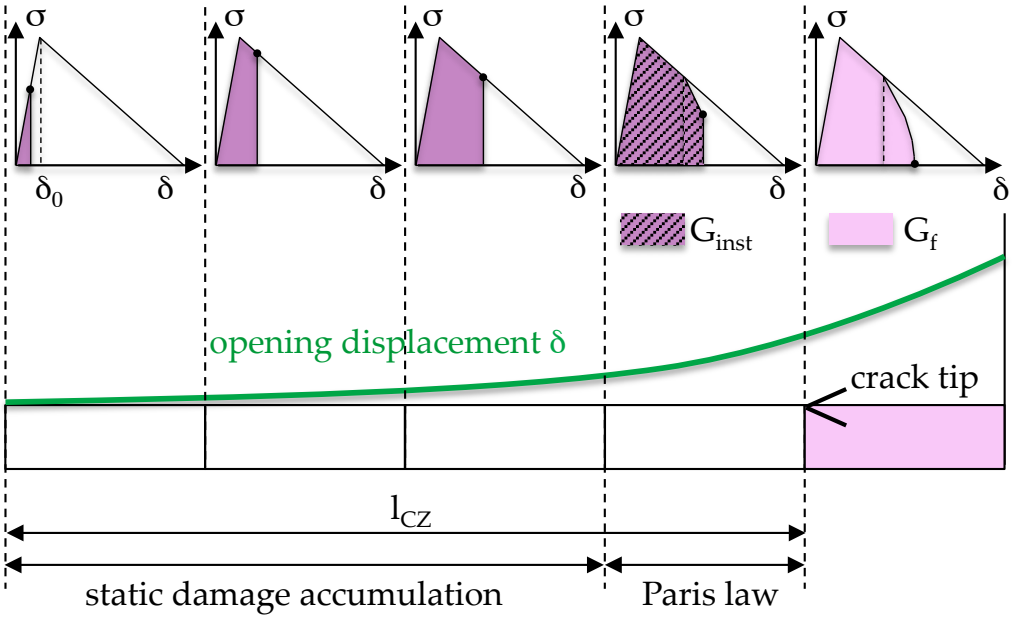


Figure 3.47.: Cohesive zone with crack tip tracing

neighbouring element, that has failed already, then $G_f = 0$. In order to speed up the algorithm, G_{inst} is updated after every cycle-jump, using the trapezoidal integration

rule. The fatigue damage rate can then be expressed as the ratio of fatigue damage left to accumulate ΔD_f and the number of cycles to failure ΔN_f, so

$$\frac{dD_f}{dN} = \frac{1 - D_s}{\Delta N_f}. \tag{3.75}$$

The increase in damage of the crack-tip element after a certain number of cycles $N + \Delta N$, where ΔN is the cycle-jump, is then calculated as

$$D_{N+\Delta N} = D_N + \frac{dD_f}{dN} \cdot \Delta N. \tag{3.76}$$

3.6.2. Results for the Kawashita-Hallett model

Figure 3.48 shows the comparison of the fatigue degradation strategy and the calibrated Paris law. The plot shows that there is a noticeable deviation from the Paris law for low applied energy release rates and large mesh size. This is due to a small number of elements n_{cz} in the cohesive zone ($2 \leq n_{cz} \leq 3$). The other noticeable error is for high energy release rates and large cycle-jumps as well as large mesh sizes. Figure 3.49 shows the relative error for these four numerical Paris laws with respect

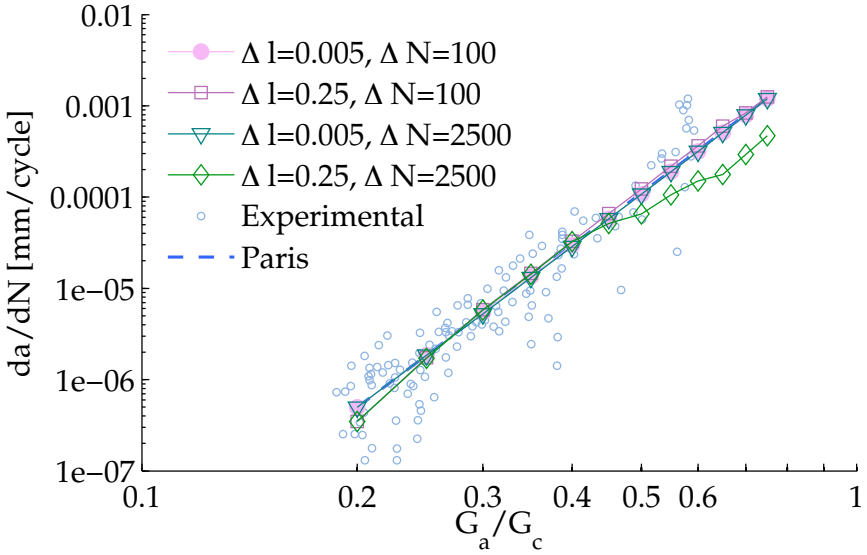


Figure 3.48.: Experimental data, paris law, and crack tip tracing model crack growth rates for different element sizes and cycle-jumps. Δl in mm, ΔN in cycles

to the input parameters. The figure shows that the error curves are similar for equal

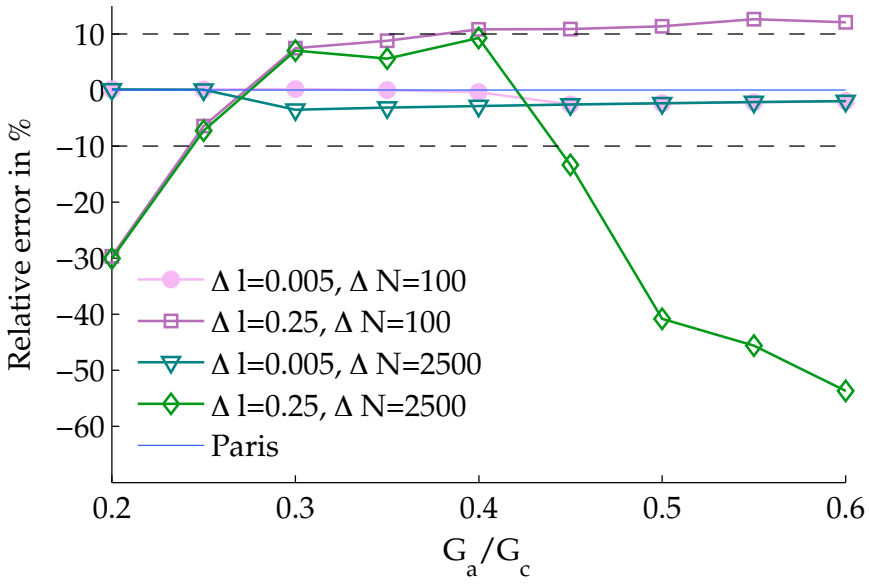


Figure 3.49.: Relative error in % in crack growth rate $\frac{da}{dN}$ for different element sizes and and cycle-jumps. Δl in mm, ΔN in cycles

element sizes, apart from the curves with the larger mesh size at high energy release rates. For low mesh-sizes, the crack-tip tracing model is the most accurate of all the models analysed with a maximum relative error $|e_r|$ below 5%. The cohesive zone length and the number of cycles to failure, which is the number of cycles it takes for the crack to advance by the length of the cohesive zone are shown in table 3.11 for a range of energy release rates. The fatigue cohesive laws are shown in figure

			Elements in CZ n_{cz}		Steps to failure n_f	
Ga/Gc	l_{cz} [mm]	N_f[cycles]	$\Delta l = 0.005$	$\Delta l = 0.25$	$\Delta N = 100$	$\Delta N = 2500$
0.25	0.69	$3.7 \cdot 10^5$	137	2.8	3700	148
0.35	0.82	$6.1 \cdot 10^4$	164	3.3	609	24
0.45	0.95	$1.6 \cdot 10^4$	190	3.8	160	6.4
0.55	1.07	$5.5 \cdot 10^3$	214	4.3	55	2.2

Table 3.11.: Crack growth parameters for crack tip tracing strategy

3.50. They are very similar for equal mesh sizes. At lower mesh sizes, the opening displacement does not change significantly when an element becomes the crack-tip element resulting in an almost vertical drop of the traction as seen in figure 3.50

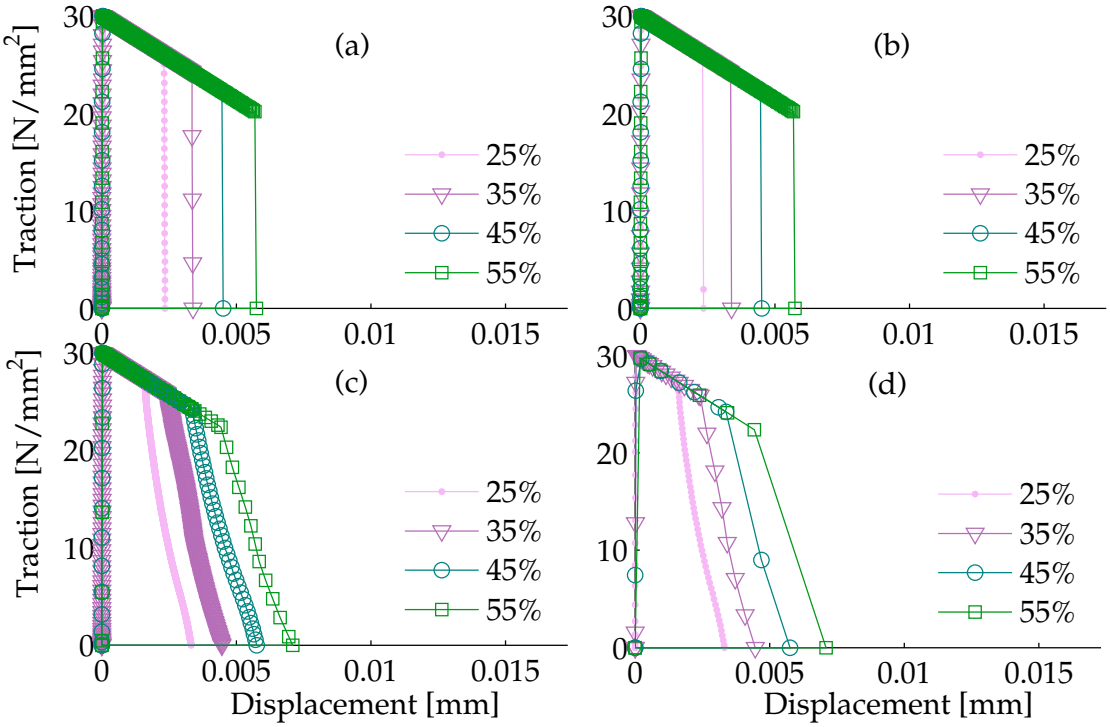


Figure 3.50.: Traction-separation curves for different percentages of G_c. (a) $\Delta l = 0.005$ mm, $\Delta N = 100$ cycles, (b) $\Delta l = 0.005$ mm $\Delta N = 2500$ cycles, (c) $\Delta l = 0.25$ mm, $\Delta N = 100$ cycles, (d) $\Delta l = 0.25$ mm, $\Delta N = 2500$ cycles

(a) and (b). For larger mesh sizes, the opening displacement continues to increase for the crack-tip element, so the slope of the fatigue cohesive law after it leaves the static curve is shallower as seen in figure 3.50 (c) and (d). If the mesh size is small (a) or the cycle-jump is large (d), the elements fail very quickly once they reach the crack-tip, so there are not many points on the fatigue cohesive law once it departs from the static law.

Figure 3.51 shows the relative error for a load level of $G_a = 0.25G_c$. The maximum cycle jump is $37,000$ cycles which means that an element fails within about 10 iterations. The maximum element size is 0.23 mm, corresponding to three elements in the cohesive zone. The maximum absolute value of the relative error is about 30% and is reached when the mesh size is quite small and the cycle-jump is large. A difference to the previous models is that the oscillations due to the number of elements in the cohesive zone are much less pronounced. The most striking feature of the plot are the diagonal waves, which are longer than in the other models and

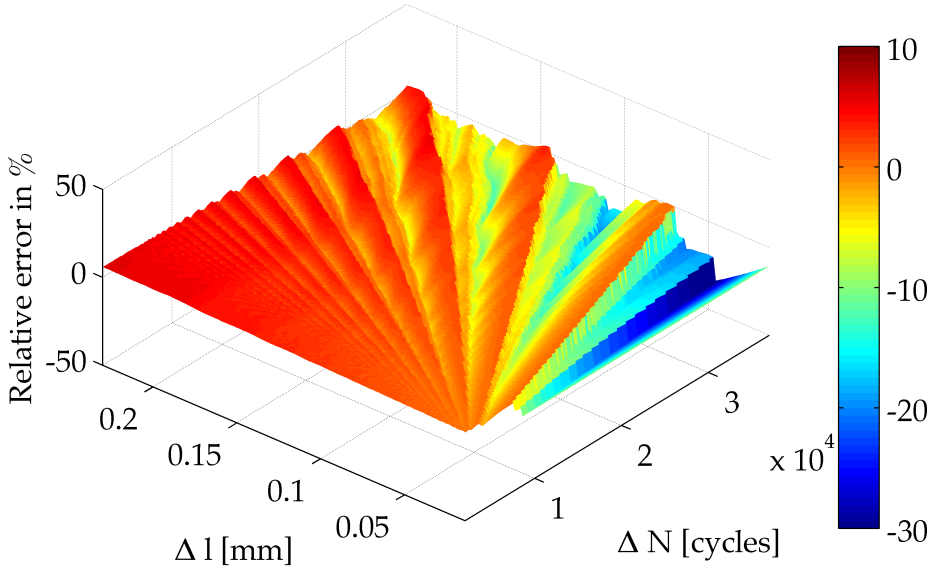


Figure 3.51.: Relative error in % of $\frac{da}{dN}$ in crack tip tracing model with respect to element size Δl and cycle jump ΔN for $G_a = 0.25G_c$

almost reach the origin. As explained earlier for the Peerlings' model, the waves' troughs mark lines of particularly good results where the ratio of element size over cycle-jump and crack growth rate is an integer

$$\frac{\frac{\Delta l}{\Delta N}}{\frac{da}{dN}} = m, m \in \mathbb{N}. \tag{3.77}$$

Figure 3.52 shows a projection of figure 3.51 onto the Δl-ΔN plane. The white lines are defined by equation (3.77) for $1 \leq m \leq 13$. They are calculated according to equation (3.77) using the input Paris law parameters $C = 0.0066$ and $m = 5.9$. For large element sizes and large cycle-jumps the original Paris law does not coincide with the local Paris law as can be observed in the Peerlings' model, so the white lines do not coincide exactly with the regions of good results.

Figure 3.53 shows a contour plot of the relative error versus the number of elements in the cohesive zone n_{cz}, where $3 < n_{cz} < 25$ and the number of steps to failure n_f, where $10 < n_f < 100$. This corresponds to 0.028 mm $< \Delta l <$ 0.23 mm and 3,700 cycles $< \Delta N <$ 37,0000 cycles. The plot shows the diagonal lines observed in figure 3.51. These create regions of slightly higher negative error when the mesh size is small and the cycle-jump is high. Figure 3.54 shows the relative error for a load level of $G_a = 0.35G_c$. The maximum cycle jump is 10,000 cycles which means

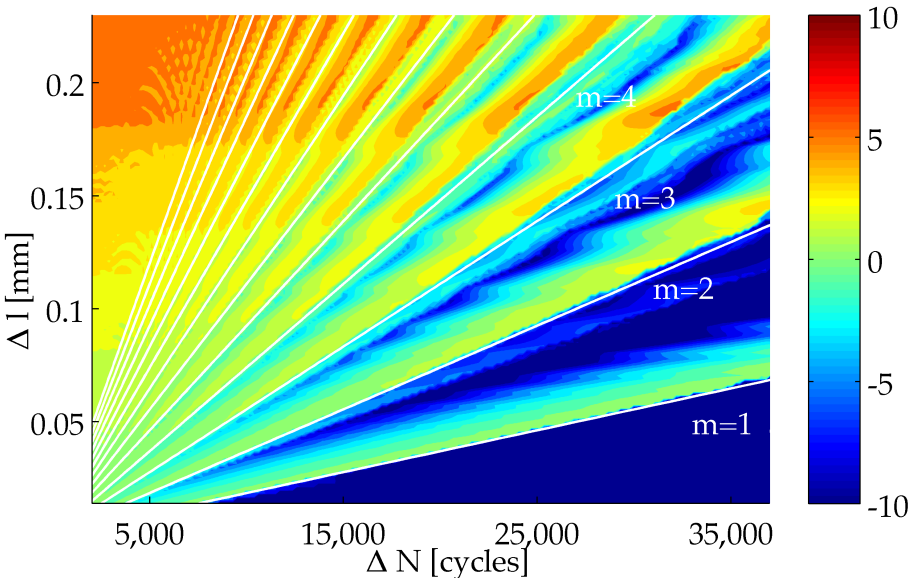


Figure 3.52.: Projection of figure 3.51 onto Δl-ΔN plane

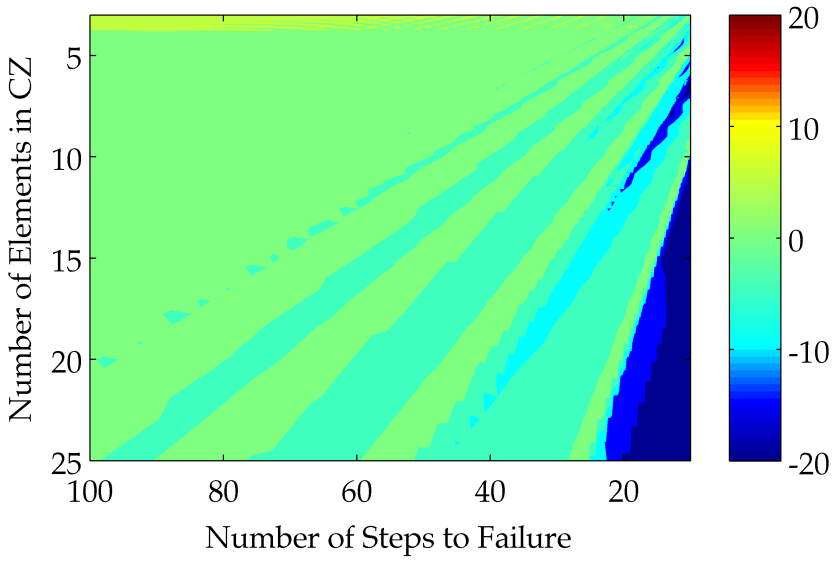


Figure 3.53.: Relative error in % of $\frac{da}{dN}$ in crack tip tracing model with respect to the number of elements in the cohesive zone and the number of cycle jumps to fail one element for $G_a = 0.25G_c$

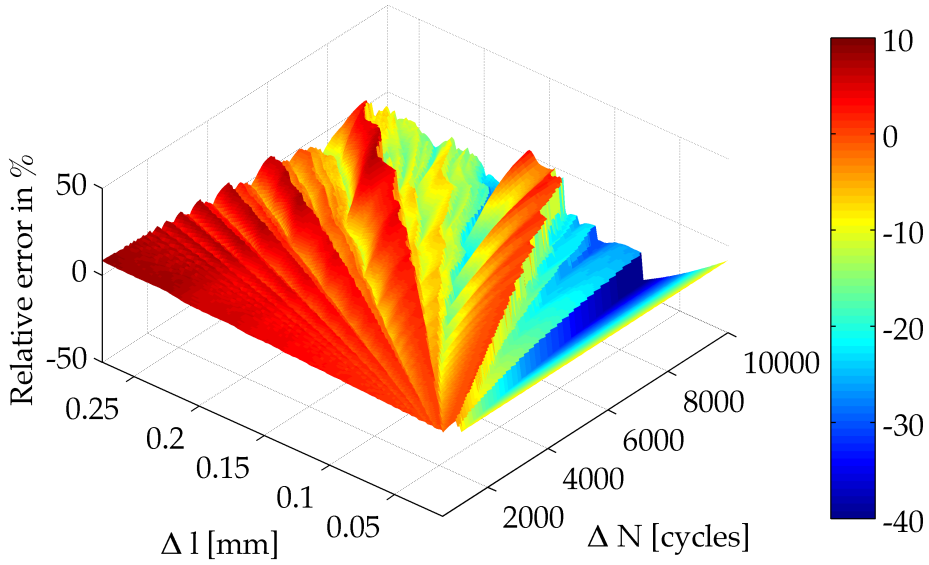


Figure 3.54.: Relative error in % of $\frac{da}{dN}$ in crack tip tracing model with respect to element size Δl and cycle jump ΔN for $G_a = 0.35G_c$

that an element fails within about 6 iterations. The maximum element size is 0.27 mm, corresponding to three elements in the cohesive zone. The maximum absolute value of the relative error is about 40% and is reached when the mesh size is quite small and the cycle-jump is large as before when $G_a = 0.25G_c$. This is the case because when failing the crack-tip element in fatigue at a small mesh-size fewer cycles are required to do so than for a larger mesh-size, so combining a large cycle-jump with a small mesh-size leads to large errors. Figure 3.55 shows a contour plot of the relative error versus the number of elements in the cohesive zone n_{cz}, where $3 < n_{cz} < 25$ and the number of steps to failure n_f, where $10 < n_f < 100$. This corresponds to 0.033 mm $< \Delta l <$ 0.27 mm and 610 cycles $< \Delta N <$ 6,100 cycles. The plot shows the diagonal lines observed in figure 3.54 and is very similar to figure 3.55. Figure 3.56 shows the relative error for a load level of $G_a = 0.45G_c$. The maximum cycle jump is 4,000 cycles which means that an element fails within about 4 iterations. The maximum element size is 0.32 mm, corresponding to three elements in the cohesive zone. The maximum absolute value of the relative error is about 40% and is reached when the mesh size is quite small and the cycle-jump is large as before for lower applied energy release rates as in the previous surface

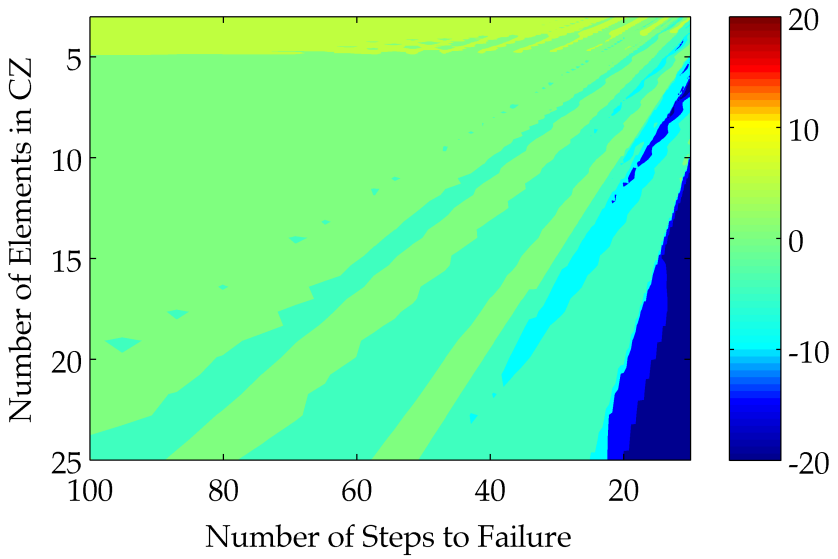


Figure 3.55.: Relative error in % of $\frac{da}{dN}$ in crack tip tracing model with respect to the number of elements in the cohesive zone and the number of cycle jumps to fail one element for $G_a = 0.35G_c$

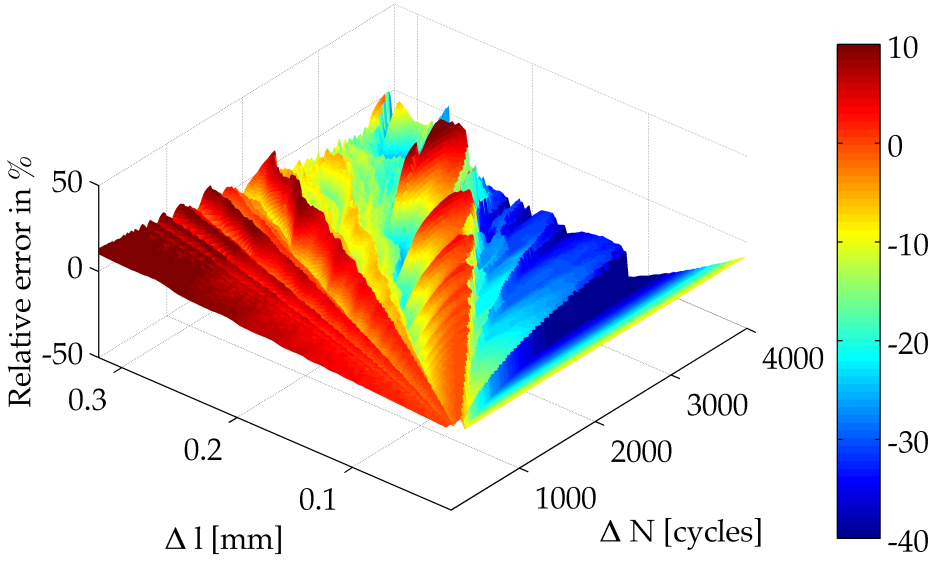


Figure 3.56.: Relative error in % of $\frac{da}{dN}$ in crack tip tracing model with respect to element size Δl and cycle jump ΔN for $G_a = 0.45G_c$

plots. Figure 3.57 shows a contour plot of the relative error versus the number of elements in the cohesive zone n_{cz}, where $3 < n_{cz} < 25$ and the number of steps to failure n_f, where $10 < n_f < 100$. This corresponds to 0.038 mm $< \Delta l <$ 0.32

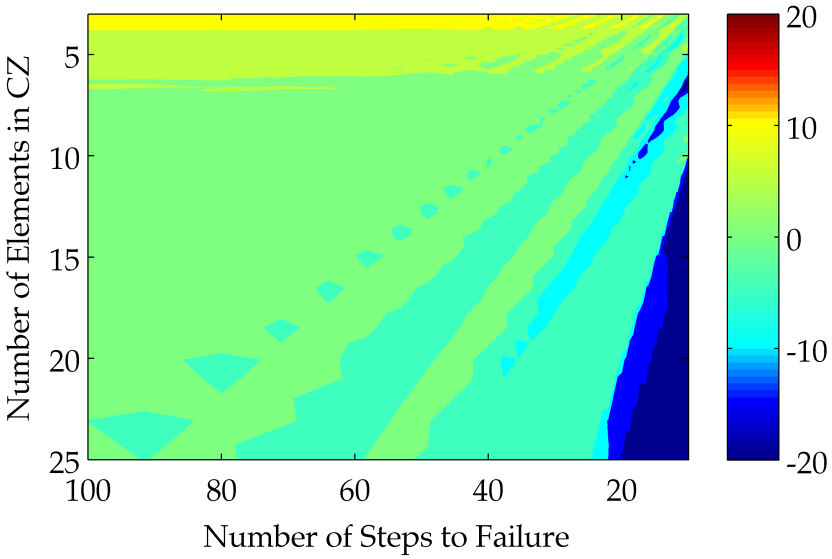


Figure 3.57.: Relative error in % of $\frac{da}{dN}$ in crack tip tracing model with respect to the number of elements in the cohesive zone and the number of cycle jumps to fail one element for $G_a = 0.45G_c$

mm and 160 cycles $< \Delta N <$ 1,600 cycles. The plot again shows the diagonal lines observed in figure 3.56 and at this load-level oscillations are occurring due to the number of elements in the cohesive zone. Figure 3.58 shows the relative error for a load level of $G_a = 0.55G_c$. The maximum cycle jump is $2,500$ cycles which means that an element fails within 2.2 iterations. The maximum element size is 0.36 mm, corresponding to three elements in the cohesive zone. The maximum absolute value of the relative error is about 50% and is reached when the mesh size is quite small and the cycle-jump is large as before for lower applied energy release rates. Figure 3.59 shows a contour plot of the relative error versus the number of elements in the cohesive zone n_{cz}, where $3 < n_{cz} < 25$ and the number of steps to failure n_f, where $10 < n_f < 100$. This corresponds to 0.042 mm $< \Delta l <$ 0.36 mm and 55 cycles $< \Delta N <$ 550 cycles. The plot again shows the diagonal lines observed in figure 3.58. Table 3.12 shows the required number of elements in the cohesive zone n_{cz}

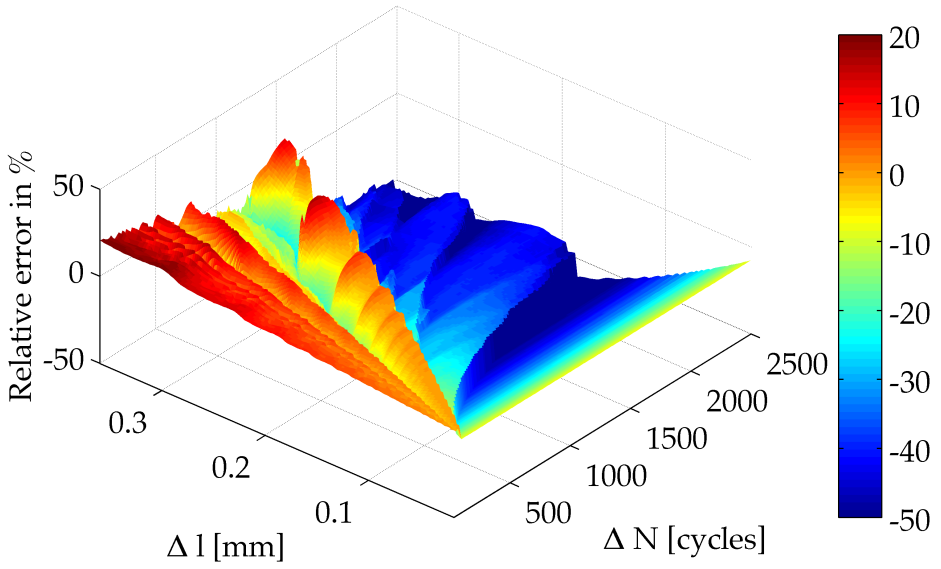


Figure 3.58.: Relative error in % of $\frac{da}{dN}$ in crack tip tracing model with respect to element size Δl and cycle jump ΔN for $G_a = 0.55G_c$

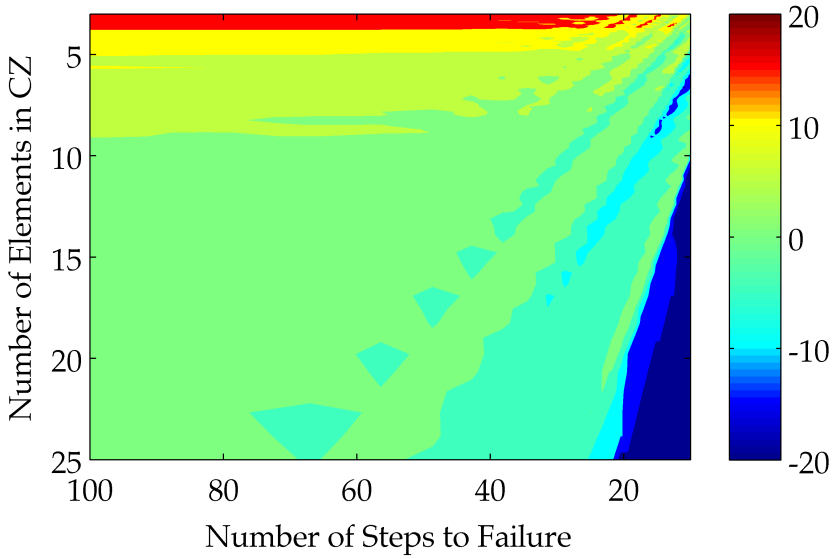


Figure 3.59.: of $\frac{da}{dN}$ in crack tip tracing model with respect to the number of elements in the cohesive zone and the number of cycle jumps to fail one element for $G_a = 0.55G_c$

and the number of steps to failure n_f, so that the relative error in absolute value is below 10% and 20 % respectively.

	$\|e_r\|$<10%		$\|e_r\|$<20%	
Ga/Gc	$n_{cz}>(\Delta l<)$	$n_f>(\Delta N<)$	$n_{cz}>(\Delta l<)$	$n_f>(\Delta N<)$
0.25	3 (0.23)	40 (9,300)	3 (0.23)	25 (14,800)
0.35	3 (0.27)	40 (1,525)	3 (0.27)	20 (3,050)
0.45	5 (0.19)	40 (640)	3 (0.32)	20 (320)
0.55	6 (0.18)	30 (185)	5 (0.21)	20 (275)

Table 3.12.: Minimum values for $n_f(\Delta N)$ and $n_{cz}(\Delta l)$ with respect to the relative errors in $\frac{da}{dN}$. Δl in [mm], ΔN in cycles

3.6.3. Summary and Discussion for the Kawashita-Hallett model

The crack-tip-tracing model is the only model which isolates fatigue purely to the crack tip. This has the disadvantage of needing an algorithm to keep track of the location of the crack front, which is not straight-forward when using a commercial FE package. On the other hand, the model is the fastest of the four models examined and it also predicts the Paris law the most accurately. Another advantage of the crack-tip tracing algorithm is that the model can deal with general 3D delamination. The sensitivity study has shown that care has to be taken when refining the mesh, because this leads to a large drop in accuracy if the cycle-jump is not adjusted accordingly. However, in an explicit FE formulation, where the strategy has originally been implemented this is not a problem because the time step will be chosen to be small due to the simulation.

3.7. Comparison of the investigated degradation strategies and Conclusion

In the previous chapter, four cycle-jump models for high-cycle fatigue delamination were examined in detail in mode I using a rapid non-FE model called the cylinder

model. The detailed analysis was able to reveal a more detailed picture of the performance of these strategies. It was shown that in order to accurately assess the performance, it is necessary to plot the relative error on a linear plot rather than on a log-log plot, which is the common method. Table 3.13 shows the input parameters and whether the models are point-local. The experimental data, the numerical Paris

Model	Input Parameters	Point-local
Peerlings'	α, β, λ, μ_1 , and μ_2	yes
Turon	m, C, l_{cz}	no
Harper	m,C, L_{cz}	yes
Hallett	m,C	no

Table 3.13.: Comparison of strategies I: input parameters and point-localness

law and the four model Paris law for fine mesh-size and cycle-jump are shown in figure 3.60. The relative error with respect to the calibrated Paris law is shown in

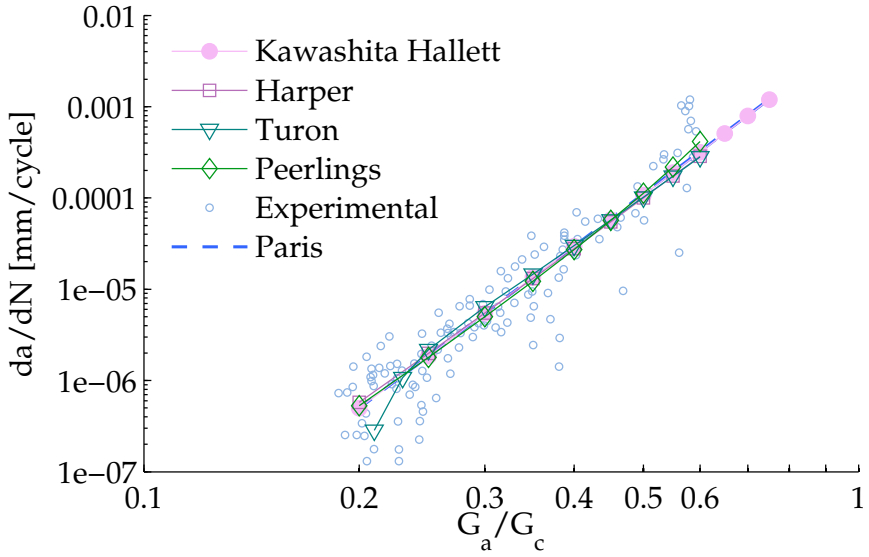


Figure 3.60.: Paris laws for $\Delta l = 0.005mm$ and $\Delta N = 100cycles/\Delta D = 0.00005$

figure 3.61. All four models have advantages and drawbacks. The Peerlings' model which has been examined first is point-local and predicts the Paris law accurately as long as the energy release rate is not too high. However, the input parameters have to be calibrated first to fit a specific Paris law. Also, the fatigue damage has

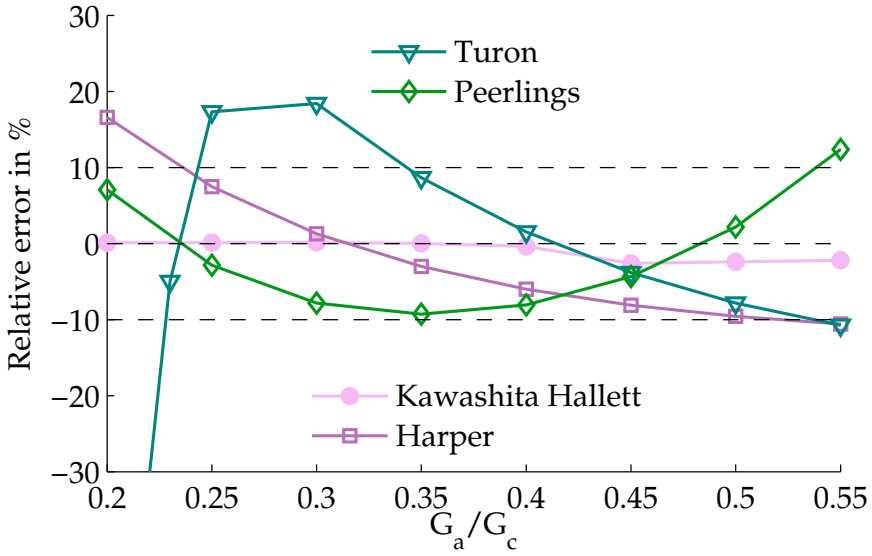


Figure 3.61.: Relative error vs. G_a for $\Delta l = 0.005$ mm and $\Delta N = 100$ cycles/$\Delta D = 0.00005$

to be found through an iterative process at every step, which makes this model the slowest. Fatigue degradation takes place in the whole cohesive zone and no information has to be exchanged between the elements during the analysis.

The Turon model on the other hand has as model input the Paris law and the cohesive zone length. It is faster than the Peerlings' model and it is the only model where the cycle-jump is adapted during an analysis for changing load-levels. If the energy release rate changes significantly during an analysis then using a maximum damage increment ΔD rather than a fixed cycle-jump ΔN is preferable. On the other hand, the maximum damage rate has to be compared at each step between all the elements (see equation), thus requiring information exchange between the elements. The model is therefore not point-local. However, it is not necessary for an element to know its position in the cohesive zone. While Turon was the only one to adapt the cycle-jump using an auxiliary variable, this adaptation is not inherent to the fatigue degradation and could be implemented into other strategies as well. On the other hand, the Turon model could be made point-local by using a fixed cycle-jump ΔN. Another problem with the Turon model is that the Paris law exponent could not be accurately reproduced and when the actual cohesive zone

length l_{cz} was used it had to adjusted to fit the input Paris law.
The model by Paul Harper is point-local thus requiring no exchange of information between the elements making it easy to implement into commercial FE software. As with the Turon model, the Paris law exponent could not be accurately reproduced. This remained the case even when the ratio of fatigue length to total cohesive zone length -one of the two model inputs along with the Paris law- was adjusted. Another problem with this model is the estimation of the cohesive zone length under fatigue as a fraction of the static cohesive zone length.
The model by Kawashita and Hallett has as input only the Paris law and thus requires the least input data of the four models. It also has the lowest error rates and is very fast. Caution has to be taken not to combine a fine mesh with a high cycle-jump as this can cause a much higher error. This is due to the fact that fatigue crack-growth takes place only in the crack-tip element and the smaller the element-size, the less cycles it takes for the crack-tip element to fail at a constant G_a, so ΔN needs to be adjusted. The model was originally implemented explicitly, where the time step is small so in its original implementation this is not a great drawback. The model is also not point-local because it requires an algorithm that keeps track of the crack-tip element and the current applied energy release rate G_a needs to be exchanged between the cohesive elements. However, this crack-tip tracing algorithm allows for the analysis of full 3D general crack cases.
The advantages and disadvantages of all the models are summarised in table 3.14. In order to give an indication of how the models compare in terms of speed, the CPU time in seconds is given in brackets for the simulation of 4,000,000 cycles with a mesh size of $\Delta l = 0.005$ mm and $\Delta N = 100$ cycles ($\Delta D = 0.00005$ for the Turon model) at a load level of $G_a = 0.25 G_c$. The models have been run in Matlab with a 2.3 GHz quad-core Intel Core i7 processor. The comparison shows that the Turon and the Kawashita/Hallett model have the same order of magnitude in terms of runtime while the Harper model is one order of magnitude slower and the Peerlings' model is two orders of magnitude slower than the fastest two.

Model	Advantages	Disadvantages
Peerlings'	+ errors for calibrated model are less than 10%	-calibration necessary
	+ point-local	-slow (230 s)
Turon	+ fast (1.7 s)	- cohesive zone length l_{cz} needed
	+ cycle-jump adapts to load level (ΔD)	- Paris law exponent is 7% too low ($m = 5.5$)
	+ able to model part I of Paris law	- information exchange required
Harper	+ fast (18.8 s)	- cohesive zone length ratio needed
	+ point-local	- Paris law exponent is 4% too low ($m = 5.65$)
Hallett	+ only input required $\frac{da}{dN}$	- information exchange required
	+ fast (1.03 s)	- inaccurate for fine mesh & high cycle-jump

Table 3.14.: Comparison of strategies II: advantages and disadvantages

4. Improvements to existing fatigue strategies and a new model

The last chapter provided a detailed overview of four cycle-jump fatigue degradation strategies. All the models discussed have some disadvantage and this chapter discusses possible solutions to solve or at least improve the existing issues for some of the models. These are discussed in the first section. The improvement made to the Peerlings' model addresses its high run time but also results in a sacrifice with respect to the accuracy. Changing the calculation of the energy release rate G_a in the Turon model improves its accuracy but the cohesive zone length still essentially remains a fitting parameter. No improvement is being made to the Harper model and the Kawashita/Hallett model which is very accurate for small time-steps but becomes inaccurate for an implicit implementation with high time steps. It is therefore still desirable to develop a new model. Some of the unsuccessful attempts that have been explored over the course of the PhD are presented. This exploration led to defining the necessary fundamental conditions for an accurate fatigue degradation strategy which are subsequently outlined. Based on these conditions, the new fatigue model is introduced which does not require calibration or a knowledge of the crack-tip location but needs only the Paris law as input. A sensitivity study is carried out and it is shown that this model is able to predict the Paris law accurately and will be implemented into a Finite element model in the next chapter.

4.1. Improving existing strategies

4.1.1. Two faster alternatives to the Peerlings' model

The Peerlings' model has two major disadvantages. One of them is its speed due to the fact that in order to calculate the fatigue damage for each integration point at each time increment, an implicit equation has to be solved iteratively. The second one is the number of model parameters that need to be calibrated when carrying out an analysis. This can only be done with an extensive parameter study and the parameters need to be recalibrated for each change in the model, for example when changing the initial stiffness K of the static constitutive law, which is a parameter that may need adjustment for numerical reasons only. This section addresses both issues. In the first part a simplification is presented, which does not significantly change the performance on the model, but results in a much faster analysis. In the second part an alternative formulation is presented, which requires fewer parameters to be calibrated.

Speeding up the Peerlings' model

The main change that can be made to speed up the Peerlings' model is to eliminate the process of solving equation 3.20 iteratively. This is achieved by setting the parameter μ_1 in equation 3.19 equal to 0. In this way the damage at $N + \Delta N$ cycles remains only on the left-hand-side of equation 3.20, so the new damage $D(N + \Delta N)$ is calculated directly as follows

$$D(N + \Delta N) = D(N) + \Delta D_s + \Delta N \frac{A}{1+\beta} e^{\lambda D(N)} \left(\frac{\delta_{\mu_2}}{\delta_c} \right)^{1+\beta}. \tag{4.1}$$

The influence of the parameters μ_1 and μ_2 on the Paris law is shown in figures 4.1 and 4.2 for an element size $\Delta l = 0.01$ mm and cycle-jump $\Delta N = 100$ cycles.

Figure 4.1 shows the numerically predicted Paris law for four different values of μ_1, where $\mu_2 = 0.7$ and figure 4.2 shows the numerically predicted Paris law for four different values of μ_2 where $\mu_1 = 0.7$. Changing the value of μ_1 does not influence the numerical Paris law, while changing the value of μ_2 changes the Paris law for higher values of G_a. The maximum difference occurs for $G_a = 0.55 G_c$. The

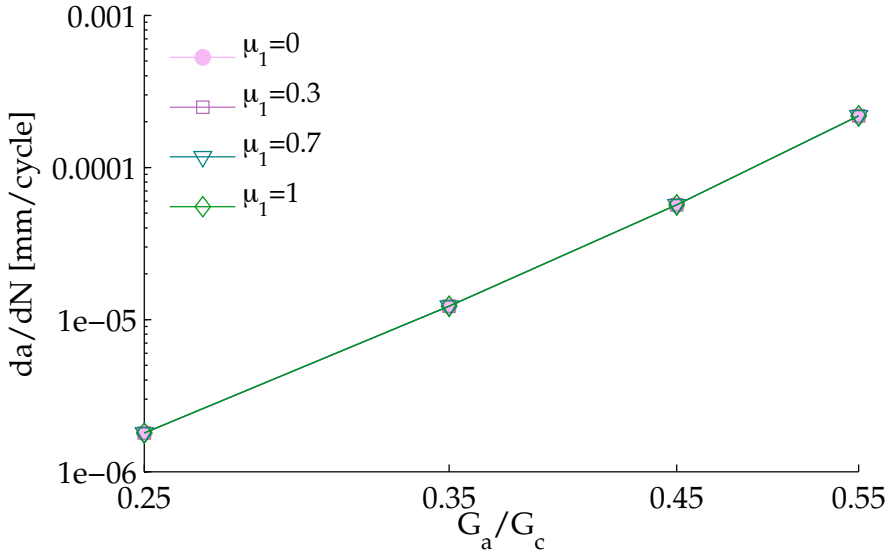


Figure 4.1.: Numerical paris law showing the influence of μ_1 for $\mu_2 = 0.7$

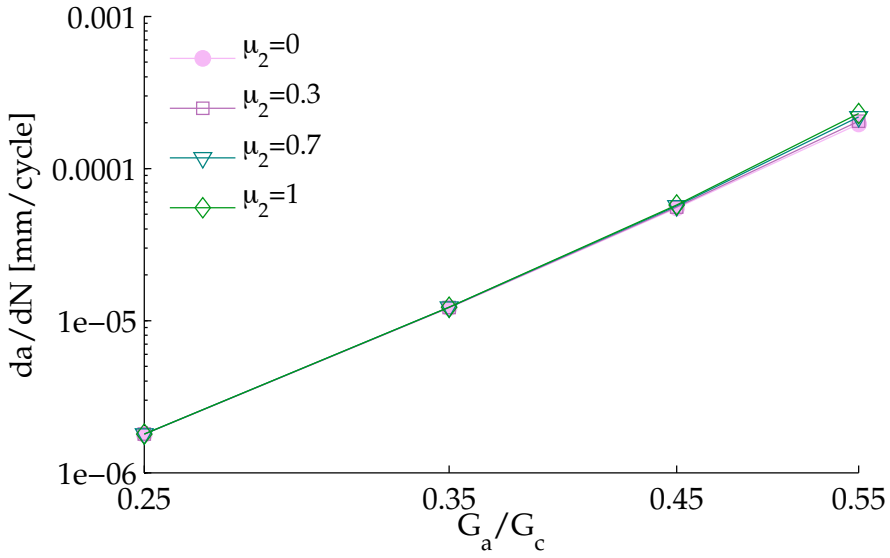


Figure 4.2.: Numerical paris law showing the influence of μ_2 for $\mu_1 = 0.7$

difference between the two numerical Paris laws where $\mu_2 = 0$ and $\mu_2 = 1$ is 17% of the calibrated Paris law value. It has been noted at the beginning of the last chapter that an analysis of the Peerlings' model has been carried out by Lopez Armas [Arm08], where different damage formulations were examined with the result that there is no significant advantage of any one damage formulation. The static damage

concept adopted here is the stiffness-based damage

$$D_s = \frac{\delta_c(\delta - \delta_0)}{\delta(\delta_c - \delta_0)}. \tag{4.2}$$

Since the initial stiffness K is usually chosen to be a large number, the stiffness-based damage increases rapidly with the displacement as shown in figure 4.3. The

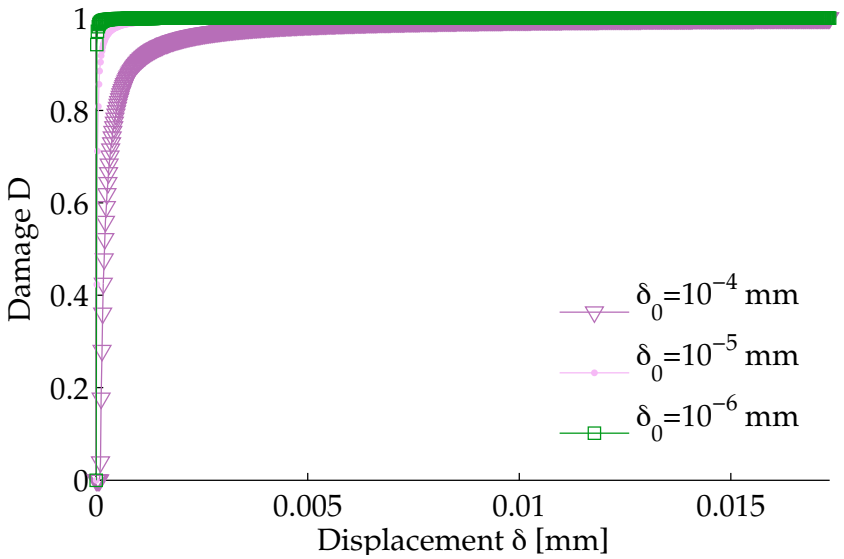


Figure 4.3.: Static damage vs displacement

figure shows that the damage increases very rapidly for small displacements δ and then grows more slowly and that the total damage is heavily influenced by the magnitude of the static damage, which explains why the choice of μ_1 and does not influence the results very much.

The difference in relative error between the implicit formulation, where $\mu_1 = 0.7$ and the explicit formulation, where $\mu_1 = 0$ is shown in figure 4.4 for an energy release rate $G_a = 0.25G_c$ with respect to the number of steps it takes to fail one element and the number of elements in the cohesive zone. The figure shows that there is no difference in error apart from along the radial lines discussed earlier, but along these lines the difference remains below 1%. The speed in seconds for the implicit damage is shown in figure 4.5 with respect the number of steps it takes to fail one element and the number of elements in the cohesive zone. The time shown is for the simulation of 2,000,000 cycles. Figure 4.6 shows the speed in seconds for the explicit damage again for the simulation of 2,000,000 cycles. The figures show

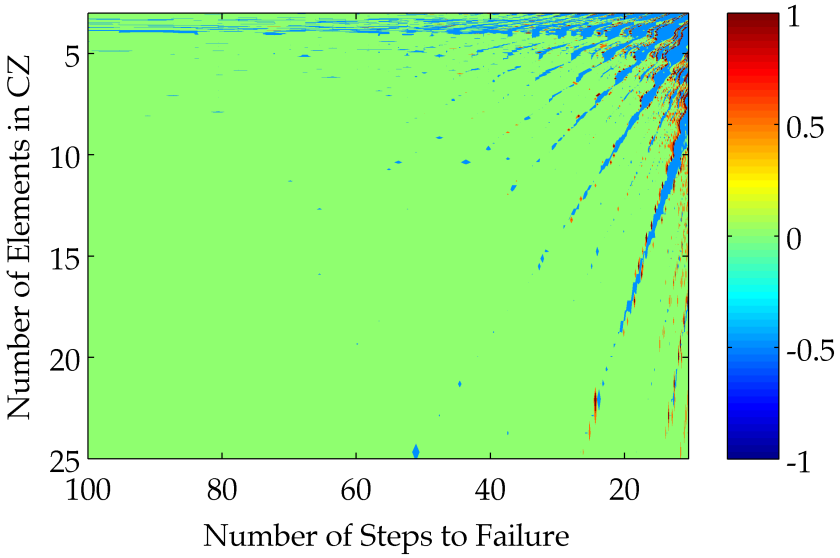


Figure 4.4.: Difference in relative error between explicit and implicit damage for $G_a = 0.25G_c$

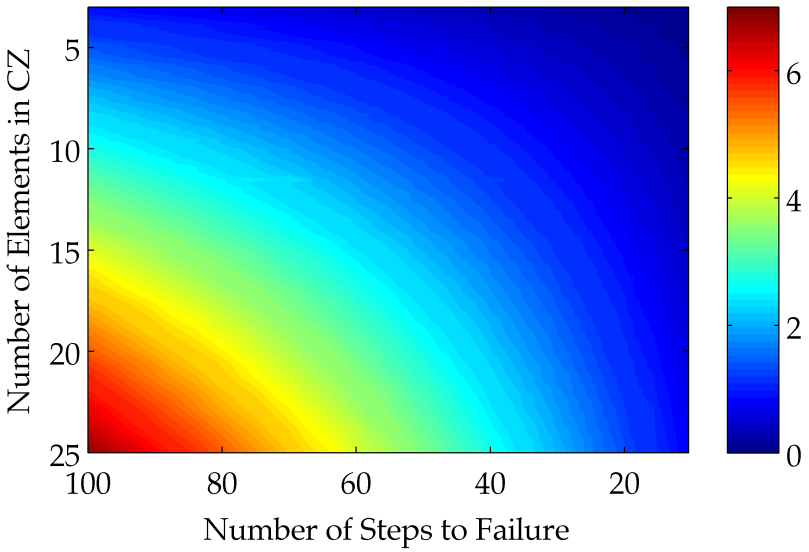


Figure 4.5.: Speed in s to simulate 2,000,000 cycles, implicit damage for $G_a = 0.25G_c$

that calculating the damage explicitly speeds up the algorithm by a factor of 20, while preserving the numerical accuracy.

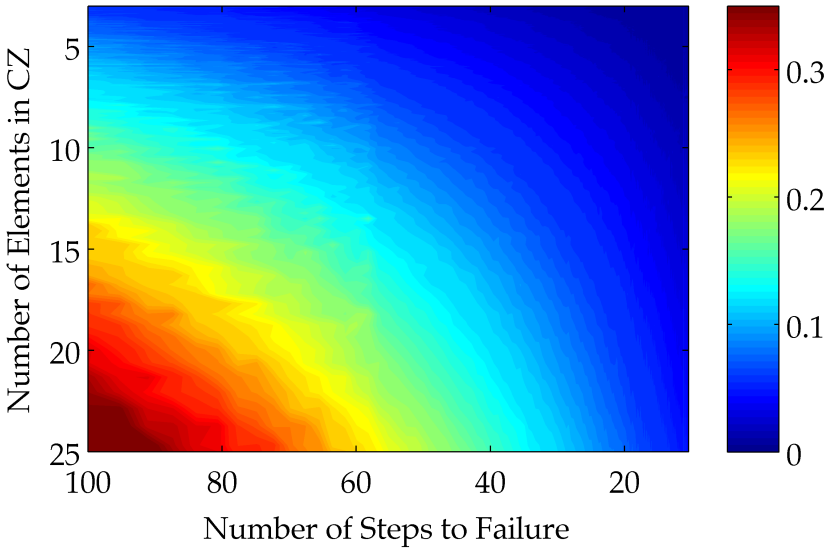


Figure 4.6.: Speed in s to simulate 2,000,000 cycles, explicit damage for $G_a = 0.25G_c$

A model with less calibration

The other drawback of the Peerlings' model is the necessity to calibrate 5 fatigue parameters, which requires a time-consuming parameter study. In the following subsection a simplified model is suggested which only has two fatigue parameters and a similar performance to the original Peerlings' model. Static damage is calculated according to equation (4.2) and the fatigue damage evolution is

$$\frac{dD_f}{dN} = A \cdot \delta(N)^B, \tag{4.3}$$

where A and B are constants that need to be calibrated. The change in fatigue damage from N cycled to $N + \Delta N$ cycles is approximated as follows

$$\Delta D_f = \Delta N \cdot A \cdot \delta(N)^B, \tag{4.4}$$

so the damage after one cycle-jump ΔN is

$$D(N + \Delta N) = D(N) + \frac{\delta_0 \delta_c}{\delta_c - \delta_0} \left(\frac{1}{\delta(N)} - \frac{1}{\delta(N + \Delta N)} \right) + \Delta D_f. \tag{4.5}$$

The calibrated constants using the same static constitutive law as previously are shown in table 4.1. Figure 4.7 shows a comparison of the numerical crack growth rates and the Paris law. The figure shows that for a high-cycle-jump the model is

$A = 160$	$B = 3.5$

Table 4.1.: Input parameters

not accurate, as is the case for the other models examined. The Paris law is underestimated for higher energy release rates and high cycle-jumps, because when approximating the fatigue damage increment ΔD_f, the displacement used is the displacement at N cycles, so for a large change in displacement this approximation becomes less accurate. Figure 4.8 shows the relative error with respect to the Paris

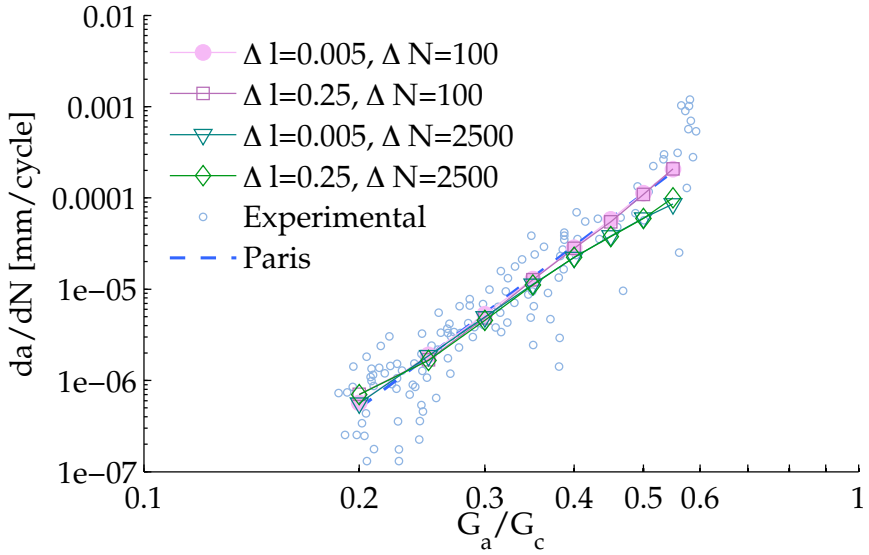


Figure 4.7.: Experimental data, paris law, and fast Peerlings' model crack growth rates for different element sizes and cycle jumps. Δl in mm, ΔN in cycles

law. As in the original Peerlings' model the error is within 10% for low cycle-jumps, but becomes large for large cycle-jumps and high energy release rates. Figure 4.9 and 4.10 show the sensitivity of the model with respect to the number of elements in the cohesive zone and the number of steps it takes to completely fail one element from the point of it entering the cohesive zone for two different values of G_a. The two figures show similar characteristics to that of the original Peerlings' model with the relative error having a similar magnitude. However, the diagonal bands are less pronounced and while the relative error in the original Peerlings' model is positive, the error in this model is negative, so the crack growth rate is underestimated. This

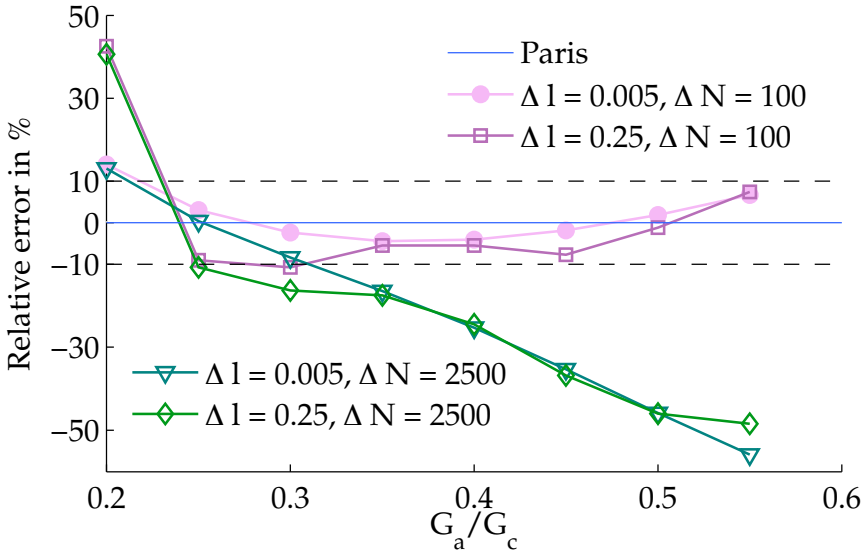


Figure 4.8.: Relative error in % in crack growth rate $\frac{da}{dN}$ for different mesh sizes and cycle-jumps. Δl in mm, ΔN in cycles

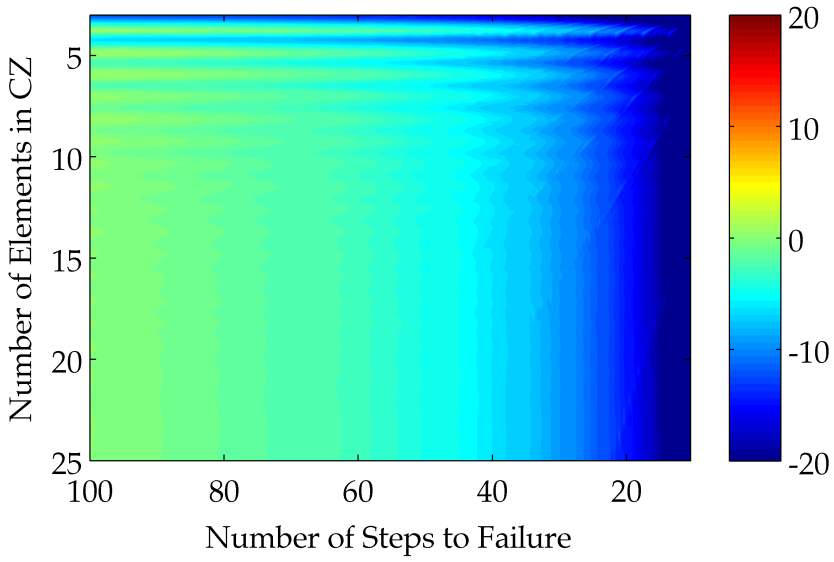


Figure 4.9.: Relative error in % of $\frac{da}{dN}$ in with respect to the number of elements in the cohesive zone and the number of cycle jumps to fail one element for $G_a = 0.25G_c$

is due to the approximation of the fatigue damage using the displacement at N cycles rather than at an intermediate value between N and ΔN cycles as is the case with the original model.

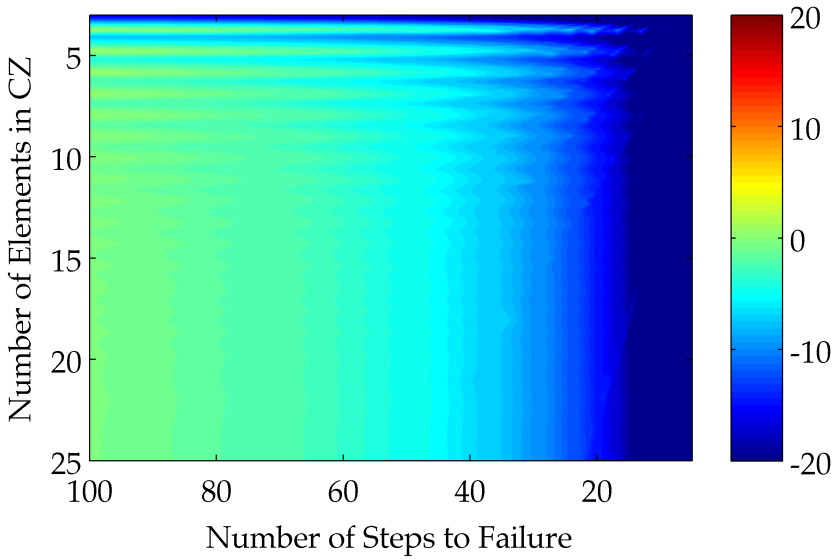


Figure 4.10.: Relative error in % of $\frac{da}{dN}$ with respect to the number of elements in the cohesive zone and the number of cycle jumps to fail one element for $G_a = 0.55G_c$

Conclusion

Using the stiffness-based damage, it is possible to speed up the Peerlings' model by calculating the damage explicitly. This makes the model about 20 times faster with the difference in relative error between the explicit and implicit calculation being less than 1%. Secondly, a simplified Peerlings' model was suggested which reduces the number of parameters to be calibrated from 5 to 2. It has been shown that this modified fatigue degradation strategy has a similar accuracy to the original model but the necessary parameter study is much less time-consuming. However, the model performs badly for high cycle-jumps and high energy release rates as shown in figure 4.8

4.1.2. Improved Paris law for the Turon model

In the original formulation by Turon an analytical equation was used to approximate the length of the cohesive zone (equation (3.33)). This equation is a variation of the following more general equation to predict the cohesive zone length l_{cz}

$$l_{cz} = ME\frac{G_c}{\sigma_0^2}, \tag{4.6}$$

where M is a model dependent factor. A comparison of commonly used models has been presented by Turon et al [TDCC05] where $0.21 < M < 1$, so there is a considerable difference in the predicted cohesive zone length l_{cz}. In the cylinder model the actual cohesive zone length has been used, however this did not lead to an accurate prediction of the input Paris law, so the cohesive zone had to multiplied by a factor. This suggests that the cohesive zone length has to be treated as a modelling parameter which needs to be adjusted. But even when the cohesive zone length is adjusted, the model still does not predict the Paris law correctly. One other prob-

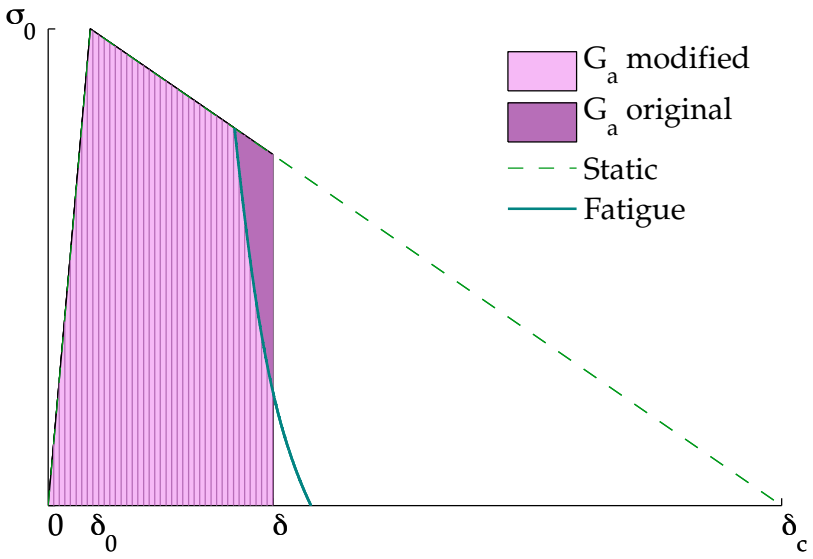


Figure 4.11.: Calculation of G_a for equation (3.44)

lem with the original model is the calculation of the applied energy release rate G_a, which is required in order to calculate the crack growth rate according to equation (3.44). G_a is calculated as the area under the static constitutive law. However, since the constitutive law changes under fatigue this will lead to an incorrect energy release rate. In order to improve the accuracy of the model, the energy release rate

should be calculated as the area under the actual fatigue law as shown in figure 4.11. Calculating the energy release rate like this leads to an improved prediction of the Paris law which is shown in figure 4.12. The relative error versus the applied

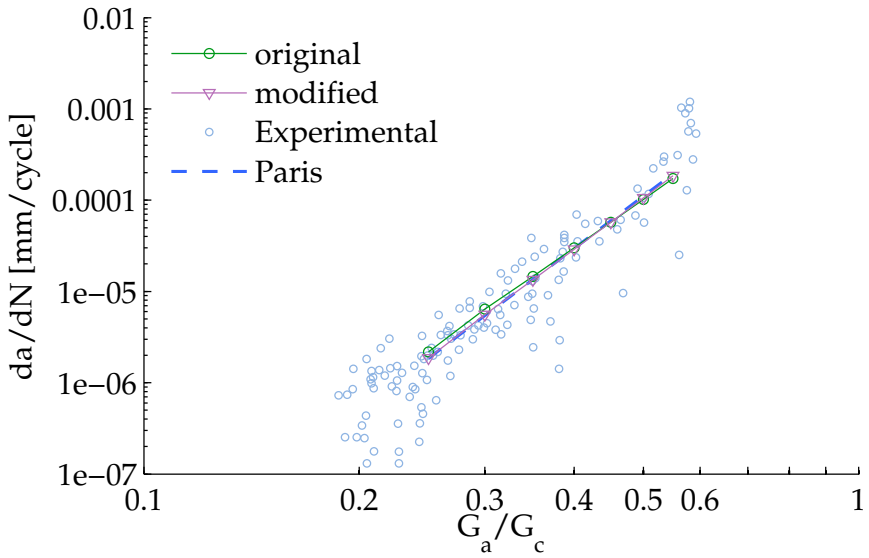


Figure 4.12.: Experimental Paris law and numerical Paris law from Turon model

energy release rate with respect to the input Paris law is shown in figure 4.13. The

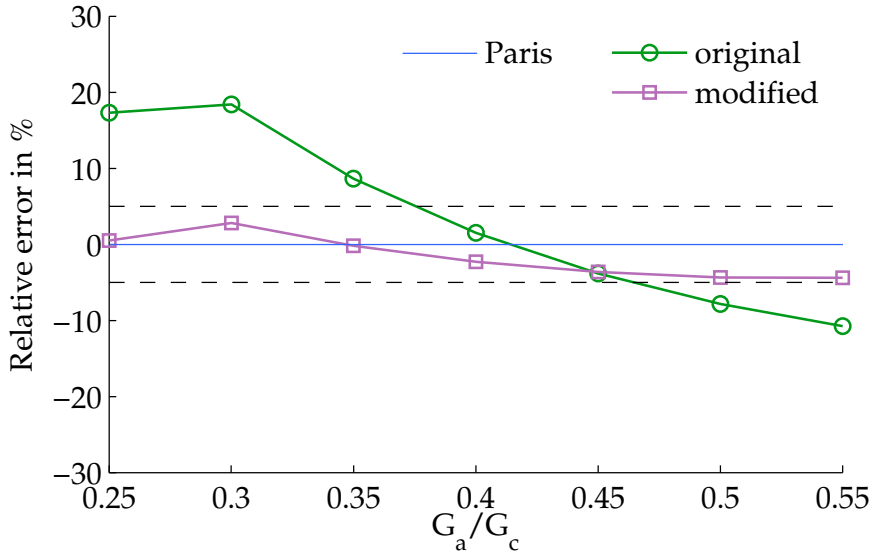


Figure 4.13.: Relative error in % of $\frac{da}{dN}$ with respect to input Paris law in Turon model

figure shows that the relative error still exhibits the same characteristics, so the ex-

ponent of the Paris law is still slightly too low, however the error is much lower and remains below 5% for the whole range of energy release rates.

Conclusion

It has been shown in the previous chapter that using the actual cohesive zone length does not lead to an accurate prediction of the crack growth rate in case of the cylinder model. Therefore, a fraction of the actual cohesive zone length was used to get a good agreement with the input Paris law introducing an extra parameter that needs to be calibrated. This modification leads to a numerical Paris law with a slightly too low exponent m. It has been shown in the previous section that this issue can be corrected by calculating the energy release rate G_a as the actual area under the fatigue traction-separation response rather than the static constitutive law. For a low element size and cycle-jump ($\Delta l = 0.01$ mm and $\Delta D = 0.00005$) this leads to a reduction in the maximum relative error from 20% to 4%.

4.2. Development and evaluation of a new strategy for fatigue-driven delamination growth

4.2.1. Unsuccessful modelling attempts

One of the great advantages of the cylinder model is, that it is relatively straightforward to implement and test possible fatigue-degradation strategies with it. Over the course of the PhD, many potential methods for the development of a new fatigue degradation strategy have therefore been explored. Two of them are outlined in the following paragraphs.

The previous chapter showed that the traction-separation curve is not fixed but depends on the fatigue degradation strategy. Therefore, a possible new fatigue degradation model could be developed with a prescribed traction-separation response where the area under the curve is G_a. A route like this is taken by Harper and Kawashite/Hallett in their models. Both of them are based on the ideal of a fatigue degradation strategy where static and fatigue degradation take place sequentially. First the elements degrade statically, following the static constitutive law and then once fatigue sets in the elements are meant to fail in fatigue only, causing a vertical drop in the constitutive law. In effect this means prescribing a traction-separation response like the one shown in figure 3.46 (a). In the Harper model, the unwanted fatigue damage accumulating during the static degradation has to be balanced with an extra damage variable, which is shown to not work very well in the cylinder model. In the Kawashita/Hallet model fatigue only takes place when an element is at the crack tip. In this way the element does not accumulate any fatigue damage while it moves through the cohesive zone until it reaches the crack tip where the additional displacement it experiences does not cause much additional static damage resulting in an almost vertical drop. In the cylinder model, trying to prescribe the fatigue constitutive law for example in a trapezoidal form as just discussed or a polynomial or exponential function was not successful because it did not lead to equilibrium.

A less rigid way of trying to ensure that the elements fail at the correct rate is to divide the area G_a under the unknown traction-separation response by the num-

ber of steps it takes to fail one element and degrade the elements so that this area is always constant as shown in figure 4.14. The new cohesive traction can then be

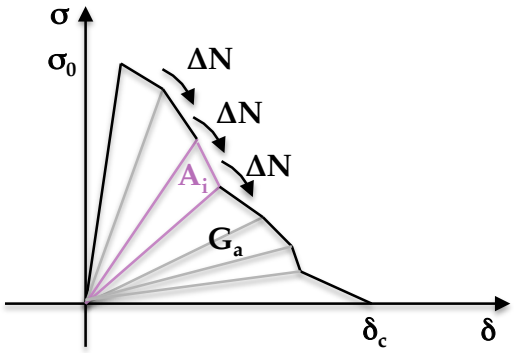


Figure 4.14.: Traction-separation response with equal area absorption

determined for example by specifying that A_i is bounded by a triangular area.
There are two fundamental problems that have occurred with these strategies. In the last case of specifying the area it was not always possible to find the moment equilibrium after each cycle-jump so the model did not converge. In the former case, where the constitutive law was specified the problems occur when the applied energy release rate changes because this will change the shape of the constitutive law, so the elements have to follow different traction-displacement curves. This happens for example at the start of the analysis when the elements follow the static constitutive law until the analysis reaches the steady-state.
Looking at these failed attempts it becomes clear that it is important to define the necessary conditions any successful fatigue degradation strategy has to satisfy. These are outlined in the next three subsections.

4.2.2. Input data from the Paris law

Since they are all based on fracture mechanics, the Paris law

$$\frac{da}{dN} = C \cdot \left(\frac{G_a}{G_c}\right)^m, \tag{4.7}$$

forms an experimental basis for all analytical models discussed in the previous chapter and also for the model in this chapter and the Paris law parameters are a direct or indirect input value for each of the fatigue degradation strategies.

4.2.3. The constitutive response of the cohesive zone in fatigue

The basis of any fatigue degradation strategy for a cohesive zone model of delamination is the static constitutive law, which is determined by the initial stiffness K, the peak traction σ_0, and the fracture toughness G_c. Various shapes for the static constitutive law have been discussed earlier. As for the static behaviour a cohesive zone develops ahead of the crack tip. The length l_{cz} of this zone will not be the same as for the static case and is initially unknown as it depends on the opening displacement in the cohesive zone, as well as the final displacement δ_f at which the elements break under fatigue loading, which is also initially unknown. In all the models discussed in the previous chapter, the simulation is carried out in two steps: first a quasi-static load is applied with the elements obeying the static traction-displacement response. Once this static equilibrium is found, blocks of loading cycles are applied leading to a degradation and eventual failure of the interface elements ideally within the correct number of cycles that the Paris law specifies. This leads to a new constitutive response. The shape is determined by the fatigue model, and the load-level. In the steady state, the integral under the constitutive response has to be equal to the applied energy release rate G_a, so

$$\int_0^{\delta_f} \sigma(\delta) d\delta = G_a. \tag{4.8}$$

For simple cases, for example in the cylinder model, G_a will be known before commencing the analysis but in general this will not be the case.

4.2.4. The link between cycles to fail an element and the delamination growth rate

Let the number of cycles it takes to completely fail one element in the steady state be N_f. This will also be the number of cycles it takes for one element to progress from the tip of the cohesive zone to the crack front. That means that while one element undergoes the complete failure process, the crack front will move forward by the length of the cohesive zone l_{cz} and N_f is therefore related to the Paris law in

the following way

$$N_f = \frac{l_{cz}}{\frac{da}{dN}(G_a)} = \frac{l_{cz}}{C\left(\frac{G_a}{G_c}\right)^m}. \tag{4.9}$$

Equations (4.8) and (4.9) are the fundamental equations guiding any fatigue process based on the Paris law and have to be fulfilled in order to get accurate crack growth. They play a key-part in the proposed strategy presented in the next subsection.

4.2.5. Description of proposed model

Input:	$\frac{da}{dN}$
Point-local:	No

This derivation is for the mode I degradation. For mode II the fatigue degradation is performed very similarly, but the damage has to be calculated with the absolute value of the relative displacement. Due to the cohesive zone length l_{cz} and the final displacement (see below) being extracted during the analysis, the model predicts the crack-growth correctly once it reaches the steady state. A bilinear constitutive law (see figure 2.37 and equation 2.46) is used for the static cohesive response. The static damage used in this model is the stiffness-based damage, which is also applied in the Peerlings' and the Turon model. The traction can then be expressed as

$$\sigma(\delta) = (1 - D_s)K\delta\,, \tag{4.10}$$

where $K = \frac{\sigma_0}{\delta_0}$. The damage is 0 before reaching the maximum traction σ_0, and increases to 1, when the displacement is greater than the critical displacement δ_c. For displacements $\delta_0 < \delta < \delta_c$, the damage is

$$D_s = \frac{\delta_c(\delta - \delta_0)}{\delta(\delta_c - \delta_0)} \tag{4.11}$$

as shown in figure 3.2. The fatigue damage rate is calculated by first calculating the final static damage $D_{s,t}$, which is the amount of static damage acquired by an element at the point of failure of that element. $D_{s,t}$ can be calculated from the opening displacement at which the element fails δ_f. This is taken to be the current displacement of the crack tip element. Choosing δ_f like this introduces a small error, since

the crack tip element has not failed yet, but the sensitivity study below shows that this error does not influence the results significantly. The total amount of static damage $D_{s,t}$ is then

$$D_{s,t} = \frac{\delta_c(\delta_f - \delta_0)}{\delta_f(\delta_c - \delta_0)}. \tag{4.12}$$

The total number of cycles N_f it takes to fail one initially undamaged cohesive element is the same number of cycles it takes for the crack to grow by the length of the cohesive zone l_{cz}. Therefore

$$N_f = \frac{l_{cz}}{\frac{da}{dN}}, \tag{4.13}$$

where

$$\frac{da}{dN} = C\left(\frac{G_a}{G_c}\right)^m, \tag{4.14}$$

according to the Paris law although any other relation between the crack growth rate and G_a could be used. In order to calculate the crack growth rate $\frac{da}{dN}$, the applied energy release rate G_a is required. This energy release rate is approximated as the area underneath the current traction-separation response of the crack tip element shown in figure 4.15. A schematic drawing of the cohesive zone is shown in figure 4.16. The cohesive zone length l_{cz} is calculated in the cylinder model as the distance between the contact point x_c and the last failed element. Since the element

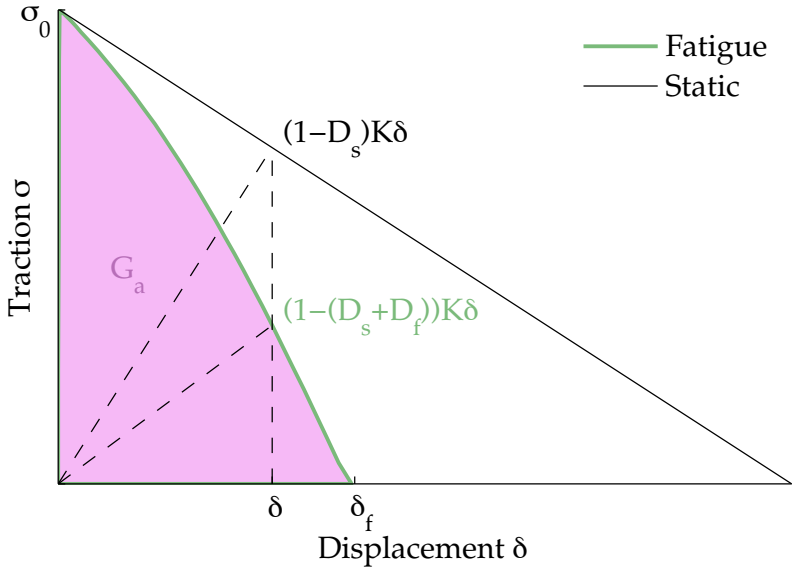


Figure 4.15.: Fatigue constitutive law

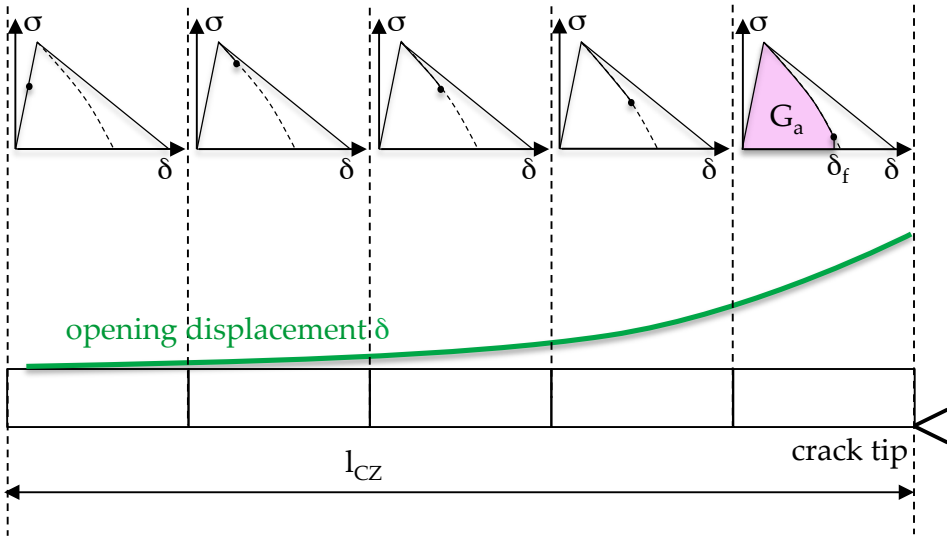


Figure 4.16.: Cohesive zone

fails when the damage reaches 1, and $D_{s,t}$ is the total amount of static damage, the total fatigue damage accumulated in an element over the failure process will be

$$D_{f,t} = 1 - D_{s,t} \tag{4.15}$$

The rate of fatigue damage accumulation can thus be calculated as

$$\frac{dD_f}{dN} = \frac{1 - D_{s,t}}{N_f}, \tag{4.16}$$

and the increase in fatigue damage for one cycle-jump is

$$\Delta D_f = \Delta N \frac{dD_f}{dN}. \tag{4.17}$$

This fatigue damage rate has to be calculated only once per cycle-jump and is identical for all elements in the cohesive zone. While static damage only accumulates when $\delta > \delta_0$, the element degrades under fatigue for all opening displacements. The damage of the ith element at the jth step can then be calculated as

$$D_i^j = D_{i,s}(\delta_i^j) + D_{i,f}^{j-1} + \Delta D_f, \tag{4.18}$$

where $D_{i,s}(\delta)$ is the current static damage depending on the opening displacement δ_i^j, $D_{i,f}^{j-1}$ is the fatigue damage from the previous step, and ΔD_f is calculated according to equation (4.17). The new traction of the ith element at the jth step is then

$$\sigma_i^j = (1 - D_i^j) K \delta_i^j. \tag{4.19}$$

4.2.6. Results from the cylinder model for the new fatigue degradation strategy

The model was implemented into the cylinder model using the same Paris law ($C = 0.0066$, $m = 5.9$) and static constitutive law ($G_c = 0.26\frac{N}{mm}$, $\delta_0 = 3.e\text{-}5\ mm$, $\sigma_0 = 30\ \frac{N}{mm^2}$) as in the previous chapter. Figure 4.17 shows experimental data, the calibrated Paris law and the numerical Paris laws for 4 different mesh sizes and cycle jumps. Figure 4.18 shows the relative error of the numerical Paris law with respect to the input Paris law. The error is very low for small mesh sizes and cycle jumps, so

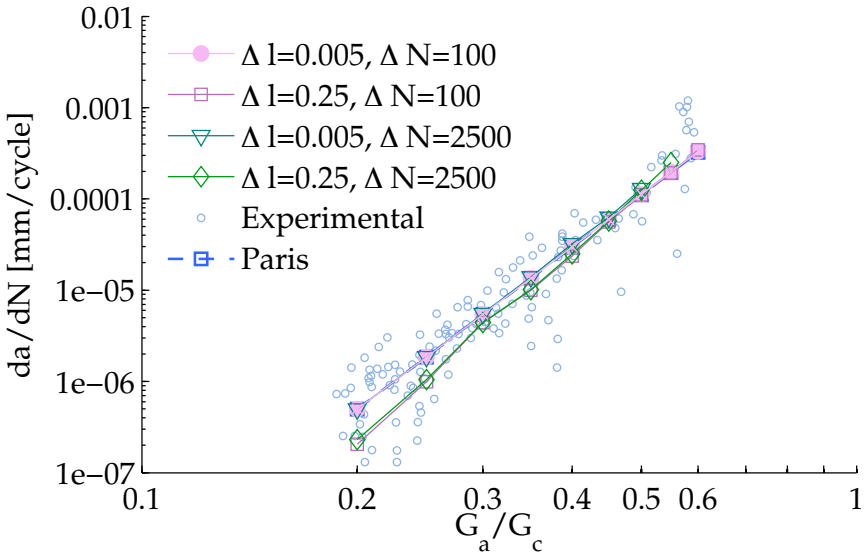


Figure 4.17.: Comparison $\frac{da}{dN}$ vs. G_a of experimental data, Paris law and numerical model

the Paris law is reproduced very accurately. When the cycle-jump is increased to 2500 cycles while keeping a small mesh size, the Paris law is accurately predicted for small energy release rates, but the error rises for higher energy release rates, because the crack-tip values of G_a, δ_f and D_{sf} are predicted less accurately. For a high mesh size and low cycle-jump the error curve can be separated into three parts: for $0.2 < \frac{G_a}{G_a} < 0.25$ the error is very high, at more than 40% lower than the input crack-growth rate. For $0.3 < \frac{G_a}{G_a} < 0.4$ the error is around 20% less than the predicted value and for $0.45 < \frac{G_a}{G_a} < 0.55$, the error is below 10%. These three zones correspond to the number of elements in the cohesive zone n_{cz}, being 3, 4,

and 5, respectively. The error plot also shows that the magnitude of the error is determined by the element size for small values of G_a and the cycle-jump for large energy release rates. Figure 4.19 shows a typical plot of the crack length vs. the

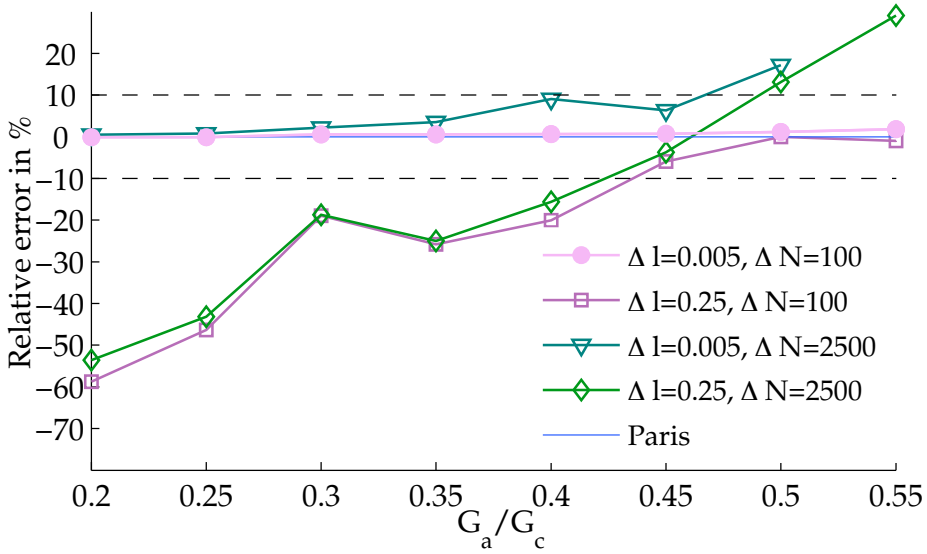


Figure 4.18.: Relative error in % in crack growth rate $\frac{da}{dN}$ for different mesh sizes and cycle-jumps. Δl in mm, ΔN in cycles

number of cycles N. There is a period of stabilisation at the start over the first few millimetres of growth because the model is first loaded statically and requires some cycles to achieve the steady state. However, these oscillations do not influence the predicted $\frac{da}{dN}$ as a function of G_a in a significant way. Figure 4.20 shows the fatigue constitutive for the four different combinations of cycle-jump and element size. The figure demonstrates that the constitutive law has a very stable shape that does not change much due to a change in Δl and ΔN. For a high element size, the traction drops in stages and the constitutive law has several points of inflection. This is the case because, when an element fails at the crack-tip, the parameters, which are taken from the crack-tip element change suddenly leading to the waviness of the constitutive law. Figure 4.21 shows the relative error in $\frac{da}{dN}$ at a load level of $G_a = 0.25G_c$. The maximum cycle jump is 40000 cycles which means that an element fails within about 12 iterations. The maximum element size is 0.25 mm, which results in three elements in the cohesive zone for this G_a. The surface plot shows oscillations

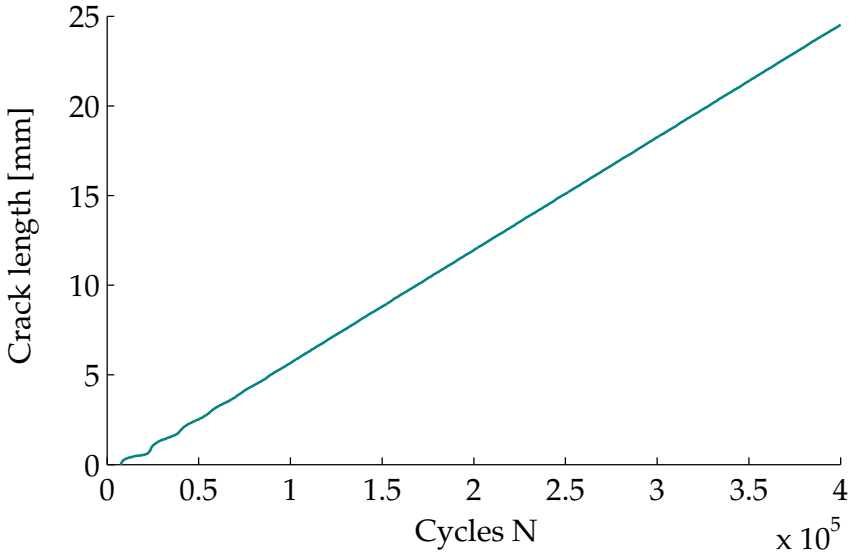


Figure 4.19.: Cycles vs. contact point at $G_a = 0.45G_c$, Δl=0.1 mm, ΔN = 500 cycles

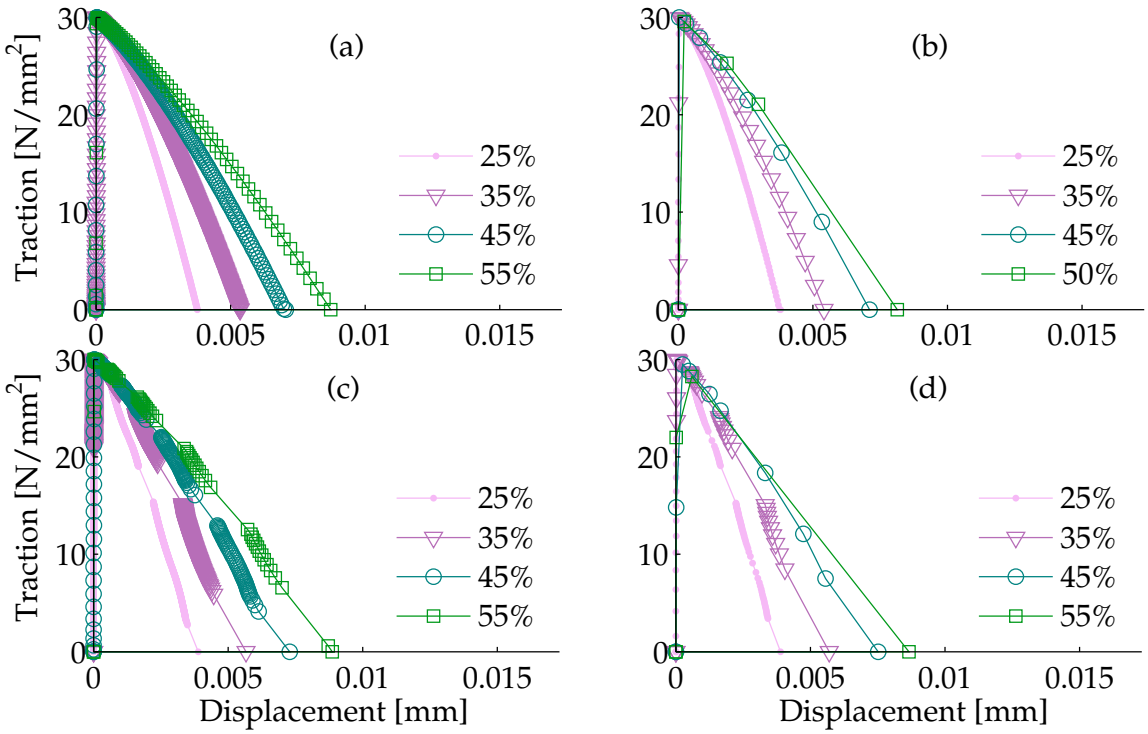


Figure 4.20.: Traction-separation response for fractions of G_c. (a) $\Delta l = 0.005$ mm, $\Delta N = 100$ cycles, (b) $\Delta l = 0.005$ mm, $\Delta N = 2500$ cycles, (c) $\Delta l = 0.25$ mm, $\Delta N = 100$ cycles, (d) $\Delta l = 0.25$ mm, $\Delta N = 2500$ cycles

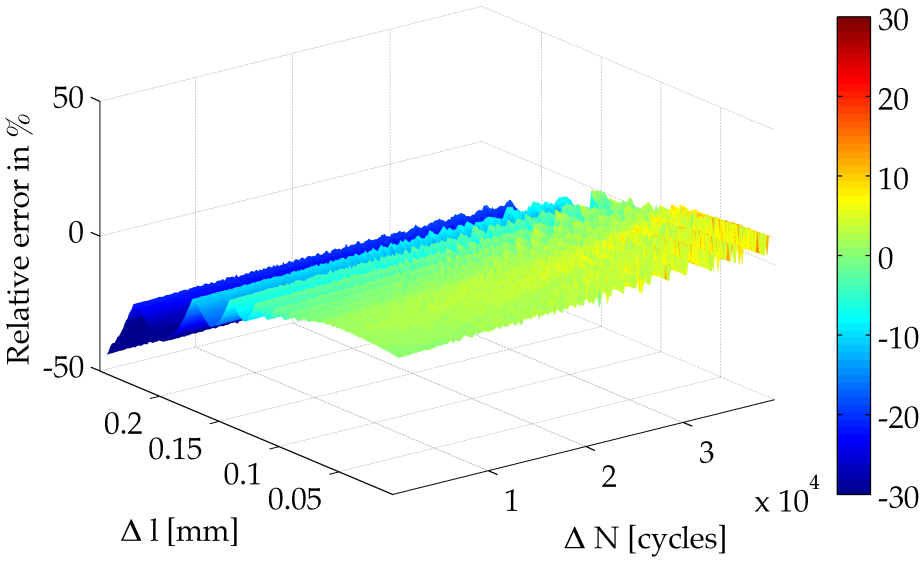


Figure 4.21.: Relative error in % of $\frac{da}{dN}$ with respect to Paris law for $G_a = 0.25G_c$ vs. element size and cycle jump

for increasing element size Δl, and a negative error, while for an increasing cycle-jump, the relative error is positive. Figure 4.22 shows the error vs. the number of elements in the cohesive zone n_{cz} and the number of steps to failure n_f, with $3 < n_{cz} < 25$ and $12 < n_f < 100$. This corresponds to 0.035 mm $< \Delta l <$ 0.25 mm and 4700 cycles $< \Delta N <$ 40,000 cycles. In order to keep the relative error e_r below an absolute value of 10%, n_{cz} should be higher than 7 ($\Delta l <$ 0.12 mm) and for $e_r <$ 20%, n_{cz} should be higher than 6 ($\Delta l <$ 0.15 mm). Figure 4.23 shows the relative error at a load level of $G_a = 0.35G_c$. The maximum cycle jump is 15,000 cycles which means that an element fails within 5 iterations. The maximum element size is 0.3 mm, when there are three elements in the cohesive zone. The surface plot shows similar characteristics to figure 4.21, but in this plot, the diagonal bands, which are a feature of the sensitivity plots for all models are more pronounced and there are oscillations with increasing cycle-jump as well as increasing element size. Figure 4.24 shows the error vs. the number of elements in the cohesive zone n_{cz} and the number of steps to failure n_f, with $3 < n_{cz} < 25$ and $12 < n_f < 100$. This corresponds to 0.041 mm $< \Delta l <$ 0.3 mm and 765 cycles $< \Delta N <$ 7,500 cycles. In order to keep the relative error e_r below an absolute value of 10%, n_{cz} should be

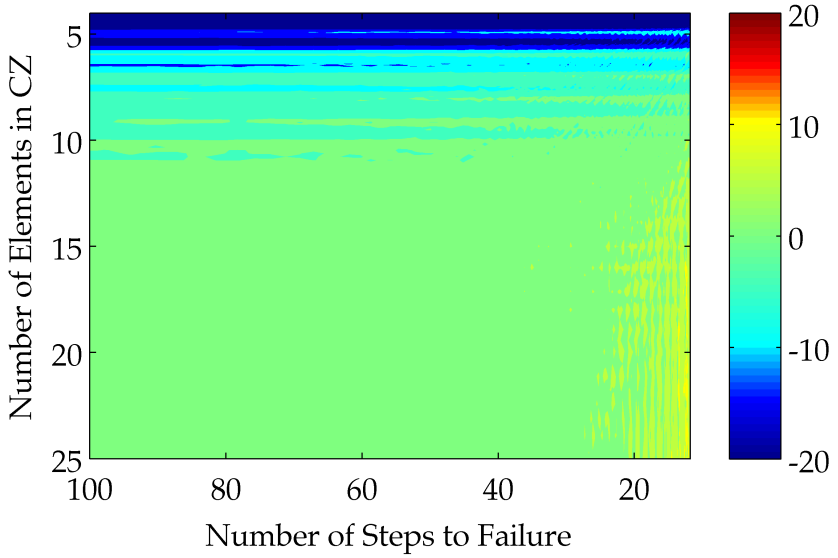


Figure 4.22.: Relative error in % of $\frac{da}{dN}$ with respect to the number of elements in the cohesive zone and the number of cycle jumps it takes to fail one element at $G_a = 0.25G_c$

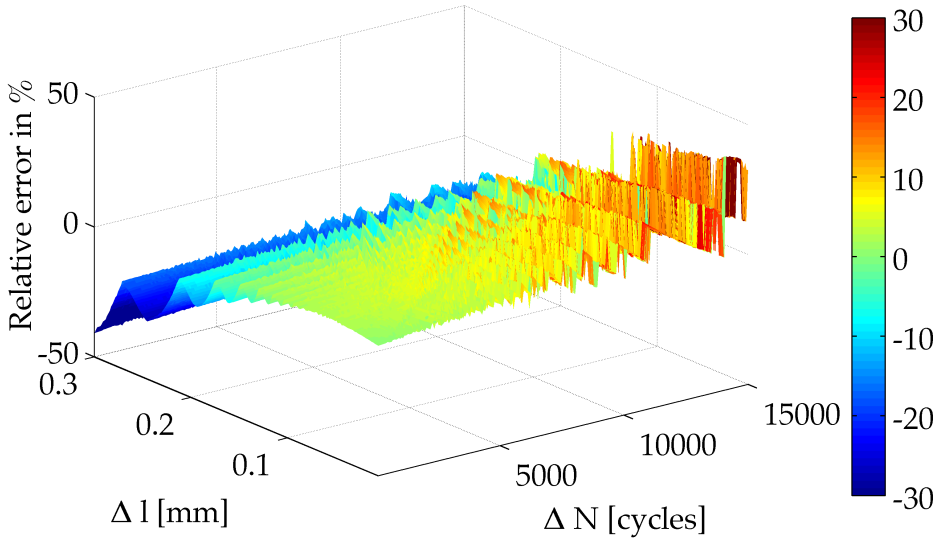


Figure 4.23.: Relative error in % of $\frac{da}{dN}$ with respect to Paris law for $G_a = 0.35G_c$ vs. element size and cycle jump

greater than 6 ($\Delta l < 0.17$ mm), and $n_f > 15$ ($\Delta N < 5100$ cycles) and for $e_r < 20\%$, n_{cz} should be higher than 5 ($\Delta l < 0.21$ mm). Figure 4.25 shows the relative error at a load level of $G_a = 0.45G_c$. The maximum cycle jump is 3,000 cycles which

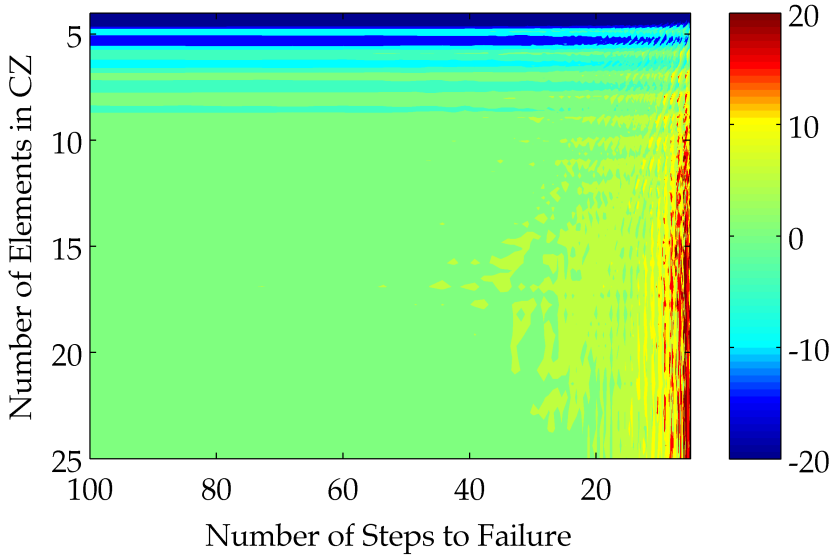


Figure 4.24.: Relative error in % of $\frac{da}{dN}$ with respect to the number of elements in the cohesive zone and the number of cycle jumps it takes to fail one element at $G_a = 0.35G_c$

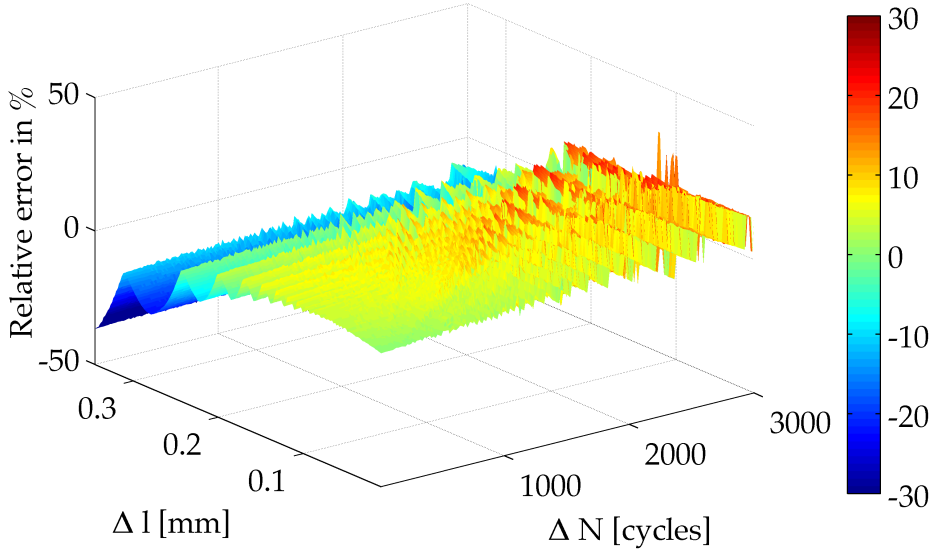


Figure 4.25.: Relative error in % of $\frac{da}{dN}$ with respect to Paris law for $G_a = 0.45G_c$ vs. element size and cycle jump

means that an element fails within 7 iterations. The maximum element size is 0.35 mm, when there are three elements in the cohesive zone. The plot shows the same characteristics as the previous two surface plots. Figure 4.26 shows the error vs. the

number of elements in the cohesive zone n_{cz} and the number of steps to failure n_f, with $3 < n_{cz} < 25$ and $12 < n_f < 100$. This corresponds to 0.047 mm $< \Delta l <$ 0.35

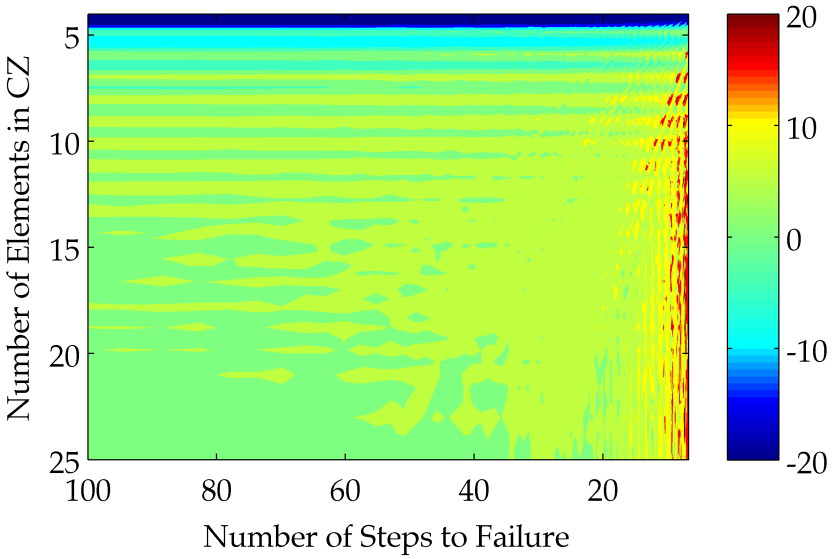


Figure 4.26.: Relative error in % of $\frac{da}{dN}$ with respect to the number of elements in the cohesive zone and the number of cycle jumps it takes to fail one element at $G_a = 0.45G_c$

mm and $199 < \Delta N < 2500$ cycles. In order to keep the relative error e_r below an absolute value of 10%, n_{cz} should be greater than 6 ($\Delta l < 0.2$ mm), and $n_f >$ 15 ($\Delta N < 1325$ cycles) and for $e_r < 20\%$, n_{cz} should be higher than 4 ($\Delta l < 0.3$ mm). Figure 4.27 shows the relative error at a load level of $G_a = 0.55G_c$. The maximum cycle jump is 1500 cycles which means that an element fails within 4 iterations. The maximum element size is 0.39 mm, when there are three elements in the cohesive zone. The plot shows the same characteristics as the previous surface plots. Figure 4.28 shows the error vs. the number of elements in the cohesive zone n_{cz} and the number of steps to failure n_f, with $3 < n_{cz} < 25$ and $10 < n_f < 100$. This corresponds to 0.053 mm $< \Delta l <$ 0.39 mm and $68 < \Delta N < 680$ cycles. In order to keep the relative error e_r below an absolute value of 10%, n_{cz} should be greater than 5 ($\Delta l <$ 0.26 mm), and $n_f >$ 15 ($\Delta N <$ 454 cycles) and for $e_r < 20\%$, n_{cz} should be higher than 4 ($\Delta l <$ 0.33 mm). The relative errors are summarised for the whole range of G_a/G_c in table 4.2.

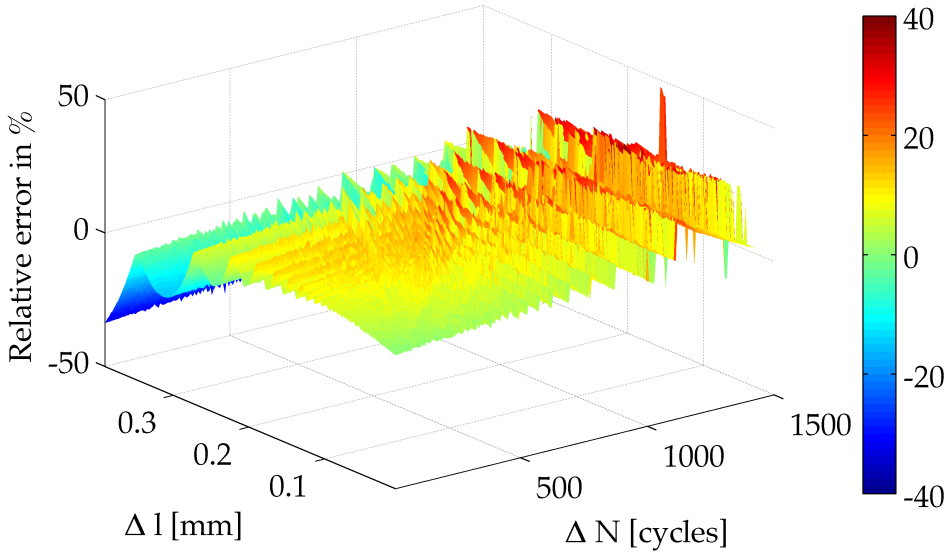


Figure 4.27.: Relative error in % of $\frac{da}{dN}$ with respect to Paris law for $G_a = 0.55G_c$ vs. element size and cycle jump

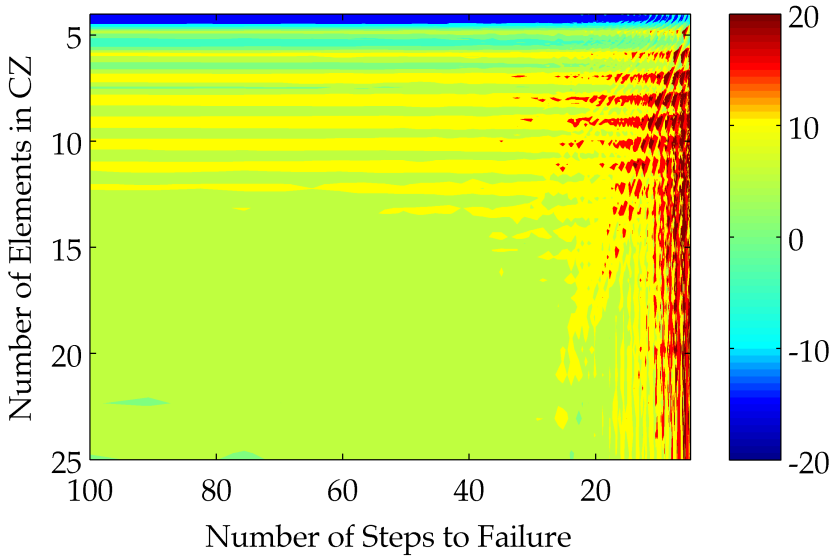


Figure 4.28.: Relative error in % of $\frac{da}{dN}$ with respect to the number of elements in the cohesive zone and the number of cycle jumps it takes to fail one element at $G_a = 0.55G_c$

	e_r<10%		e_r<20%	
Ga/Gc	n_{cz} (Δl <) >	n_f >(ΔN <)	n_{cz} (Δl <) >	n_f >(ΔN <)
0.25	7 (0.12)	12 (40,000)	6 (0.15)	12 (40,000)
0.35	6 (0.17)	15 (5100)	5 (0.21)	10 (7500)
0.45	6 (0.2)	15 (1325)	5 (0.3)	10 (2500)
0.55	5 (0.26)	15 (453)	4 (0.33)	10 (680)

Table 4.2.: Minimum values for $n_f(\Delta l)$ and $n_{cz}(\Delta l)$ with respect to the relative errors in $\frac{da}{dN}$. Δl in [mm], ΔN in cycles

4.2.7. Discussion of the new model

The proposed model has been implemented into the cylinder model in mode I. The model is able to predict the input Paris law accurately. As opposed to the Peerlings', Turon, and Harper model, there is no input required apart from the Paris law itself and it therefore requires no calibration. Also, since the necessary information is taken from the crack-tip element, which is the element with the maximum current applied energy release rate, no crack-tip tracing algorithm is necessary and the elements do not have to know their relative position in the cohesive zone. However, this means that, as opposed to the Kawashita/Hallett model which can adapt to 3D crack growth and curved crack fronts, further development is required. Along a curved crack front the applied energy release rate will be non-constant so calculating G_a as the maximum of all active elements in the cohesive zone is not sufficient. Therefore, in the case of 3D cracks, the calculation of the cohesive zone length has to be newly defined. A sensitivity study was conducted to examine the relative error in the Paris law prediction. This showed that a minimum number of 7 elements should be present in the cohesive zone for the model to be accurate, while the maximum cycle-jump depends heavily on the magnitude of G_a and should be chosen accordingly. If the approximate range of G_a is unknown or varies over time, an alternative would be to adjust the cycle-jump as in Turon's model, by introducing a maximum damage per increment to insure an adaptation of ΔN to the load level.

4.3. Conclusions for the improvements and the new model

In this chapter, improvements have been proposed for two of the models examined in the previous chapter. For the Peerlings' model, a faster alternative has been presented by changing the way fatigue damage accumulation is calculated, which makes the model 20 times faster. Also, since the Peerlings' model needs to be calibrated before a simulation, an alternative was proposed which requires the calibration of only 2 instead of 5 parameters making the model calibration much more straight-forward. However, the improvements in speed and calibration time also lead to a lack of accuracy for high energy release rates and cycle-jumps.
For the Turon model a different way of calculating the applied energy release rate G_a was proposed resulting in a more accurate numerical Paris law. Despite the improvement in accuracy, the cohesive zone length still has to be adjusted to give good results introducing a fitting parameter to the model. In the next section, some conditions were outlined for a fatigue model to give an accurate representation of the Paris law and some unsuccessful modelling attempts were presented. A model was then proposed for simulating high-cycle fatigue delamination, that does not require any calibration and only needs the Paris law as input, as well as not requiring knowledge of the position of the crack-tip. The model was examined and it was found that the Paris law can be predicted very accurately. A sensitivity study was then undertaken to examine the relative error in the numerical Paris law for various element sizes and cycle-jumps and to give an error envelope with respect to Δl and ΔN. In its current implementation, the model is only able to predict fatigue crack growth in 2D for a straight crack-front in pure modes with a regular mesh. Further development is necessary to make the model work in more general situations The model needs to be adapted to be able to simulate mixed-mode cases. This could be achieved by implementing one of the mixed-mode models discussed in earlier chapters. Also, for curved crack-fronts, the applied energy release will not be constant and in a general 3D crack growth the cohesive zone length calculation has to be newly defined. This would have to be done by defining crack growth directions

along which the number of active elements (with displacement greater than zero and damage less than one) is then multiplied by the element length Δl. For an irregular mesh, the element lengths of these active elements have to be summed up to obtain the cohesive zone length. For each of these directions the applied energy release rate would be obtained from the element with highest value to ensure crack growth at the correct rate.

In the next chapter, the model in its current state will be implemented in a finite element code and used to simulate mode I and mode II delamination in a DCB and an ELS specimen that are only one element wide, so that the calculation of G_a and l_{cz} is quite straight-forward.

5. Finite element implementation of the improved fatigue model

In the last chapter the development towards an improved fatigue degradation strategy for cohesive zone modelling of delamination growth was outlined. This development resulted in a new fatigue-degradation strategy that only needs the Paris law as input, which was subsequently presented. A sensitivity study was then undertaken to examine the relative error in the numerical Paris law for various element sizes and cycle-jumps and it was found that the new model is able to predict the Paris law accurately. In its current implementation, the model is only able to predict fatigue crack growth in 2D for a straight crack-front in pure modes with a regular mesh. All tasks from the previous chapter were carried out in the cylinder model which allowed the rapid evaluation of new potential strategies.

This chapter describes the implementation of the fatigue model into a cohesive finite element and presents an evaluation of its performance within a full FE model. In the first section of the chapter some basic theory for the cohesive element is presented and the implementation of the model into ABAQUS is discussed. In the second section results are presented from high-cycle fatigue simulations of a double cantilever beam (DCB) mode I specimen and an end-loaded split test (ELS) mode II specimen. These results are compared to the results of the original implementation of three of the the four models discussed in chapter 3.

5.1. Implementation of the interface element

5.1.1. Equilibrium for the cohesive crack

Only in this section, cohesive tractions will be labeled $\boldsymbol{t}$ rather than σ, and relative displacements $\boldsymbol{\Delta u}$ instead of δ, in alignment with the variable name conventions of standard finite element text books. The derivation below follows that of Moes and Belytchko [MB02]. Consider the domain Ω containing a crack with boundary conditions as shown in figure 5.1. Tractions $\boldsymbol{F}$ are imposed on Γ_f and displacements,

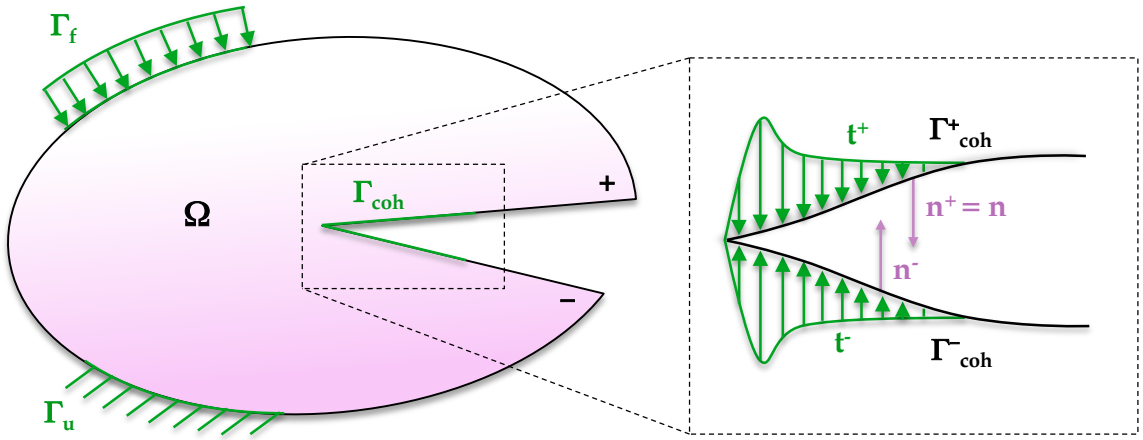


Figure 5.1.: Body with cohesive crack

which are assumed to be 0, are prescribed on Γ_u. The part of the crack where cohesive tractions act across the crack is called Γ_{coh}, and a positive side and a negative side of the crack face are defined, labeled with + and - respectively. The partial differential equations for static equilibrium in the absence of body forces is

$$\nabla \cdot \sigma = 0 \quad \text{on } \Omega \tag{5.1}$$

$$\sigma \cdot \boldsymbol{n} = \mathbf{F} \quad \text{on } \Gamma_f \tag{5.2}$$

$$\sigma \cdot \boldsymbol{n}^+ = -\sigma \cdot \boldsymbol{n}^- = \boldsymbol{t}^+ = -\boldsymbol{t}^- \quad \text{on } \Gamma_{coh}. \tag{5.3}$$

$\boldsymbol{t}^+$ and $\boldsymbol{t}^-$ are the closing tractions in the cohesive zone and $\boldsymbol{n}^+$ and $\boldsymbol{n}^-$ the cohesive zone surface normals. In addition, kinematic equations are required, which consist of the relationship between displacements and strains in Ω, the displacement boundary conditions on Γ_u, and the definition of relative displacements on

Γ_f

$$\boldsymbol{\epsilon} = \frac{1}{2}(\boldsymbol{\nabla u} + (\boldsymbol{\nabla u})^T) \equiv \boldsymbol{\epsilon(u)} \quad \text{on } \Omega \tag{5.4}$$

$$\boldsymbol{u} = 0 \quad \text{on } \Gamma_u \tag{5.5}$$

$$\boldsymbol{\Delta u} = \boldsymbol{u}^+ - \boldsymbol{u}^- \quad \text{on } \Gamma_{coh}. \tag{5.6}$$

Finally, the constitutive relationship on $\boldsymbol{\Omega}$ relating stresses and strains and the cohesive constitutive law relating the traction $\boldsymbol{t}$ and the displacement jump $\boldsymbol{\Delta u}$ need to be defined

$$\boldsymbol{\sigma} = \boldsymbol{C} : \boldsymbol{\epsilon} \quad \text{on } \Omega \tag{5.7}$$

$$\boldsymbol{t} = \boldsymbol{t}(\boldsymbol{\Delta u}) \quad \text{on } \Gamma_{coh}. \tag{5.8}$$

The strong form of the problem is then transformed into the a weak form suitable for finite element modelling, where the displacement field $\boldsymbol{u}$ must be an element of the subset of functions $\mathcal{U}$ in the function space $\mathcal{V}$ which vanish on Γ_u:

$$\boldsymbol{u} \in \mathcal{U} = \{\boldsymbol{v} \in \mathcal{V} \mid \boldsymbol{v} = 0 \text{ on } \Gamma_u\}. \tag{5.9}$$

The precise mathematical nature of the function space $\mathcal{V}$ depends on the regularity of the solution. The weak form of the equilibrium equation is then

$$\int_\Omega \boldsymbol{\sigma} : \boldsymbol{\epsilon}(\boldsymbol{v}) d\boldsymbol{x} = \int_{\Gamma_f} \boldsymbol{F} \cdot \boldsymbol{v} d\boldsymbol{s} + \int_{\Gamma^+_{coh}} \boldsymbol{t}^+ \cdot \boldsymbol{v} d\boldsymbol{s} + \int_{\Gamma^-_{coh}} \boldsymbol{t}^- \cdot \boldsymbol{v} d\boldsymbol{s} \ \ \forall \boldsymbol{v} \in \mathcal{U}, \tag{5.10}$$

where $\boldsymbol{dx}$ and $\boldsymbol{ds}$ are volume and surface differentials respectively. Keeping in mind that $\boldsymbol{t} = \boldsymbol{t}^+ = -\boldsymbol{t}^-$, equation 5.10 can be simplified to

$$\int_\Omega \boldsymbol{\sigma} : \boldsymbol{\epsilon}(\boldsymbol{v}) d\boldsymbol{x} - \int_{\Gamma_{coh}} \boldsymbol{t}(\boldsymbol{\Delta u}) \cdot \boldsymbol{\Delta v} d\boldsymbol{s} = \int_{\Gamma_f} \boldsymbol{F} \cdot \boldsymbol{v} d\boldsymbol{s}, \tag{5.11}$$

where $\boldsymbol{\Delta v} = \boldsymbol{v}^+ - \boldsymbol{v}^-$.

5.1.2. Discretization of the cohesive zone

After the discretization of 5.11, the equilibrium problem posed in the last section is solved using the implicit finite element solver ABAQUS/Standard (abbreviated ABAQUS in the rest of the chapter). The fatigue damage model is implemented

into a user-defined cohesive element. This can be done in ABAQUS with the subroutine UEL, which requires the user to specify the element stiffness matrix and the residual force vector, which will be described in the following subsection. The interface element used here is developed for three-dimensional models but has one dimension less than the continuum elements in the domain. Due to its application in three dimensional simulations it will be called a 3D element. The element has 8 nodes or four node-pairs. The displacements of the top and the bottom surface are approximated with standard Lagrangian linear shape functions. Figure 5.2 shows a schematic drawing of the element with the local $\xi\eta$ coordinate system and the global xyz- system. In the undeformed state the coordinates of the top and the bottom surface coincide but the two surfaces are shown at a slight distance from each other for clarification. The node numbering follows ABAQUS conventions. This

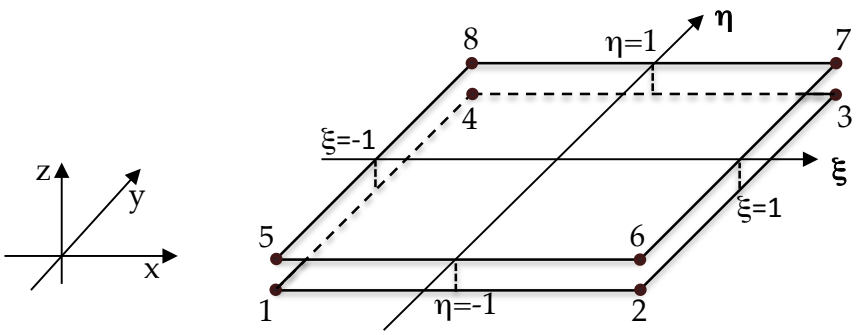


Figure 5.2.: Cohesive element

element is a zero-thickness element, where the lower and upper surface coincide initially. The element has 24 degrees of freedom, and following ABAQUS convention, the vector of nodal displacements $\boldsymbol{u_N}$ is

$$\boldsymbol{u_N} = (u_x^1\, u_y^1\, u_z^1 \cdots u_x^8\, u_y^8\, u_z^8)^T \in \mathbb{R}^{24} \tag{5.12}$$

A matrix operator $\boldsymbol{\Phi}$ can be defined as follows

$$\boldsymbol{\Phi} = [-\boldsymbol{I_{12\times 12}} \mid \boldsymbol{I_{12\times 12}}], \boldsymbol{\Phi} \in \mathbb{R}^{12\times 24}, \tag{5.13}$$

where $\boldsymbol{I_{12\times 12}} \in \mathbb{R}^{12\times 12}$ is an identity matrix, so that the vector of relative nodal displacements between the top and the bottom surface $\boldsymbol{\Delta u_N}$ of the four node pairs is defined as

$$\boldsymbol{\Delta u_N} = \boldsymbol{\Phi u_N}, \text{ where } \boldsymbol{\Delta u_N} \in \mathbb{R}^{12}. \tag{5.14}$$

The matrix H is defined in the following way

$$\boldsymbol{H} = \begin{pmatrix} N_1 & 0 & 0 & N_2 & 0 & 0 & N_3 & 0 & 0 & N_4 & 0 & 0 \\ 0 & N_1 & 0 & 0 & N_2 & 0 & 0 & N_3 & 0 & 0 & N_4 & 0 \\ 0 & 0 & N_1 & 0 & 0 & N_2 & 0 & 0 & N_3 & 0 & 0 & N_4 \end{pmatrix} \in \mathbb{R}^{3\times 12}, \quad (5.15)$$

where N_i are the standard shape functions. The relative displacement jump $\boldsymbol{\Delta u}$ can then be written in terms of the nodal displacement jump $\boldsymbol{\Delta u_N}$ as

$$\boldsymbol{\Delta u} = \boldsymbol{H\Phi\Delta u_N} = \boldsymbol{Bu_N}, \text{ where } \boldsymbol{\Delta u} \in \mathbb{R}^3, \boldsymbol{B} \in \mathbb{R}^{3\times 24}. \quad (5.16)$$

The tractions $\boldsymbol{t}$ are related to the relative displacement jump through the constitutive matrix $\boldsymbol{D} \in \mathbb{R}^{3\times 3}$,so

$$\boldsymbol{t} = \boldsymbol{D\Delta u}. \quad (5.17)$$

In the equilibrium equation (5.11), the cohesive elements contribute only to the integral over Γ_{coh}, which is the second term on the left-hand side of the equation. For one element, the integral in matrix notation using equations (5.16) and (5.17) becomes

$$-\int_{S_e} (\boldsymbol{\Delta v})^T \boldsymbol{t} dS = -\int_{S_e} (\boldsymbol{B} v_N)^T \boldsymbol{DBu_N} dS = -{v_N}^T \int_{S_e} \boldsymbol{B}^T \boldsymbol{DB} dS \boldsymbol{u_N} \quad (5.18)$$

where $\boldsymbol{v} \in \mathcal{V}_h$ is a discretized test function. The element stiffness matrix $K_{el} \in \mathbb{R}^{24\times 24}$ is thus

$$\boldsymbol{K_{el}} = -\int_{S_e} \boldsymbol{B}^T \boldsymbol{DB} dS \quad (5.19)$$

and the residual force vector $\boldsymbol{f} \in \mathbb{R}^{24}$ is

$$\boldsymbol{f} = \int_{S_e} \boldsymbol{B}^T \boldsymbol{t} dS. \quad (5.20)$$

Practically, the integrals in equations (5.19) and (5.20) are not calculated in the global coordinate system but in the reference $\xi\eta$-coordinate system (see figure 5.2). Figure 5.3 shows the global xyz coordinate system and the cohesive element with its top and bottom surfaces the separation of which defines the relative displacements. The Jacobian matrix $\boldsymbol{J} \in \mathbb{R}^{2\times 3}$ of the coordinate transformation from the global

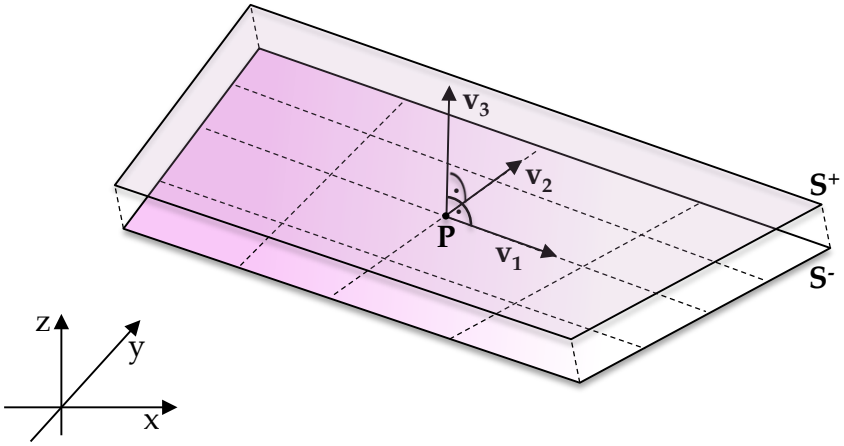


Figure 5.3.: Global and local coordinate system

three-dimensional to the local two-dimensional curvilinear coordinate system can be written as

$$\boldsymbol{J} = \begin{pmatrix} \frac{\partial \boldsymbol{x}}{\partial \xi} \\ \frac{\partial \boldsymbol{x}}{\partial \eta} \end{pmatrix} = \boldsymbol{N}_{\xi,\eta} \cdot \boldsymbol{C}_{xyz} = \begin{pmatrix} \frac{\partial N_1}{\partial \xi} & \frac{\partial N_2}{\partial \xi} & \frac{\partial N_3}{\partial \xi} & \frac{\partial N_4}{\partial \xi} \\ \frac{\partial N_1}{\partial \eta} & \frac{\partial N_2}{\partial \eta} & \frac{\partial N_3}{\partial \eta} & \frac{\partial N_4}{\partial \eta} \end{pmatrix} \begin{pmatrix} x_1 & y_1 & z_1 \\ x_2 & y_2 & z_2 \\ x_3 & y_3 & z_3 \\ x_4 & y_4 & z_4 \end{pmatrix}, \tag{5.21}$$

where $(x_i, y_i, z_i), i = 1, .., 4$ are the coordinates of the nodes of the undeformed element in the global coordinate system. This is consistent with the assumption of small deformations.

Large deformations can be taken into account by defining the local coordinate system on the midsurface between S^+ and S^- as has been done by Goyal et al [GJD04] and Turon [Tur06]. In that case, $\boldsymbol{C}_{xyz}$ in equation (5.21) becomes

$$\boldsymbol{C}_{xyz} = \begin{pmatrix} x_1 & y_1 & z_1 \\ x_2 & y_2 & z_2 \\ x_3 & y_3 & z_3 \\ x_4 & y_4 & z_4 \end{pmatrix} + \frac{1}{2} \begin{pmatrix} \Delta u_{N1} & \Delta u_{N2} & \Delta u_{N3} \\ \Delta u_{N4} & \Delta u_{N5} & \Delta u_{N6} \\ \Delta u_{N7} & \Delta u_{N8} & \Delta u_{N9} \\ \Delta u_{N10} & \Delta u_{N11} & \Delta u_{N12} \end{pmatrix}, \tag{5.22}$$

where $\Delta u_{Ni}, i = 1, .., 12$ are the components of the vector $\boldsymbol{\Delta u_N}$ defined in equation (5.14). The two row vectors of $\boldsymbol{J}$

$$v_\xi := \frac{\partial \boldsymbol{x}}{\partial \xi} \in \mathbb{R}^3 \quad \text{and} \quad v_\eta := \frac{\partial \boldsymbol{x}}{\partial \eta} \in \mathbb{R}^3 \tag{5.23}$$

define the orientation in space of the tangential plane at a point P on the surface. Generally, v_ξ and v_η are not orthogonal, but they can be used to define the orthonormal basis (v_1, v_2, v_3), shown in figure 5.3 as follows

$$v_3 = \frac{v_\xi \times v_\eta}{\|v_\xi \times v_\eta\|}, \qquad v_1 = \frac{v_\xi}{\|v_\xi\|}, \quad \text{and} \quad v_2 = \frac{v_1 \times v_3}{\|v_1 \times v_3\|}, \tag{5.24}$$

where v_3 is the unit normal vector to the tangential plane. The orthogonal matrix Θ composed of the three basis vectors expresses the rotation of the cohesive element in the global coordinate system, where $\boldsymbol{\Theta} \in \mathbb{R}^{3\times 3}$ is

$$\boldsymbol{\Theta} = (v_1 \;\; v_2 \;\; v_3). \tag{5.25}$$

The stiffness matrix in equation (5.19) can now be calculated in the local coordinate system as follows

$$\boldsymbol{K_{el}} = -\int_{S_e} \boldsymbol{B}^T \boldsymbol{D} \boldsymbol{B} d\boldsymbol{S} = -\int_{\xi=-1}^{\xi=1} \int_{\eta=-1}^{\eta=1} \hat{\boldsymbol{B}}^T \boldsymbol{\Theta}^T \hat{\boldsymbol{D}} \boldsymbol{\Theta} \hat{\boldsymbol{B}} |\boldsymbol{J_s}| d\eta d\xi \tag{5.26}$$

where $\hat{\boldsymbol{B}}$ is the matrix of local shape functions multiplied by the relative displacement operator (analogous to equation (5.15) and (5.16)) in local coordinates and $|\boldsymbol{J_s}| := \|v_\xi \times v_\eta\|$ is the surface element. The integration is performed using an appropriate quadrature rule, so that equation (5.26) becomes

$$-\int_{\xi=-1}^{\xi=1} \int_{\eta=-1}^{\eta=1} \hat{\boldsymbol{B}}^T \boldsymbol{\Theta}^T \hat{\boldsymbol{D}} \boldsymbol{\Theta} \hat{\boldsymbol{B}} |\boldsymbol{J_s}| d\eta d\xi = \sum_{i=1}^{n_i} w_i \hat{\boldsymbol{B}}^T \boldsymbol{\Theta}^T \hat{\boldsymbol{D}} \boldsymbol{\Theta} \hat{\boldsymbol{B}} |\boldsymbol{J_s}| (\xi_i, \eta_i), \tag{5.27}$$

In the case of the 3D cohesive element with linear basis functions, a two-point integration rule was chosen in each coordinate direction, so $n_i = 4$. The most common quadrature rule for the integration of a finite element is the Gauss quadrature, which gives accurate values for polynomials of degree $2n - 1$, where n is the number of integration points in each coordinate direction. However, Gauss quadrature has been shown to produce oscillations in the traction profile of cohesive elements for stiffnesses K higher than 1000 in linear as well as quadratic elements [SdB93]. Schellekens et al therefore suggest using Newton Cotes quadrature, as do Alfano et al [AC01] and it has been widely used for cohesive elements [GCA88], [BW08], [BLS95]. The interface element was therefore originally integrated with a 2x2 Newton Cotes rule. However, this led to a wrinkling of the crack front. In the case

when the crack front was made up of only one cohesive element it caused one-sided delamination and eventual divergence of the simulation. This phenomenon was also observed more recently by Davila et al [DCT08] when simulating skin-stiffener debonding where it delayed the separation of the flange tip. In the light of these experiences the cohesive element is integrated using a 2x2 Gauss quadrature. Since the oscillations are caused by excessively high stiffnesses which occur during the elastic phase of the debonding process, the initial stiffness was set to a value of $K = 300,000 \frac{N}{mm^3}$, which leads to acceptable results.
In equation (5.26), the matrix $\hat{\boldsymbol{D}}$ determines the constitutive law of the cohesive element. For pure modes, the relative displacements and the tractions are uncoupled, so for example for pure mode I, using the constitutive law from equation 3.8, $\hat{\boldsymbol{D}}$ simply becomes

$$\hat{\boldsymbol{D}} = \begin{pmatrix} E_x & 0 & 0 \\ 0 & E_y & 0 \\ 0 & 0 & (1-D) \end{pmatrix}, \tag{5.28}$$

where D is the damage. E_x and E_y are dummy stiffnesses, preventing the stiffness matrix from becoming singular. The damage D is calculated according to the fatigue degradation strategy outlined in the previous chapter. One adjustment has been made to the fatigue algorithm described in the last chapter: only elements, which are on the softening part of the constitutive law i.e. elements with a relative displacement $\delta > \delta_0$ are considered to be a part of the numerical cohesive zone and acquire fatigue damage, in accordance with Harper [HH08]. In mode I this leads to a reduction of the cohesive zone length to about 50 % of the original value,when the length is determined from the end of the compressive zone to the crack-tip, while in mode II, the cohesive zone length is 7% of the original value. This is because in mode II there is no compressive zone, which means that the cohesive tractions are very small but non-zero over a long range of elements.

5.1.3. Implementation into the finite element solver

Since the damage is a function of the relative displacement the stiffness matrix will be nonlinear so $\boldsymbol{K} = \boldsymbol{K}(\boldsymbol{u})$ and the displacements for each increment in the analysis

have to be found iteratively. The standard algorithm ABAQUS uses to calculate the displacement field is a Newton-Raphson algorithm. This requires the user to provide a tangent stiffness matrix

$$\boldsymbol{K}_{el,t} = \frac{\partial \boldsymbol{K}_{el}}{\partial \boldsymbol{u}}. \tag{5.29}$$

Due to the quadratic convergence of the Newton algorithm, using the tangent stiffness matrix $\boldsymbol{K}_{el,t}$ rather than the secant stiffness $\boldsymbol{K}_{el}$ is generally recommended in the literature [AC01]. In the case of a quasi-static analysis it can be easily provided because the damage $D(\Delta u)$ is an analytical function of the displacements. When modelling fatigue delamination however, the damage is unknown as an analytical function. The tangent stiffness matrix can therefore only be calculated by approximating the change in damage with respect to the displacements from earlier increments, a procedure which itself incurs a numerical error. Therefore, the secant stiffness was used in the subsequent simulations. In this case ABAQUS can be instructed to use a quasi-Newton algorithm which still has a superlinear rate of convergence. The quasi-Newton method is most successful when the stiffness matrix is not changing much from iteration to iteration which is generally the case when simulating high-cycle fatigue. It can only be used for symmetric systems of equations. The input file usage in ABAQUS is

```
*SOLUTION TECHNIQUE, TYPE=QUASI-NEWTON
```

The quasi-Newton method works well in combination with the line search method which helps to prevent divergence of equilibrium iterations resulting from the inexact Jacobian produced by the quasi-Newton method. The line search method is activated by default when the quasi-Newton method is used [Das11].
The user element has been written in Fortran 90 and compiled into an object file using gfortran. The input file together with the user element object file is then passed to ABAQUS. The post processing of the results is done in Matlab. The input file usage for the user element in ABAQUS is

```
*USER ELEMENT,TYPE=U1,NODES=8,COORDINATES=3, I PROPERTIES=1,
PROPERTIES=8, VARIABLES=20
```

This specifies the name, the number of nodes, the dimension, the integer input properties, the real valued input properties and the number of user element variables respectively. The 20 user element variables (SVARS) store the damage, the relevant displacement (mode I or II), the relevant traction, the fatigue damage and the energy release rate at each of the 4 integration points. Static unloading and reloading is taken into account as shown in figure 5.4 for mode II and a reversed load: if the absolute value of the relative displacement drops, the static damage from the previous increment is lower than the current damage, and the elements follow the curve $\sigma = (1 - D)K\delta$, upon reloading, where D is the highest value of damage reached.

The 8 real and the integer input properties are specified as follows

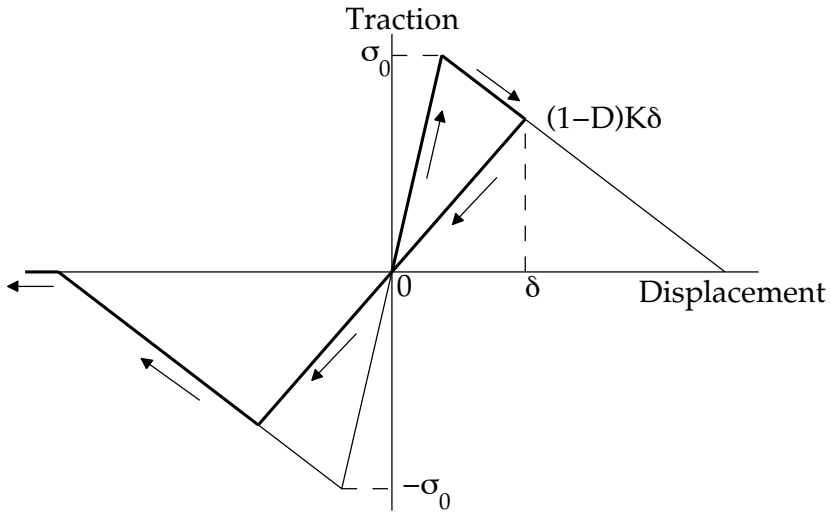


Figure 5.4.: Reversed loading in mode II

```
*UEL PROPERTY
```

$G_c \;\; \sigma_0 \;\; K \;\; E_x \;\; E_y \;\; C \;\; m \;\; \Delta_l \;\; Nlgeom$

Nlgeom is the integer property which is either 1 or 0 and specifies whether to assume large deformations. If *Nlgeom*=1 then $\boldsymbol{C_{xyz}}$ is calculated according to equation (5.22), otherwise as in equation (5.21). The cycles are applied during a `STATIC` step to the nodes of the cohesive elements in the form of a field which is defined in terms of the step time.

*STEP,INC=inc_{max}, AMPLITUDE=STEP

*STATIC

Δt_{ini}, t_{end}, Δt_{min}, Δt_{max}

Here inc_{max} is the maximum number of increments used during the step. t_{ini}, t_{end}, Δt_{min}, and Δt_{max} are the initial time increment, the step time, the minimum time increment and the maximum time increment. The amplitude for the field is defined as follows

*AMPLITUDE,NAME=fatiguecycles, TIME=STEP TIME, DEFINITION=TABULAR

t_{start}, N_{start}, t_{end}, N_{end}

Here, t_{start}, N_{start} are the step time from when cycles are applied, which is set to 0, and N_{start} is the starting number of cycles already applied, which is also set to 0. t_{end} and N_{end} are the step time and the number of cycles reached at the end of the step. The field is then applied to the nodes in *nodeset*

*FIELD, AMPLITUDE=fatiguecycles

nodeset, 1

Using this method it is now possible to control the cycle-jump ΔN as follows. First, ΔN and the total number of cycles to be simulated N_{end} is chosen, so that N_{end} *mod* ΔN=0. The total number of increments is then

$$n_{inc} = \frac{N_{end}}{\Delta N} \tag{5.30}$$

The initial, minimum and maximum time increment are set equal, so $\Delta t_{ini} = \Delta t_{min} = \Delta t_{max}$. This stops ABAQUS from adjusting the time increment according to the rate of convergence and guarantees that the same amount of pseudo time passes in each increment. In the simulations performed below $\Delta t_{min} := 0.001$. The total step time is then set to

$$t_{end} = \Delta t_{min} \cdot n_{inc}, \tag{5.31}$$

so a total number of N_{end} cycles will be simulated with a cycle-jump ΔN. As the fatigue degradation strategy is not point-local, it requires information from all elements in order to determine the cohesive zone length, the crack growth rate and

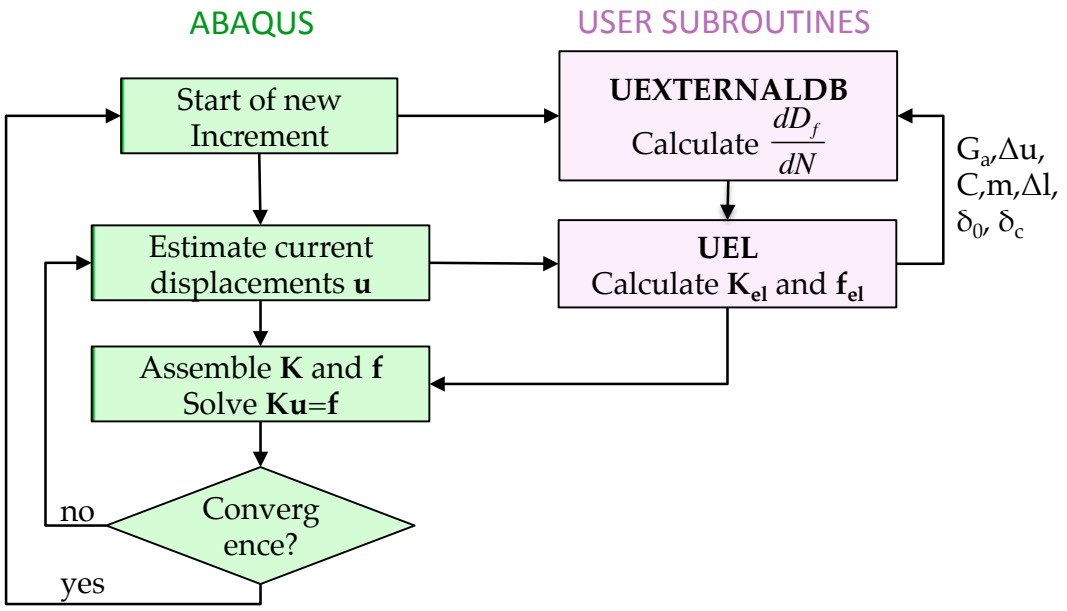


Figure 5.5.: Information exchange of subroutines and solver

the increase in fatigue damage. These calculations are not performed within `UEL` but within the user subroutine `UEXTERNALDB`, which then passes back the fatigue damage change to `UEL`. `UEXTERNALDB` is called at the start of the analysis and at the beginning of each increment. Data is passed between subroutines using a Fortran `COMMON` block. The information exchange between the subroutines and ABAQUS during an increment of the solution is shown in figure 5.5. Employing `UEXTERNALDB` is not strictly necessary, because all cohesive elements have access to the required data, which is stored in the `COMMON` block and the calculation of $\frac{dD_f}{dN}$ could therefore be carried out in `UEL`, but it is much more computationally efficient to use `UEXTERNALDB` since it gets called only once at the start of an increment, while UEL is called for every iteration and every user element. The Fortran90 code of the user element can be found in Appendix A.

5.2. Investigation of the finite element implementation

5.2.1. Features common to both test cases

In the following implementation, the cohesive zone length l_{cz} is calculated as the number of active elements multiplied by the element length Δl. Active elements are those that have a displacement $\delta > \delta_0$ and damage less than one, $D < 1$. The energy release rate G_a can be found as the maximum value among the energy release rates of the active elements. In its current implementation the model will therefore only work for a model with a regular mesh which is one element wide. The following FE models meet both those requirements. The main difference between the cohesive zone length calculation in this chapter and in the last is that the cohesive zone only starts once the elements reach the softening part of the constitutive law where $\delta > \delta_0$. This calculation was adapted because in mode II the number of elements where $0 < |\delta| < \delta_c$ is very large rendering the cohesive zone artificially long.
The material used for the double cantilever beam and the end loaded split simulation is HTA/6376C. Its orthrotropic material properties are shown in table 5.1. The same material has been used by Robinson et al [RGT$^+$05], Turon [TCCD07] and Harper [Har08]. The beams are modelled with threedimensional incompatible mode 8-noded brick elements (called C3D8I in ABAQUS).

Material properties		
E_{11} = 120 GPa	E_{22} = 10.5 GPa	E_{33} = 10.5 GPa
G_{12} = 5.25 GPa	G_{13} = 5.25 GPa	G_{23} = 3.48 GPa
ν_{12} = 0.3	ν_{13} = 0.3	ν_{23} = 0.51

Table 5.1.: Material properties of HTA/6376C from [ASG01]

5.2.2. Fatigue simulation of the Double Cantilever Beam

For comparing the implemented fatigue model to the actual input Paris law, a double cantilever beam specimen was simulated. The geometry is shown in figure 5.6. Table 5.2 states the interface properties and the Paris law parameters. By keep-

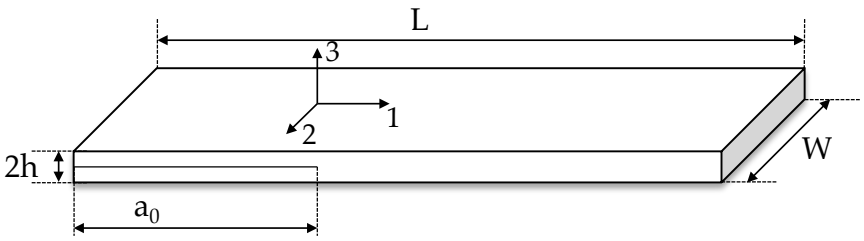


Figure 5.6.: DCB specimen, L = 50 mm, h = 1 mm, a_0 = 20 mm, W= 1 mm

Interface properties		
Fracture toughness	$G_{Ic} = 0.26\ \frac{N}{mm}$	
Interface	σ_0 = 30 MPa	K = 300,000
Paris law	C = 0.0066	m = 5.9

Table 5.2.: Mode I interface properties

ing the applied energy release rate G_a independent of crack length it is possible to generate single points on the Paris plot and then compare them to the input values. A constant G_a was achieved by loading each arm of the DCB with two forces of equal magnitude P and opposite direction at a distance d mm from each other. The applied moment to the arm of the beam is then

$$M = Pd. \tag{5.32}$$

The finite element mesh, the loading and the boundary conditions are shown in figure 5.7. The moment is related to the applied energy release rate in the following way according to [MC97]

$$G_a = \frac{M^2}{E_{11} W I} \quad , \tag{5.33}$$

where I is the second moment of area of one arm of the beam, W is the width of the beam, and E_{11} is the Young's modulus in the longitudinal direction. The simulation is performed in two steps: in a first step the quasi-static load P, where

$$P = \frac{\sqrt{G_a \cdot E_{11} \cdot W \cdot I}}{d} \tag{5.34}$$

is applied. In the second step, P is kept constant and the field for modelling the fatigue cycles described in the previous section is applied. The ABAQUS input file

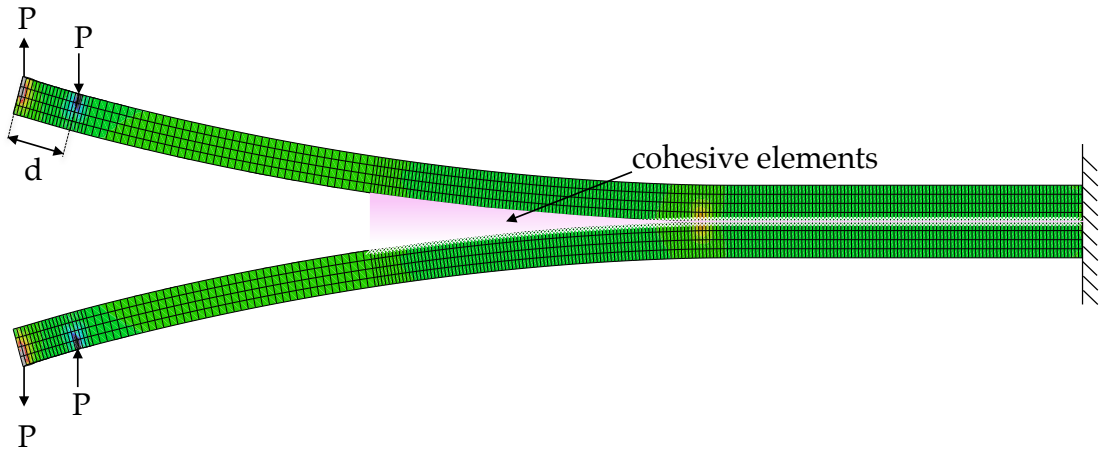


Figure 5.7.: Loading of DCB FE model

for the DCB can be found in Appendix B. The numerically predicted $\frac{da}{dN}$ vs. G_a and the input Paris law are shown in figure 5.8 together with experimental data from Asp et.al [ASG01]. In this graph, only the curve where $\Delta N = 0.2$ mm can be clearly seen to deviate from the input Paris law. The cycle-jump ΔN in the Paris plot is not

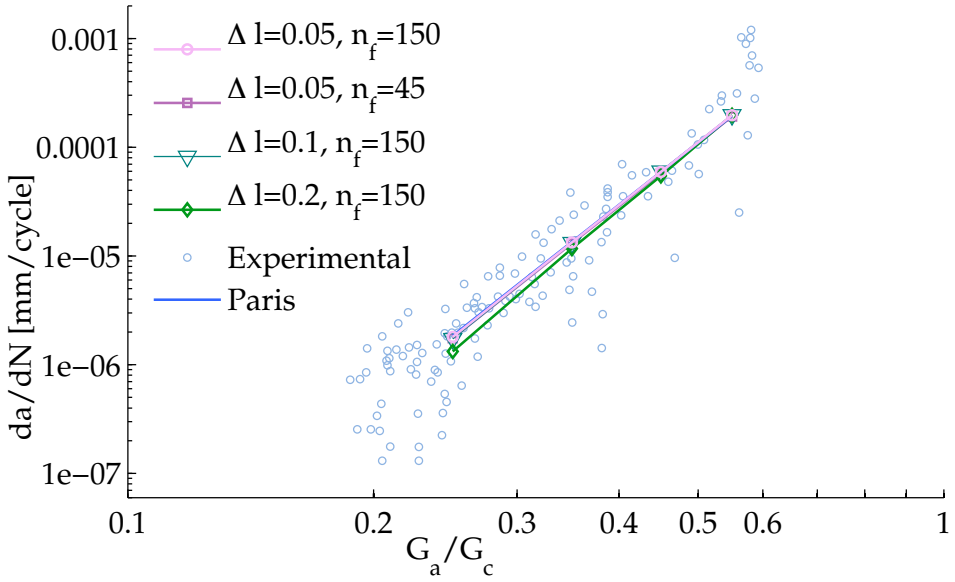


Figure 5.8.: Paris law,experimental data and numerical results

constant across the range of G_a. Instead ΔN for each loading is calculated so that an element fails within a specified number, n_f, of cycle-jump increments. This is also the number of increments it takes for the element to pass through the whole of the

cohesive zone. The cohesive zone lengths, number of elements in the cohesive zone and the cycle-jump with respect to the applied load are shown in table 5.3. The

		Elements in CZ n_{cz}			Cycle-jump ΔN	
Ga/Gc	l_{cz} [mm]	$\Delta l = 0.05$	$\Delta l = 0.1$	$\Delta l = 0.2$	$n_f = 150$	$n_f = 50$
0.25	0.4	8	4	2	1600	4900
0.35	0.53	10.5	5.5	2.5	275	815
0.45	0.63	12.5	6.5	3	75	220
0.55	0.68	13.5	7	3.5	25	75
1	1.0	20	10	5	-	-

Table 5.3.: Cohesive zone length, and cycle-jump in mode I

numerical plots show good very good agreement with the input Paris law as long as there are enough elements in the cohesive zone. The relative error with respect to the input Paris law is shown in figure 5.9. All four graphs have decreasing rel-

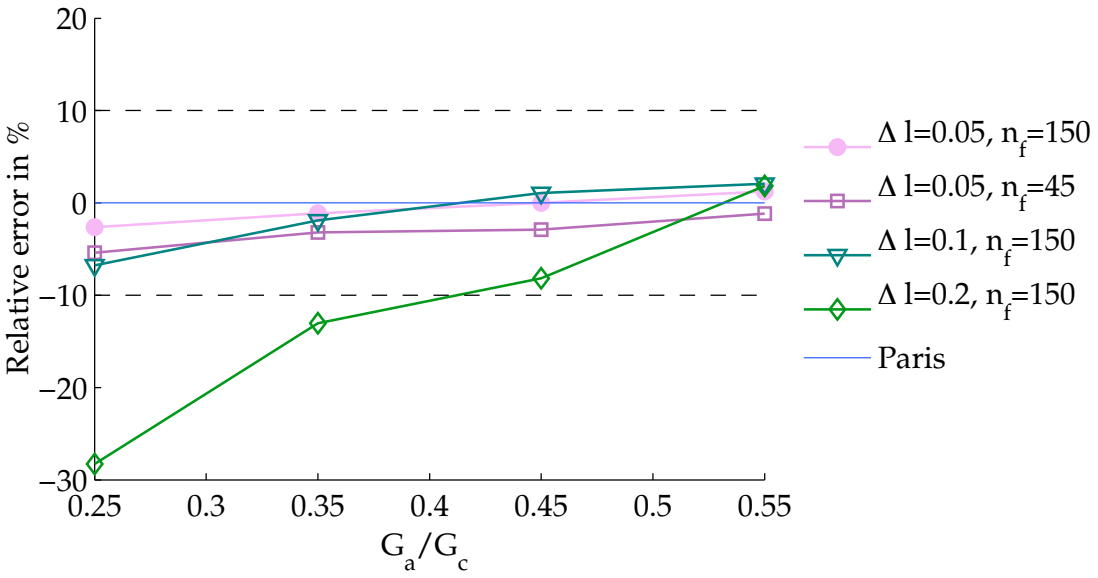


Figure 5.9.: Relative error in Paris law

ative errors (in absolute value) for increasing load levels and this decrease is most drastic when the element size is 0.2 mm. For this element size the algorithm is not able to predict the Paris law accurately (within a 10% error range) for $G_a < 0.4G_c$. This is the range where the number of elements in the numerical cohesive zone

falls below 3. Decreasing n_f and thus increasing the cycle-jump makes the relative error (again in absolute value) slightly higher. Figure 5.10 shows the constitutive behaviour of the cohesive element in fatigue for a range of applied energy release rates. The element size is $\Delta l = 0.05$ mm and the number of increments to failure

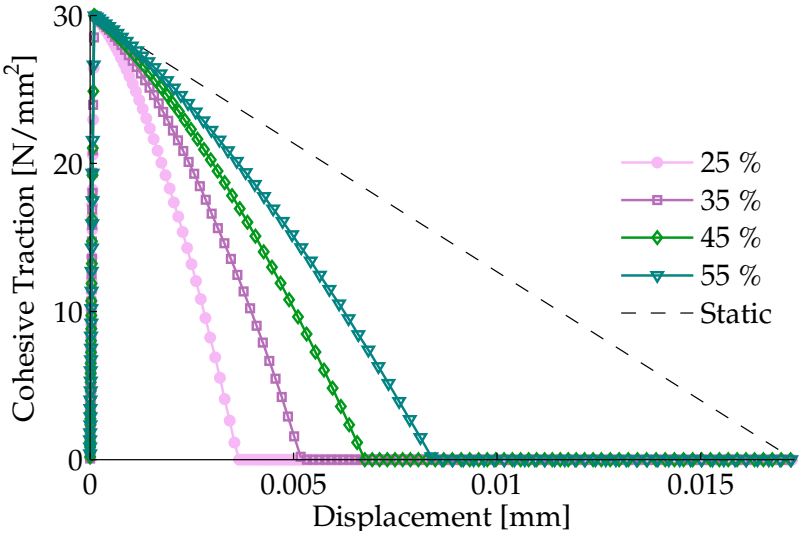


Figure 5.10.: Fatigue constitutive behaviour in mode I for a range of G_a as a percentage of G_c, $\Delta l = 0.05$ mm, $n_f = 50$

is $n_f = 50$. Figure 5.11 shows crack length vs. cycles for three different mesh sizes at $G_a = 0.25G_c$ and $n_f = 150$. In the FE model the crack length is increased by Δl, when an element fails, so the graphs have steps with the height of the element size. The crack growth rate $\frac{da}{dN}$, which is the slope of the lines is calculated by taking into account a whole number of steps.

The parameter that links the input Paris law to the cohesive element behaviour is the applied energy release rate G_a, which is shown in figure 5.12 for different applied loads with respect to the analysis increments rather than the cycles so that all graphs have the same domain on the x-axis. The element size in these graphs is $\Delta l = 0.05$ mm and $n_f = 150$. G_a is calculated as the maximum of the areas underneath the constitutive law of all integration points of all elements and is thus obtained from the crack-tip element. The value calculated for G_a is an underprediction for most increments. This is because every time a new element becomes the crack-tip element after the old crack-tip element has just failed, this new ele-

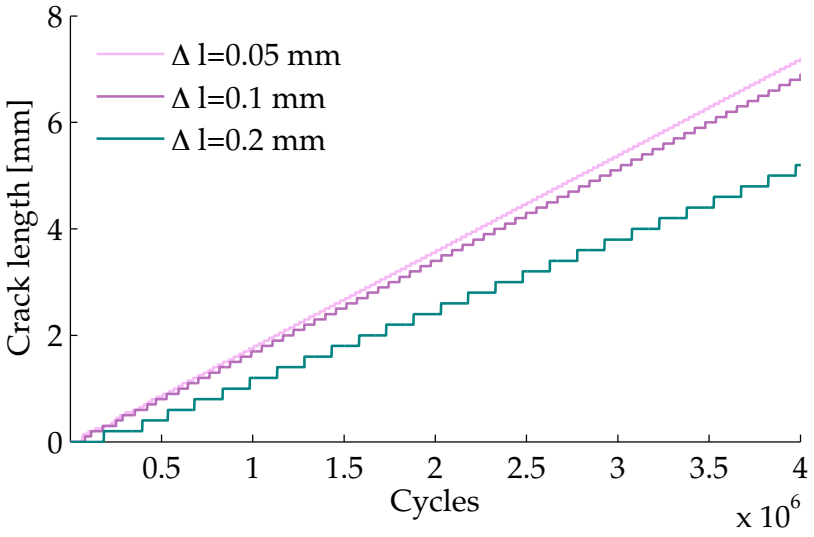


Figure 5.11.: Cycles vs. Crack growth for different mesh sizes

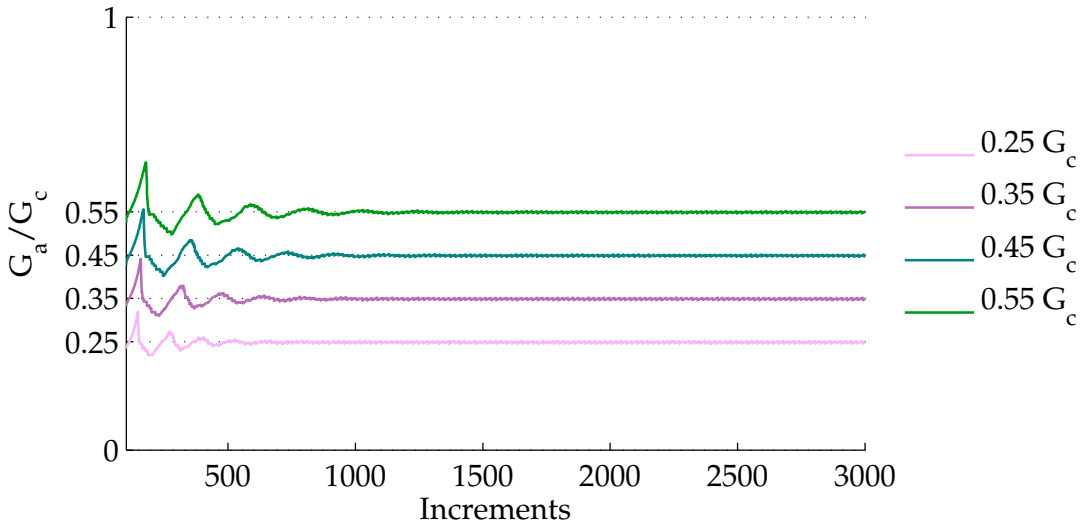


Figure 5.12.: Analysis increments vs. applied energy release rate G_a

ment has not yet reached the final and actual value of G_a, so G_a will always be most accurate just before an element fails. This causes steady-state oscillations in G_a which increase with increasing element size. Additionally to the steady-state oscillations, all four curves show pronounced oscillations at the beginning of the analysis. The peaks coincide with the crack length being a whole number of cohesive zone lengths, where the first peak corresponds to the first element failing,

and it takes about three cohesive zone lengths until the curves stabilise. However, these oscillations only have a very minor influence on the crack growth with respect to cycles (see figure 5.11), most likely because the oscillations do not significantly influence the average value of G_a, so even though the damage rate decreases and increases while an element undergoes the failure process, the average is the correct value. Figure 5.13 shows the cohesive zone length, the traction and the displacement profiles in the cohesive zone for the small and the large element size $\Delta l = 0.05$ mm and $\Delta l = 0.2$ mm respectively for $G_a = 0.25G_c$ at $N = 1,000,000$ cycles with respect to the distance from the current crack tip (the location of the last failed element). The figure shows that with only three elements in the cohesive

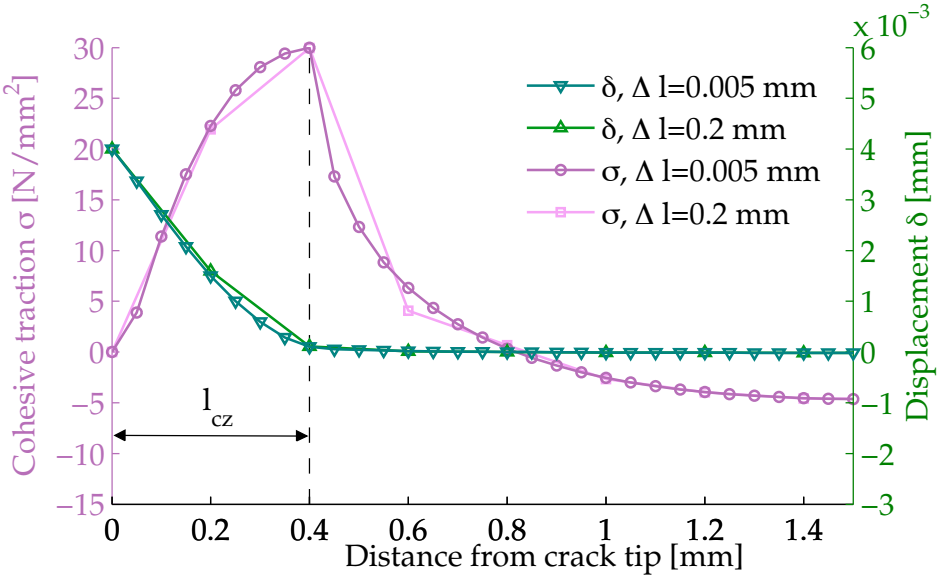


Figure 5.13.: Cohesive zone profile of traction and displacement for coarse and fine mesh at $G_a = 0.25G_c$, $N = 1,000,000$ cycles

zone, the traction and the displacement profiles can not be approximated very accurately thus leading to a significant error in the crack growth rate.

Some numerical data is available to compare the performance of the finite element implementation of this model to that of the other models. Harper [Har08], Turon [Tur06] and Robinson [RGT+05] have all used the same material HTA6376/C to simulate mode I fatigue delamination and the same experimental data on which the Paris law is based by Asp et. al [ASG01]. The interface properties which dif-

fer slightly from each other are shown in table 5.4 as well as the mesh size. The cycle-jump has not been specified in any of the three studies. A comparison of the

		new model	Harper	Turon	Robinson
G_Ic	$[\frac{N}{mm}]$	0.26	0.26	0.26	0.26
σ_0	$[\frac{N}{mm^2}]$	30	15/30	30	30
K	$[\frac{N}{mm^3}]$	$3 \cdot 10^5$	10^5	10^6	$3 \cdot 10^7$
Δl	$[mm]$	0.05	0.075	0.05	0.25

Table 5.4.: Comparison of material and interface properties between different studies

relative errors from these studies and the new model is shown in figure 5.14. The

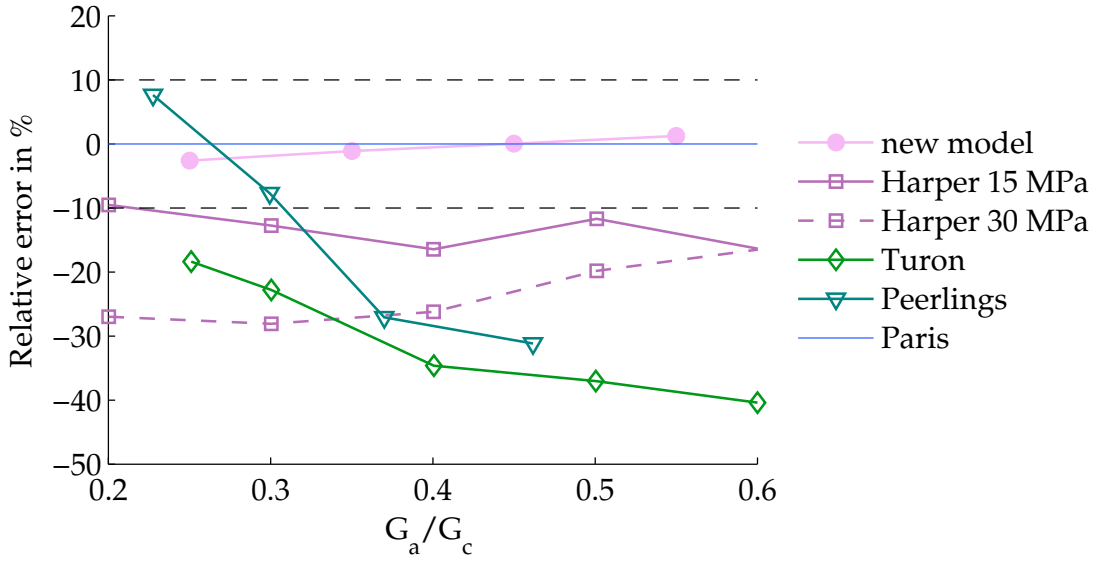


Figure 5.14.: Relative error in Paris law compared to previous models

figure demonstrates a very good performance of the new fatigue model compared to previous models. Harper 'refined the mesh' in the cohesive zone by changing the traction σ_0. For σ_0 = 15 MPa, there are 32 elements in the quasi-static cohesive zone and for σ_0 = 30 MPa there are 16 elements compared to 20 elements for the new model, ≥20 elements for the model by Turon and 8-10 in the Peerlings' model.

5.2.3. Fatigue simulation of the End-loaded split specimen

In this section, the results for mode II delamination are presented. It was simulated with an end-loaded split (ELS) test. The geometry of the specimen is shown in figure 5.15. The right-hand side of the ELS is built-in, so that L is the free length of the specimen. Table 5.5 states the interface properties and the mode II Paris law

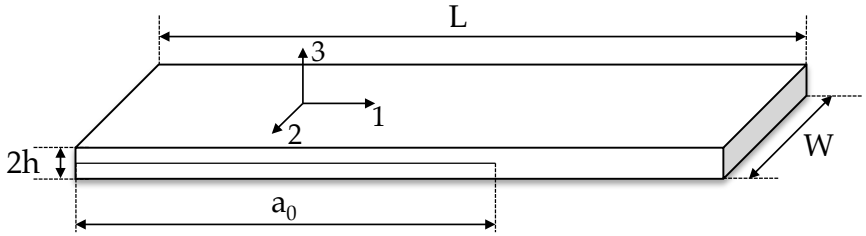


Figure 5.15.: ELSspecimen, $a_0 = 60$ mm, $L = 90$ mm, $W = 1$ mm, $h = 1$ mm

parameters. As in the double cantilever beam, the applied energy release rate was

Interface properties		
Fracture toughness	$G_{IIc} = 1.002\ \frac{N}{mm}$	
Interface	$\sigma_0 = 60$ MPa	$K = 300{,}000$
Paris law	$C = 0.1392$	$m = 4.46$

Table 5.5.: Mode II interface properties

kept independent of crack length by applying two loads P of opposite direction (see figure 5.16) at a distance $d = 3$ mm to each arm, so that each arm is loaded with a moment

$$M = P \cdot d. \tag{5.35}$$

The finite element mesh, the loading and the boundary conditions are shown in figure 5.16. The moment in mode II is related to the energy release rate G_a according to [RDW04] in the following way

$$G_a = \frac{3}{4} \frac{M^2}{W \cdot E_{11} \cdot I} \tag{5.36}$$

where W is the width of the beam, I the second moment of area of one arm, and E_{11} the Young's modulus in the longitudinal direction. The load P with respect

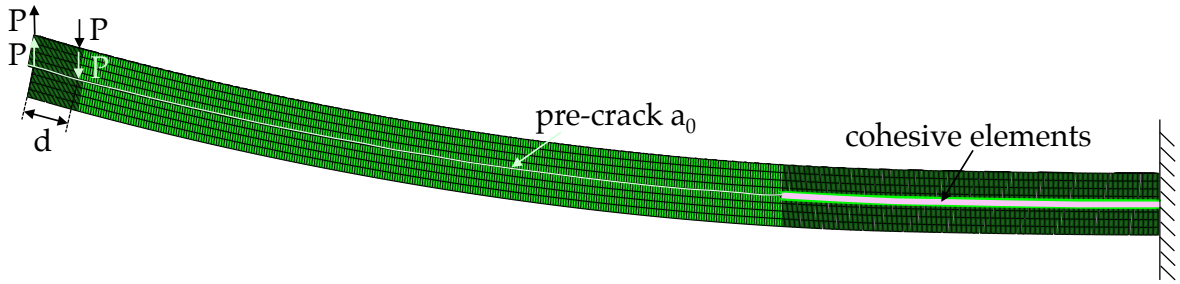


Figure 5.16.: Loading of ELS FE model

to the desired energy release rate G_a can then be calculated from equations (5.35) and(5.36) as

$$P = \frac{1}{d}\sqrt{\frac{4}{3}G_a \cdot W \cdot E_{11} \cdot I}. \tag{5.37}$$

As with the DCB, the loading is applied in one quasi-static step where the load is ramped up to P followed by a fatigue step with constant load P. The numerically predicted $\frac{da}{dN}$ vs. G_a plots and the input Paris law are shown in figure 5.17 together with experimental data from [ASG01] for three different element sizes Δl and three different values of the number of increments to failure n_f. Since the cohesive zone

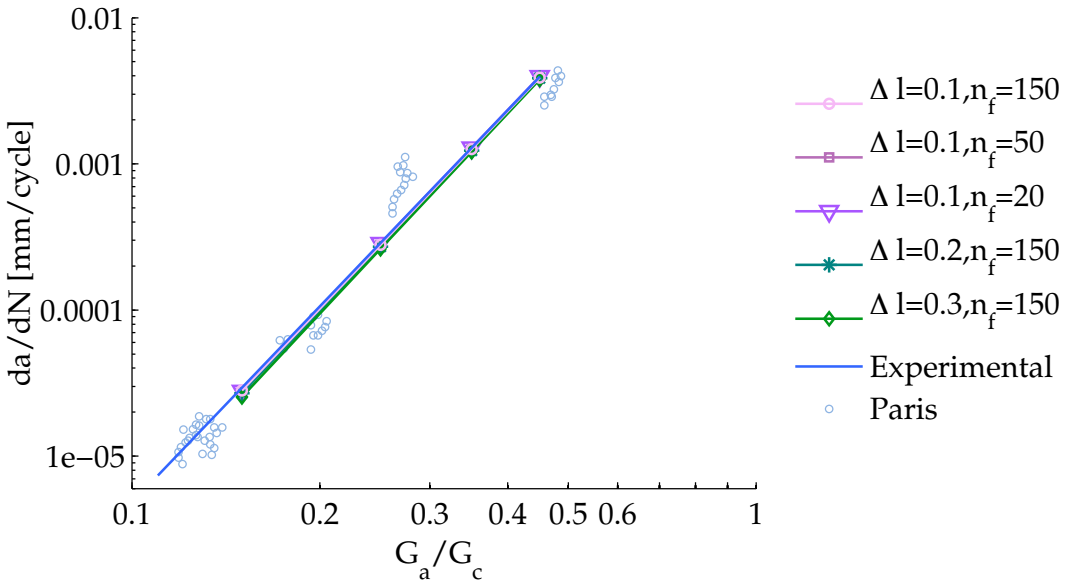


Figure 5.17.: Paris law, experimental data, and numerical results

length in mode II is much higher, the element sizes are greater than for mode I. Table 5.6 shows the cycle-jump ΔN corresponding to n_f and the number of elements

in the cohesive zone at different loads. All curves in figure 5.17 show good agree-

		Elements in CZ n_{cz}			Cycle-jump ΔN		
Ga/Gc	l_{cz} [mm]	Δl=0.1	Δl=0.2	Δl=0.3	n_f=150	n_f=50	n_f=20
0.15	1.05	10.5	5.5	3.5	238	714	1784
0.25	1.45	14.5	7.5	5	34	101	253
0.35	1.8	18	9	6	10	29	72
0.45	2.15	21.5	11	7	4	11	28
1	3.8	38	19	13	-	-	-

Table 5.6.: Cohesive zone length, and cycle-jump in mode II

ment with the input Paris law. The relative error with respect to the Paris law is shown in figure 5.18. With respect to the number of elements in the cohesive zone,

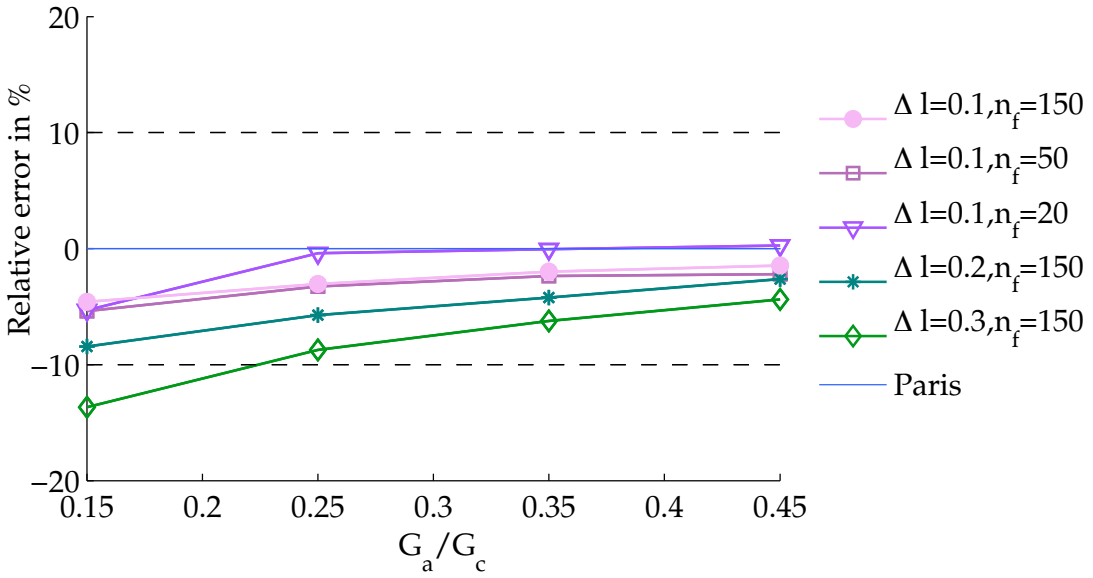


Figure 5.18.: Relative error in Paris law

the errors (in absolute value) are slightly higher than for mode I. Also, while the errors in mode I become positive for higher load levels, all the errors in mode II are negative. The algorithm is able to predict the Paris law within a 10% error if there are more than 4 elements in the cohesive zone, which is the same number required as in mode I. Also analogous to mode I, the error can be seen to decrease with a lower mesh size and with increasing load levels. Both a lower mesh size

and higher load levels lead to a higher number of elements in the cohesive zone n_{cz}, but n_{cz} is not the only factor influencing the error since the error is lower (in absolute value) for $\Delta l = 0.2$ mm and $G_a = 0.45G_c$ ($n_{cz} = 7$) than for $\Delta l = 0.1$ mm and $G_a = 0.15G_c$ ($n_{cz} = 10.5$). There are three curves with the same mesh size but different cycle-jumps. For $n_f = 150$ and $n_f = 50$ there is only a very small difference in error, suggesting that increasing the cycle-jump beyond $n_f = 50$ is unnecessary. However, for $n_f = 20$, which is the coarsest cycle-jump, the error is lower than for the other two curves. This is probably due to the fact that for a higher ΔN the difference in the relative displacements for an element from one increment to the next is greater, so when the crack-tip element fails, the final displacement δ_f is greater. This means that G_a is slightly over predicted leading to a slightly higher value of $\frac{da}{dN}$ which counteracts the general under prediction of G_a and in this case, for $G_a > 0.25G_c$ the two effects cancel each other and lead to very little error. Refining the time-increment therefore does not necessarily lead to a lower error. The constitutive response in fatigue for the four different load levels is shown in figure 5.19 for an element size $\Delta l = 0.1$ mm and $n_f = 50$. Applying the loading as

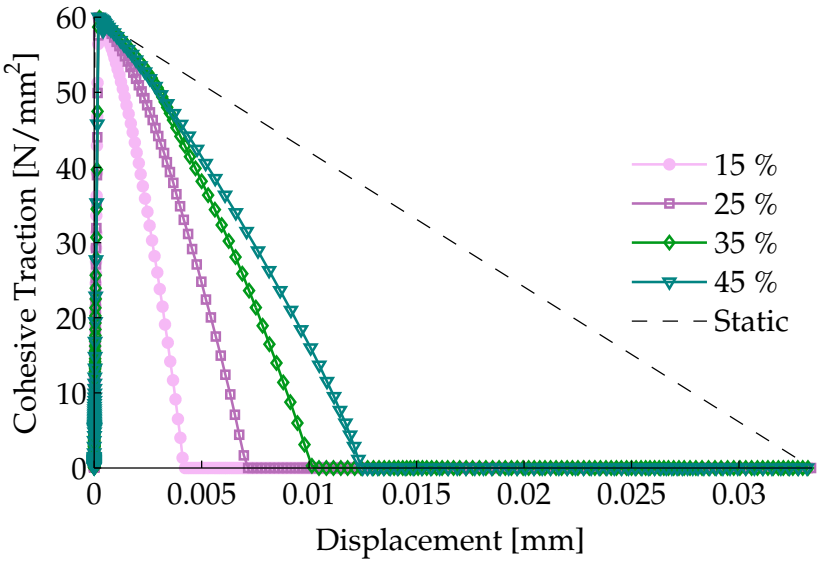


Figure 5.19.: Fatigue constitutive response in mode II for a range of G_a as a percentage of G_c, $\Delta l = 0.1$ mm, $n_f = 50$

shown in figure 5.16 leads to negative relative displacements and therefore negative

tractions. However, for better readability and an easier comparison to mode I, the curves have been reflected about the origin, which corresponds to reversing the direction of P. Although the interface parameters differ from those for mode I and the loading range is different, the curves are qualitatively similar to those in figure 5.10. Figure 5.20 shows crack length vs. cycles for different values of n_f with $\Delta l = 0.1$ mm. The final crack-length is 8 mm, which is the same shown in mode I. For both

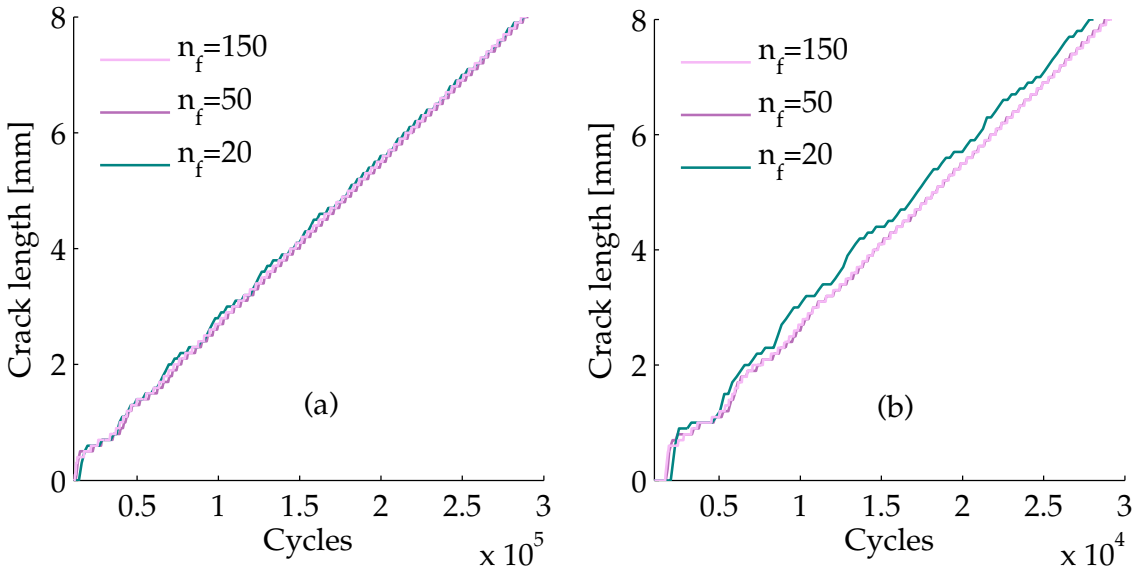


Figure 5.20.: Crack growth vs. Cycles, (a) $G_a = 0.15G_c$, (b) $G_a = 0.25G_c$

load levels the curves show oscillations, but for $G_a = 0.25G_c$ the crack growth rate is slightly higher and the oscillations are more distinct for the coarser cycle-jump, than for $G_a = 0.15G_c$, where all three curves are very similar. As opposed to the mode I curves, these crack- growth curves show slight oscillations at the beginning which gradually become smaller. Figure 5.21 shows the applied energy release rate calculated from the area under the cohesive stress-displacement response of the crack tip element for different loads with respect to the analysis increments. Again, the curves look qualitatively similar to those in figure 5.12. As in mode I there are large oscillations at the start of the analysis which peak when the crack length has reached a multiple of the cohesive zone length. The number of cohesive zone lengths it takes for the crack to grow until the oscillations become quite small is the same as in mode I: three cohesive zone lengths. Since the cohesive zone in mode II

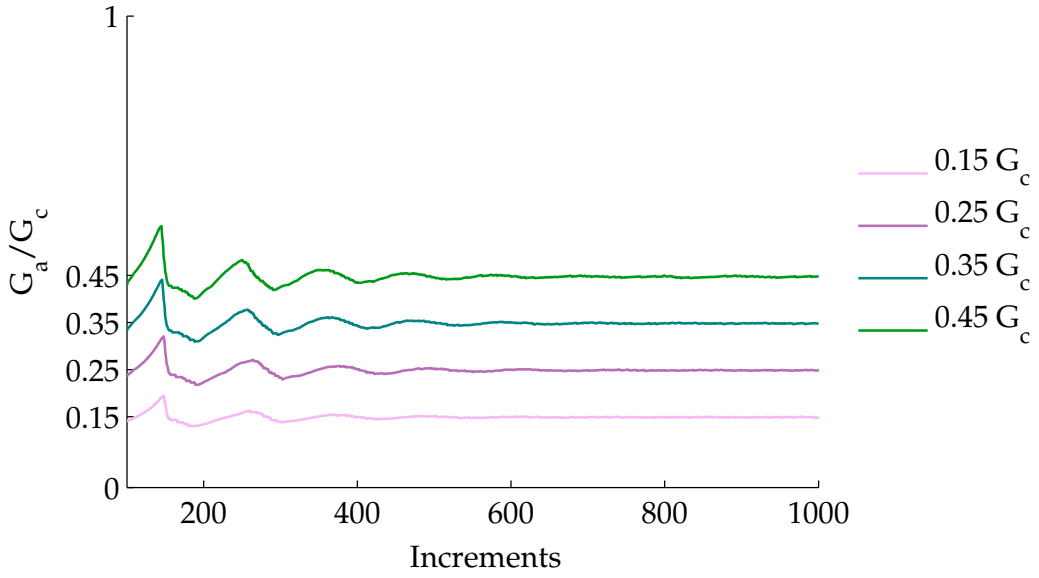


Figure 5.21.: Analysis increments vs. applied energy release rate G_a for $\Delta l = 0.1$ mm, $n_f = 150$(obtained from crack tip)

is almost four times as long as in mode I, the crack has to grow four times longer before the oscillations die down. This explains why the cycles vs. crack growth curves are slightly wavy in mode II (figure 5.20) but not in mode I (figure 5.11) . Figure 5.22 shows the cohesive zone length, the traction and the displacement profiles in the cohesive zone for the small and the large element size $\Delta l = 0.1$ mm and $\Delta l = 0.3$ mm respectively for $G_a = 0.15G_c$ at $N = 1,000,000$ cycles with respect to the distance from the current crack tip (the location of the last failed element). The figure shows that with only three elements in the cohesive zone, the traction and the displacement profiles can not be approximated very accurately as in mode I which leads to a significant error in the crack growth rate. Numerical data is available for mode II to compare the finite element implementation of the model with those of the previous models by Harper, Turon and Robinson. The material properties are again the same in all the four implementations and the Paris law is based on data by [ASG01]. The interface properties used for the different implementations are summed up in table 5.7. The number of elements in the cohesive zone for the new model was $n_{cz} = 38$. Harper [Har08] performed simulations for two different mesh sizes $\Delta l = 0.125$ mm and $\Delta l = 0.25$ mm. With a quasi-static cohesive zone-

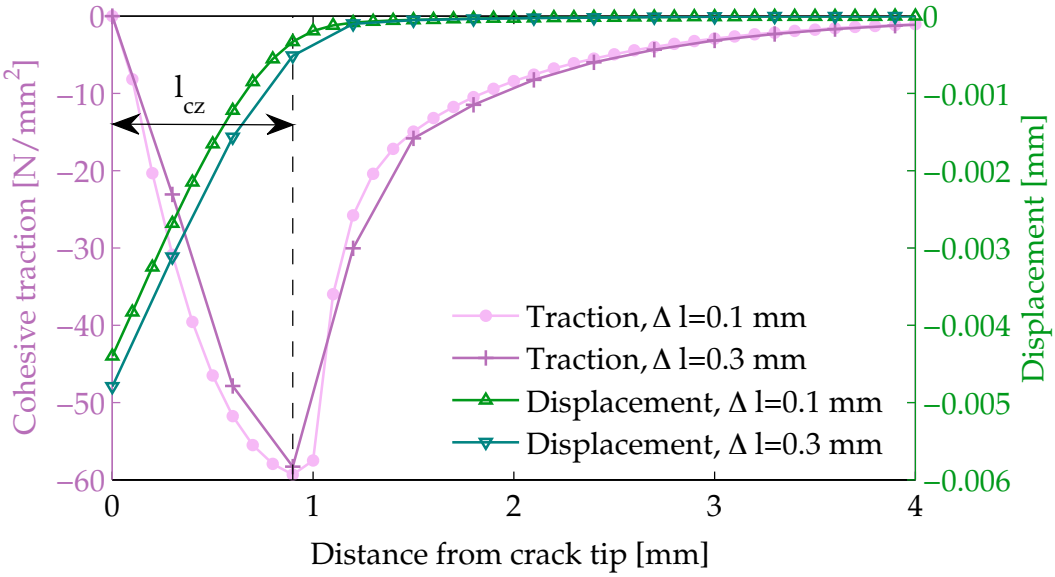


Figure 5.22.: Cohesive zone profile of traction and displacement for coarse and fine mesh at $G_a = 0.15G_c$, $N = 1,000,000$ cycles

		new model	Harper	Turon	Robinson
G_{IIc}	$[\frac{N}{mm}]$	1.002	1.002	1.002	1.002
σ_0	$[\frac{N}{mm^2}]$	60	60	30	30
K	$[\frac{N}{mm^3}]$	$3 \cdot 10^5$	10^5	10^6	$1.18 \cdot 10^8$
Δl	$[mm]$	0.1	0.125/0.25	0.05	-

Table 5.7.: Comparison of material and interface properties between different studies, mode II

length of $l_{cz} = 4.1$ mm, the number of elements in the cohesive zone was $n_{cz} = 33$ and $n_{cz} = 16$ respectively. The results for both mesh sizes differ very little from each other so only one curve ($\Delta l = 0.125$ mm) is included here. Turon used a mesh size of $\Delta = 0.05$ mm. The cohesive zone length is unknown, but given he used the same material and a similar model $n_{cz} \approx 60$. For the implementation by Robinson et al the mesh size is unknown. None of the studies specify the cycle-jump. Figure 5.23 shows a comparison of the error for the different implementations. Compared to the previous studies, the new model performs very well. The error in the new model is slightly higher than for mode I but the relative errors of the other models

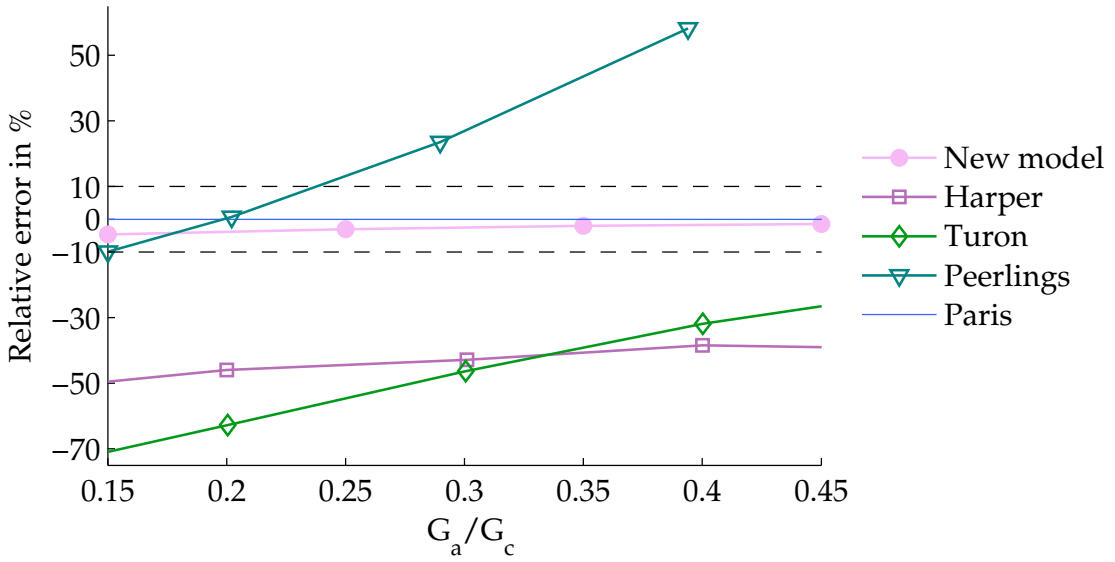


Figure 5.23.: Relative error in Paris law compared to previous models

are significantly larger with the maximum error in the Turon model being about 70 % even though it probably has the finest mesh.

5.3. Conclusion

In this chapter, details of the implementation of a cohesive element for modelling high-cycle fatigue delamination into the finite element software ABAQUS have been presented and an outline has been given of one possibility to apply cycle jumps to ABAQUS models. The fatigue degradation strategy incorporated into the element is the new failure model proposed in the previous chapter. The cohesive element has then been used to simulate delamination of a double cantilever beam and an end-loaded split test to demonstrate its ability to predict the Paris law behaviour in mode I and mode II respectively.

The results demonstrate very good performance of the finite element simulations in both mode I and mode II. The model is able to predict the Paris law correctly to within a 10 % error as long as there are at least 4 elements in the cohesive zone. The model has been tested with several values for the number of cycle jumps to fail one element n_f and the element size Δl. In mode I, decreasing n_f and thus increasing

the cycle-jump leads to a slightly higher error. In mode II where the relative error is generally negative, increasing the cycle-jump led to an improvement in the error for the very low value $n_f = 20$.

Both in mode I and mode II, the new fatigue failure model was compared to the original FE implementations of the Peerlings' model, the Turon model and the Harper model which were examined with the cylinder model in chapter 3. All three simulations were of similar specimens with the same material properties and Paris law, and with similar interface properties (see tables 5.4 and 5.7 for mode I and mode II respectively). The comparison demonstrated that the new failure model presents a significant improvement over the previous fatigue delamination strategies (for mode I see figure 5.14 and for mode II figure 5.23). The fourth strategy examined in chapter 3, the Kawashita/Hallett model, was not included in this comparison because a different Paris law and different material properties were used for the simulation but its performance in the cylinder model implementation suggests a similarly good prediction of the Paris law.

6. Conclusions and Future Work

6.1. Conclusions

6.1.1. Comparison of existing fatigue models

The first objective of this PhD was a detailed investigation and comparison of existing models for high-cycle fatigue-driven delamination using cohesive zone models. To this end, four models have been examined in mode I using the simple non-FE cylinder model to see whether they can reproduce the Paris law. This examination goes above the previous study by Lopez-Armas [Arm08] in three points: firstly, two additional models have been examined. These are the Harper and the Kawashita/Hallett model. Secondly, in the previous examination sensitivity studies were only conducted for a one value of the applied energy release rate. Thirdly, in this thesis a clear comparison is made between the models and advantages and disadvantages of each strategy are highlighted. In this PhD, sensitivity studies across a range of energy release rates were performed so that the accuracy of the models could be compared in terms of varying cycle-jump and element size, which was not done previously. The investigation also revealed that demonstrating the accuracy of a fatigue model by plotting the crack growth vs. applied energy release rate on a log-log plot next to the Paris law which is the current standard (see [RGT$^+$05], [Tur06], [Har08]) is insufficient. This is because large errors are hard to identify on a log-log plot (see figure 3.1). In this study the error of the models with respect to the Paris law have therefore been plotted on linear axes giving a nuanced impression of the accuracy of a strategy.

The detailed analyses revealed a more detailed picture of the performance of these strategies. All four models have advantages and drawbacks.

The point-local Peerlings' model predicts the Paris law accurately as long as the energy release rate is not too high. However, the input parameters have to be calibrated first to fit a specific Paris law.
The Turon model is not point-local and has the Paris law and the cohesive zone length as an input. It is fast and its greatest advantage is that it is the only model where the cycle-jump is adapted to changing load-levels. It is possible though to use a fixed cycle-jump in the Turon model and also to adapt the cycle-jump in the other models. The Paris law exponent could not be accurately reproduced with this model. Also, when the actual cohesive zone length was used, rather than a prediction, it was found that the length had to be selected to achieve a close approximation of the Paris law exponent.
The model by Harper is point-local. The Paris law exponent could not be accurately reproduced even when the ratio of fatigue length to total cohesive zone length was adjusted. Another problem with this model is the estimation of the cohesive zone length under fatigue as a fraction of the static cohesive zone length.
The model by Kawashita and Hallett is not point-local and requires as input only the Paris law. It has the lowest error rates and is very fast. Combining a fine mesh with a high cycle-jump causes a high error and has to be avoided. However, the model was originally implemented in an explicit finite element code where the time steps are small so this would not be a problem. An algorithm is required that keeps track of the crack-tip element and the current applied energy release rate needs to be exchanged between the cohesive elements. This algorithm allows for the simulation of 3D delamination cases. The advantages and disadvantages of all the models have been summarised in table 3.14.

6.1.2. Improvement to existing fatigue models

The second objective of the PhD was to find possible improvements or design flaws in the examined models based on the previous investigation.
Improvements have been proposed for the Peerlings' and the Turon models and tested in the cylinder model.
One of the main disadvantages of the Peerlings' model is its speed. A faster al-

ternative has been proposed and implemented into the cylinder model. This was achieved by calculating the accumulation of fatigue damage explicitly rather than implicitly. Studies with the cylinder model show that the loss of accuracy is very small compared to the previous implementation (less than 0.5%). However, the model runs 20 times faster. The other big disadvantage of this model is the need to calibrate five fatigue parameters. An alternative formulation for the fatigue damage accumulation was proposed which requires only two parameters to be calibrated, making the model calibration much easier to use. The implementation in the cylinder model suggests that care has to be taken for big cycle-jumps where this new damage formulation leads to a significant error (up to 50%) in the Paris law.
For the Turon model a different way of calculating the applied energy release rate was proposed. Previously, the static constitutive response law was used to calculate the applied energy release rate G_a during each step, while in the new implementation G_a is calculated from the fatigue response. This change leads to a more accurate numerical Paris law. In the original implementation the relative error in the crack growth rate was up to 20% while in the improved formulation it is less than 5% (see figure 4.13).

6.1.3. Development of an improved fatigue model

The third and one of the main objectives of the thesis was to develop a fatigue degradation strategy.
This objective was also carried out using the cylinder model. Compared to a full FE model the cylinder model has the great advantage that it is possible to try adaptations to old fatigue degradation strategies and new strategies very quickly and efficiently. This has led to numerous ideas for new strategies, which eventually turned out to be unsuccessful. The biggest problem in the development of a new degradation strategy was the transition of the simulation from an initial static equilibrium where the elements follow the static constitutive law to a steady state where the elements follow the fatigue constitutive response. A brief outline of some of these ideas has then been presented. In order to develop a new model it was essential to define the necessary conditions for a fatigue model to give an accurate representa-

tion of the Paris law. These involve calculating the number of cycles it takes to fail an element in the cohesive zone which is dependent on the cohesive zone length, the applied energy release rate and the input Paris law (equations (4.8),(4.9)). Based on these conditions, a new degradation strategy for cohesive elements was devised for the simulation of high-cycle fatigue-driven delamination. This strategy does not require any calibration like the Peerlings' model, only needs the Paris law as input like the Kawashita/Hallett model, and does not require knowledge of the position of the crack-tip. The investigation with the cylinder model demonstrated that the Paris law can be predicted very accurately. A sensitivity study was then undertaken to examine the relative error in the numerical Paris law for various element sizes and cycle-jumps and it was demonstrated that the model is not very sensitive to changes in element size and cycle-jump in mode I. This fatigue degradation strategy was then chosen to be implemented into FE model.

6.1.4. Finite element implementation of the new fatigue model

The fourth objective was to implement the chosen fatigue degradation strategy into the FE software ABAQUS.

Details of this implementation have been presented in chapter 5. The new fatigue degradation strategy was incorporated into a user-defined element (UEL) written in Fortran 90 and the cohesive element was used to simulate fatigue-driven delamination in a double cantilever beam and an end-loaded split specimen. The results demonstrate very good accuracy of the finite element simulations in both mode I and mode II. The model is able to predict the Paris law correctly to within a 10 % error as long as there are at least 4 elements in the cohesive zone. In mode I, increasing the cycle-jump leads to a slightly higher error. In mode II where the relative error is generally negative, increasing the cycle-jump led to an improvement in the error (see figures 5.9 and 5.18).

Both in mode I and mode II, the new failure model was compared to other published FE-based simulations of fatigue-driven delamination of similar specimens with the same material properties and Paris law, and similar interface properties. The comparison demonstrated that the new failure model presents a significant im-

provement over the three existing fatigue delamination strategies it was compared to (see figures 5.14 and 5.23 for mode I and mode II respectively). One of the strategies examined in previous chapters- the crack-tip tracing model- was not included in this comparison because a different Paris law and different material properties were used for the FE simulation. A comparison of the crack tip tracing model and the new model using the cylinder model suggests similar good predictions of the Paris law. The Kawashita/Hallett model requires an additional algorithm to locate the position of the crack tip, which is not necessary in the new fatigue failure model. However, this crack-tip tracing algorithm makes it applicable to full 3D crack propagation and curved crack fronts. The new model in its current form is not applicable to these simulation cases.

6.2. Suggestions for future work

6.2.1. Further improvements of the new fatigue degradation strategy

Resolving current problems

The model was shown to have oscillations in the crack length vs. cycles graph, which are due to the transition from a quasi-static equilibrium to the fatigue steady state. After the static equilibrium is found, the area under the constitutive response of the first element is G_a. Therefore, the element should fail instantly according to the fatigue algorithm. However, the relative displacement increases and so G_a is over-predicted, which cause the biggest oscillation at the beginning of the fatigue analysis. One obvious possibility to try to avoid this initial over-prediction is to artificially apply fatigue loading cycles during the initial static step, so that when 'static' equilibrium is found, the remaining cohesive traction is so low that the first element is about to fail. However, it is difficult to estimate how many 'cycles' should be applied and even then the oscillations did not disappear, because the constitutive response of the first element achieved in this way was not identical to the steady-state even though the area underneath the stress-displacement graph was correct. The model has not been tested under non-constant fatigue loading, where the constitutive response also changes shape but it is likely that there would also be oscillations in the crack vs. cycles curve.

Mixed-mode adaptation

In order to make it applicable to more realistic loading cases, the proposed new fatigue degradation strategy should be modified to be able to be able to take into account mixed-mode delamination. This could be achieved by using the model by Blanco for the mixed-mode Paris law [BGAC04] which has successfully been used before and mixed-mode criterions proposed by Camanho et al. [CD02].

Refinement of the Paris law

The Paris could also be adapted to consider the R-ratio as has previously been done by Allegri et al. [AJMH11]. There also exist variations that extend its validity to all three regions of fatigue crack propagation for example the model by Martin et al. [MM90] could be incorporated into the current implementation.

More general loading cases

The analysis cases considered in this PhD do not contain the full complexity of a curved delamination front. The model requires as input the cohesive zone length l_{cz}. For a 3D delamination the cohesive zone length would have to be defined in a new way from the current procedure where only the number of active elements is counted. In addition to the active number of elements a direction of delamination would be required in order to determine the process zone.

Cohesive element formulation

Studies on the use of cohesive elements have shown that one of the drawbacks of this method is the need for a relatively fine mesh with at least four elements in the cohesive zone. This makes cohesive zone models computationally quite expensive. A recent study by Alvarez et al. [ÁBGK14] suggests that using higher-order cohesive elements may alleviate the problem of excessive mesh refinement. The fatigue degradation strategy could also be implemented into a quadratic cohesive element which might allow for a coarser mesh.

Validation

Finally, the fatigue degradation strategy should be validated against experimental results in a more complex simulation than the fatigue delamination of a DCB or ELS specimen, for example the delamination of a stiffener runout.

6.2.2. Reliance on experimental data and data acquisition

One big drawback of the models on high-cycle fatigue delamination is their reliance on the Paris law. Even though it has been shown in the literature to be applicable to the simulation of delamination in composites, the fact remains that the Paris law is phenomenological in nature and provides no insight into the actual physical processes that lead to fatigue delamination. Experimental data has to be acquired for each material system and then the Paris law has to be curve-fitted and there is currently only an experimental test standard for measuring the delamination growth onset which is then adapted to measure crack propagation under cyclic loading in composites. The experimental data always has much scatter, so one step towards improving the reliability of these models is to improve experimental techniques on one hand to reduce scatter. On the other hand the statistical distribution of the data should be considered in the model and stochastical sensitivity studies should be performed.

6.2.3. Alternative numerical techniques

In this PhD the fatigue model has been implemented into a commercial finite element software with an interface element. Cohesive elements have two advantages: there is no need for remeshing during the analysis and it is possible to capture the crack initiation. The extended finite element method promises an even more flexible approach because cracks can grow within an element. XFEM is now available in some commercial finite element packages, and presents a possible alternative to cohesive elements for future implementations of degradation strategies for high-cycle fatigue-driven delamination.

A. User-defined element (UEL) for modelling mode I fatigue delamination in ABAQUS

```
SUBROUTINE UEL(RHS,AMATRX,SVARS,ENERGY,NDOFEL,NRHS,NSVARS,PROPS,NPROPS,
    COORDS,MCRD,NNODE,U,DU,V,A,JTYPE,TIME,DTIME,KSTEP,KINC,&
JELEM,PARAMS,NDLOAD,JDLTYP,ADLMAG,PREDEF,NPREDF,LFLAGS, MLVARX,DDLMAG,
    MDLOAD,PNEWDT,JPROPS,NJPROP,PERIOD)
!ABAQUS 6.10 user element for threedimensional analysis of fatigue
    delamination in mode I using an eightnoded cohesive element.
!The position of the nodes is as follows in the local coordinate system:
!Node1=Node5(-1,-1), Node2=Node6(1,-1), Node3=Node7(1,1), Node4=Node8
    (-1,1)

!This subroutine is to simulate mode I fatigue
!The cohesive element number in the input file must not exceed 1000 (
    otherwise change dimensions in common block in UEL & UEXTERNALDB)
!There are 8 real input properties, these are GIc sigmaI_0 K Ex Ey C m
    Delta_l
!and one integer input property: NlGeom
!There are 20 SVARS
!These are (in blocks of 4, one variable for each integration point)
!Total damage (1-4)
!deltaI (5-8)
!sigma (9-12)
!Fatigue damage (13-16)
!Ga (17-20)

IMPLICIT NONE
```

```
TYPE Int_point
  DOUBLE PRECISION Coordinates(2)
  DOUBLE PRECISION weight
END TYPE Int_point

!Variables from ABAQUS

INTEGER, INTENT(in)              ::NDoFEl !Number of degrees of freedom
INTEGER, INTENT(in)              ::NRHS   !Number of right hand sides
INTEGER, INTENT(in)              ::NSVars !Number of userdefined variables
DOUBLE PRECISION, INTENT(in)     ::Props(*) !real property values
INTEGER, INTENT(in)              ::NProps  !Number of real property values
DOUBLE PRECISION, INTENT(in)     ::Coords(MCRD,*) !element coordinates
INTEGER, INTENT(in)              ::MCRD !dimension or something
INTEGER, INTENT(in)              ::NNode !number of nodes
DOUBLE PRECISION, INTENT(in)     ::U(NDOFEL) !displacements
DOUBLE PRECISION, INTENT(in)     ::DU(MLVARX,*) !incremental displacements
DOUBLE PRECISION, INTENT(in)     ::V(NDOFEL) !Velocities
DOUBLE PRECISION, INTENT(in)     ::A(NDOFEL) !Accelerations
INTEGER, INTENT(in)              ::JType !element type
DOUBLE PRECISION, INTENT(in)     ::Time(2) !(current step time,total time)
DOUBLE PRECISION, INTENT(in)     ::DTime !time increment
INTEGER, INTENT(in)              ::KStep !current step number
INTEGER, INTENT(in)              ::KInc !current increment number
INTEGER, INTENT(in)              ::JElem !user-assigned element number
DOUBLE PRECISION, INTENT(in)     ::Params(*) !solution procedure paras
INTEGER, INTENT(in)              ::NDLoad !id of active distributed load
INTEGER, INTENT(in)              ::JDLTyp(MDLOAD,*) !distr. load types
DOUBLE PRECISION, INTENT(in)     ::ADLMag(MDLOAD,*) !distr. load magnitude
DOUBLE PRECISION, INTENT(in)     ::Predef(2,NPREDF,NNODE)
INTEGER, INTENT(in)              ::NPredf !Number of predefined variables
INTEGER, INTENT(in)              ::LFlags(*) !current solution procedure
INTEGER, INTENT(in)              ::MLVarX !dimensioning for RHS
DOUBLE PRECISION, INTENT(in)     ::DDLMag(MDLOAD,*) !inc distr load
INTEGER, INTENT(in)              ::MDLoad !number of distributed loads
DOUBLE PRECISION, INTENT(inout) ::PNewDT !ratio of new time increment
INTEGER, INTENT(in)              ::JProps(NJprop) !integer property values
```

```
INTEGER, INTENT(in)              ::NJProp !no. integer property values
DOUBLE PRECISION, INTENT(in)     ::Period !time period of cureent step
DOUBLE PRECISION, INTENT(out)    ::RHS(Mlvarx,NRHS) !residual vectors
DOUBLE PRECISION, INTENT(out)    ::AMatrx(NDoFel,NdoFel) !stiffness matrix
DOUBLE PRECISION, INTENT(out)    ::SVars(Nsvars) !solution state variables
DOUBLE PRECISION, INTENT(out)    ::Energy(8) !energy

!User element variables
INTEGER,Parameter           ::No_Int_points=4 !No. integration points
INTEGER                     ::Int_number      !current int point number
INTEGER                     ::NLGeom          !Nonlinear Geometry
DOUBLE PRECISION            ::sigmaI_0!interfacial strength mode I
DOUBLE PRECISION            ::GIc   !fracture toughness mode I
DOUBLE PRECISION            ::Ex,Ey !Elastic stiffness inplane
DOUBLE PRECISION            ::K !Initial elastic stiffness
DOUBLE PRECISION            ::sigma(3) !Interface stresses
DOUBLE PRECISION            ::delta(3) !Interface displacements
DOUBLE PRECISION            ::Shape(NNode)!shape func values at int point
DOUBLE PRECISION            ::Deriv(2,NNode) !shape func derivatives
DOUBLE PRECISION            ::JMatrix(2,3) !Jacobean Matrix
DOUBLE PRECISION            ::Bmatrix(3,Ndofel)!Shape function matrix B
DOUBLE PRECISION            ::DMatrix(3,3) !D Matrix
DOUBLE PRECISION,ALLOCATABLE::DTanMatrix !Tangent stiffness matrix
DOUBLE PRECISION            ::v3_norm ! norm of v3, ||v3||
DOUBLE PRECISION            ::v_loc(3,3) !vectors on element surface
DOUBLE PRECISION            ::Coordinates(2) !Coords of integration point
DOUBLE PRECISION            ::tDamage !total damage
DOUBLE PRECISION            ::fDamage !fatigue damage
DOUBLE PRECISION            ::prevDamage !Damage from last increment
DOUBLE PRECISION            ::prevdelta,prevGa !Values previous incs
DOUBLE PRECISION            ::prevsigma,prevdamfat !Values previous incs
INTEGER                     ::i,j,l,ii
DOUBLE PRECISION            ::Cycles !Current no. cycles,Predef(1,1,1)
DOUBLE PRECISION            ::DeltaN !Current cycle inc,Predef(2,1,1)
DOUBLE PRECISION            ::Ga
INTEGER                     ::Fatigue!switch (0-No fatigue, 1-Fatigue)

!COMMON block variables for UEL
```

```
DOUBLE PRECISION :: C !Paris law constant (out)
DOUBLE PRECISION :: m !Paris law constant (out)
DOUBLE PRECISION :: Delta_l !Element size (out)
DOUBLE PRECISION :: delta_0 !Damage initialisation (out)
DOUBLE PRECISION :: delta_c !final displacement (out)
INTEGER          :: Lcz_array(1000) !Array of active elements (out)
DOUBLE PRECISION :: Ga_array(4000)  !Array of energy release rates (out)
DOUBLE PRECISION :: delta_array(4000)!Array of corr disps (out)
DOUBLE PRECISION :: sigma_array(4000)!Array of tractions
INTEGER          :: Broken_els_array(1000) !Array of broken elements(out)
DOUBLE PRECISION :: dDf_dN !Fatigue damage rate (in)
COMMON /kfatigueexchange/C,m,Delta_l,delta_0,delta_c,Lcz_array,Ga_array,
    delta_array,dDf_dN,Broken_els_array,sigma_array

TYPE (Int_point) Int_point_array(No_Int_points) !derived data type array
    to store integration point coordinates and weight

!-----------------------------------------------------------
!Initializing output variables
!-----------------------------------------------------------
!Initializing Svars in the very first call
IF ((KStep .EQ. 1) .AND. (KInc .EQ. 1)) THEN
  Svars=0.d0
END IF
RHS=0.d0
AMatrx=0.d0
Energy=0.d0
delta=0.d0
sigma=0.d0
v_loc=0.D0
JMatrix=0.D0
Bmatrix=0.D0
DMatrix=0.D0
v3_norm=0.D0

Fatigue=0

!-----------------------------------------------------------
```

```
!Definition of properties
!-------------------------------------------------------------
CALL Properties(GIc,sigmaI_0,K,Ex,Ey,C,m,Delta_l,NLGEOM,NProps,NJProp,
    Props,JProps)

!Calculate initial and final displacement for uexternaldb
delta_0=sigmaI_0/K
delta_c=2.d0*GIc/sigmaI_0

!-------------------------------------------------------------
!Position and weight of integration points
!-------------------------------------------------------------
!These are integration points for Gauss quadrature
Int_point_array(1)%Coordinates(1)=-1.d0/DSQRT(3.d0)
Int_point_array(1)%Coordinates(2)=-1.d0/DSQRT(3.d0)
Int_point_array(1)%weight=1.d0

Int_point_array(2)%Coordinates(1)=1.d0/DSQRT(3.d0)
Int_point_array(2)%Coordinates(2)=-1.d0/DSQRT(3.d0)
Int_point_array(2)%weight=1.d0

Int_point_array(3)%Coordinates(1)=-1.d0/DSQRT(3.d0)
Int_point_array(3)%Coordinates(2)=1.d0/DSQRT(3.d0)
Int_point_array(3)%weight=1.d0

Int_point_array(4)%Coordinates(1)=1.d0/DSQRT(3.d0)
Int_point_array(4)%Coordinates(2)=1.d0/DSQRT(3.d0)
Int_point_array(4)%weight=1.d0

!-------------------------------------------------------------
!Loop over integration points
!-------------------------------------------------------------
Int_Number=0

DO i=1,No_Int_points
  Int_Number=Int_Number+1
!-------------------------------------------------------------
!Shapefunction and shapefunction derivative values
```

```
!-----------------------------------------------------------
  Coordinates(1)=Int_point_array(i)%Coordinates(1)
  Coordinates(2)=Int_point_array(i)%Coordinates(2)

  CALL Shapefunction(Deriv,Shape,Coordinates,Nnode)
!-----------------------------------------------------------
!Calculate cartesian coordinates of Integration points, compute local
   vectors v1, v2, and v3
!and Jacobian matrix
!-----------------------------------------------------------
  CALL Jacobi(v_loc,Jmatrix,v3_norm,Coords,Nnode,shape,Deriv,Ndofel,U,
     MCRD,Nlgeom)
!-----------------------------------------------------------
!Define shape function matrix B
!-----------------------------------------------------------
  CALL BMat(Bmatrix,Shape,Ndofel,v_loc,Nnode)
!-----------------------------------------------------------
!Calculation of relative displacements delta=B*U
!-----------------------------------------------------------
  delta=MATMUL(BMatrix,U)

!-----------------------------------------------------------
!Constitutive law tensor
!-----------------------------------------------------------
  IF (PREDEF(1,1,1) .GT. 0.d0) THEN
     Fatigue=1
     Cycles=Predef(1,1,1)
     DeltaN=Predef(2,1,1)
     !DeltaN=500
  ELSE
     Fatigue=0
  END IF

  prevdamage = Svars(Int_Number)
  prevdelta  = Svars(4+Int_Number)
  prevsigma  = Svars(8+Int_Number)
  prevDamfat = Svars(12+Int_Number)
  prevGa     = Svars(16+Int_Number)
```

```
  CALL Dmat(DMatrix,tDamage,fdamage,dDf_dN,K,sigmaI_0,GIc,Fatigue,delta,
     prevdelta,prevdamage,prevDamfat,Cycles,DeltaN)

!-------------------------------------------------------------
!Calculation of cohesive stresses sigma
!-------------------------------------------------------------
  sigma=Matmul(Dmatrix,delta)
!-------------------------------------------------------------
!Calculation of applied energy release rate Ga
!-------------------------------------------------------------
  IF ((prevdelta .LT. delta_0) .AND. (delta(3) .GT. delta_0)) THEN
    Ga=0.5d0*delta_0*sigmaI_0+0.5d0*(DABS(delta(3))-delta_0)*(DABS(sigma
       (3))+sigmaI_0)
  ELSEIF (delta(3) .GT. delta_0) THEN
    Ga=prevGa*GIc+0.5d0*(DABS(delta(3))-DABS(prevdelta))*(DABS(sigma(3))+
       DABS(prevsigma))
  ELSE
    Ga=0.d0
  END IF

  !Norming Ga against Gc
  Ga=Ga/GIc
  !If element broken at integration point discount value of Ga
  IF (tdamage .GE. 1.d0) THEN
     Ga=0.d0
  END IF
  Svars(Int_Number)=tdamage
  Svars(4+Int_Number)=delta(3)
  Svars(8+Int_Number)=sigma(3)
  Svars(12+Int_Number)=fdamage
  Svars(16+Int_Number)=Ga

  !Save applied energy release rate and displacement at integration point
      for uexternaldb
  Ga_array(4*(JElem-1)+Int_Number)=Ga
  delta_array(4*(JElem-1)+Int_Number)=delta(3)
  sigma_array(4*(JElem-1)+Int_Number)=sigma(3)
```

```
!-----------------------------------------------------------
!Determine right hand side
!-----------------------------------------------------------
  DO j=1,Ndofel
    Do l=1,3
    RHS(j,1)=RHS(j,1)-BMatrix(l,j)*sigma(l)*v3_norm
    END DO
  END DO
!-----------------------------------------------------------
!Compute stiffness matrix K
!-----------------------------------------------------------
  CALL STIFF(Amatrx,Bmatrix,Dmatrix,Ndofel,Int_Number,No_Int_points,
      v3_norm)

END DO
!Determine whether the element is active in the cohesive zone, save in
    lcz_array
!Conditions:
!(1) delta at any integration point >0
!(2) Damage at all integration points <1

i=0
ii=0
DO j=1,No_Int_points
  IF(Svars(j) .GE. 1.d0) THEN
    i=i+1
  END IF
  IF(Svars(4+j) .GT. delta_0) THEN
    ii=ii+1
  END IF
END DO

IF ((i .LT. 4) .AND. (ii .GT. 0)) THEN
   Lcz_array(JELEM)=JElem
ELSE
   Lcz_array(JELEM)=0
END IF
```

```
IF (i.EQ.4) THEN
   Broken_els_array(Jelem)=1
END IF
END SUBROUTINE uel


!-----------------------------------------------------------
!Subroutine to assign loacal variables to physical and problem properties
!-----------------------------------------------------------
SUBROUTINE Properties(GIc,sigmaI_0,K,Ex,Ey,C,m,Delta_l,NLGEOM,NProps,
   NJProp,Props,JProps)
IMPLICIT NONE
INTEGER,INTENT(in)              ::NProps,NJProp
DOUBLE PRECISION, INTENT(in)    ::Props(NProps)
INTEGER, INTENT(in)             ::JProps(NJProp)
DOUBLE PRECISION,INTENT(out)    ::GIc,sigmaI_0,K,Ex,Ey,C,m,Delta_l
INTEGER, INTENT(out)            ::NLGEOM

GIc= Props(1)
sigmaI_0=Props(2)
K=Props(3)
Ex=Props(4)
Ey=Props(5)
 C=Props(6)
m=Props(7)
Delta_l=Props(8)
NLGeom=JProps(1)

END SUBROUTINE Properties

!-----------------------------------------------------------
!Subroutine to define values of shapefunctions and their derivatives at
   an integration point
!-----------------------------------------------------------
SUBROUTINE Shapefunction(Deriv,Shape,Coordinates,Nnode)
IMPLICIT NONE
INTEGER,INTENT(in)              ::Nnode
DOUBLE PRECISION, INTENT(in)    ::Coordinates(2)
```

```
DOUBLE PRECISION,INTENT(out)     ::Deriv(2,Nnode)
DOUBLE PRECISION,INTENT(out)     ::Shape(Nnode)
INTEGER                          ::i,j

Shape(1)=-0.25D0*(1.D0-Coordinates(1))*(1.D0-Coordinates(2))
Shape(2)=-0.25D0*(1.D0+Coordinates(1))*(1.D0-Coordinates(2))
Shape(3)=-0.25D0*(1.D0+Coordinates(1))*(1.D0+Coordinates(2))
Shape(4)=-0.25D0*(1.D0-Coordinates(1))*(1.D0+Coordinates(2))
Shape(5)=-Shape(1)
Shape(6)=-Shape(2)
Shape(7)=-Shape(3)
Shape(8)=-Shape(4)

Deriv(1,1)=-0.25D0*(1.D0-Coordinates(2))
Deriv(1,2)=0.25D0*(1.D0-Coordinates(2))
Deriv(1,3)=0.25D0*(1.D0+Coordinates(2))
Deriv(1,4)=-0.25D0*(1.D0+Coordinates(2))
Deriv(1,5)=Deriv(1,1)
Deriv(1,6)=Deriv(1,2)
Deriv(1,7)=Deriv(1,3)
Deriv(1,8)=Deriv(1,4)

Deriv(2,1)=-0.25D0*(1.D0-Coordinates(1))
Deriv(2,2)=-0.25D0*(1.D0+Coordinates(1))
Deriv(2,3)=0.25D0*(1.D0+Coordinates(1))
Deriv(2,4)=0.25D0*(1.D0-Coordinates(1))
Deriv(2,5)=Deriv(2,1)
Deriv(2,6)=Deriv(2,2)
Deriv(2,7)=Deriv(2,3)
Deriv(2,8)=Deriv(2,4)
END SUBROUTINE Shapefunction

SUBROUTINE Jacobi(v_loc,JMatrix,v3_norm,Coords,Nnode,shape,Deriv,NDofel,U
   ,MCRD,Nlgeom)
IMPLICIT NONE
INTEGER,INTENT(in)               ::Nnode,NDofel,MCRD,Nlgeom
DOUBLE PRECISION, INTENT(in)     ::U(NDofel)
DOUBLE PRECISION, INTENT(in)     ::Coords(MCRD,NNode)
```

```
DOUBLE PRECISION, INTENT(in)    ::Deriv(2,Nnode)
DOUBLE PRECISION, INTENT(in)    ::Shape(Nnode)
DOUBLE PRECISION, INTENT(out)   ::JMatrix(2,3)
DOUBLE PRECISION, INTENT(out)   ::v_loc(3,3)
DOUBLE PRECISION, INTENT(out)   ::v3_norm
DOUBLE PRECISION                ::Coords_nl(3,4)
INTEGER                         ::i
DOUBLE PRECISION                ::v1_norm
!-------------------------------------------------------------
!Calculating the Jacobian
!-------------------------------------------------------------
IF(NLGEOM .EQ.1) THEN
!For nonlinear geometry update the nodal coordinates with the average
   displacements between top and bottom nodes
  DO i=1,4 !Loop over the corners of the element
    Coords_nl(1,i)=Coords(1,i)+0.5D0*(U(3*(i-1)+1)+U(3*(i+3)+1))!x-
       coordinates
    Coords_nl(2,i)=Coords(2,i)+0.5D0*(U(3*(i-1)+2)+U(3*(i+3)+2))!y-
       coordinates
    Coords_nl(3,i)=Coords(3,i)+0.5D0*(U(3*(i-1)+3)+U(3*(i+3)+3))!z-
       coordinates
  END DO
  JMatrix=MATMUL(Deriv(1:2,1:4),TRANSPOSE(coords_nl(1:3,1:4)))
ELSE
  JMatrix=MATMUL(Deriv(1:2,1:4),TRANSPOSE(coords(1:3,1:4)))
END IF

!-------------------------------------------------------------------
!Define local coordinate vectors
!-------------------------------------------------------------------
!-------------------------------------------------------------------
!v1=vxi/||vxi||
!-------------------------------------------------------------------
v1_norm=DSQRT(JMatrix(1,1)**2+JMatrix(1,2)**2+JMatrix(1,3)**2) !Norm of
   v1
v_loc(1,1)=JMatrix(1,1)/v1_norm
v_loc(1,2)=JMatrix(1,2)/v1_norm
```

```
v_loc(1,3)=JMatrix(1,3)/v1_norm

!--------------------------------------------------------------------
!v3=vxi x veta
!--------------------------------------------------------------------
v_loc(3,1)=JMatrix(1,2)*JMatrix(2,3)-JMatrix(2,2)*JMatrix(1,3)
v_loc(3,2)=JMatrix(2,1)*JMatrix(1,3)-JMatrix(1,1)*JMatrix(2,3)
v_loc(3,3)=JMatrix(1,1)*JMatrix(2,2)-JMatrix(2,1)*JMatrix(1,2)
v3_norm=DSQRT(v_loc(3,1)**2+v_loc(3,2)**2+v_loc(3,3)**2)!Norm of v3
v_loc(3,1:3)=v_loc(3,1:3)/v3_norm !Normalized v3

!--------------------------------------------------------------------
!v2=v1 x v3
!--------------------------------------------------------------------
v_loc(2,1)=v_loc(3,2)*v_loc(1,3)-v_loc(1,2)*v_loc(3,3)
v_loc(2,2)=v_loc(1,1)*v_loc(3,3)-v_loc(3,1)*v_loc(1,3)
v_loc(2,3)=v_loc(3,1)*v_loc(1,2)-v_loc(3,2)*v_loc(1,1)
END SUBROUTINE Jacobi

SUBROUTINE BMat(Bmatrix,Shape,Ndofel,v_loc,Nnode)
IMPLICIT NONE
INTEGER,INTENT(in)              ::Nnode,NDofel
DOUBLE PRECISION, INTENT(in)    ::Shape(Nnode)
DOUBLE PRECISION, INTENT(in)    ::v_loc(3,3)
DOUBLE PRECISION, INTENT(out)   ::Bmatrix(3,Ndofel)

DOUBLE PRECISION                ::B_loc(3,Ndofel)
INTEGER                         ::i
!--------------------------------------------------------------------
!B Matrix in local coordinates B=[N -N]
!--------------------------------------------------------------------
B_loc=0.D0
DO i=1,NNode
  B_loc(1,3*(i-1)+1)=Shape(i)
  B_loc(2,3*(i-1)+2)=Shape(i)
  B_loc(3,3*(i-1)+3)=Shape(i)
END DO
!--------------------------------------------------------------------
```

```
!B Matrix in global coordinates B=V*[N -N]
!-------------------------------------------------------------------
Bmatrix=Matmul(v_loc,B_loc)
END SUBROUTINE Bmat

SUBROUTINE Dmat(DMatrix,tDamage,fdamage,dDf_dN,K,sigmaI_0,GIc,Fatigue,
   delta,prevdelta,prevdamage,prevDamfat,Cycles,DeltaN)
IMPLICIT NONE
INTEGER, INTENT(in)             ::Fatigue
DOUBLE PRECISION, INTENT(in)    ::K,sigmaI_0,GIc
DOUBLE PRECISION, INTENT(in)    ::delta(3)
DOUBLE PRECISION, INTENT(in)    ::prevdamage
DOUBLE PRECISION, INTENT(in)    ::prevdelta
DOUBLE PRECISION, INTENT(in)    ::prevDamfat
DOUBLE PRECISION, INTENT(in)    ::Cycles
DOUBLE PRECISION, INTENT(in)    ::DeltaN
DOUBLE PRECISION, INTENT(in)    ::dDf_dN
DOUBLE PRECISION, INTENT(inout) ::Dmatrix(3,3)
DOUBLE PRECISION, INTENT(out)   ::tDamage
DOUBLE PRECISION, INTENT(out)   ::fdamage

DOUBLE PRECISION                ::deltaI
DOUBLE PRECISION                ::deltaI_0
DOUBLE PRECISION                ::deltaI_c
DOUBLE PRECISION                ::sdamage
DOUBLE PRECISION                ::prevsdamage
!-------------------------------------------------
!Mode I static
!-------------------------------------------------
prevsdamage=prevdamage-prevDamfat
sDamage=prevdamage
deltaI=delta(3)
deltaI_c=2.D0*GIc/sigmaI_0 !final displacement
deltaI_0=sigmaI_0/K        !mode I damage threshold

IF (sdamage .LT. 1.D0) THEN
!1 If the element is not broken calculate static damage
   sDamage=0.D0
```

```
   If((deltaI .GT. deltaI_0).AND.(deltaI .LT. deltaI_c))THEN
   !2 Check whether delta is above delta_0 and below delta_c
      sDamage=deltaI_c*(deltaI-deltaI_0)/(deltaI*(deltaI_c-deltaI_0))
   ELSEIF (deltaI .GT. deltaI_c) THEN
   !2 Damage is 1 when delta exceeds delta_c
      sDamage=1.D0
   ELSE
   ! no damage when delta is below delta_0
      sDamage=0.D0
   END IF
ELSE
!1 cap the static damage at 1
   sdamage=1.d0
END IF

IF (sdamage .LT. prevsdamage) THEN
!If model unloads, keep previous damage
   sdamage=prevsdamage
END IF

!-----------------------------------------------------
!Mode I fatigue
!-----------------------------------------------------
IF (Fatigue .EQ. 1) THEN
   IF (deltaI .GT. deltaI_0) THEN
      fdamage=prevDamfat+DeltaN*dDf_dN
   ELSE
      fdamage=0.d0
   END IF
ELSE
   fdamage=prevDamfat
END IF

tdamage=sdamage+fdamage

IF (tdamage .GT. 1.d0) THEN
   tdamage=1.d0
END IF
```

```
Dmatrix=0.D0
Dmatrix(1,1)=K
Dmatrix(2,2)=K
Dmatrix(3,3)=(1.D0-tDamage)*K
!-------------------------------------------------
!End Mode I
!-------------------------------------------------
END SUBROUTINE Dmat

SUBROUTINE Stiff(Amatrx,Bmatrix,Dmatrix,Ndofel,Int_Number,No_Int_points,
   v3_norm)
IMPLICIT NONE
INTEGER,INTENT(in)              ::Ndofel,No_Int_Points,Int_Number
DOUBLE PRECISION, INTENT(in)    ::Dmatrix(3,3)
DOUBLE PRECISION, INTENT(in)    ::Bmatrix(3,Ndofel)
DOUBLE PRECISION, INTENT(out)   ::Amatrx(Ndofel,Ndofel)
DOUBLE PRECISION, INTENT(in)    ::v3_norm

DOUBLE PRECISION                ::Stiff_contribution(Ndofel,Ndofel)

!Secant stiffness matrix
Stiff_contribution=0.D0
Stiff_contribution=Matmul(Transpose(Bmatrix),Matmul(Dmatrix,Bmatrix))*
   v3_norm
Amatrx=Amatrx+Stiff_contribution
END SUBROUTINE Stiff

SUBROUTINE UEXTERNALDB(LOP,LRESTART,TIME,DTIME,KSTEP,KINC)
IMPLICIT NONE

INTEGER, INTENT(in):: LOP !Indicates at what point uexternaldb is
   currently called
INTEGER, INTENT(in):: Lrestart !Indicates whether the analysis was
   restarted
DOUBLE PRECISION, INTENT(in)    ::Time(2) !(current value of time step,
   total time)
DOUBLE PRECISION, INTENT(in)    ::DTime !time increment
```

```
INTEGER, INTENT(in)              ::KStep !current step number
INTEGER, INTENT(in)              ::KInc !current increment number
!LOP=0 start of the analysis.
!LOP=1 start of the current analysis increment (call is repeated if
   Increment does not converge)
!LOP=2 end of the current analysis increment
!LOP=3 end of the analysis
!LOP=4 beginning of a restart analysis

!LRESTART=0 indicates that an analysis restart file is not being written
   for this increment.
!LRESTART=1 indicates that an analysis restart file is being written for
   this increment.
!LRESTART=2 indicates that an analysis restart file is being written for
   this increment and that only one increment is being retained per step
    so that the current increment overwrites the previous increment in
   the restart file

!TIME(1)-Value of current step time.
!TIME(2)-Value of current total time.
DOUBLE PRECISION :: Active_els !Number of active elements
DOUBLE PRECISION :: Ga !Applied energy release rate
INTEGER          :: Ga_pos !Position of maximum energy release rate in
   vectore
DOUBLE PRECISION :: N_f !Number of cycles to fail one element
DOUBLE PRECISION :: Lcz !Cohesive zone length
DOUBLE PRECISION :: D_stat_fail !Static damage at failure displacement
DOUBLE PRECISION :: da_dN !Paris law
DOUBLE PRECISION :: delta_Ga !Displacement for element with maximum Ga
DOUBLE PRECISION :: broken_els
INTEGER          :: iii

!COMMON block variables for Uexternaldb
DOUBLE PRECISION :: C !Paris law constant (in)
DOUBLE PRECISION :: m !Paris law constant (in)
DOUBLE PRECISION :: Delta_l !Element size (in)
DOUBLE PRECISION :: delta_0 !Damage initialisation (in)
DOUBLE PRECISION :: delta_c !final displacement (in)
```

```
INTEGER          :: Lcz_array(1000) !Array of active elements (in)
DOUBLE PRECISION :: Ga_array(4000)  !Array of energy release rates (in)
DOUBLE PRECISION :: delta_array(4000)!Array of corresponding
    displacements(in)
DOUBLE PRECISION :: sigma_array(4000)
DOUBLE PRECISION :: dDf_dN !Fatigue damage rate (out)
INTEGER          :: Broken_els_array(1000) !Array of broken elements (out
    )
COMMON /kfatigueexchange/C,m,Delta_l,delta_0,delta_c,Lcz_array,Ga_array,
    delta_array,dDf_dN,Broken_els_array,sigma_array

IF(LOP .EQ. 0) THEN
   Lcz_array=0
   Ga_array=0.d0
   delta_array=0.d0
   Broken_els_array=0
END IF
!Determine fatigue crack growth rate at the start of the increment
IF ((KInc .GT. 1) .OR. (Kstep .GT. 1)) THEN
   IF (LOP .EQ. 1) THEN
      !Determine the number pf broken elements in the analysis
      broken_els=COUNT(Broken_els_array.GT.0)

      !Determine number of active elements in the analysis
      Active_els=COUNT(Lcz_array.GT.0)

      !Calculate cohesive zone length
      Lcz=DBLE(Active_els)*Delta_l

      !Find maximum G value,its position and corresponding displacement
      Ga=MAXVAL(Ga_array)
      Ga_pos=MAXLOC(Ga_array,1)
      delta_Ga=delta_array(Ga_pos)

      !Calculate crack growth rate
      da_dN=C*Ga**m

      !Calculate number of cycles to failure
```

```
      IF((Lcz .EQ. 0.d0) .OR. (da_dN .EQ. 0.d0)) THEN
         dDf_dN=0.d0
      ELSE
         N_f= Lcz/da_dN
         !Calculate final static damage
         D_stat_fail=(delta_Ga-delta_0)*delta_c/(delta_Ga*(delta_c-
             delta_0))
         IF (D_stat_fail .LT. 0.d0) THEN
            D_stat_fail=0.d0
         END IF
         !Find fatigue damage rate
         dDf_dN=(1.D0-D_stat_fail)/N_f
      END IF
   END IF
ELSE
   dDf_dN=0.d0
END IF
END SUBROUTINE UEXTERNALDB
```

B. Input file for fatigue delamination simulation of the DCB

```
*HEADING
DCB
**
** FATIGUE SIMULATION OF DCB
**
*NODE
1, 0.00, 0.00, 0.00
1001,50.00, 0.00, 0.00
2001, 0.00, 1.00,0.00
3001,50.00, 1.00, 0.00
4001, 0.00, 0.00, 0.25
5001,50.00, 0.00, 0.25
6001, 0.00, 1.00, 0.25
7001,50.00, 1.00, 0.25
8001, 0.00, 0.00, 0.5
9001,50.00, 0.00, 0.5
10001, 0.00, 1.00, 0.5
11001,50.00, 1.00, 0.5
12001, 0.00, 0.00, 0.75
13001,50.00, 0.00, 0.75
14001, 0.00, 1.00, 0.75
15001,50.00, 1.00, 0.75
16001, 0.00, 0.00, 1.0
17001,50.00, 0.00, 1.0
18001, 0.00, 1.00, 1.0
19001,50.00, 1.00, 1.0
20001, 0.00, 0.00, 1.0
21001,50.00, 0.00, 1.0
```

```
22001, 0.00, 1.00, 1.0
23001,50.00, 1.00, 1.0
24001, 0.00, 0.00, 1.25
25001,50.00, 0.00, 1.25
26001, 0.00, 1.00, 1.25
27001,50.00, 1.00, 1.25
28001, 0.00, 0.00, 1.5
29001,50.00, 0.00, 1.5
30001, 0.00, 1.00, 1.5
31001,50.00, 1.00, 1.5
32001, 0.00, 0.00, 1.75
33001,50.00, 0.00, 1.75
34001, 0.00, 1.00, 1.75
35001,50.00, 1.00, 1.75
36001, 0.00, 0.00, 2.0
37001,50.00, 0.00, 2.0
38001, 0.00, 1.00, 2.0
39001,50.00, 1.00, 2.0
*NGEN,NSET=A
1, 1001
2001, 3001
4001, 5001
6001, 7001
8001, 9001
10001, 11001
12001, 13001
14001, 15001
16001, 17001
18001, 19001
20001, 21001
22001, 23001
24001, 25001
26001, 27001
28001, 29001
30001, 31001
32001, 33001
34001, 35001
36001, 37001
```

```
38001, 39001
**************************
**
** nsets
**
**************************
*NSET,NSET=BOTFRONT
1,2001
*NSET,NSET=BOTBACK
33,2033
*NSET,NSET=TOPFRONT
36001,38001
*NSET,NSET=TOPBACK
36033,38033
*NSET,NSET=CLAMP
501,2501,4501,6501,
8501,10501,12501,14501,
16501,18501,20501,22501,
24501,26501,28501,30501,
32501,34501,36501,38501
*NGEN,NSET=COHNODES
16101, 16501
18101, 18501
20101, 20501
22101, 22501
**************************
**
** GENERATION OF ELEMENTS **
**
**************************
*ELEMENT,TYPE=C3D8I
1001,1,3,2003,2001,4001,4003,6003,6001
2001,20001,20003,22003,22001,24001,24003,26003,26001
3001,41,45,2045,2041,4041,4045,6045,6041
4001,20041,20045,22045,22041,24041,24045,26045,26041
5001,201,202,2202,2201,4201,4202,6202,6201
7001,20201,20202,22202,22201,24201,24202,26202,26201
**
```

```
*ELGEN,ELSET=SOLIDO
1001, 20, 2,,,,4,4000,30
2001, 20, 2,,,,4,4000,30
3001, 40, 4,,,,4,4000,50
4001, 40, 4,,,,4,4000,50
5001, 400,1,,,,4,4000,401
7001, 400,1,,,,4,4000,401
**
*USER ELEMENT,TYPE=U1,NODES=8,UNSYMM,COORDINATES=3,
I PROPERTIES=1, PROPERTIES=8, VARIABLES=20
1,2,3
*ELEMENT,TYPE=U1
1,16201,16202,18202,18201,20201,20202,22202,22201
*ELGEN,ELSET=INTER
1, 400,1
*UEL PROPERTY,ELSET=INTER
**
** GIc sigma_0 K Ex Ey C m deltal Nlgeom
0.26, 30.0, 300000.00, 10000.0,10000.0,0.0066,5.9,0.05,1
**
**
*ORIENTATION,NAME=OR1
1.,0.,0.,0.,1.,0.
3,0.
*SOLID SECTION,MATERIAL=CFRP,ELSET=SOLIDO,ORIENTATION=OR1
*MATERIAL,NAME=CFRP
*ELASTIC,TYPE=ENGINEERING CONSTANTS
120.E+03,10.5E+03,10.5E+03,0.3,0.3,0.51,5.25E+03,5.25E+03
3.48E+03
**
** BOUNDARY CONDITIONS**
**
*BOUNDARY
CLAMP,ENCASTRE
**
*PREPRINT,ECH=NO,HISTORY=NO,MODEL=NO
*RESTART,WRITE,FREQ=4,OVERLAY
**
```

```
******************
**
** STEP 1 **
**
******************
*STEP, AMPLITUDE=RAMP, INC=10000
Static loading
*STATIC
0.01,1.0,,0.01
*CLOAD
TOPFRONT,3,7.9672
TOPBACK,3,-7.9672
BOTFRONT,3,-7.9672
BOTBACK,3,7.9672
*SOLUTION TECHNIQUE, TYPE=QUASI-NEWTON
**
** largest residual, ratio of solution correction, , , alternative
   residual
** convergence criterion
**
*CONTROLS,PARAMETERS=FIELD,FIELD=DISPLACEMENT
.05,1.0
*CONTROLS,PARAMETERS=TIME INCREMENTATION
1500,1500,,1500,1500
*CONTROLS,PARAMETERS=LINE SEARCH
4,4,0.25,0.25,0.15
*END STEP
*****************
**
** STEP 2 **
**
*****************
*STEP,INC=10000, AMPLITUDE=STEP
Fatigue loading
*STATIC
0.001,1.1,,0.001
*CLOAD
TOPFRONT,3,7.9672
```

```
TOPBACK,3,-7.9672
BOTFRONT,3,-7.9672
BOTBACK,3,7.9672
*****************************
** Amplitude  definition to define cycles
*****************************
*AMPLITUDE,NAME=amp, TIME=STEP TIME, DEFINITION= TABULAR
0.,0., 1.1,5394600.
*****************************
** Field  definition to define cycles
*****************************
*FIELD, AMPLITUDE=amp
COHNODES, 1
*SOLUTION TECHNIQUE, TYPE=QUASI-NEWTON
*CONTROLS,PARAMETERS=FIELD,FIELD=DISPLACEMENT
.05,1.0
*CONTROLS,PARAMETERS=TIME INCREMENTATION
1500,1500,,1500,1500
*CONTROLS,PARAMETERS=LINE SEARCH
4,4,0.25,0.25,0.15
*END STEP
*************************
** END **
*************************
```

Bibliography

[13a] ASTM D5528 13. *Standard Test Method for Mode I Interlaminar Fracture Toughness of Unidirectional Fiber-Reinforced Polymer Matrix Composites*. ASTM International.

[13b] ASTM D6671 / D6671M 13. *Standard Test Method for Mixed Mode I-Mode II Interlaminar Fracture Toughness of Unidirectional Fiber Reinforced Polymer Matrix Composites*. ASTM International.

[9711] ASTM D6115 97. *ASTM D6115 - 97(2011) Standard Test Method for Mode I Fatigue Delamination Growth Onset of Unidirectional Fiber-Reinforced Polymer Matrix Composites*. ASTM International, 2011.

[ÁBGK14] D. Álvarez, B.R.K. Blackman, F.J. Guild, and A.J. Kinloch. Mode i fracture in adhesively-bonded joints: A mesh-size independent modelling approach using cohesive elements mode i fracture in adhesively-bonded joints: A mesh-size independent modelling approach using cohesive elements. *Engineering Fracture Mechanics*, 115:73–94, 2014.

[AC01] G. Alfano and J.W. Chrisfield. Finite element interface models for delamination analysis of laminated composites: mechanical and computational issues. *International Journal for Numerical Methods in Engineering*, 50:1701–1736, 2001.

[AJMH11] G. Allegri, M.I. Jones, M.R.Wisnom, and S.R. Hallett. A new semi-empirical model for stress-ratio effect on mode ii fatigue delamination growth. *Composites Part A*, 42(7):733–740, 2011.

[ALC95] O. Allix, P. Ladeveze, and A. Corigliano. Damage analysis of interlaminar fracture specimens. *Composite Structures*, 31(1):61–74, 1995.

[Alf06] G. Alfano. On the influence of the shape of the interface law on the application of cohesive-zone models. *Composites Science and Technology*, pages 723–730, 2006.

[And94] J. Andersons. Methods of fatigue prediction for composite laminates. a review. *Mechanics of Composite Materials*, 6:545–554, 1994.

[Arm08] Carlos Alberto Lopez Armas. *Evaluation of Consitutive Laws for the Computer Simulation of Fatigue-driven Delamination in Composite Materials*. PhD thesis, Imperial College London, 2008.

[ASG01] L.E. Asp, A. Sjoergen, and E.S. Greenhalgh. Delamination growth and thresholds in a carbon/epoxy composite under fatigue loading. *Journal of Composites Technology and Research*, 23:55 – 68, 2001.

[BA11] O. Bacarreza and M.H. Aliabadi. A novel methodology for fatigue delamination growth analysis of composites. *Key Engineering Materials*, 488-489:763–766, 2011.

[Bar10] Ever J. Barbero. *Introduction to Composite Materials Design*. CRC Press, 2010.

[BB99] T. Belytchko and T. Black. Elastic crack growth in finite elements with minimal remeshing. *International Journal for Numerical Methods in Engineering*, 45(5):601–620, 1999.

[BBD08] A.J. Brunner, B.R.K Blackman, and P. Davies. A status report on delamination resistance testing of polymer-matrix composites. *Engineering Fracture Mechanics*, 75(9):2779–2794, 2008.

[BGAC04] N. Blanco, E. K. Gamstedt, L. E. Asp, and J. Costa. Mixed-mode delamination growth in carbon-fibre composite laminates under cyclic loading. *International Journal of Solids and Structures*, 41(15):4219 – 4235, 2004.

[Bha10] V.B. Bhandari. *Design of Machine Elements*. Tata Mc Graw Hill, 2010.

[BHSL08] D. Benzerga, A. Haddi, A. Seddak, and A. Lavie. A mixed-mode damage model for delamination growth applied to a new woven composite. *Computational Materials Science*, 41:515–521, 2008.

[BK96] M.L. Benzeggagh and M. Kenane. Measurement of mixed-mode delamination fracture toughness of unidirectional glass/epoxy composites with mixed-mode bending apparatus. *Composites Science and Technology*, 56:439–449, 1996.

[BL88] J.C. Brewer and P.A. Lagace. Quadratic stress criterion for initiation of delamination. *Journal of Composite Materials*, 22:1141–1155, 1988.

[Bla04] N. Blanco. *Variable mixed-mode delamination in composite laminates under fatigue conditions:testing and analysis*. PhD thesis, Univeristat de Girona, 2004.

[BLS95] E.J. Barbero, R. Luciano, and E. Sacco. Three-dimensional plate and contact/friction elements for laminated composite joints. *Computers and Structures*, 54(4):689–703, 1995.

[BMP09] A.J. Brunner, N. Murphy, and G. Pinter. Development of a standardized procedure for the characterization of interlaminar delamination propagation in advanced composites under fatigue mode i loading conditions. *Engineering Fracture Mechanics*, 2009.

[Boy85] Howard E. Boyer. *Atlas of fatigue curves*. ASM International, 1985.

[BSPT13] A.J. Brunner, S. Stelzer, G. Pinter, and G.P. Terrasi. Mode ii fatigue delamination resistance of advanced fiber-reinforced polymer-matrix laminates: Towards the development of a standardized test procedure. *International Journal of Fatigue*, 50:57–62, 2013.

[BST02] B.G.Kumar, R.P. Singh, and T.Nakamura. Degradation of carbon fibre reincorced epoxy composites by ultraviolet radiation and condensation. *Journal of Composite Materials*, 36(4), 2002.

[BW08] C. Balzani and W. Wagner. An interface element for the simulation of delamination in unidirectional fiber-reinforced composite laminates. *Engineering Fracture Mechanics*, 75:2597–2615, 2008.

[CCK+99] J. Chen, M. Crisfield, A.J. Kinloch, E.P. Busso, F.L. Matthews, and Y. Qiu. Predicting progressive delamination of composite material specimens via interface elements. *Mechanics of Composite Materials and Structures*, 6:301–317, 1999.

[CD02] P.C. Camanho and C.G. Davila. Mixed-mode decohesion finite elements for the simulation of delamination in composite materials. Technical report, NASA, 2002.

[Chu10] Deborah D.L. Chung. *Composite Materials: Science and Applications*. Springer, 2010.

[CLSG02] N. Chandra, H. Li, C. Shet, and H. Ghonem. Some issues in the application of cohesive zone models for metal-ceramic interfaces. *International Journal of Solids and Structures*, 39:2827–2855, 2002.

[CMH12] CMH-17. *Polymer Matrix Composites: Guidelines for Characterisation of Structural Materials*, 1g edition, 2012.

[dAPO99] A. de Andres, J.L. Perez, and M. Ortiz. Elastoplastic finite element analysis of three-dimensional fatigue crack growth in aluminium shafts subjected to axial loading. *International Journal of Solids and Structures*, 36:2231–2258, 1999.

[Das11] Dassault Systèmes. *ABAQUS 6.11 Documentation*, 2011.

[Dav96] P. Davies. Development of a standard mode ii shear fracture test procedure. In *ECCM 7*, pages 9–16, 1996.

[DC03] A.J. Davies and P.T. Curtis. Fatigue in aerospace applications. In *Fatigue in Composites*, chapter 26. Woodhead Publishing, 2003.

[DCT08] Carlos G. Davila, Pedro P. Camanho, and Albert Turon. Effective simulation of delamination in aeronautical structures using shells and cohesive elements. *Journal of Aircraft*, 45(2):663–672, April 2008.

[dMG14] M.F.S.F. de Moura and J.P.M. Gonçalves. Development of a cohesive zone model for fatigue/fracture characterization of composite bonded joints under mode ii loading. *Internation Journal of Adhesion and Adhesives*, 2014.

[DP01] J. Degrieck and W. Van Paepegem. Fatigue damage modelling of fibre-reinforced composite materials: Review. *Applied Mechanics Reviews*, 54(4):279–300, 2001.

[Dug60] D. S. Dugdale. Yielding of steel sheets containing slits. *Journal of the Mechanics and Physics of Solids*, 8(2):100 – 104, 1960.

[EHF09] A.M. Elmarakbi, N. Hu, and H. Fukunaga. Finite element simulation of delamination growth in composite materials using ls-dyna. *Composites Science and Technology*, pages 2383–2391, 2009.

[Evi13] Arthur J. Mc Evily. *Metal Failures*. Wiley, 2013.

[Fua06] Chantal Fualdes. Composites @ airbus, damage tolerance methodology. In *FAA Workshop for Composite Damage Tolerance and Maintenance*, 2006.

[GADI09] I. Guiamatsia, J.K. Ankersen, G. A. O. Davies, and L. Iannucci. Decohesion finite element with enriched basis functions for delamination. *Composites Science and Technology*, pages 2616–2624, 2009.

[GB98] P.H. Geubelle and J. Baylor. Impact-induced delamination of laminated composites: a 2d simulation. *Composites Part B Engineering*, 29:589–602, 1998.

[GCA88] A. Gens, I. Carol, and E.E. Alonso. An interface element for the analysis of soil-reinforcement interaction. *Computers and Geotechnics*, 7:133–151, 1988.

[GH87] C.G. Gustafson and M. Hojo. Delamination fatigue crack growth in unidirectional graphite/epoxy laminates. *Journal of Reinforced Plastics and Composites*, 6(1):36–52, 1987.

[GHMJ08] S. Giannis, P. L. Hansen, R. H. Martin, and D. T. Jones. Mode i quasi–static and fatigue delamination characterisation of polymer composites for wind turbine blade applications. *Energy Materials Materials Science and Engineering for Energy Systems*, 3(4):248–256, 2008.

[GJD04] Vinay K. Goyal, Eric R. Johnson, and Carlos G. Davila. Irreversible constitutive law for modeling the delamination process using interfacial surface discontinuities. *Composite Structures*, 65:289–305, 2004.

[GS95] M.D. Gilchrist and N. Svensson. A fractorgraphic analysis of delamination within multidirectional carbon/epoxy laminates. *Composites Science and Technology*, 55:195–207, 1995.

[HAKK07] A. Hosoi, Y. Arao, H. Karasawa, and H. Kawada. High-cycle fatigue characteistics of quasi-isotropic cfrp laminates. *Advanced Composite Materials*, 16:151–166, 2007.

[Har03] Bryan Harris. *Fatigue in Composites*, chapter A historical review of the fatigue behaviour of fibre-reinforced plastics. Woodhead Publishing, 2003.

[Har08] Paul Harper. *Fatigue of Composite Truss Structures*. PhD thesis, University of Bristol, 2008.

[HH08] Paul W. Harper and Stephen R. Hallett. Cohesive zone length in numerical simulations of composite delamination. *Engineering Fracture Mechanics*, 75(16):4774–4792, 2008.

[HH10] P.W. Harper and S.R. Hallett. A fatigue degradation law for cohesive interface elements – development and application to composite materials. *International Journal of Fatigue*, 2010.

[HMP76] A. Hillerborg, M. Modeer, and P.-E. Petersson. Analysis of crack formation and crack growth in concrete by means of fracture mechanics and finite elements. *Cement and Concrete Research*, 6(6):773 – 781, 1976.

[HOGT94] M. Hojo, S. Ochiai, C.G. Gustafson, and K. Tanaka. Effect of matrix resin on delamination fatigue crack growth in cfrp laminates. *Engineering Fracture Mechanics*, 49(1):35–47, 1994.

[HR73] Z. Hashin and A. Rotem. A fatigue failure criterion for fibre reinforced materials. *Journal of Composite Materials*, pages 448–464, 1973.

[HTGH87] M. Hojo, K. Tana, C.G. Gustafson, and R. Hayashi. Effect of stress ratio on near-threshold propagation of delamination fatigue cracks in unidirectional cfrp. *Composites Science and Technology*, 29:273–292, 1987.

[HTO91] H. Hojo, K. Tsuda, and K. Ogasawara. Form and rate of corrosion of corrosion-resistant frp resins. *Advanced Composite Materials*, 1(1):55–67, 1991.

[JSGW07] W. Jiang, S.R, B.G. Green, and M.R. Wisnom. A concise interface constitutive law for analysis of delamination and splitting in composite materials and its application to scaled notched tensile specimens. *International Journal for Numerical Methods in Engineering*, 69:1982–1995, 2007.

[KB97] M. Kenane and M.L. Benzeggagh. Mixed-mode delamination fracture toughness of unidirectional glass/epoxy composites under fatigue loading. *Composites Science and Technology*, 57(5):597–605, 1997.

[KCKA10] H. Khoramishada, A.D. Crocombea, K.B. Katnama, and I.A. Ashcroft. Predicting fatigue damage in adhesively bonded joints using a cohesive zone model. *International Journal of Fatigue*, 32(7):1146–1158, 2010.

[KH12] Luiz F. Kawashita and Stephen R. Hallett. A crack tip tracing algorithm for cohesive interface element analysis of fatigue delamination propagation in composite materials. *International Journal of Solids and Structures*, 49:2898–2913, 2012.

[KZSB11] M. Kenane, Z.Azari, S.Benmedakhene, and M.L. Benzeggagh. Experimental development of fatigue delamination threshold criterion. *Composites Part B*, 42:367–375, 2011.

[LL12] B. Landry and G. LaPlante. Modeling delamination growth in composites under fatigue loadings of varying amplitudes. *Composites Part B*, pages 533–541, 2012.

[LSD99] J. Lemaitre, J.P. Sermage, and R. Desmorat. A two scale damage concept applied to fatigue. *International Journal of Fracture*, 97:67–81, 1999.

[maa08] *Maaximus Description of Work*, 2008.

[MALA85] T. Mohlin, A.F.Blom, L.A.Carlsson, and A.I.Gustavsson. *Delamination Growth in a Notched Graphite/Epoxy Laminate under Compression Fatigue Loadingotched Graphite/Epoxy Laminate under Compression Fatigue Loading*. ASTM, 1985.

[Mar03] R. Martin. *Fatigue in Composites*, chapter Delamination Fatigue, pages 173–187. Woodhead, 2003.

[MB02] Nicloas Moes and Ted Belytchko. Extended finite element method for cohesive crack growth. *Engineering Fracture Mechanics*, 69:813–833, 2002.

[MC97] Y Mi and M.A. Crisfield. Analytical derivation of the load/displacement relationship for the dcb and mmb and prood of the fea formulation. Technical report, IC-AERO Report 97-02, 97.

[MCHD98] Y. Mi, M. A. Crisfield, H.B. Hellweg, and G. A. O. Davies. Progressive delamination using interface elements. *Journal of Composite Materials*, 32:1242–1272, 1998.

[MD99] R.H. Martin and B.D. Davidson. Mode ii fracture toughness evaluation using a four point bend end notched flexure test. *Platics, Rubber, and Composites*, 28(8):401–406, 1999.

[Mer03] *Merriam-Webster Collegiate Dictionary, 11th edition*. Merriam Webster,U.S, 2003.

[MG05] S. Maiti and P.H. Geubelle. A cohesive model for fatigue failure of polymers. *Engineering Fracture Mechanics*, 72(5):691–708, 2005.

[MH11] Michael May and Stephen R. Hallett. An advanced model for initiation and propagation of damage under fatigue loading – part i: Model formulation. *Composite Structures*, pages 2340–2349, 2011.

[miy04] *Fatigue life prediction of CFRP laminates under temperature and moisture environments*, volume 36. SEM International Congress and Exposition on Experimental and Applied Mechanics, 2004.

[MM90] R.H. Martin and G.B. Murri. *Characterisation of mode I and mode II delamination growth and thresholds in AS4/PEEK composites*, pages 251–270. ASTM, 1990.

[MP12] F. Moroni and A. Pirondi. A procedure for the simulation of fatigue crack growth in adhesively bonded joints based on a cohesive zone model and various mixed-mode propagation criteria. *Engineering Fracture Mechanics*, 89:129–138, 2012.

[Mur12] Gretchen B. Murri. Evaluation of delamination growth characterization methods under mode i fatigue loading. In *ASTM D30 Meeting*, 2012.

[NBV22] P. Naghipour, M. Bartsch, and H. Voggenreiter. Simulation and experimental validation of mixed mode delamination in multidirectional cf/peek laminates under fatigue loading. *International Journal of Solids and Structures*, 48:1070–1081, 2022.

[Nee87] A. Needleman. A continuum model for void nucleation by inclusion debonding. *Journal of Applied Mechanics*, 54(3):525–531, 1987.

[Nee90] A. Needleman. An analysis of decohesion along an imperfect interface. *International Journal of Fracture*, 42:21–40, 1990.

[NROR01] O. Nguyen, E.A. Repetto, M. Ortiz, and R.A. Radovitzky. A cohesive model of fatigue crack growth. *International Journal of Fracture*, 110:351–369, 2001.

[O'B81] T.Kevin O'Brien. Characterisation of delamination onset and growth in a composite laminate. Technical Report 81940, NASA Langley Research Center, 1981.

[O'B09] T. Kevin O'Brien. Development of a composite delamination fatigue life prediction methodology. Technical report, NASA Langley Research Center, 2009.

[OP99] M. Ortiz and P. Pandolfi. Finite-deformation irreversible cohesive elements for three-dimensional crack-propagation analysis. *International Journal for Numerical Methods in Engineering*, 44:1267 – 1282, 1999.

[Paa90] M.H.J.W. Paas. *Continuum damage mechanics with an application to fatigue*. PhD thesis, Technical University Eindhoven, 1990.

[PAR13] J.A. Pascoe, R.C. Alderliesten, and R.Benedictus. Methods for the prediction of fatigue delamination growth in composites and adhesive bonds- a crictical review. *Engineering Fracture Mechanics*, (112-113):72–96, 2013.

[PBRdB62] R. Peerlings, W. Brekelmans, and M. Beers R. de Borst. The mathematical theory of equilibrium cracks in brittle fracture. *Advan. Appl. Mech.*, 7:55–129, 1962.

[PBRdB00] R. Peerlings, W. Brekelmans, and M. Beers R. de Borst. Gradient-enhanced damage modelling of high-cyclic fatigue. *International Journal for Numerical Methods in Engineering*, 49:1457 – 1569, 2000.

[PGA61] P. Paris, M. Gomez, and W. Anderson. A rational analytical theory of fatigue. *Trend in Engineering*, 13:9–14, 1961.

[PIR06] S.T. Pinho, L. Iannucci, and P. Robinson. Formulation and implementation of decohesion elements in an explicit finite element code. *Composites Part A*, 37(778-789), 2006.

[PM10] A. Pirondi and F. Moroni. A progressive damage model for the prediction of fatigue crack growth in bonded joints. *The Journal of Adhesion*, 86:501–521, 2010.

[Pro12] Proceedings of the Institution of Mechanical Engineers, Part L: Journal of Materials Design and Applications. *A review of advances in fatigue and life prediction of fibre reinforced composites*, 2012.

[QCA01] Y. Qiu, M.A. Crisfield, and G. Alfano. An interface element formulation for the simulation of delamination with buckling. *Engineering Fracture Mechanics*, 68:1755–1776, 2001.

[QR06] M. Quaresimin and M. Ricotta. Life prediction of bonded joints in composite materials. *International Journal of Fatigue*, 28:1166–76, 2006.

[RA02] D. Revuelta and A.Miravete. Fatigue damage in composite materials. *International Applied Mechanics*, 38(2), 2002.

[RC90] J.R. Reeder and J.H. Crews. Mixed-mode bending method for delamination testing. *AIAA Journal*, 28(7):1270–1276, 1990.

[RDW04] J.R. Reeder, K. Demarco, and K.S. Whitley. The use of doubler reinforcement in delamination toughness testing. *Composites Part A: Applied Science and Manufacturing*, 35(11):1337–1344, 2004.

[Rei91] K.L. Reifsneider, editor. *Fatigue of Composite Materials*. Elsevier, 1991.

[RGT+05] Paul Robinson, Ugo Galvanetto, Davide Tumino, Giordano Bellucci, and David Violeau. Numerical simulation of fatigue-driven delamination using interface elements. *International Journal for Numerical Methods in Engineering*, 63(13):1824–1848, 2005.

[Ric80] J. R. Rice. The mechanics of earthquake rupture. In *in Physics of the Earth's Interior, edited by A.M. Dziewonski and E. Boschi*, pages 555–649, 1980.

[RS03] K.L. Roe and T. Siegmund. An irreversible cohesive zone model for interface fatigue crack growth simulation. *Engineering Fracture Mechanics*, pages 209–232, 2003.

[R.T81] R.Talreja, editor. *Fatigue of composite materials: damage mechanisms and fatigue-life diagrams*, volume 378. Proceedings of the Royal Society, 1981.

[Rus82] A.J. Russell. On measurement of mode ii interlaminar fracture energies. Technical report, Materials DREP report 82-0, 1982.

[Sal72] M.J. Salkind. Fatigue of composites. In *Composite Materials: Testing and Design (2nd Conference)*. ASTM, 1972.

[SdB93] J.C.J. Schellekens and R. de Borst. On the numerical integration of interface elements. *International Journal for Numerical Methods in Engineering*, 36:43–66, 1993.

[SGL08] Sergio Sadaba, Carlos Gonzalez, and Javier L. Lorca. Virtual testing of composites laminate coupons. 2008.

[Sie04] T. Siegmund. Anumericalstudyoftransientfatiguecrackgrowth by use of an irreversible cohesive zone model. *International Journal of Fatigue*, pages 929–939, 2004.

[ST09] M. Quaresimin L. Susmel and R. Talreja. Fatigue behaviour and life assesment of composite laminates under multiaxial loadings. *International Journal of Fatigue*, 32:2–16, 2009.

[SvDG11] M. Samimi, J.A.W. van Dommelen, and M.G.D. Geers. A self-adaptive finite element approach for simulation of mixed-mode delamination using cohesive zone models. *Engineering Fracture Mechanics*, 78:2202–2219, 2011.

[Tal87] R. Talreja. *Fatigue of Composite Materials*. Technomic, 1987.

[Tal08] R. Talreja. Damage and fatigue in composites- a personal account. *Composites Science and Technology*, 68:2585–2591, 2008.

[Tay03] T.E. Tay. Characterization and analysis of delamination fracture in composites: An overview of developments from 1990 to 2001. *Applied Mechanics Review*, 56(1), 2003.

[TC07] D. Tumino and F. Cappello. Simulation of fatigue delamination growth in composites with different mode mixtures. *Journal of Composite Materials*, 41(20), 2007.

[TCCD07] A. Turon, J. Costa, P.P. Camanho, and C.G. Davila. Simulation of delamination in composites under high-cycle fatigue. *Composites Part A: Applied Science and Manufacturing*, 38(11):2270 – 2282, 2007.

[TDCC05] A. Turon, C.G. Davila, P.P. Camanho, and J. Costa. An engineering solution for using coarse meshes in the simulation of delamination with cohesive zone models. Technical Report NASA/TM-2005-213547, NASA, 2005.

[TH92] V. Tvergaard and J.W. Hutchinson. The relation between crack growth resistance and fracture process parameters in elastic-plastic solids. *Journal of the Mechanics and Physics of Solids*, 40:1377–1397, 1992.

[TT95] H. Tanaka and K. Tanaka. Mixed-mode growth of interlaminar cracks in carbon/epoxy laminates under cyclic loading. In *Proceedings of ICCM 10, Whistler, Canada*, pages 181–189, 1995.

[Tur06] A. Turon. *Simulation of delamination in composites under quasi-static and fatigue loading using cohesive zone models*. PhD thesis, Univeristat de Girona, 2006.

[WACS02] M.M. Abdel Wahab, I.A. Ashcroft, A.D. Crocombe, and P.A. Smith. Numerical prediction of fatigue crack propagation lifetime in adhesively bonded structures. *International Journal of Fatigue*, 24:705–09, 2002.

[XA93] X.-P. Xu and A.Needleman. Void nucleation by inclusion debonding in a crystal matrix. *Modelling and Simulation in Materials Science and Engineering*, 1(2):111, 1993.

[XN94] X.-P. Xu and A. Needleman. Numerical simulations of fast crack growth in brittle solids. *Journal of the Mechanics and Physics of Solids*, 42(9):1397 – 1434, 1994.

[YMRC01] B. Yang, S. Mall, and K. Ravi-Chandar. A cohesive zone model for fatigue crack growth in quasibrittle materials. *International Journal of Solids and Structures*, pages 3927–3944, 2001.